Multi-wavelength studies of protoplanetary discs

Veronica Roccatagliata
Max-Planck-Institut für Astronomie

Heidelberg 2010

Dissertation in Astronomy
submitted to the
Combined Faculties for the Natural Sciences and for Mathematics
of the Ruperto-Carola University of Heidelberg, Germany.
for the degree of
Doctor of Natural Sciences

presented by

Dipl.-Phys. Veronica Roccatagliata
born in Venezia, Italy

Oral examination: 28. 04. 2010

Multi-wavelength studies of protoplanetary discs

Referees: **Prof. Dr. Thomas Henning**
Prof. Dr. Sebastian Wolf

This thesis is dedicated
to **Davide, Giovanni & Elena**

Contents

Abstract

The early evolutionary stages of a pre-main sequence star are characterised by the formation of a dense accretion disc. These discs provide the environment and material in and from which planets are expected to form. At this epoch circumstellar material is accreting onto the central star, while small dust grains in the disc interior coagulate into larger objects and gravitationally settle into the mid-plane. These are the first steps of planet formation. The study of the dust properties (e.g. grain size distribution, dissipation timescale) in protoplanetary discs is then fundamental to understand how planets form.
In this thesis I present three works aimed at studying the formation, dissipation and long term evolution of protoplanetary discs, respectively. The first project investigates the properties of the young binary system Haro 6-10. I present the results of multi-wavelength high spatial resolution observations of Haro 6-10 aimed at characterising the large- and small-scale structures of the binary system.
The second project is a combined infrared (Spitzer/IRAC) and X-ray (Chandra/ACIS) survey of the OB association IC 1795. This program is aimed at studying the evolution of protoplanetary discs in regions of massive star formation.
The last project is the deepest single dish millimetre survey of debris discs around solar-type stars to date. The aim of this work is to study the evolution of the debris dust mass with time and to characterise the structure of these discs.

Zusammenfassung

Die frühen Entwicklungsphasen eines Vor-Hauptreihensternes sind durch die Bildung einer dichten Akkretionsscheibe gekennzeichnet. Diese Scheiben stellen die Umgebung dar und liefern das Material, aus dem Planeten entstehen. Zu diesem Zeitpunkt wird zirkumstellares Material auf den Zentralstern akkretiert und kleine Staubteilchen im Inneren der Scheibe koagulieren zu grösseren Objekten. Diese siedeln sich dann auf Grund der Gravitation in der Mittelebene der Scheibe an. Dies beschreibt die ersten Schritte in der Planetenentstehung. Daher ist es wichtig die Staubeigenschaften (z. B. die Verteilung der Teilchengroesse, Zeitskala der Dissipation) in protoplanetaren Scheiben zu untersuchen, um die Entstehung von Planeten zu verstehen.
In der vorliegenden Dissertation werde ich drei verschiedenen Arbeiten vorstellen, die das Ziel hatten, die Entstehung, Dissipation und Langzeitentwicklung der protoplanetaren Scheiben zu erforschen. Das erste Projekt untersucht die Eigenschaften des jungen Doppelsystems Haro 6-10. Anhand von multi-spektralen, räumlich hochaufgelösten Beobachtungen sollen die Strukturen dieses Doppelsystems auf grossen und kleinen Skalen charakterisiert werden.
Des Weiteren wird die Entwicklung von protoplanetaren Scheiben in Regionen massereicher Sternentstehung studiert. Die hier vorgestellten Ergebnisse basieren dabei auf einer Durchmusterung der OB Assoziation IC 1795, die aus Infrarotbeobachtungen mit Spitzer/ IRAC und Chandra/ACIS Beobachtungen im Röntgenbereich kombiniert wurde.
Das letzte Projekt befasst sich mit der tiefsten Durchmusterung von Debris-Scheiben um sonnenähnliche Sterne, die bis heute mit einem Einzelteleskop im Millimeterbereich durchgeführt wurde. Das Ziel dieser Studie ist die zeitliche Entwicklung der Staubmasse in den Debris-Scheiben zu untersuchen und die Struktur dieser Scheiben zu charakterisieren.

1 Introduction

Circumstellar discs around pre-main sequence stars are important because they regulate the formation of the star through the mass accretion process. Moreover these discs are the birth-sites of planetary systems, hence the often used term 'protoplanetary disc'. In order to understand the star- and planet formation processes, the study of the physical mechanisms in protoplanetary discs is required. One of the most widely accepted theory of star-formation, known as the *nebular hypothesis*, was originally formulated in the 18th century by Emanuel Swedenborg and later elaborated and expanded upon by Immanuel Kant and Pierre-Simon Laplace. The basic idea is that a star forms from the collapse of a molecular cloud under its own gravity. To conserve the initial angular momentum of the cloud, a circumstellar disc-like structure forms around the proto-star. Through this disc the nebular material is accreted into the star and angular momentum is transported outward. These discs have typical masses (10^{-3}-10^{-2}M$_\odot$) and sizes comparable to what is expected for the primitive solar nebula (see e.g. Andrews & Williams, 2008, for a extended review).

Direct observations of protoplanetary discs took flight from the early 80's when new infrared instruments became available. At these wavelengths, young stars showed a strong luminosity excess above the stellar photosphere. It was soon realised that such an infrared excess is origi-

nated in the circumstellar material: the dust grains present in the latter absorb the UV and optical stellar radiation and re-emit it at longer wavelengths. The infrared excess is different from source to source. In particular, younger systems show a much stronger excess compared to older stars. By measuring the slope of the spectral energy distribution (SED) between 1 μm and 20 μm Lada (1987) classified young stars in distinct classes. Each class is associated with a different stage of the star formation process, ranging from the early phase, when the proto-star is still embedded in its parent molecular cloud (strong excess), to the final stage where the star has reached the main sequence and the circumstellar material is dispersed (no excess).
The disc emission extends from $\sim$ 1 μm to millimetre wavelengths and the emission at different wavelengths is associated with different regions of the disc. For a solar-type star, near-infrared emission traces the hot dust in the disc surface layers close to the central star at 0.003-0.1 AU (see Fig. 1.1). Between 0.2 and 10 AU, the disc emits in the mid-infrared wavelength range, while the outer regions of the disc (10-100 AU) emit in the far-infrared and millimetre. In reality, a circumstellar disc has a vertical temperature gradient as well. The coldest (millimetre) emission comes not only from the outer part of the disc but also from the disc mid-plane which is shielded from the stellar radiation and is colder than the outer layers.
Modelling of the SED is widely used to infer the physical properties of the disc. However, due to the high degeneracy of the parameter space, the modelling of the SED alone does not allow to fully constrain the structure of the disc. This degeneracy can be reduced by combining high-resolution images at different wavelengths (e.g., Wolf et al., 2003). In the last decades the onset of 8m class telescopes (e.g. the Very Large Telescope (VLT) and W. M. Keck Observatory) and long baseline interferometers (e.g. VLTI, SMA, PdBI), has enormously improved the spatial and spectral resolving power in observational astronomy. These facilities allow to resolve the circumstellar discs at different wavelengths (e.g. Fig. 1.2). Comparing these high resolution images to the theoretical predictions of the radiative transfer models, it is possible to constrain the size of the disc as well as to infer which physical mechanisms take place in its interior (e.g. Wolf et al., 2008, 2003; Sauter et al., 2009).

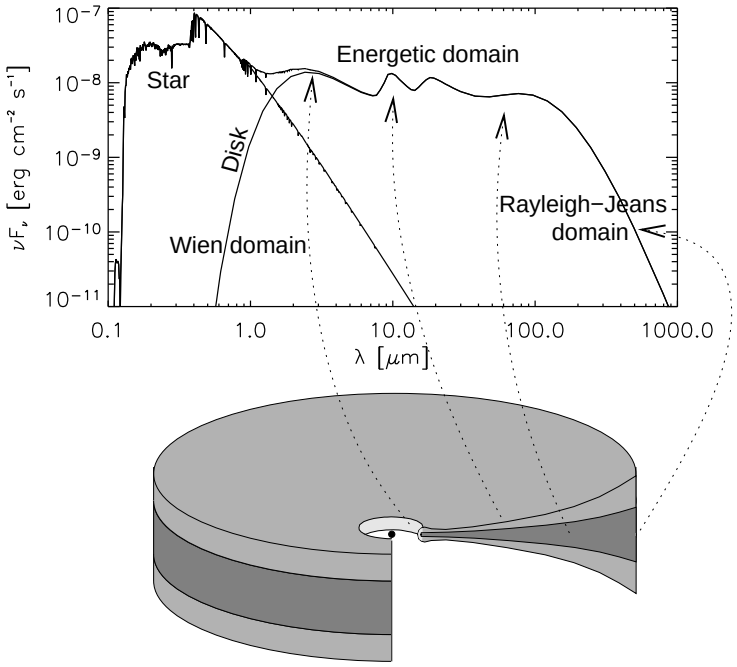

Figure 1.1 *From Dullemond et al. (2007)*: Build-up of the SED of a flaring protoplanetary disc and the origin of various components.

1.1 Disc evolution

Discs are observed to evolve very fast and to dissipate their dust within a few Myr years from the collapse of the molecular cloud. In order to address the lifetime of the disc and to test the planet formation theories, astronomers have analysed the fraction of stars with disc in young clusters at different ages. The first studies were done using the emission in the near-infrared which traces the inner part of the disc (Haisch et al., 2001). In young clusters (∼1 Myr) the fraction of discs is about 90%-80%. In about 3-4 Myr the fraction of discs is reduced down to 50%-40%. At 5 Myr the disc fraction drops to ∼20% and after 10 Myr almost all discs are dissipated. More recently these studies have been updated in the mid-infrared wavelength range using the Spitzer Space Telescope. The trend identified (e.g. Hernández et al., 2007) is consistent with the original study of Haisch et al. (2001) (see Fig. 1.3).

In a similar fashion it is possible to trace the evolution of gas in discs. In

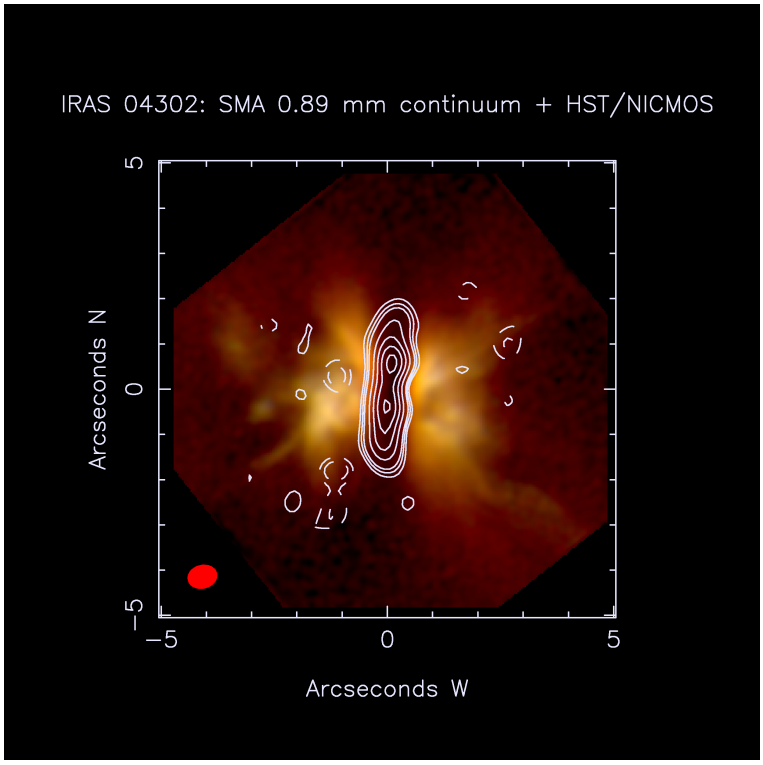

Figure 1.2 *From Wolf et al. (2008)*: Submillimetre map of the Butterfly Star (894 μm, contour lines), overlayed on the near-infrared scattered light map (Padgett et al., 1999). The size and orientation of the synthesised beam are indicated in the lower left of the figure.

particular authors have measured the fraction of accreting stars in young clusters at different ages (e.g. Fedele et al., 2010; Sicilia-Aguilar et al., 2010). The decrease of the fraction of discs which are accreting material into the central is similar to the dissipation of the dust. However, at each age the fraction of accreting stars is lower than the fraction of stars with infrared excess. This might suggest that accretion is stopped before all the dust is dissipated in the disc. These studies suggest a mean disc lifetime of $< 3 \times 10^6$ yr. This is a strong constraint on the time available to form giant planets.

The major mechanisms responsible for the dissipation of the disc material are:

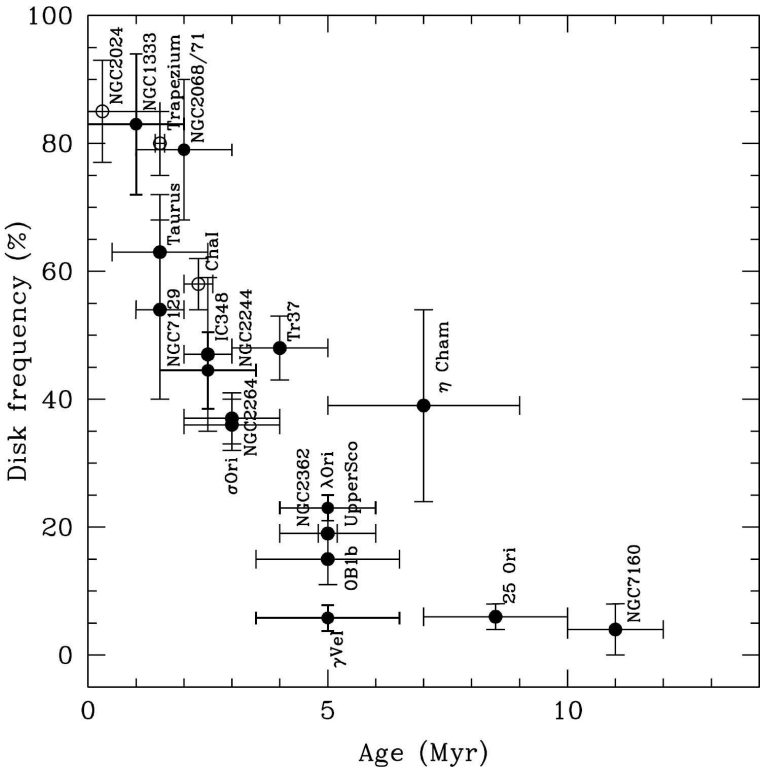

Figure 1.3 *From Hernández et al. (2007)*: Open circles represent the disc frequency for stars in the TTS mass range, derived using JHKL observations and filled symbols represent the disc frequency calculated for stars in the TTS mass range using IRAC data.

1. mass accretion (Hartmann, 1998);
2. disc photoevaporation by the radiation of the central star or by an external radiation (e.g. Clarke et al., 2001; Alexander et al., 2007);
3. planet formation.

The **accretion** of mass from the circumstellar disc into the central star enhances the infrared emission, while the infall of material onto the photosphere of the central star causes a high-temperature optical/UV continuum emission (*veling*); in the case of high accretion rate the photospheric absorption lines are not visible and strong emission lines become dominant. Typical mass accretion rates for solar-type stars are $\sim 10^{-7 \div -8} M_{\odot}/yr$. Considering only the accretion as disc dissipation

mechanism, the disc would disappear in > 10 Myr (Hartmann, 1998), a value that is too long compared to the observed disc lifetime.
The **photoevaporation** process refers to the mass-loss from a circumstellar disc due to radiative heating of the disc material, either from the central star or by an external heating source. Clarke et al. (2001) investigated the effect of the EUV (hν >13.6 eV) radiation from a central low-mass star alone. They found that the combination of EUV radiation with disc viscosity (accretion) is very efficient in removing disc material on a timescale comparable to the observed lifetime. The most recent development of this model by Gorti & Hollenbach (2009) includes the far- ultraviolet (FUV; 6 eV< $h\nu$ <13.6 eV) and X-rays radiation from the accreting star as additional source of photoevaporation.
The conventional models of **planet formation** are via *"core accretion"* and *"gravitational instabilities"*. The *"core-accretion"* planet formation model (Pollack et al., 1996) predicts the formation of giant planets in *3 steps*:

- The formation of a solid core through accretion of planetesimals that were formed by sedimentation and coagulation of small dust grains;
- As the core is massive enough (∼15-20 $M_\oplus$) it will attract gas and form a gaseous envelope;
- Runaway gas accretion occurs and the envelope is attracted onto the core to form the planet's atmosphere.

This model is highly dependent on the dust content (Ida & Lin, 2004) and hence it favours the hypothesis that planet formation is enhanced by the high metallicity of the host star. According to these models, the formation of giant planets lasts ∼10 Myr. Tidal interactions between the proto-planet and the disc, can cause migration of the planet. If planet migration is taken into account (e.g. Alibert et al., 2005), the giant planet formation is much faster (∼3Myr).

The *"gravitational instability"* model of planet formation (Boss, 1997) predicts that a gravitational instability develops in the proto-planetary disc. The instability takes place when a region in the disc becomes cool or develops an high surface density. This forms clumps of gas and dust which become the cores of the proto-planets. In this model, planets form in less than 1 Myr.

Observations can put some constrains on the two theories presented: The timescale predicted by the *"core accretion"* model might be too long compared to the typical dissipation timescale of circumstellar discs of about 3 Myr. The *"gravitational instability"* models are not efficient instead in forming close-in planets, which have been mostly observed so far.

1.2 Debris disc phase

After the dissipation of gas and dust from the disc, the dust grains are removed from the optically thin disc by radiation pressure, Poynting-Robertson drag or dust sublimation on timescales shorter than the stellar pre-main sequence lifetime (Backman & Paresce, 1993; Meyer et al., 2007). Nevertheless, an infrared excess above the stellar photosphere has been discovered around more than 300 pre- and main-sequence stars. These stars are thought to host a remnant *debris* of the primordial accretion disc. Backman & Paresce (1993) suggested that the infrared excess of these objects comes from small dust particles that are the products of collisions of larger bodies. Thus, a debris disc should consist of a 'second generation' of small dust particles, larger bodies and, possibly, planets. The formation of large bodies is thought to be faster in the inner part of the disc (Kenyon & Bromley, 2004). As a consequence, new small dust particles will be produced by collisions first in the inner region of the disc and later further out (Kenyon & Bromley, 2004). During this phase, small dust particles are continuously produced in the disc.

1.3 About this thesis

In this thesis I present three studies concerning formation, dissipation, and long term evolution of circumstellar discs around pre-main sequence stars.

Multi-wavelength analysis of the young binary Haro 6-10: What can we learn about binary formation?
During the early phases of star-formation a binary system may form and both the components may be surrounded by a disc. Although these discs are usually aligned, misaligned discs in binary systems have been also observed. The discovery of these sources has some important implications on the binary formation scenario. In order to investigate this particular class of objects, I have carried out a multi- wavelengths study of Haro 6-10, a young binary system with an infrared companion. I combined different kind of observations: optical photometry obtained with HST, near-infrared photometry with VLT/NACO, mid-infrared spectroscopy and interferometry obtained respectively with TIMMI2 (at the 3.6m ESO telescope) and VLT/MIDI. In chapter 2, the analysis of this unique collection of data is presented.

Disc lifetime in OB associations: Does the environment influence the disc evolution?
Although most of the stars are born in high mass environments, previous studies on disc evolution were mainly concentrated on low-mass star-forming regions. To investigate how high mass stars in OB associations influence disc evolution, I have carried out an infrared survey (with Spitzer/IRAC) of OB associations with various ages. In particular, this survey combines infrared (IRAC) with X-ray (Chandra/ACIS) observations. Combining the two datasets is a powerful technique to remove as much as possible contamination due to field stars and background objects in the Spitzer/IRAC survey. The case of IC 1795 is presented in chapter 3.

Debris disc evolution: How the dust is removed from debris discs? Is the structure of debris disc around solar-type stars similar to our solar system?
The dissipation of debris discs takes place by radiation pressure and/or Poynting-Robertson drag. By studying the evolution of the debris dust mass with time is possible to infer which mechanism is the major responsible for the dust removal (Dominik & Decin, 2003; Wyatt et al.,

2007a,b; Löhne et al., 2008). The structure and the typical grain size of debris discs around solar-type stars can be determined by modelling their SEDs. I carried out a survey in the millimetre wavelengths of debris discs around solar-type stars older than 30Myr. The analysis and results of this study are included in chapter 4.

The conclusions of the thesis and the future work are drawn in chapter 5.

2

Multi-wavelength observations of the young binary system Haro 6-10

Based on the paper: 'Multi-wavelength observations of the young binary system Haro 6-10' - Roccatagliata V., Ratzka Th., Henning Th., Wolf S., Bouwman J., Leinert Ch. - To be submitted to A&A

2.1 Introduction

The formation of binary and multiple systems seems to be a common phenomenon in star formation (e.g. Mathieu et al., 2000). Surveys of young star-forming regions with high spatial resolution allow a statistical description of the binary parameters and a comparison between regions of various ages and with different environments (e.g. Leinert et al., 1993; Duchêne et al., 2007). Binarity has been studied also in young stellar clusters of various ages to investigate its relation to the evolution of protoplanetary discs (e.g. Clarke & Pringle, 1991b; Bouwman et al., 2006). During the first stages of star-formation, a binary or multiple system may form. The formation of a binary takes place when the core of the

molecular cloud in gravitational collapse fragments. The fragmentation process is caused either by an initial density perturbation of the molecular cloud ('prompt initial fragmentation'; Pringle, 1989), or an asymmetric instability in the rotational disc or ring. These precess are called *direct fragmentation* and *rotational fragmentation*, respectively.
After the formation of the binary system, a disc forms only around the primary star (and not around the secondary) if only gas with low angular momentum is accreting onto the star. If the secondary star is surrounded by a disc, necessarily also the primary harbours a circumstellar disc (Bate & Bonnell, 1997). According to the fragmentation scenario of binary formation the discs tend to have similar inclinations. If however, two spatially distinguished parts of the molecular cloud collapse under their own gravity and successively interact gravitationally and form a binary system, this may originate two misaligned discs (e.g. Bate et al., 2000). Under more complicated initial conditions, a small cluster can be formed. The interaction between stars with discs can cause a dissipative encounter (e.g. Clarke & Pringle, 1991b). This lead to the formation of binary or multiple systems via capture of the passing object and thus with misaligned discs. In dense star-forming regions, a massive accretion disc may enable the capture of a passing star (Clarke & Pringle, 1991a). The observed inclination of the two discs may not reflect their initial inclination. This is the case when strong tidal interactions can align the discs. In a small cluster, a few percent of the stars can experience a tilt of few degrees during the star encounters in one million years (Heller, 1993). The tilt of a disc can also be induced by gravitational interaction of a passing object causes (Bate et al., 2000).
Studying disc alignment requires observations of protoplanetary discs around young binary stars with high spatial resolution. Previous studies on disc alignment determined the inclination by means of polarimetry (e.g. Monin et al., 1998; Wolf et al., 2001; Monin et al., 2006), the position of the jet (e.g. Eislöffel et al., 1996; Davis et al., 1997), and direct observations (e.g. Koresko, 1998; Stapelfeldt et al., 1998a). Another technique, that allows to directly measure size, inclination and orientation of the inner parts of protoplanetary discs is long-baseline interferometry at infrared wavelengths. A recent interferometric study of T Tau showed that the discs in this triple system are misaligned (Ratzka et al., 2009). Therefore, the formation process of T Tau probably has been highly dynamic.

I present in this chapter a multi-wavelength, high-resolution obser-

vational survey of the young binary system Haro 6-10 (GV Tau, IRAS 04263+2426). Haro 6-10 is a T Tauri binary system residing within the L 1524 molecular cloud. It is composed of the optically visible source Haro 6-10 S and the infrared companion (IRC) Haro 6-10 N. With an angular separation of 1.″2, Haro 6-10 N is located ∼160 AU north of Haro 6-10 S at the given distance. The binary system was firstly resolved by Leinert & Haas (1989) using speckle interferometry. Haro 6-10 N has a very red spectral energy distribution and is brighter than Haro 6-10 S at wavelengths larger than 4 μm. The binary system is variable, particularly in the near-IR, on a timescale as short as a month (Leinert et al., 2001). Leinert et al. (2001) suggest that the variability of Haro 6-10 S is associated to inhomogeneities in the circumstellar material, while the variable behaviour of the northern component is likely associated to a variable accretion mechanism. The first resolved images in the near-infrared of this system, obtained by Menard et al. (1993), suggest the presence of a flat circumbinary envelope, or disc.
The infrared spectrum of Haro 6-10 between 8 and 13 μm has been interpreted by Hanner et al. (1998) by an optically thick plus an optically thin emission, where the optically thin emission could be associated to an envelope, while the optically thick emission is associated to a disc, the star itself, or to a featureless dust continuum. The Spitzer/IRS spectrum (between 5-36 μm; Furlan et al., 2008) shows a broad silicate absorption feature at 10 μm, but the spatial resolution of the instrument is too low and the two sources are not resolved.
Reipurth et al. (2004) obtained high-resolution 3.6 cm observations with the VLA. In the 3.6 cm map the two components of the binary are spatially resolved. At this wavelength the radio continuum emission originates from shock-ionised gas very close to the outflow exciting source (e.g. Anglada et al., 1998). Reipurth et al. (2004) suggest that Haro 6-10 S is the driving source of the large outflow activity seen in the near-infrared image. Gibb et al. (2007) detected HCN and C_2H_2 in absorption around Haro 6-10 N. According to the rotational temperature of these molecules, this emission is associated with the inner region of a flared disc around Haro 6-10 N. Almost one year later absorption was detected toward Haro 6-10 N also by Doppmann et al. (2008) with an equivalent width and radial velocities similar to those detected by Gibb et al. (2007).

In this work, I am using a multi-wavelength approach, including VLTI mid-infrared interferometry, to characterise the binary system Haro 6-10.

This chapter of the thesis is organised as follows: in section 2.2 I present the archival optical and near-infrared observations, and our mid-infrared spectroscopic and interferometric observations. The data reduction and the results are described in section 2.3. The analysis and the discussion of the results are presented in sections 2.4 and 2.5, respectively. Conclusions are drawn in section 2.6.

2.2 Observations

In this section I present the observations collected from the literature and our new TIMMI2 and VLT/MIDI observations of Haro 6-10 N and S.

2.2.1 Archival Optical and Near-infrared images

HST imaging observations of Haro 6-10 were obtained as part of the WFPC2 snapshot survey of nearby T Tauri stars (HST 7387 program, PI: K. Stapelfeldt) on 25th November 1998, using the HST PC1 (Planetary Camera 1) and the HST WF3 (Wide-Field Camera 3), which have a spatial scale of $0.05''\text{px}^{-1}$ and $0.1''\text{px}^{-1}$, respectively. The observations have been carried out with the F814W and F606W filters and consist of one exposure of 120 seconds with the F814W filter, and 2 exposures of 200 and 600 seconds with the F606W filter. The calibrated data are available in the ESO-ST-ECF Science Archive Facility[1].
I include in our analysis also archival near-infrared NACO/VLT observations of Haro 6-10 N and S obtained on December 02 2003 (Program ID: 072.C-0321(A), PI: J.Bouvier). Also these data are available in the ESO/ST-ECF Science Archive Facility[1]. While the HST images are unpublished, the NACO data were published in the context of an high-resolution survey of multiple young stellar systems (Duchêne et al., 2007).

2.2.2 TIMMI2 infrared spectra

Haro 6-10 was observed in two campaigns in February and December 2002 with the TIMMI2 spectrograph mounted at the 3.6 m ESO telescope at La Silla (Chile).

[1] http://archive.eso.org

Individual spectra have been already presented in Przygodda (2004). These spectra show significant temporal changes in the overall shape and absolute flux levels. The northern, infrared component brightens at 13 μm from about 20 Jy in February to about 30 Jy in December 2002. The southern component tends to become fainter at short wavelengths with a less pronounced or maybe broader silicate absorption feature.

2.2.3 MIDI/VLTI observations

I obtained two mid-infrared interferometric measurements of both Haro 6-10 S and Haro 6-10 N with MIDI at the VLTI during the Guaranteed Time Observations (GTO) in December 2004 and November 2005. The first observations were carried out using the baseline UT2-UT3, and the second observations with the baseline UT3-UT4. Details of the observations are listed in Table 2.2.
The interferometric observations with MIDI were carried out using the standard procedure for high sensitivity mode: an acquisition image is acquired at 8.7 μm, followed by the measurements of the spectrally dispersed correlated flux and the single-dish spectra. Spectrally resolved visibilities are defined as the ratio of these two quantities. The spectral resolution is $\lambda/\Delta\lambda \sim$30 since I used the prism. A detailed description of the MIDI observing sequence is reported, e.g., in Ratzka et al. (2009).
Soon after each scientific observation, the sequence is repeated for a standard star of known diameter. These calibrators are required to determine instrumental and atmospheric effects. The accuracy of each visibility point, of about 5%, allows us to use all the calibrators of the night acquired in the same observation mode. The calibrators, partly spectro-photometric, also served to calibrate the absolute flux as well as the correlated fluxes. For details see Table 2.2.

2.3 Data reduction and results

2.3.1 Optical HST photometry

I used the calibrated data of Haro 6-10 already processed by the standard data reduction pipeline[2] which is available at the ESO-ST-ECF Science Archive Facility. Cosmic rays in each single exposure have been removed

[2]http://archive.eso.org/archive/hst/

using a specific idl code (van Dokkum, 2001). Haro 6-10 S is saturated in the long exposure of 600 sec in the F606W filter. Fig. 2.3 shows the F606W combined 800 sec exposure (with Haro 6-10 S replaced by the non-saturated pixel in the 200 sec exposure), and the 120 sec exposure obtained with the F814W filter.
Aperture photometry of the short exposure in both the filters (F606W and F814W) was carried out on Haro 6-10 N and Haro 6-10 S.
An aperture of 0.50″ (corresponding to 5 pixels and 10 pixels in the F606W and F814W filter, respectively) has been adopted for the aperture photometry of the bright Haro 6-10 S object. The sky was estimated in an annulus between 0.55″ and 1.55″ and 0.6″ and 1.2″ in the two filters, respectively. An aperture of 0.2″ has been adopted for the aperture photometry of the faint infrared companion Haro 6-10 N in both filters. Due to a non-perfect cleaning of the cosmic rays and due to saturation of the central pixel, the long 600 sec exposure in the F606W filter cannot be used to compute aperture photometry.
The final magnitudes have been computed, including the gain ratio correction of the PC1 and WF3 cameras and using the zero points and gain ratios from Holtzman et al. (1995). The values obtained are in Table 2.3.

2.3.2 Near-infrared photometry with NACO.

NACO observations of Haro 6-10 were reduced with the data reduction pipeline provided by ESO[3]. Both components of the binary system were saturated in the L-band exposure. We derived the zero-points of the photometry from standard stars observed at the beginning and the end of the night. An aperture of 0.2″(corresponding to 15 pixels) has been adopted for the aperture photometry of the components and the sky was estimated in an annulus between 0.30″and 0.35″. The results of aperture photometry are reported in Table 2.3.

2.3.3 TIMMI2 mid-infrared spectroscopy

The spectra of Haro 6-10 S and its infrared companion are only separated by a few pixels on the TIMMI 2 detector: For this reason I re-analysed the data of February 6 and December 26 with a different method to check how large the effect of the extraction method on the spectral variations

[3]http://www.eso.org/sci/data-processing/software/pipelines/naco/

is. With the aim to optimise the spectrum extraction I have first fitted the preprocessed bi-dimensional TIMMI 2 spectrum with a double Gaussian for each wavelength column (Fig. 2.1). In this way the two spectra of each binary component are traced. Besides the fitted spectra, the fitting routine delivers synthetic images that can be compared to the original files. I found that with exception of the wings, the results of the fits are of good quality. The calibrators were also fitted and extracted with a Gaussian function to avoid systematic errors.
Correction for the telluric absorption as well as absolute flux calibration was achieved by means of observations of spectro-photometric standard stars observed at different airmasses during each night; the extracted spectrum of each standard star was flux-calibrated using the spectral templates by Cohen et al. (1999). Finally the spectra of Haro 6-10 S/N were scaled with the flux calibrated standard star spectra. The wavelength dispersion solution derived by Przygodda (2004) was applied. The final TIMMI 2 spectra are shown in Fig. 2.2. The error bars reflect the standard error of the two measurements during each of the two observing campaigns.
For the southern source the spectra now seem to be stable in the course of 2002. They show a similar shape than the MIDI spectrum taken two years later (see below), but the absolute level is about three times larger. For the northern component the change in flux in the upper part of the N-band remains. However, the MIDI spectrum of Haro 6-10 N resembles the TIMMI2 data from February 2002 very well.

2.3.4 MIDI visibility

The data reduction of interferometric data with MIDI has been performed with the MIA+EWS 1.5 data reduction software provided by the MIDI consortium[4]. The results of the data reduction are the raw correlated spectrum $\mathrm{F}_{\mathrm{raw}}^{\mathrm{CORR}}$ and the total (single-dish) raw spectrum $\mathrm{F}_{\mathrm{raw}}$. I mainly used the results of the EWS package and MIA only to confirm these results. I used EWS, which determines the correlated flux $\mathrm{F}_{\mathrm{raw}}^{\mathrm{CORR}}$ based on a "coherent" algorithm. It thus allows to compute the raw visibilities from

$$V_{\mathrm{raw}} = \frac{F_{\mathrm{raw}}^{\mathrm{CORR}}}{F_{\mathrm{raw}}}, \tag{2.1}$$

[4]http://www.strw.leidenuniv.nl/∼koehler/MIA+EWS-Manual/index.html

where F_{raw} is the geometrical mean of the total fluxes of the incoming beams from telescope A and B, e.g. $F_{raw} = \sqrt{F^{A}_{raw} \cdot F^{B}_{raw}}$.

The calibrated visibilities of the science object are obtained dividing the raw visibilities, V_{raw}, by the instrumental visibilities, V_{instr}, derived from one or more calibrators observed within the same night, usually the closest in time. In Table 2.2 I compile the calibrators observed during each night. Only those calibrators, observed closest in time to the science target, have been used to calibrate the final visibilities. The other calibrators were used to check the stability of the transfer function. The error associated to the calibrated visibility of the science targets is the standard deviation resulting from calibration with different calibrator stars for each night.

2.3.5 MIDI spectroscopy

As part of the observing scheme, MIDI acquires the N-band spectrum of the target (spectral resolution equal to that of interferometric signal) with both telescopes separately. MIDI spectra are extracted using the MIA+EWS software. In this regards I used the three observations of the spectro-photometric standard star HD 37160 obtained in December 2004 (see Table 2.2). In Fig. 2.2 I compare MIDI and TIMMI2 spectroscopy. Results are very similar, expect for Haro 6-10 S where TIMMI2 yields a slightly larger absolute flux calibration. This is likely due to the better spatial resolution of the VLT compared to the 3.6m telescope; the TIMMI2 spectrum of Haro 6-10 S is likely contaminated by the northern component (see also discussion in section 2.2).

2.3.6 Correlated flux

To flux calibrate the correlated spectrum one can use the following equation

$$F^{CORR}_{cal} = V_{cal} \cdot F_{cal} \tag{2.2}$$

where V_{cal} is the calibrated visibility and F_{cal} is the flux-calibrated spectrum. Alternatively, one may calibrate the raw correlated flux, F^{CORR}_{raw}, by means of spectro-photometric standards (for which, by definition, $F^{CORR} = F$). The results obtained using the two methods for

bright sources agree well, while there are some discrepancies for the faint Haro 6-10 S source. I decided to compute the correlated flux from Eq. 2.2.

2.4 Analysis

In this section, I present the analysis of our multi-wavelength survey of Haro 6-10. I analyse first the large-scale structure of the binary by investigating visual and near-infrared images as well as mid-infrared spectra. In a second step I examine the geometrical properties of the protoplanetary discs around the binary components through mid-infrared interferometry.

2.4.1 Large-scale morphology in the optical and near infrared

Figure 2.3 shows the WFPC2/HST optical images and the VLT/NACO near-infrared images. Both components of the binary system are resolved from the optical to the mid-infrared wavelengths. While in the optical the infrared companion is only barely detected, it becomes brighter in H band. Almost equal in brightness in K-band, Haro 6-10 N is brighter than the southern companion at longer wavelengths. The photometric results and the brightness ratios are shown in Table 2.3.
The resolution of 0.05″/px and 0.1″/px of the HST images allows to disentangle structures and the filaments in the environment of the Haro 6-10 binary system never observed before. An arc like structure is clearly resolved at ∼6″E and ∼3″W from the southern component of the binary. Previous observations (e.g. Leinert et al., 2001; Koresko et al., 1999) discovered the arc-like structure in the east side only. A filament or jet-like structure toward the southern component is departing from the eastern part of the arc-like structure. These filament structures become fainter in H and K-band and are undetectable at longer wavelengths. The origin of such an arc-like structure may have the following explanations: 1) it is circumstellar material with an arc-like shape simply illuminated by the central star, or 2) it represents the circumstellar material shocked by an outflow or 3) is the projection of the scattered light of a cavity in the circumbinary envelope.

The existence of an outflow is supported by the resolved extended emission of H_2 at 6.5″in the south direction and is consistent with the

filament structure (Doppmann et al., 2008). On the other hand, the existence of a cavity in an envelope has been suggested around a similar system, T Tau N, by Momose et al. (1996) and Stapelfeldt et al. (1998b). In this picture, a wide-angle wind creates oblique shocks when interacting with the molecular environment. Spectral high-resolution line imaging is necessary to discriminate among the two scenarios for Haro 6-10.

2.4.2 Optical extinction

To derive the optical depth of the circumstellar material I fitted the continuum with a first-order polynomial to the TIMMI2 spectrum between 8 and 13 μm, assuming that at these wavelengths only the continuum contributes to the observed spectrum[5]. A similar approach was presented by Quanz et al. (2007). I compute the optical depth $\tau_{\rm silicate}$ using the following equation:

$$F_{obs}(\lambda) = F_{cont}(\lambda)e^{-\tau_{\rm silicate}} \tag{2.3}$$

and from this I derive the extinction $A_{\rm silicate}$

$$A_{\rm silicate} = -2.5log_{10}(e^{-\tau_{\rm silicate}}) \tag{2.4}$$

The optical extinction A_V was computed using the relation $A_V/\tau_{9.7} = 19.3$ from Mathis (1998). All the values are listed in Table 2.4. I derive an average visual extinction of 18.7±4.1 mag for Haro 6-10 N and 13.0±3.8 mag for Haro 6-10 S. Our value are higher than the value obtained by Leinert et al. (2001) of 10.6±0.8 mag for Haro 6-10 N and 7.0±0.7 mag for Haro 6-10 S, using the ice-absorption profile. The spectra of Haro 6-10 N and Haro 6-10 S are compared with the profile of the silicate present in the interstellar medium (ISM) measured by (Kemper et al., 2004) (dotted line in Fig. 2.6). The spectra of Haro 6-10 N and S show a profile similar to the interstellar medium.
An analysis of the dust composition, using, e.g., a simple fitting of the N band spectrum (as done for Herbig and TTauri stars by Bouwman et al., 2001; Schegerer et al., 2006, respectively) is beyond the goal of this work and would have required a better quality of the spectra.

[5]The result does not change when I use an higher order polynomial fit (instead of a first-order) because it would better reproduce the shape of the absorption, but not the depth of the absorption.

2.4.3 Small-scale morphology: Geometry of the discs

In this section I introduce the model adopted to interpret the MIDI interferometric measurements. Using a Gaussian brightness distribution we first estimate the size of the emitting region. An alternative approach is the simultaneous modelling of the spectral energy distribution (SED) and of mid-infrared interferometric measurements, using a radiative transfer model (e.g. Schegerer et al., 2008; Ratzka et al., 2009; Schegerer et al., 2009). This has the advantage to reproduce in a more realistic way the physical structure of the circumstellar disc. However, the degeneracy in the parameter space can be reduced only by combining high-resolution images at different wavelengths (e.g., Wolf et al., 2008, 2003; Sauter et al., 2009).

Gaussian brightness distribution
Using a Gaussian brightness distribution I estimate the size of the emitting region from the observed visibilities. This is a reasonable first approximation already applied for barely resolved (high visibility) objects (e.g. by Quanz et al., 2006). The visibility of such a distribution is computed as

$$V(f) = V_0 \ \exp\left(-3.56 \ f^2 \ \Theta^2\right) \tag{2.5}$$

where Θ is the Full Width Half Maximum (FWHM; in arcsec) of the Gaussian distribution, and f the spatial frequency in arcsec^{-1}. For each baseline the emitting-sizes of the two discs are reported in Table 2.5 as function of wavelength. These values are given in astronomical units (AU) assuming a distance of 140 pc. I average the results obtained within 3 wavelengths bins: 13.0 - 12.1 μm, 12.0 - 10.0 μm and 9.8 - 7.9 μm. The associated errors are computed as the standard deviation of the averaged values. I notice that the emitting size increases with wavelength. Such a behaviour is expected for thermal disc emission, where the temperatureof the disc decreases with the distance from the central star.
Physical - Geometrical Model
A simple Gaussian brightness distribution is not able to reproduce the observed visibility of both sources (see Fig. 2.5). I note that the change in the slope of the visibility with wavelength may suggest the presence of two different emitting regions contributing to the mid-infrared flux. I introduce here a more complex (geometrical) model which takes into account also the spectrum and correlated flux of the emitting source. I

model simultaneously the MIDI spectrum infrared flux (integrated over the beam width of 0.4″) and the correlated fluxes corresponding to a spatial scales of 0.07″ and 0.03″ for the 28 m and 62 m projected baselines, respectively.

In a circumstellar disc, in first approximation, I expect a radial decrease of the temperature as a function of the distance from the central star. In the case of flaring discs, a decrease of the disc temperature is expected also in vertical direction from the surface to the mid-plane. The mid-infrared flux is therefore expected to come from the inner part of the disc close to the central star. In this simplified view I approximate the emitting source with two black bodies of different temperatures: each black-body is characterised by a Gaussian brightness distribution (a similar approach was used by Jaffe et al., 2004). In order to reproduce the dust absorption feature between 8 and 13 μm the silicate absorption profile is included. In particular, I use the absorption profile derived from ISO[6] towards the centre of the galaxy (Kemper et al., 2004) which is consistent with the absorption profile of Haro 6-10 N and S (see section 2.4.2).

For each binary component, the mid-infrared spectrum is computed as

$$F_{\rm tot}(\lambda) = (F_{\rm bb1} \cdot e^{-\tau_1 \cdot \frac{\tau(\lambda)}{\tau(\lambda_c)}} + F_{\rm bb2} \cdot e^{-\tau_2 \cdot \frac{\tau(\lambda)}{\tau(\lambda_c)}}) \cdot cos(i) \qquad (2.6)$$

where $F_{\rm bb1}$ and $F_{\rm bb2}$ are the two black-body emitters at a temperature of T_1 and T_2, respectively, and i is the inclination of the disc. The value $\tau(\lambda)$ is the extinction profile measured between 8 and 13 μm in the direction of the galactic centre, and $\tau(\lambda_c)$ correspond to the maximum of $\tau(\lambda)$. τ_1 and τ_2 are the average extinctions computed in Sect. 2.4.2, for Haro 6-10 N and Haro 6-10 S, respectively. The visibility is computed as

$$V_{\rm tot}(\lambda) = f \cdot V_{\rm gauss1} + (1 - f) \cdot V_{\rm gauss2} \qquad (2.7)$$

where, $f = \frac{F_{\rm bb1}}{F_{\rm tot}}$, and the visibility of a Gaussian brightness distribution is $V_{\rm gauss1,2} = exp\frac{-(\pi \cdot f \cdot FWHM_{1,2})}{4 \cdot log(2)}$ [7].

The Gaussian brightness distribution was rotated by a position angle PA and inclined (as described e.g. in Fedele et al., 2008) to take into

[6] Infrared Satellite Observatory

[7] $FWHM_{1,2} = r_{1,2}/d$, with $r_{1,2}$ is the radius of the emitting region (in AU) and d is the distance of the source (in pc)

account the orientation of the disc. The free parameters of the model are:

1. the temperatures, T_1 and T_2, of the two black-body emissions,
2. the emitting sizes r_1 and r_2 of the two black bodies corresponding to the FWHM of the two Gaussian brightness distributions,
3. the inclination (i) and the position angle (PA) of the Gaussians.

A first "best" model was found minimising the reduced χ^2 (χ^2 divided by the number of free parameters of the fit). In order to estimate the final best fit parameters and the uncertainties on these quantities, I ran a Monte Carlo simulation, assuming a normal error distribution of the measured visibilities. I simulated 1000 random data-sets around the observed values (as done in Fedele et al., 2008). The "best" parameters previously computed are used as input parameters for the Monte Carlo simulation.
The final best fit parameters and associated uncertainties correspond to peak and the peak broadening of the histograms from the simulations (Fig. 2.9). These values are listed in Table 2.6.
For Haro 6-10 N I found that the emission within 1.5 AU from the central star has a temperature of $900K$ and a second colder emission at $150K$ originates within 10 AU from the central star.
For Haro 6-10 S I found an emission within 1.0 AU from the central star with a temperature of $900K$ and a second colder emission at $100K$, originating within 7 AU from the central star.
The disc of Haro 6-10 N is seen close to edge-on ($i = 80^o$), while Haro 6-10 S is almost face-on ($i = 10^o$). The derived inclinations of the binary components are consistent with the fact that the central star of Haro 6-10 S is visible in the optical, while the star of Haro 6-10N is obscured by an additional extinction represented by the circumstellar disc and it is only barely visible in the optical. These results are consistent with the general appearance of the binary system described in section 2.4.1. In the case of Haro 6-10 N, the model fits the observations very well (see Fig. 2.7), while for Haro 6-10 S the model fitting is less accurate (see Fig. 2.8); the model reproduces quite well the mid-infrared spectrum, the correlated spectra and the absolute value of the visibility, but does not fit its shape. Nevertheless, the disc inclination is constrained quite well since the peak of histogram is narrow around the inclination of 10^o.

2.5 Discussion

In this section I compare our results with previous work and discuss which mechanism might have formed the binary system Haro 6-10.

Comparison to previous work
The main results of our study are that Haro 6-10 is embedded in a common envelope (which causes the mid-infrared absorption feature in both components of the binary system), and that the two discs of the binary system are misaligned.
Observational studies of the disc inclinations in young binary systems have been carried out in the last years, using different techniques: polarimetric and direct observations of protoplanetary discs or indirect observations via the position of the jet from the protostellar object which is expected to be perpendicular to the disc. Recently also long-baseline infrared interferometry was used to measure the geometrical properties of circumstellar discs in binary systems.
Polarimetric studies on the disc orientations have been carried out by, e.g., Monin et al. (1998); Wolf et al. (2001); Monin et al. (2006). They all observed T Tauri stars and found that discs tend to be aligned in young binaries. Jensen et al. (2004), in particular, found a tendency for binary systems discs to be nearly (but not exactly) aligned with each other, and for those in triple and quadruple systems to be misaligned.
There are also cases of misaligned discs from observations of misaligned jets from protostellar objects (e.g. Davis et al., 1994), inferred jet precession (e.g. Eislöffel et al., 1996; Davis et al., 1997) and direct observations (e.g. Koresko, 1998; Stapelfeldt et al., 1998a). A recent interferometric study of T Tau showed that the discs in this triple system are misaligned (Ratzka et al., 2009): The circumstellar disc of the northern component is seen almost edge-on, while the southern component is surrounded by a face-on disc. Especially the disc around T Tau Sa, the most massive star in the system, is seen almost edge-on. The formation process of T Tau thus has to have been highly dynamic. However, these cases of misaligned discs do not represent yet a statistical significant sample.

How Haro 6-10 has been formed?
One of the most important results of our study is that the two discs of Haro 6-10 are misaligned. Therefore, the most probable scenario is the formation via fragmentation of two different parts of the collapsing

molecular cloud combined with other dynamical processes related to the cloud or the protostars.
The misalignment of the discs cannot be caused by an infall of external material with a different angular momentum onto the binary orbit, because the accretion would have re-aligned the two discs (Bate et al., 2000). Only infall on one of the components might lead to a tilt of that component, when the transported angular momentum is large enough. Also capture of the companion is an unlikely explanation, because for solar-mass stars the capture rates are insufficient even when circumstellar discs increase the interaction cross section considerably (Heller, 1995). For the central part of the Orion Nebula Cluster (ONC) with its stellar density of 10^4 stars pc^{-3} Boffin et al. (1998) found a capture rate of only $0.1\,Myr^{-}1$, i.e. the probability to form a binary star within 1 Myr is only 10% . For environments like the Taurus-Auriga star-forming complex, with stellar densities of around 10 stars pc^{-3} the capture rate is two orders of magnitude lower. However, disc-assisted capture is efficient for dense environments and massive stars with large disks (Moeckel & Bally, 2006, 2007b,a). However, no final conclusion about the formation scenario can be drawn yet. More about the dynamics of the system has to be known. Nonetheless, our observations of Haro 6-10 show another system that has misaligned discs. Many of the binaries harbouring infrared companions might be surrounded by an edge-on and a face-on disc.

2.6 Conclusions

In this chapter of the thesis I presented a multi-wavelength study of the young binary system Haro 6-10 combining optical images obtained with HST/WFPC2 with the diffraction-limited images obtained with VLT/NACO in the near-infrared. In the mid-infrared I combine the spectroscopic and interferometric observations obtained with TIMMI2 and VLTI/MIDI, respectively. This unique collection of data enables us to characterise the large-scale and small-scale structure of Haro 6-10 and to draw the following conclusions:

1. Both components of the binary system Haro 6-10 are embedded in a common envelope. The envelope has a dust composition similar to the interstellar medium.

2. Each component of the system has a circumstellar disc-like struc-

ture typical of young stars.

3. The discs are highly misaligned: the northern component is seen almost edge-on toward the line of sight and the southern component an almost face-on disc.

4. The most probable scenario is the formation via fragmentation of two different parts of the collapsing molecular cloud combined with other dynamical processes related to the cloud or the protostars.

2.7 Appendix: Spectral Energy Distribution

I compile the spectral energy distributions (SEDs) of the two components of the binary system combining our new results in the optical, near and mid-infrared, together with the photometry from the literature. All the fluxes, together with the instrument, the beam size of the observations, and the references, are listed in Table 2.7. In Fig. 2.10 I show the SEDs of the single component. In the wavelength range 12-1000 μm the binary system is not resolved. At 1.2 mm the emission is again resolved. The flux is the same for the two components. Since the emission at this wavelength is associated to the mid-plane of the entire disc and is optically thin, the mass of the disc is proportional to the flux in the millimetre wavelength. This implies that the discs of Haro 6-10 N and S have the same mass.

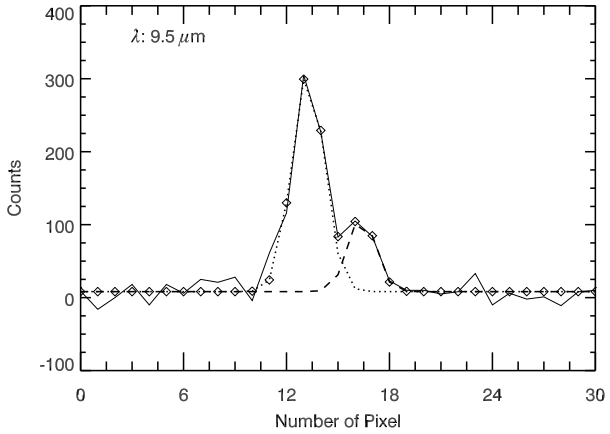

Figure 2.1 Perpendicular (to the dispersion direction) cut of a TIMMI 2 bi-dimensional spectrum obtained on December 26 along with the double Gaussian function fit utilised for the spectra extraction. Data are shown as solid line, fit with diamonds. The fit to each component is shown as dotted line for the northern component and dashed line for the southern component.

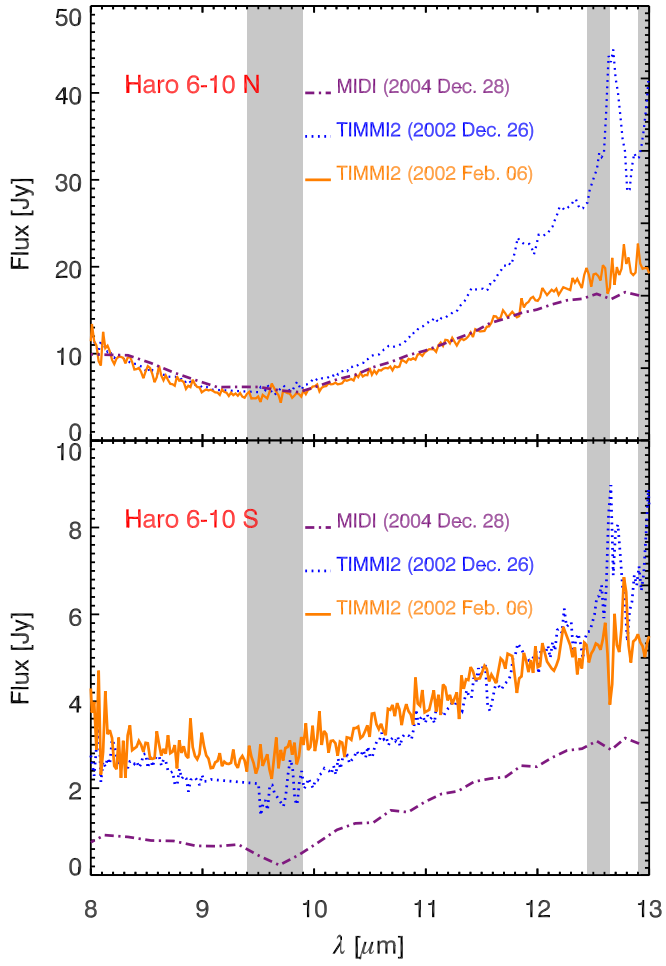

Figure 2.2 TIMMI 2 spectrum of Haro 6-10 N (IRC) (top) and Haro 6-10 S (below). The gray highlighted pattern correspond to strong atmospheric O_3 and CO_2 absorption bands at 9.6 and 12.5 μm, respectively. The measurements in these regions are not considered in our following analysis.

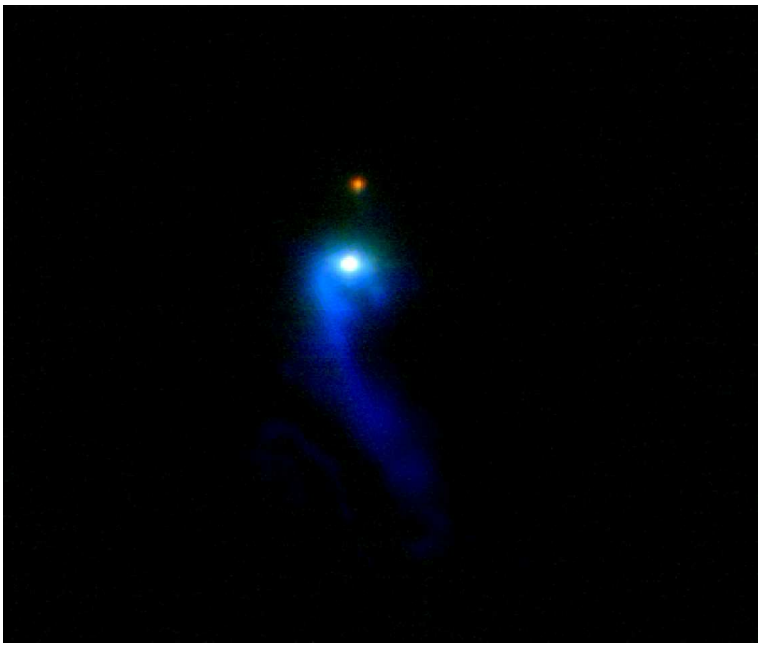

Figure 2.3 Colour-composite image of Haro 6-10. The blue, green and red colours correspond respectively to the photometric bands F606W (HST), H and K_s (NACO). The dimension of the image is $12'' \times 10''$. North is up, East is left. The flux of the north component (Haro 6-10N) is 0.3% of the flux of the southern component (Haro 6-10S) in the optical HST band and increase up to 2.4% in K band. An arc like structure is resolved in the optical (becoming fainter at longer wavelengths) at $\sim 6''$E and $\sim 3''$W from Haro 6-10S. A filament or jet-like structure toward Haro 6-10S is departing from the eastern part of the arc-like structure.

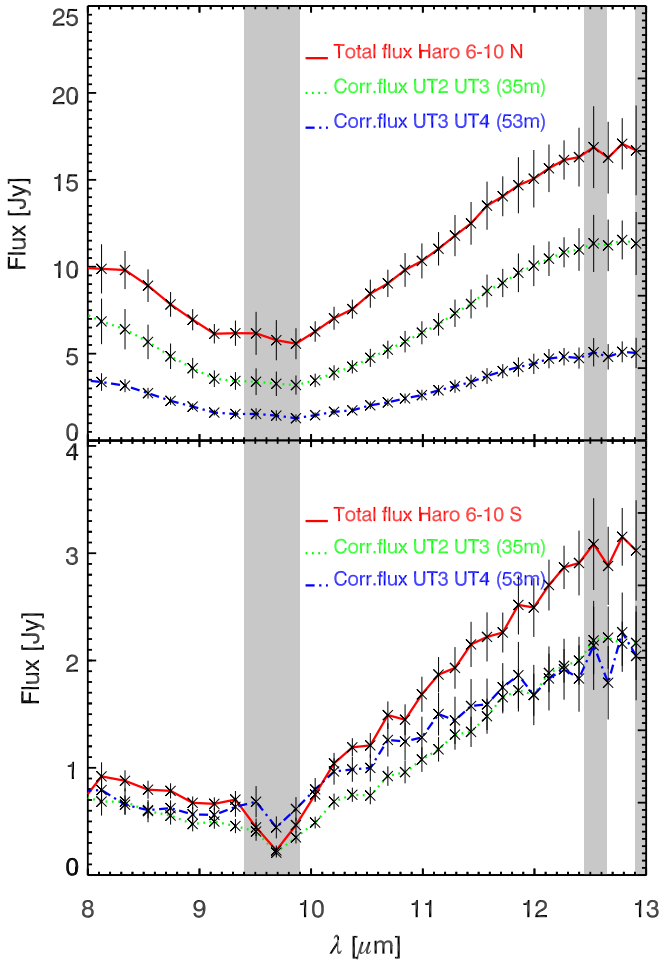

Figure 2.4 MIDI spectrum (solid lines) and correlated fluxes of Haro 6-10 N (top) and Haro 6-10 S (bottom) obtained with the UT2-UT3 (dashed lines) and UT3-UT4 (dotted lines) baseline respectively. The gray vertical regions are strongly affected by the atmospheric O_3 and CO_2 absorption bands at 9.6 and 12.5 μm, respectively.

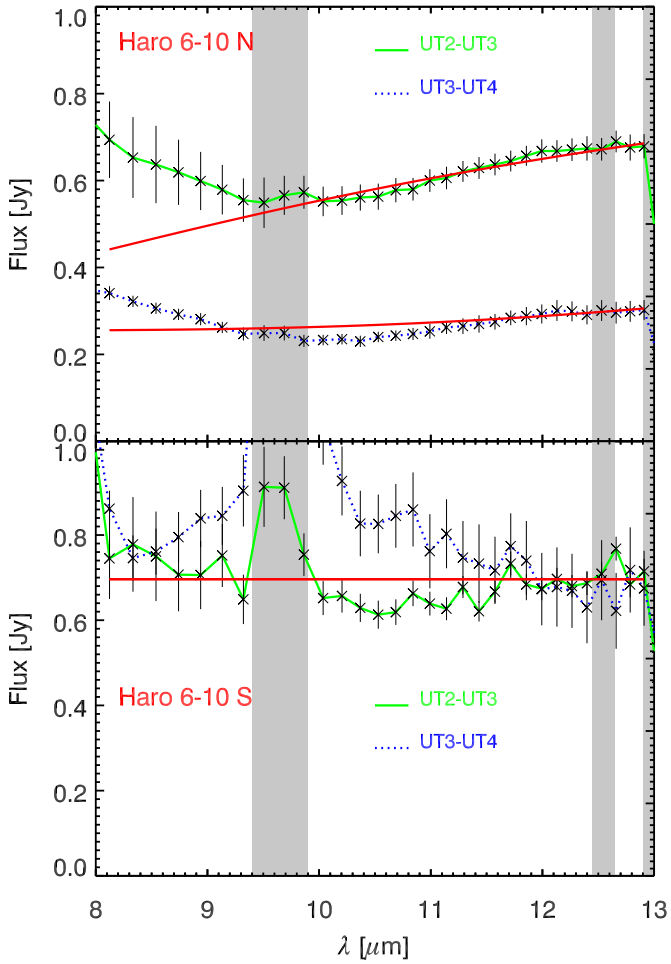

Figure 2.5 Calibrated visibilities of Haro 6-10 N (top) and Haro 6-10 S (bottom). The continuous lines represent the best fit using a Gaussian brightness distribution model.

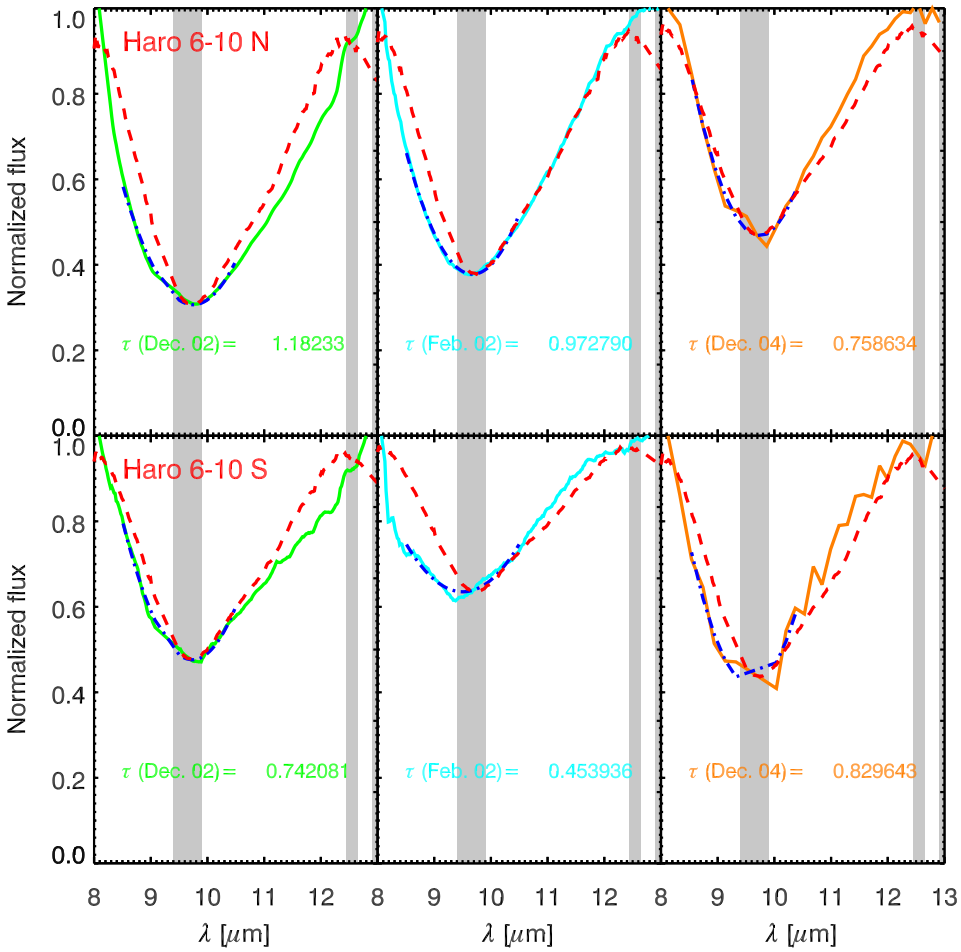

Figure 2.6 Normalised spectra of Haro 6-10 N (top), Haro 6-10 S (bottom) obtained with TIMMI2 on February and December 2002 and with MIDI on December 2004, with the computed maximum optical depth. A second-order polynomial fit has been fitted to the data between 8.8 and 10.2 μm (dot-dashed lines) to compute the maximum optical depth (τ). For comparison the ISM silicate profile from Kemper et al. (2004) is overplotted (dashed red lines).

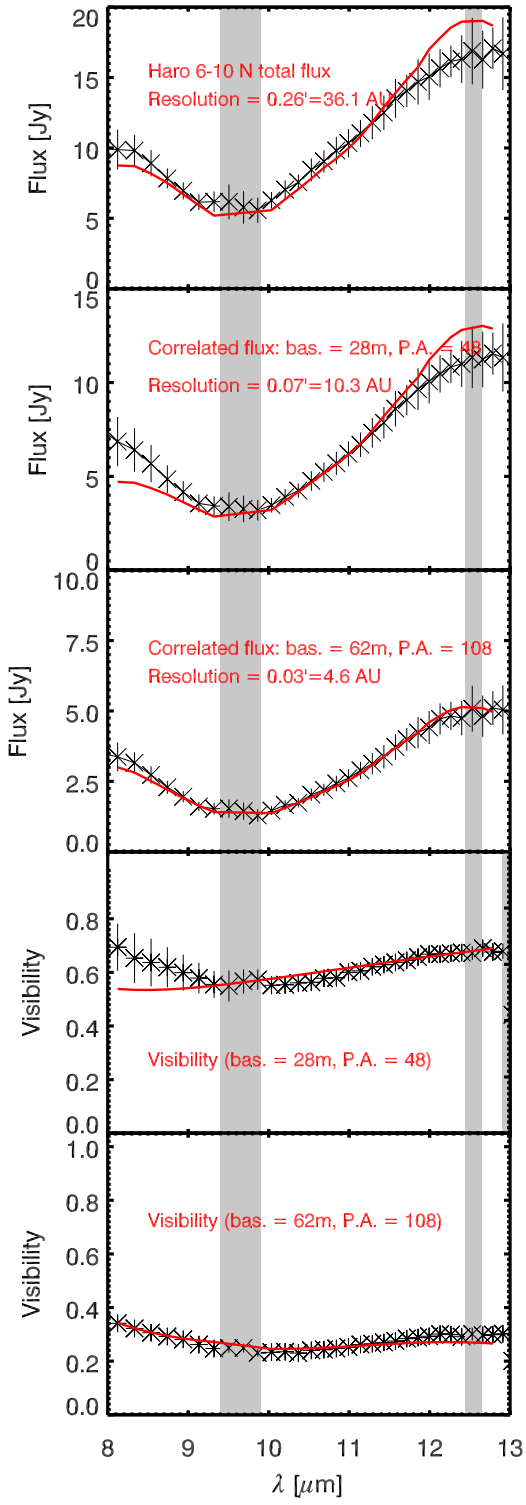

Figure 2.7 MIDI spectrum, correlated fluxes and visibilities for Haro 6-10 N. The red solid line represents the model best fit.

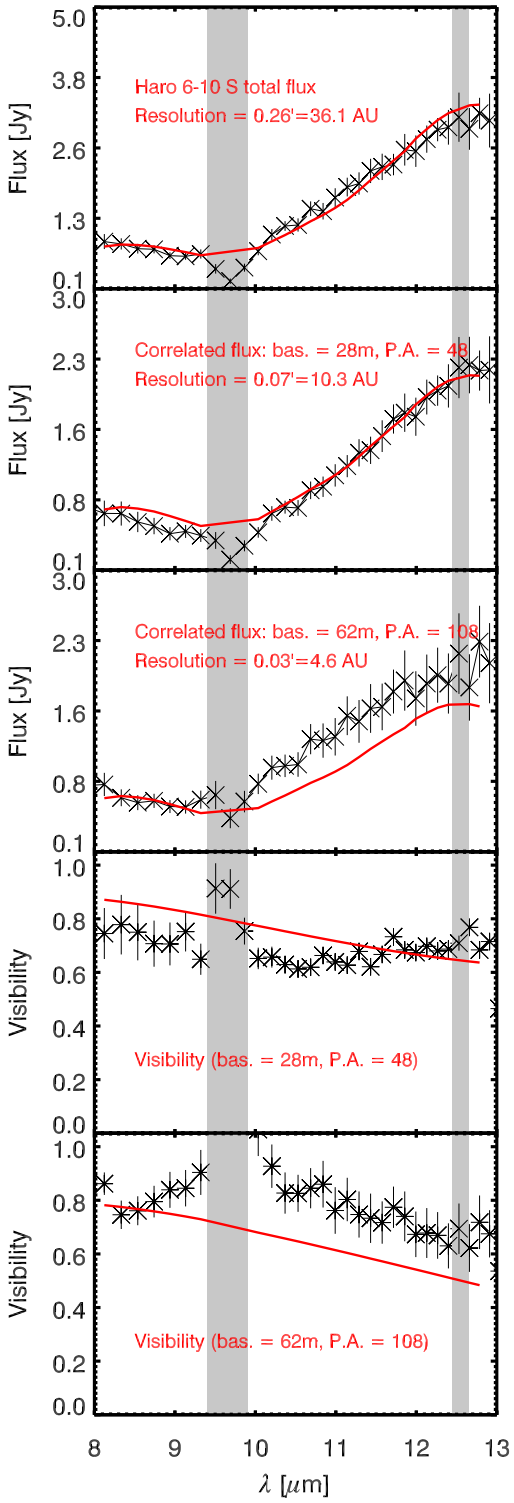

Figure 2.8 MIDI spectrum, correlated fluxes and visibilities for Haro 6-10 S. The red solid line represents the model best fit.

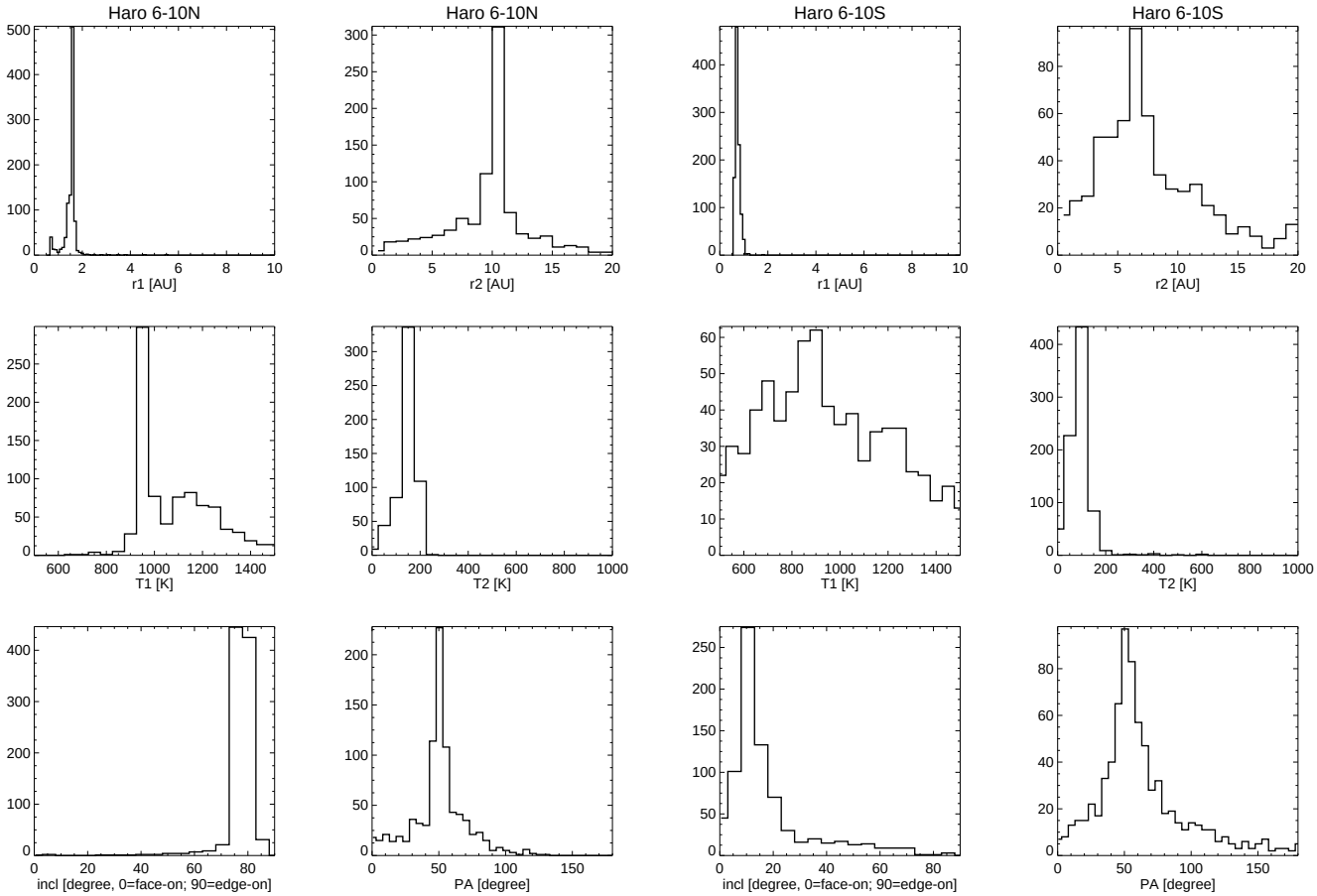

Figure 2.9 Histograms of the best fit parameters computed using 1000 Monte Carlo simulations for Haro 6-10 N (left) and Haro 6-10 S (right).

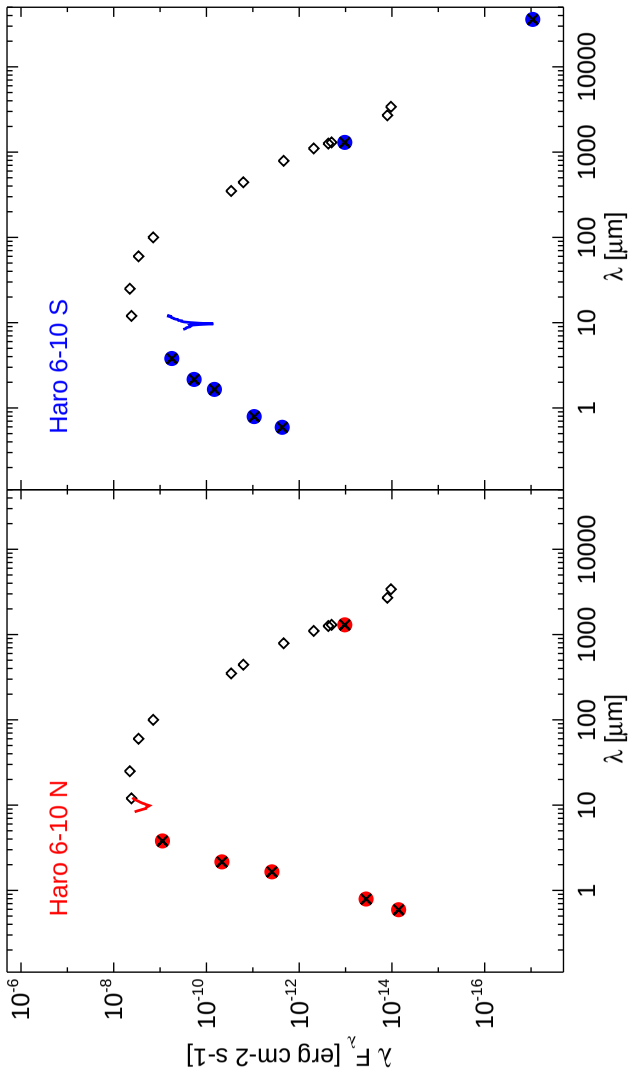

Figure 2.10 Spectral energy distribution (SED) of Haro 6-10. The empty diamond points represent the photometric measurements of the unresolved binary. The fluxes of the single components are presented as red (Haro 6-10N) and in blue (Haro 6-10S) filled dots. The continuous lines represent the MIDI spectra of both the components.

Table 2.1 Log of TIMMI 2 observations of Haro 6-10 and of the spectrophotometric standard stars.

Date	UT	Objects	Airmass
2002 Feb. 06	00:10	HD32887	1.02
	00:41	GVTau	1.71
	00:53	GVTau	1.73
	01:41	HD29139	1.56
	07:46	HD123139	1.11
2002 Dec. 26	00:42	HD29139	1.82
	01:35	GVTau	1.84
	01:51	GVTau	1.78
	05:00	HD32887	1.07

Table 2.2 Log of MIDI observations of Haro 6-10 N and S and calibrators observed. ⋆: calibrators used to obtain the final calibrated visibilities and fluxes.

Date	UT	Objects	Airmass	Proj. Baseline [m]	Pos. Angle [deg]	Notes
				[UT2-UT3]		
2004 Dec. 28	00:18	HD37160	2.08	27.61	14.61	Calibrator⋆
	01:01	Haro 6-10 N	1.73	28.43	48.67	Science
	02:38	Haro 6-10 S	1.60	38.13	52.15	Science
	03:10	HD37160	1.22	39.98	43.62	Calibrator⋆
	04:08	HD37160	1.21	43.61	46.24	Calibrator⋆
	05:26	HD50778	1.03	46.43	42.72	Calibrator
	06:10	HD94510	1.43	45.17	15.53	Calibrator
	07:02	HD49161	1.40	46.61	45.68	Calibrator
	07:45	HD94510	1.25	44.00	32.44	Calibrator
				[UT3-UT4]		
2005 Nov. 23	04:17	Haro 6-10 N	1.56	62.13	106	Science
	05:22	Haro 6-10 S	1.54	58.60	95.6	Science
	05:41	Haro 6-10 N	1.56	56.80	92.6	Science
	06:09	HD25604	1.61	50.53	85.4	Calibrator⋆
	07:49	HD33042	1.23	61.60	116.5	Calibrator

Table 2.3 Calibrated magnitude obtained with HST and VLT/NACO.

	Haro 6-10 N [mag]	Haro 6-10 S [mag]	flux ratio
V (F606W)	23.4	17.2	0.003
I (F814W)	21.0	15.0	0.004
H	14.2±0.1	11.1±0.1	0.06
Ks	10.7±0.1	9.2±0.1	0.24

Table 2.4 Optical depths and extinction values as derived from the spectra in Fig. 2.6.

Object	Date	$\tau_{\rm silicate}$	$\lambda_{\rm silicate}$	$A_{\rm silicate}$	A_V
Haro 6-10 N	2002 Feb.	1.0	9.7	1.1	18.8
	2002 Dec.	1.2	9.7	1.3	22.8
	2004 Dec.	0.8	9.7	0.8	14.6
Haro 6-10 S	2002 Feb.	0.5	9.5	0.5	8.8
	2002 Dec.	0.7	9.7	0.8	14.3
	2004 Dec.	0.8	9.3	0.9	16.0

Table 2.5 Derived emitting size using a Gaussian brightness distribution.

	Derived Θ [AU]			
	Haro 6-10 N		Haro 6-10 S	
λ	UT2-UT3	UT3-UT4	UT2-UT3	UT3-UT4
[μm]	[28 m]	[62 m]	[28 m]	[62 m]
8.9	4.2±0.5	3.0±0.3	2.5±0.5	2.6±0.3
11.0	5.0±0.1	3.8±0.1	3.5±0.1	3.5±0.3
12.6	5.3±0.7	4.2±0.2	3.8±0.5	4.3±0.2

Table 2.6 Best fit parameters of the visibility model.

Parameters	Haro 6-10 N	Haro 6-10 S
r_1 [AU]	1.5±0.5	1.0±0.5
r_2 [AU]	10±2	7±3
T_1 [K]	900±100	900±300
T_2 [K]	150±50	100±50
incl [^{o}]	80±10	10±5
diskPA [^{o}]	50±20	50±20

Table 2.7 Spectral energy distribution with photometry from the literature (references in the last column) of Haro 6-10 N and Haro 6-10 S.

λ [μm]	Flux [Jy]	Flux [Jy]	Flux [Jy]	Instrument	Beam size [$''$]	Reference
0.593	0.001±0.000	0.00778±0.00000	0.00002	HST	0.5	this work
0.792	0.004±0.002	0.1089	0.00042	HST	0.5	this work
1.650	0.242±0.189	0.03703±0.00341	0.00213 0.00020	NACO	0.2	this work
2.160	0.482±0.351	0.13288±0.01224	0.03338 0.00307	NACO	0.2	this work
12.000	16.60±2.200	–	–	IRAS		Chandler et al. (1998)
25.000	37.60±3.200	–	–	IRAS		Chandler et al. (1998)
60.000	58.40±9.700	–	–	IRAS		Chandler et al. (1998)
100.000	47.00±11.000	–	–	IRAS		Chandler et al. (1998)
350.000	3.420±0.250	–	–	JCMT/UKT14	19	Dent et al. (1998)
443.000	2.370±0.500	–	–	JCMT/UKT14	19	Chandler et al. (1998)
790.000	0.571±0.049	–	–	JCMT/UKT14	16	Chandler et al. (1998)
1104.000	0.179±0.017	–	–	JCMT/UKT14	19	Chandler et al. (1998)
1260.000	0.099±0.030	–	–	JCMT/UKT14	21	Chandler et al. (1998)
1300.000	–	0.04500±0.00500	0.04500±0.00500	PdBI		A. Dutrey (privat comm.)
2700.000	0.011±0.001	–	–	OVRO	3.0	Hogerheijde et al. (1997)
3400.000	0.012±0.002	–	–	OVRO	6.0	Hogerheijde et al. (1997)
36000.00	–	0.00011± 0	0.00001	VLA	0.29x0.26	Reipurth et al. (2004)

3

Disc Evolution in OB Associations: the case of IC 1795

Based on the paper: 'Disc Evolution in OB Associations: a deep Spitzer/IRAC survey of IC 1795' - Roccatagliata V., Bouwman J., Henning Th., Gennaro M., Townsley L., Feigelson E., Kim S. J., Sicilia-Aguilar A., Lawson W.A. - To be submitted to ApJ

3.1 Introduction

Although most solar-type and low mass stars form in OB associations, most discs studies around PMS stars deal with regions of low-mass star formation in the Gould Belt (e.g. Hartmann et al., 2005; Winston et al., 2007; Hatchell et al., 2007; Sicilia-Aguilar et al., 2008; Evans et al., 2009) and nearby moving groups (e.g. Sicilia-Aguilar et al., 2009).
An exception is the Orion Nebular Cluster (e.g. Hillenbrand, 1997; Hillenbrand et al., 1998), the nearest ($\sim$410 pc; Jeffries, 2007), young (≈ 1 Myr; Hillenbrand, 1997), dense and rich cluster with the O6 star, θ^1Ori C, in the centre. The shape of the discs close to ionising sources suggests

that they may be truncated through photoevaporation caused by the intense radiation field of the Trapezium stars (e.g. O'dell & Wong, 1996). Rich clusters containing luminous O stars ought to be ideal locations to investigate if phenomena such as photoevaporation can be partly responsible for disc dissipation.

In this chapter, I present the analysis of protoplanetary discs around young stars in the IC 1795 OB association. I obtained infrared imaging data of the IC 1795 OB association with the Infrared Array Camera (IRAC; Fazio et al., 2004) on board the *Spitzer Space Telescope* (Werner et al., 2004). To define the cluster membership of IC 1795 we carried out a deep survey with the Advanced CCD Imaging Spectrometer (ACIS) detector on board the *Chandra X-ray Observatory* (Weisskopf et al., 2002). The IC 1795 cluster belongs to the diffuse HII region in the W3 giant molecular cloud complex. This region is located in the Perseus arm, which contains several spectacular regions of high- and low-mass star formation: W3 North, W3-Main and W3-OH. IC 1795 hosts one O9.7I star and two B stars which have been spectrally classified by Oey et al. (2005). The cluster is assumed to lie at the same distance as W3-OH. From maser kinematics this has been accurately measured to be 2.0 kpc (Xu et al., 2006; Hachisuka et al., 2006).

Oey et al. (2005) derived an approximate age of 3-5 Myr and they propose that this OB association, triggered by the neighbouring W4 superbubble, is triggering new star formation in the young massive regions W3-North, W3-Main and W3-OH.

The X-rays morphology of these regions suggests, however, that only the W3-OH structures are consistent with collect-and-collapse triggering process caused by shocks from the older IC 1795 cluster (Feigelson & Townsley, 2008). In the X-ray maps the W3-Main cluster does not show the elongated and patchy structure of a recently triggered star cluster, and instead it appears to have formed in an earlier episode. Previous *IRAC* observations of the entire W3 region, presented by Ruch et al. (2007), revealed that a large fraction of Class II sources lie within the central cluster IC 1795. However, no analysis of the spatial distribution and disc fraction of the cluster has been performed so far.

This chapter is organised as follows: in section 3.2 I present our *Spitzer* and *Chandra* observations, along with the data reduction. Results are shown in section 3.3. Sections 3.4 and 3.5 include the analysis of the cluster (membership, age, infrared properties of the stars). In section 3.6 I discuss our results in terms of disc evolution. Conclusions are drawn in

section 3.7.

3.2 Observations and data reduction

3.2.1 *IRAC* observations

IC 1795 was observed in 2007 September [1] with all 4 channels centred at 3.6 μm, 4.5 μm, 5.8 μm, 8.0 μm respectively, using a 3x4 mosaic pattern, with pointings separated by 220″ and aligned with the array axes. The resulting images provide a full coverage in all four channels over a 14′ x12′ area.
The images have been obtained in High Dynamical Range Mode in order to obtain unsaturated measurements for all observed cluster members. A short exposure of 144 frames of 0.4 sec each and a long exposure of 10.4 sec per 144 frames have been carried out. The average long exposure over the entire mosaic is 520 sec in each channel. The long and the short exposures were analysed separately to avoid saturation of bright sources in the long exposures.
The raw data were processed and calibrated with the IRAC pipeline (version S16.1.0) and the Basic Calibrated Data (BCD) were downloaded from the *Spitzer* archive[2]. The final mosaics were created using the MOPEX pipeline (version 18.2.2)[3]: the software takes the individual BCD frames and combines them to create a mosaic of the observed region, removing cosmic rays and bad pixels from the single frames. In Figs. 3.1-3.2 I show the mosaics of the long exposures at 3.6 μm/4.5 μm and 5.8 μm/8.0 μm of IC 1795. Due to the mosaic configuration, the exposures of ch1 and ch3 cover part of W3-Main, while ch2 and ch4 cover part of W3-OH.

3.2.2 *IRAC* photometry

I used the APEX/MOPEX package to perform PSF-photometry for every detection. In particular, I used the APEX MultiFrame pipeline, where the detection of the point sources is done on the final mosaic

[1] *Spitzer* program ID 30726, PI J. Bouwman
[2] http://archive.spitzer.caltech.edu/
[3] http://ssc.spitzer.caltech.edu/postbcd/download-mopex.html

in order to pick up also the fainter objects, while the PSF photometry is carried out on each frame separately. As the background was highly variable, it has been computed in a small area of 8x8 pixels and subtracted before performing PSF-photometry. Instead of PSF fitting, APEX uses the point-response function (PRF) fitting method. The PRF is the response of the detector array pixels to a point source and combines information on the PSF, the detector sampling and the intra-pixel sensitivity variation. I used the standard PRFs provided in APEX. The point-source positional uncertainties and the flux uncertainty (Δ_{PRF}) are computed from the covariance matrix calculated from the "best-fit" to the data.
The calibration uncertainties (Reach et al., 2005) are dominated by the array-location-dependent photometric correction which can introduce an uncertainty of up to 10% of the flux (peak-to-peak). However, since the pixel phase effect decreases as the square root of the number of dithers (12 in our case), I conservatively adopt a value of 5%. The colour correction and the absolute calibration error are of on the order of a few %. Overall the final flux calibration error (Δ_{cal}) is smaller than 10% of the flux. The total flux uncertainty is:
$\Delta_{flux} = \sqrt{\Delta^2_{PRF} + \Delta^2_{cal}}$.
Only sources with a signal-to-noise (S/N) flux measurement larger than 6 are considered. The detection limit of our IRAC survey in 3.6 μm band is 16.5 mag. However, I have cases where the high variability of the background did not enable us to detect all the sources with brightness between 15.5-16.5 mag at 3.6 μm. The final photometric catalog was created, combining the results on short and long exposures separately. For objects detected in both exposures (and not saturated), I adopt the photometry measured in the long exposure.

3.2.3 *ACIS* observations

Our X-ray catalog was generated from a mosaic of *Chandra* observations consisting of the 7 exposures of W3 presented by Feigelson & Townsley (2008) and an additional exposure of IC 1795. This is a 50.0 ks exposure obtained on 2007 December 4 centred on $(\alpha_{J2000}, \delta_{J2000})$ = (02:26:33.60,+62:00:35.99) with the 4-CCD ACIS Imaging Array subtending $17' \times 17'$. The data were reduced using procedures implemented in the IDL-based *Tools for ACIS Review and Analysis (TARA)* and *ACIS Extract* software packages. The algorithms are described in Broos et al.

(2009) and are available online[4]. Their application to stellar populations in other star-forming regions include M 17 (Broos et al. 2007), the Rosette Nebula (Wang et al., 2008, 2009), and NGC 6334 (Feigelson et al., 2009).

Summarising briefly here, the *Chandra* satellite telemetry data are subject to various cleaning operations, and the image is aligned to the 2MASS/*Hipparcos* astrometric frame. A superset of tentative sources is identified by a combination of wavelet-based source detection, peaks in image tiles with point spread function removed by a maximum-likelihood image reconstruction, and visual inspection for close multiple sources. Photons are extracted from each tentative source in the broad soft, hard and total X-ray bands, and photon counts are compared to the locally measured background. Local backgrounds are essential due to the different exposures from overlapping ACIS exposures. Source significance is evaluated statistically by the quantity P_B, the probability based on Poisson statistics that the observed source counts would be present given the observed local background rate.

Choosing a source significance limit $P_B < 1\%$ in at least one broad band, I find 2192 X-ray sources in the *Chandra* mosaic covering the W3-North, W3 Main, W3-OH, and IC 1795 regions. Source properties including X-ray spectra, absorptions, luminosities, and variability, will be presented in a forthcoming paper (Townsley et al., in preparation). For the present study, we consider only the X-ray source positions and error circles. Typical estimated 1σ error circle radii are $0.2 - 0.5''$, but can exceed $1''$ for sources far off-axis. Note that the *Chandra* positional errors are often considerably smaller than IRAC positional errors shown in Fig. 3.3 (panels A and B).

3.2.4 Near-infrared and optical surveys of IC 1795

I have also analyzed optical and near-infrared photometry. Optical *V*- and *I*-band photometry in the Bessell system were obtained with the 90Prime imager (Williams et al., 2004) at the Bok 2.3m telescope at Steward Observatory on the night of October 7, 2005 and October 3, 2007. The limiting magnitude is 22 mag in *V*. Detailed information about observations and data reduction will be described in a forthcoming paper by Jose' et al. (in preparation). Near-infrared photometry of IC 1795 in

[4]http://www.astro.psu.edu/xray/docs/TARA

J (1.25μm), H (1.65μm) and Ks (2.17μm) bands is taken from the Two Micron All Sky Survey (2MASS Skrutskie et al., 2006). The 3σ limiting sensitivity of this survey is 17.1, 16.4 and 15.3 mag for the three bands, respectively.

3.3 The IRAC point source catalog

3.3.1 Positions of the IRAC sources

In each IRAC channel, the distribution of the source positions as a function of their error was analysed. In Fig. 3.3 I show this analysis for channel 1. Considering only the flux uncertainties (computed with the PRF fitting), we found that sources with a larger position error are the fainter targets (with a larger uncertainty in the flux). The final photometric catalogs have been filtered for position errors, rejecting sources with positional errors in RA and DEC larger than 3.6″, which is ∼2 times the FWHM of the PSF in all IRAC channels. The histograms of the source positions in panels E-F of Fig. 3.3 show a bimodal structure which reflects the distribution of stars in IC 1795 and W3-Main (ch1-ch3), and of stars in IC 1795 and W3-OH (ch2-ch4). From the peak of the histogram centred on IC 1795 (panels E-F of Fig. 3.3), the centre of the cluster was found to be ($\alpha_{J2000}, \delta_{J2000}$) = (02:26:39.02, +62:00:41.24). In panels A-B of Fig. 3.4, I analyze the density distribution of all infrared sources (D_{star}). D_{star} is computed as the total number of sources in a ring (N), defined between two consecutive radii from the cluster centre divided by the ring area ($A_{\rm ring}$). The annuli start at 60″ from the centre of the cluster and end at 330″. The width of each annulus is 30". The errors in the density distribution are computed as $\sqrt{N}/A_{\rm ring}$. In panel A of Fig. 3.5 the density distribution of sources detected at least in one IRAC channel has been analysed as a function of the distance from the cluster centre. I notice that D_{star} peaks at 90″ and smoothly declines until 330″ with the exception of a second minor peak at ∼270″ (panel B of Fig. 3.4).

3.3.2 Photometry of the IRAC sources

The four Spitzer channels were matched using the IDL procedure *match_xy.pro* in the IDL-based *Tools for ACIS Review and Analysis (TARA)* package[5] (Broos et al. 2009).
The total number of point sources detected decreases as the IRAC wavelength increases due to a decrease in sensitivity. In particular, within 330″ from the cluster centre, I detect 918, 841, 303 and 243 sources at 3.6 μm, 4.5 μm, 5.8 μm and 8.0 μm respectively. 143 objects were detected in all four IRAC channels.
The colour-colour diagram (CCD) of the sources detected in all four IRAC channels and the colour-magnitude diagram (CMD) of the sources detected at 3.6 μm and 4.5 μm (the most sensitive) are shown in panels C-D of Fig. 3.4 (including the sources detected in all four bands). Megeath et al. (2005) proposed a conversion scheme from IRAC colours to source classification (Class 0,I,II,III sources). The results of this classification for our sources are summarised in Table 3.1. Using the CMD in panel C of Fig. 3.4, I distinguish between sources with infrared excess (characteristic of circumstellar discs around young star; [3.6]-[4.5]>0.2 mag) and "photospheric sources" without infrared excess ([3.6]-[4.5]<0.2 mag) . The "excess-threshold" adopted here ([3.6]-[4.5] = 0.2 mag) takes into account two factors: 1) model isochrones computed in the IRAC bands do not predict [3.6]-[4.5] colours exceeded 0.1 mag; see section 3.5.1 and Appendix 3.8.1 for details; 2) the maximum uncertainty of our photometry (0.07 mag). Out of 592 sources detected at 3.6 μm and 4.5 μm, 327 show an infrared excess and 265 are classified as "photospheric" sources. In the following sections I will call "infrared sources" objects detected at least in one *Spitzer* channel, and "excess sources" objects with [3.6]-[4.5]>0.2 mag.

Ruch et al. (2007) analysed the IRAC observations of the entire W3 region available in the Spitzer archive (GTO PID 127) and obtained with a total exposure time of 63.6 s in all IRAC channels. This corresponds to our short exposure, and it is almost one order of magnitude shorter than our long exposure time. They performed PSF photometry, using a version of DAOPHOT modified by the Galactic Legacy Infrared Mid-Plane Survey Extraordinaire (GLIMPSE) team.
Within 330″ from the centre of the cluster, they identified 77 sources visible in all four IRAC channels. With our deeper infrared survey I

[5]http://www.astro.psu.edu/xray/docs/TARA

detected 143 sources.There are however some differences between the two surveys: At 3.6μm and 4.5μm I do confirm 76 sources previously identified by Ruch et al. (2007), while 1 source has a position error larger than 3.6″ and it is not included in our analysis. At 5.8μm I confirmed the detection of 60 sources. Of the remaining 17 sources, 3 have position errors larger than 3.6″, while 14 have not been detected by the PRF fitting method performed in APEX. At 8.0μm I identified 32 sources. Of the remaining 45 sources, 26 have position errors larger than 3.6″, while 19 have not been detected with APEX. I inspected all the non-matched detections (14 at 5.8μm and 19 at 8.0μm) in our deeper survey: In all cases I find that the local background is highly variable compared to the source brightness and for this reason I did not detect any point-source with our PRF fitting method.
In summary I confirm 32 sources out of 77 sources detected by Ruch et al. (2007) in all four IRAC channels. In addition to these sources I identified 111 new sources in all the channels.

3.4 Cluster membership

To fully understand the evolution of protoplanetary discs in a large population of young stars, I need to study a sample that was previously identified in a disc-unbiased way.
Many photometric surveys of protoplanetary discs have been pursued with Spitzer, but Spitzer-only samples can suffer an important limitation: despite the excellent characterisation of discs provided for by sensitive IRAC surveys, all but the most sensitive surveys biases the ratio of disced systems to non-disced systems in favour of the disc sources.
Optical spectroscopy is widely used to identify cluster membership in star-forming regions. This is mainly based on two spectral features: emission of the Hα line and absorption of the Li line at 6708Å. These powerful tools are very good in identifying young stars but are limited to low-mass stars (spectral type of K – M). An alternative, robust, approach to study the complete population of a young stellar cluster is to combine sensitive X-ray and infrared observations (e.g. Mercer et al., 2009; Stelzer & Scholz, 2009; Wang et al., 2008; Getman et al., 2009). PMS stars are indeed found to be highly active in the X-ray regime and are typically characterized by an infrared excess.
Sensitive X-ray surveys are effective in identifying pre-main sequence

stellar populations due to their enhanced magnetic flaring compared to older stars (e.g. Feigelson et al., 2007). Flux-limited X-ray samples have the advantage of selecting young stars both with and without discs, but have the disadvantage of missing stars with fainter bolometric luminosities and lower masses. X-ray selected samples are complementary to *Spitzer* samples because they suffer less contamination from Galactic field stars or from diffuse nebular emission than infrared surveys. Getman et al. (2009) provide details on the relationships between stellar samples selected in *Chandra* and *Spitzer* surveys of a star-forming region. The high-spatial resolution telescope on the *Chandra X-ray Observatory* is essential to resolve crowded regions such as the IC 1795 and the W3 complex.
For IC 1795 I classified as cluster members sources detected in both, our infrared and X-ray, surveys. I also considered as potential members sources detected by *Spitzer* which show an infrared excess at 4.5μm but lack an X-ray counterpart. This approach is fundamental studying the properties of a cluster as distant as IC 1795, that can be strongly contaminated by background and foreground stars.

3.4.1 Cluster membership based on X-ray detection

Chandra source locations are matched to IRAC source locations using the IDL procedure *match_xy.pro* in the TARA package[6] (Broos et al. 2009). Associations between *Chandra* and *Spitzer* sources are assumed to be real when the probability that the X-ray and infrared sources are coincident exceeds 99%, assuming bivariate Gaussian error distributions for the two source positions. Within 330″ from the cluster centre, I find 280 associations between X-ray and infrared sources, and 9 cases where a single IRAC source has two or more possible *Chandra* counterparts. We did not find a single *Chandra* source with two or more possible IRAC counterparts. The *Chandra-Spitzer* matched positions are listed in Table 3.2. The corresponding optical, 2MASS, and IRAC photometry is compiled in Table 3.3. I analyzed the distribution of infrared sources with X-ray counterpart as a function of the distance from the cluster centre (panels A-B of Fig. 3.5). I found that the distribution peaks at ∼90″ from the centre, declines until almost 200″ and then remains constant until 330″ expept for a second peak at ∼270″. This is similar to

[6]http://www.astro.psu.edu/xray/docs/TARA

what I have noted previously (section 3.3.1, panel B of Fig. 3.4).
The number of X-ray sources alone, with and without infrared counterpart, and infrared sources (e.g. detected at least in one *Spitzer* channel) without X-ray counterpart are summarized in Table 3.1. The final catalog of the IC 1795 cluster members is in Table 3.3.

3.4.2 X-ray contamination

In this section I discuss the sources of contamination of an X-ray survey. The sensitivity limit to X-ray sources in the IC 1795 cluster using the *ACIS Extract* methods is approximately $L_x \sim 5 \times 10^{29}$ erg s^{-1} in the *Chandra* total band, $0.5 - 8$ keV, assuming moderate absorption around $N_H \sim 10^{21} - 10^{22}$ cm^{-2} ($A_V \sim 0.5 - 5$mag) and source spectra typical of PMS stars. This is not a well-established value due to differences in source spectra, spatial variations in extinction, loss of sensitivity off-axis due to degradation of the *Chandra* point spread function, and gain of sensitivity in some regions due to overlapping exposures in the W3 ACIS mosaic. In this work I use only the X-ray positions. A more detailed analysis of the X-ray observations will be presented in a forthcoming paper (Feigelson et al. in preparation). I estimate the completeness limit to be around $L_x \sim 1 \times 10^{30}$ erg s^{-1}. Based on the well-established empirical correlation between X-ray luminosity and stellar mass (Telleschi et al., 2007), this X-ray limit corresponds to a mass limit of around 1 $M_\odot$.
A fraction of the X-ray sources should be uniformly distributed contaminants unrelated to the IC 1795 cluster (see discussion in Getman et al., 2006). First, about $\sim 30 - 40$ faint and heavily-absorbed X-ray sources in a 100 arcmin^2 region (which is of the order of the cluster size) will be background extragalactic objects, mainly quasars and AGNs, seen through the molecular material in the W3 complex and Galaxy along the line-of-sight. Second, roughly $20 - 30$ lightly-absorbed X-ray sources in a 100 arcmin^2 region should be foreground stars and ~ 10 sources background stars. I expect that most of these contaminants will not have an infrared counterpart and so will not contribute to our source list. These extragalactic and Galactic contaminants in the X-ray sample will exhibit a random spatial distribution, as is clearly shown for X-ray sources without infrared counterpart in panels E-F of Fig. 3.5. However few quasars can have IRAC colours and X-ray fluxes as CTTS. This last source of contamination can be only be removed with a optical spectroscopy.

3.4.3 Cluster member candidates and IR contamination

I need to characterise the infrared sources detected with IRAC which do not show an X-ray counterpart. Using the CMD in panel D of Fig. 3.6, I distinguish between sources with infrared excess ([3.6]-[4.5]>0.2) and "photospheric" sources without infrared excess ([3.6]-[4.5]<0.2. In panels C-D of Fig. 3.5 the spatial distribution of the excess sources is similar to the distribution of the cluster, while the flat distribution of sources without excess suggests that these are not related to the cluster. Table 3.4 gives the 3σ upper limits of the 340 non-X-ray infrared excess sources. The standard deviation (σ) of the background was computed within a 10x10 pixel box centred on the X-ray position.

3.4.4 Infrared colour-colour and colour-Magnitude Diagrams of the cluster members.

In panels A-B of Fig. 3.6 the CCD and CMD of the cluster members detected within $330''$ from the center of the cluster are shown. Out of 837 sources detected in ch1 and ch2, I find 479 IRAC excess sources[7].
In panel A of Fig. 3.6 the 143 sources detected in all IRAC channels are shown. In Table 3.1 I summarised the classification of the discs using the IRAC colours from Megeath et al. (2005). For comparison in panels C-D of Fig. 3.6 I plot the IRAC detections with no X-ray counterpart: I notice that sources with and without infrared excess in the CMD of panel D reach 3.6μm$\sim$16 mag, while in the CMD of panel B sources without excess have 3.6μm magnitudes down to 15.5 mag, and only few sources with excess have 3.6μm magnitudes larger than 14 mag.

3.5 Age and Mass Distribution of the cluster members

In this section I estimate the age, the mass distribution and the completeness of our *Spitzer* survey of IC 1795.

[7]defined as [3.6]-[4.5] > 0.2

3.5.1 Age of the cluster

The ages of PMS associations are usually estimated by comparing the location of association members in a CMD or Hertzsprung-Russell diagram, to isochrones resulting from the predictions of PMS evolutionary model grids. This comparison usually makes use of dereddened optical photometry unaffected by the presence of a protoplanetary disc. However, for IC 1795 members I have extensive 2MASS and IRAC infrared photometry. Thus to optimise the isochronal fitting of IC 1795 members, I first look for the best colour to distinguish between sources with and without infrared excess. This is needed to clean the CMD of the infrared-excess sources.
I assume that the J magnitude is not affected by infrared excess (which in the different classes of discs would usually start, at least, from the H-band) and thus is sensitive to the stellar mass. I compiled different CMDs, combining in different ways the J, 3.6μm and 4.5μm magnitudes. The advantage of using the J-[3.6] or J-[4.5] combinations is that photospheric and infrared excess sources are clearly separated in colour. However the disadvantage is that the J magnitude is highly affected by extinction along the line of sight.The advantage of using the [3.6]-[4.5] combination instead, is that at these wavelengths interstellar extinction is very low (see the module of the extinction A_V in Fig. 3.9). I thus use the [3.6] vs. [3.6]-[4.5] CMD to distinguish between objects with and without infrared excess.

Figs. 3.7-3.8 show the CCDs and CMDs in the near-infrared and optical planes, respectively. The filled circles with different shapes represent the different classes of discs (see panel A of Fig. 3.6 for the symbol key). Overlaid on the diagrams are the 3 Myr and the 5 Myr isochrones obtained using the FRANEC evolutionary code (see Appendix 3.8.1). I reddened the isochrones with $A_V = 2$ mag which is the minimum extinction expected for a cluster at distance of 2 kpc. Without any information of possible differential extinction within the cluster, from these CMDs it is not possible to distinguish the different isochrones. The positions of the sources can be either affected by additional extinction, or by a spread in age, as well as by undetected binarity.
The best choice is to use the isochrones computed in the IRAC colours and compare them to the sources without infrared excess as shown in Fig. 3.9. Given the independent estimate of the distance of 2.0 kpc (e.g. Xu et al., 2006) and given that in the IRAC bands the foreground ex-

tinction for our cluster is negligible, the only parameter that determines the vertical position of the Main-Sequence Turn-On (*MSTON*; see appendix 3.8.1) is the age of the cluster. In Fig. 3.9 I show the 1 Myr, the 3 Myr and the 5 Myr isochrones. I checked that an error in the distance of ±0.2 kpc would not overlap these isochrones. From the *MSTON* I can conclude that the cluster is younger than 5 Myr and it likely has an age between 3 and 5 Myr. This is consistent with earlier estimates (Oey et al., 2005). Due to the presence of other stars with a 3.6μm magnitude in the range of 12.5 - 14 mag which do not follow the shape of the isochrones, I investigate the possibility of a spread in age of the cluster members. I first notice that the 1 Myr isochrone does not reproduce the distribution of the sources on the CMD (Fig. 3.9). The random spatial distribution of the photospheric sources with different [3.6] mag suggests that instead of a spread in age of the cluster due to different star forming episodes, the remaining stars with 3.6μm = 12-14 mag are probably binary stars. In section 3.5.2 I test such a hypothesis by including the binarity in a simulation of the cluster .

3.5.2 Luminosity and Mass Functions of IC 1795

The comparison of the observed and theoretical luminosity function enables us to estimate the completeness limit of our *Spitzer-Chandra* survey. I compiled the observed luminosity function using the 3.6μm magnitude as tracer of the stellar photosphere. To have a description of the entire stellar population of IC 1795, the observed luminosity function includes cluster members with and without infrared excess and cluster member candidates (defined in section 3.4.3). I used the method described in Appendix 3.8.2 to determine the "photospheric" 3.6μm magnitude of the sources with infrared excess. The same has been done for the cluster member candidates.

I computed the theoretical luminosity function using a galactic initial mass function (IMF) (Kroupa, 2002) and the 4 Myr and 5 Myr isochrones respectively. The number of simulated stars is normalized in such a way that in each simulation I have the same total number of simulated and observed stars below a certain magnitude which represents the completeness of our survey. I compare the simulations obtained using a completeness value of 13.5 mag, 13.75 mag, 14 mag, 14.25 mag, 14.5 mag and 15 mag at 3.6μm. I conclude that the completeness of our survey at 3.6μm was 14 mag

I notice, however, that for both ages of 4 Myr and 5 Myr, the simulations do not well-reproduce the number of sources in the 3.6μm magnitude range of $13 - 14$. This might be an effect of a binary population unresolved in the cluster. To test this, I ran simulations with 30% and 50% binary fractions, with primary and secondary masses drawn independently from the same IMF. The outcomes are little different from our original calculations, suggesting our simulation of the luminosity function is little affected by the binary fraction, or the 1 Myr difference in age between the 4 Myr or 5 Myr isochrones.

In order to convert the completeness expressed in magnitude into the corresponding stellar mass value, I now extract the mass function of IC 1795. Using the 4 Myr and 5 Myr isochrones, from the observed luminosity function I derived the stellar masses and hence construct the mass function for the cluster. I used the method described in Appendix 3.8.3 to assign a stellar mass to each source. The mass function is computed using the 4 Myr and the 5 Myr isochrone to convert the 3.6μm magnitudes to stellar masses (see Fig. 3.10). Using an isochrone of 4 Myr the derived mass function departs from the theoretical IMF (Kroupa, 2002) at M$\sim$1 $M_{\odot}$, while using the 5 Myr this value changes to 1.2 $M_{\odot}$; these masses correspond to the estimated completeness at 3.6μm of 14.0 mag.

3.6 Disc evolution: effect of the stellar mass and the environment

The goal of our study is to investigate the disc evolution in high-mass star-forming region. In this section, I discuss the disc-bearing sources of the cluster members[8], as function of the (1) stellar mass, (2) spatial distribution of cluster members, (3) distance from the O-type star. Finally I discuss our results in the context of previous studies of disc evolution in low- and high-mass environments.

3.6.1 Disc fraction vs stellar mass and spatial distribution

I examine the mass dependence of disc emission, but only few stars have been spectrally classified so far. A detailed spectral classification of the

[8]defined in section 3.4.1 as Spitzer sources with an X-ray counterpart

cluster members is in preparation (Kim et al. 2009, in preparation).
The disc fraction was first computed using the 3.6μm magnitude as a tracer of stellar photosphere (Fig. 3.11).
In order to define the binning in 3.6μm magnitude to compute the fraction of sources with and without infrared excess, I follow the method described in Appendix 3.8.2.
Between 3.6μm = 10-12 mag, the disc fraction rapidly increases from 20% to 50%, it remains constant at 60-40% between 12 and 14.5 mag. Since this is the first work where the disc fraction is computed using the IRAC magnitudes and derived from them the corresponding stellar mass, I also used as a proxy for mass, the J magnitudes as it is usually done in literature (e.g. Hernández et al., 2007), also if only ∼80% of our IRAC sources have a near infrared counterpart. These bands are relatively unaffected by disc excess emission but strongly affected by the extinction. The 4 Myr isochrone (see section 3.5.1) has been used to convert the J magnitudes to get masses. In these bands the relation between mass and magnitude is almost unique (see Fig. 3.12).
In Fig. 3.13 (panel A) I show the CMD using the J magnitude as photospheric tracer and the [3.6]-[4.5] IRAC colours to define the sources with and without infrared excess. After the histograms of sources with and without excess (panel B of Fig. 3.13), the disc fraction is shown in panel C. This is computed as the fraction between sources with and without excess in bins of one magnitude. The errors are computed as the square root of the number of sources in each bin. The corresponding mass is reported in the upper x-axis.
The disc fraction is found to increase from 20% to 60% for J magnitudes from 11 to 15. This corresponds approximately to masses between 8.4 and 0.8 $M_{\odot}$. The disc fraction remains constant around 50% toward lower masses. An increasing trend is clear down to 15 magnitudes even after taking into account the uncertainty in the disc fraction.
Taking into account only solar-type stars with masses ∼1 $M_{\odot}$, up to which our population sample is complete (see discussion in section 3.5.2), the disc fraction is 50%.
This value is consistent with the disc fraction of solar-type stars previously computed with the 3.6μm magnitude. An analysis of the disc fraction as a function of stellar mass was presented by Hernández et al. (2007) in a Spitzer study of σOri. In their work the lowest fraction of discs was observed in the highest mass stars (in the HAeBe range). They found a marginal evidence that the disc fraction declines toward

lower masses (into the brown dwarf range), in agreement with results from Lada et al. (2006) for the young (2-3 Myr) stellar group IC 348. Nevertheless, including the error bars, the disc fraction in σOri was also consistent with no mass dependence toward lower masses.

Previous studies proposed that the different star-forming regions in the W3 molecular-cloud have been triggered by ionising winds from IC 1795 (Oey et al., 2005; Feigelson & Townsley, 2008). If, however, a triggered star-formation took place in IC 1795 itself, a different distribution a of sources with and without discs and with an age gradient is expected (e.g. the Cepheus B star-forming region; Getman et al., 2009).
In Fig. 3.14 I show the spatial density distribution of sources with and without infrared excess.
The disc fraction (f_d) is defined as the ratio between the number of sources with discs ($N_{\rm disc}$) and the total number of sources (with and without discs; $N_{\rm tot}$). The fraction f_d was computed in consecutive rings. Within the uncertainties, the disc fraction remains constant across the IC 1795 region at about 50%.
This result argues against a triggered star formation scenario for IC1795. A constant disc fraction as a function of the distance from the centre of the cluster was also found in σ Ori (Oliveira et al., 2006) using K and L-band observations. This result is however in contrast with Hernández et al. (2007) who instead found an evidence for a higher disc fraction near the cluster centre for σ Ori.

3.6.2 Influence of the O star in the cluster: disc photoevaporation and cluster dynamics

In this section I check if the effects of the O9 star on the disc fraction and on the dynamics of IC 1795.
I notice that the O9 star lies at 120″ from the projected spatial centre of the cluster. In order to study the influence of the O star in the cluster I now re-centre the cluster on the O star. Fig. 3.15 shows the spatial density distributions of sources with and without excess, and the corresponding disc fraction (panel E). As expected, sources without infrared excess now show a peak in their spatial density distribution at 120″ from the O star, which corresponds to the offset distance.
The spatial distribution observed is almost constant at different distances

from the O star also within the first 60″ from the center of the star (which corresponds to 0.58 pc at the cluster distance).
Despite the theoretical expectations of Johnstone et al. (1998) who predict evidence of photoevaporation only for discs closer than 0.3 pc (which correspond to 30″ for a cluster at 2kpc) from a O6, I could not define the first annulus smaller, since the number of sources was not statistically significant. I decide however to check if in the first annulus the disc fraction was different than the value computed further.
If the UV radiation from the O star is responsible for the photoevaporation of the nearby discs, I would expect fewer sources with excess near the O star and a higher excess fraction further away from the O star. A behavior consistent with the expectation of Johnstone et al. (1998) was found by Balog et al. (2007) and by Mercer et al. (2009). From the analysis of the 2-3 Myr NGC2244 cluster Balog et al. (2007) found a smaller disc fraction within 0.5 pc from the O star compared to the fraction obtained at larger distances. However they found only a trend of the disc fraction and not a complete lack of them (as predicted by Johnstone et al., 1998).

Finally, I investigate whether mass segregation acted on the dynamics of the cluster. The time scale of mass segregation is of the order of the relaxation time $t_{\rm relax}$ in which a cluster reaches some level of kinetic energy equipartition, with the massive stars sinking to the core and low-mass stars moving to the cluster halo (e.g. Bonatto et al., 2006).
Although some degree of mass segregation occurs earlier, the position of massive stars in rich young clusters generally reflects the cluster's initial conditions. In IC 1795, the high mass stars are not preferentially concentrated in a different region compared lower mass members. The positions e.g. of the massive stars in the Trapezium cluster in Orion indicate that they formed in, or near, the center of the cluster (Bonnell & Davies, 1998).
I estimate the two-body dynamical relaxation time scale $t_{\rm relax}$ of IC 1795 using the formula (e.g. Bonatto et al., 2006):

$$t_{\rm relax} \approx (N/8\ln N) t_{\rm cross} \tag{3.1}$$

where $t_{\rm cross} = 2R/v_{\rm disp}$ is the characteristic time for a star to cross a cluster of radius R and velocity dispersion $v_{\rm disp}$. Adopting a radius of the cluster $R \sim 3.2pc$ (see section 3.3.1) and using a rough estimate for the unmeasured velocity dispersion $v_{\rm disp} \sim 3kms^{-1}$ (Binney & Tremaine,

1987), and $N \sim 540$ stars (see section 3.5.2), I obtain $t_{\rm relax} \sim 23$ Myr for IC 1795. I note that the actual number of cluster members may be higher than described here, leading to an even larger $t_{\rm relax}$.
As the cluster age is 5–6 times less than its relaxation time, I did not find any evidence of mass segregation in IC 1795. A similar result have been found in NGC 2244 by Wang et al. (2008, 2009) and in NGC 6334 (Feigelson et al., 2009).

3.6.3 Disc evolution

Based on the IRAC colours, the fraction of disc of stars with masses $\sim$1 $M_\odot$ in IC 1795 is 50%$\pm$10% (see section 3.6.1).
In Fig. 3.16 I compare our result with the disc fraction of other star forming regions found in the literature. The mid-infrared probes the circumstellar dust beyond the inner 5 AU of the disc, I study the evolution of this part of the disc as a function of cluster age and environment. I then include Taurus and the Coronet cluster at 1 Myr (Hartmann et al., 2005; Sicilia-Aguilar et al., 2008), IC 348 at 2-3 Myr (Lada et al., 2006), σ Ori at 3 Myr (Hernández et al., 2007), Tr 37 at 4 Myr (Sicilia-Aguilar et al., 2006; Mercer et al., 2009), and NGC 2362 at 5 Myr (Dahm & Hillenbrand, 2007). The fractions of cluster members with discs in these clusters decrease from 80% to 20% with age.
Our result is consistent with the disc fraction around solar type stars in Tr 37 (Sicilia-Aguilar et al., 2006), an OB association with an age similar to IC 1795.
The fraction of stars with mid-infrared disc emission as a function of the age of the stellar group in low mass and high mass environments is shown in Fig. 3.16.
However there are a number of bias effects complicating the disc fraction from literature which may affect our conclusions:
- the cluster membership;
- the uncertainty on the age of the cluster;
- the disc fraction which is not always computed in specific stellar mass range;
- unresolved binarity;
Most of the disc fractions from the literature are computed for clusters within 1kpc, while IC 1795 is $\sim$2 kpc. This allow them to have a membership down to M-type stars. However, since the cluster membership has been defined, in most of the cases, using optical spectroscopy (as I

discussed in section 3.4), the cluster memberships are not complete for intermediate mass objects.
Our work is instead complete to $\sim$1 $M_{\odot}$, which corresponds to early-K spectral types. Therefore a comparison between the disc fraction of 50%$\pm$10% found for IC 1795 and that of other clusters might be misleading, e.g. for lower masses where our survey is incomplete, I expect to miss part of the photospheric population.
Given all uncertainties, I find that IC 1795 follows the smooth decline of the disc fraction with age observed for other clusters. These studies and our result seem to indicate that the decline of disc fraction with age is similar for both low- and high-mass clusters.

3.7 Summary

In this chapter I presented a deep Spitzer/IRAC survey of the OB association IC 1795.
Combining the infrared Spitzer/IRAC observations with a deep X-ray Chandra/ACIS survey I carefully establish the cluster membership of the cluster. IRAC sources with infrared excess (characteristic of circumstellar disc around young star) without X-ray counterpart are classified as cluster member candidates.
The spatial distribution of the cluster was found to be asymmetric around the cluster centre, nor around the massive O and B type stars.
The disc fraction was analysed as a function of the distance from the cluster centre as well as a function of the stellar mass. In the first case, the fraction of disc was computed in a series of concentric circles (each 30″) from the centre to the outer radius: within the errors, the discs were constantly 50% of the total sources number.
This suggests that only one star-formation event occurred in IC 1795 and that probably it was not triggered by external ionisation shocks.
Using the [3.6] IRAC magnitude as tracer for the stellar mass I find that the disc fraction is $\sim$20% for masses $>$2 $M_{\odot}$ and $\sim$50% for masses $<$2 $M_{\odot}$, down to our survey completeness, 1 $M_{\odot}$: I confirm that the dissipation of discs around high-mass stars ($>$2 $M_{\odot}$) is faster compared to the dissipation around stars of 1-2 $M_{\odot}$.
The age of the cluster was determined via the position of the Class III stars (stars with no discs) on the [3.6] – [3.6]-[4.5] colour-magnitude diagram. Compared to optical and near-infrared CMDs, this one has the

advantage that different isochrones are more separated and the interstellar extinction is negligible. For IC 1795 I determine an age of 3 – 5 Myr. As theoretically expected, I did not find any a variation on the disc fraction within 0.6 pc from the massive star. No evidence of mass segregation has been found in IC 1795, which would explain that the highest mass stars not in the centre of the cluster.
Measurements of the disc fractions in low mass and high mass environment have been collected from the literature and I found that the temporal evolution is comparable in high mass and low mass clusters.

3.8 Appendix

3.8.1 Evolutionary model

The isochrones adopted for the analysis have been computed using the FRANEC evolutionary code. I briefly describe here the physical inputs in the code and for detailed explanation the reader can refer to (Chieffi & Straniero, 1989; Degl'Innocenti et al., 2008). The opacity tables are from Ferguson et al. (2005) for $\log T[K] < 4.5$ and from Iglesias & Rogers (1996) for higher temperatures. The equation of state (EOS) is described in Rogers et al. (1996). Both opacity tables and EOS are calculated for a heavy elements mixture equal to the solar mixture of Asplund et al. (2005). Our models are completely self-consistent, with a *unique* solar chemical composition, $(Y, Z) = (0.27, 0.02)$, in the whole structure. The value of the mixing length parameter adopted in the models is $\alpha_{MLT} = 1.6$.

Transformations from the theoretical ($log(T_{eff}[K])$, $log(L/L_{\odot})$) to the observational planes have been performed via synthetic photometry. In particular I have computed the isochrones in the 2MASS and $VI_{\rm Bessell}$ photometric systems and for the first time in the IRAC photometric system. The filter throughputs and zero points of the IRAC photometric system are defined in Reach et al. (2005). I used stellar spectra generated with both the ATLAS9 (see Castelli & Kurucz (2003)) and PHOENIX (Brott & Hauschildt (2005)) model atmospheres codes.

The ATLAS9 grid of models is limited to temperatures higher than 3500 K; corresponding isochrones have then a lower cut in mass at values of 0.36 $M_{\odot}$ and 0.38 $M_{\odot}$ for 3 and 5 Myr respectively. The PHOENIX grid can cover a region of lower temperatures (T > 2000 K) but has an

upper limit in temperature of 10000 K. This corresponds to 2.96 $M_{\odot}$ and 2.56 $M_{\odot}$ for 3 and 5 Myr respectively.

Mid-infrared isochrones

In the mid-infrared (MIR) CMDs, the part of the isochrone for intermediate-to-high mass stars that have reached already the Main Sequence (MS) is almost vertical. Lower mass stars are still in the PMS phase. The PMS objects are cooler and with a lower surface gravities; their spectra at the MIR wavelengths are no longer described by an (approximate) black body exponential tail, as in the MS phase. Due to the presence of spectral features the PMS isochrones show a bending towards redder colours.

PMS stars have larger radii when they are at the top of their Hayashi track, and the radii become smaller as the stars evolve and contract. In the totally-convective phase the effective temperature does not change much, leaving the observed colour almost unchanged, even though the change in surface gravity slightly affects the shape of the emerging spectrum. But with decreasing age, the change in radius heavily affects the total luminosity. For this reason mid-infrared PMS isochrones are no longer age-degenerate as they are in the MS phase; on the contrary different PMS isochrones are well separated in the MIR CMDs and can be used for age-dating the cluster, or, at least, setting some constraint on its age.

In particular, the transition phase between PMS to MS is characterised by a hook-shaped bending in the isochrone. As the age increases, the hook and the red PMS branch move towards higher magnitudes (lower luminosities). When an independent estimate of the distance and the extinction is available, as in our case, the Main-Sequence Turn-On (MSTON) can be used as upper limit for the age of a cluster. After placing an isochrone in the CMD, if no star is observed below the MSTON, at colour equal zero, then the cluster must be younger than the given isochrone.

3.8.2 Disc fraction in the [[3.6],[3.6]-[4.5]] CMD

Fig. 3.17 shows the [[3.6]-[4.5], V] CMD. In this diagram the presence of the circumstellar disc causes the object to move horizontally towards red colours. This is because the disc emission affects only slightly the V

magnitude (e.g. through optical veiling produced by mass accretion). In the [[3.6]-[4.5],[3.6]] CMD instead, the disc emission affects also the y-axis ([3.6] mag). As a consequence the presence of the disc will move the object towards red colours obliquely.
To properly compute the disc fraction as a function of the [3.6] magnitude (and hence stellar mass) it is necessary to take into account this effect. What I have to do is to calculate the isomass in the [3.6] magnitude in the [[3.6]-[4.5],[3.6]] CMD. This was computed in the following way: I select all stars in a series of horizontal slices in the [[3.6]-[4.5], V] CMD (central V = 20.5; 21.5 mag and bin = 0.5 mag). I look for the position of the same objects (highlighted with the same symbols) in the [[3.6],[3.6]-[4.5]] CMD. I extrapolate the median inclination of the position of these sources in this CMD for each magnitude bin. Finally, I computed the disc fraction in a series of bins counting the sources in the oblique slices.

3.8.3 Relation between 3.6μm IRAC magnitude and stellar mass

Due to the spread of the sources along the isochrone, I assign the most probable mass by taking into account the photometric uncertainty via a maximum-likelihood method. I define the Likelihood function for the i-th observed star as:

$$\mathcal{L}^i(m_j) = \frac{1}{2\pi\,\sigma^i_{3.6}\,\sigma^i_{4.5}} \times \exp\left(-\chi^2/2\right)\ ; \tag{3.2}$$

where:

$$\chi^2 = \left(\frac{[3.6]^i_{obs} - [3.6]^j_{th}}{\sigma^i_{3.6}}\right)^2 + \left(\frac{[4.5]^i_{obs} - [4.5]^j_{th}}{\sigma^i_{4.5}}\right)^2\ ; \tag{3.3}$$

here the j index runs on the masses along the isochrone and σ^i are the photometric uncertainties for the i-th star and subscripts *obs* and *th* stand for observed and predicted quantities respectively. Since I use the magnitude-magnitude space the uncertainties can be considered uncorrelated and the χ^2 assumes the form of eq. (3.3). I assign to the i-th data point the mass value m_{j*} for which $\mathcal{L}(m_j)$ has its maximum.

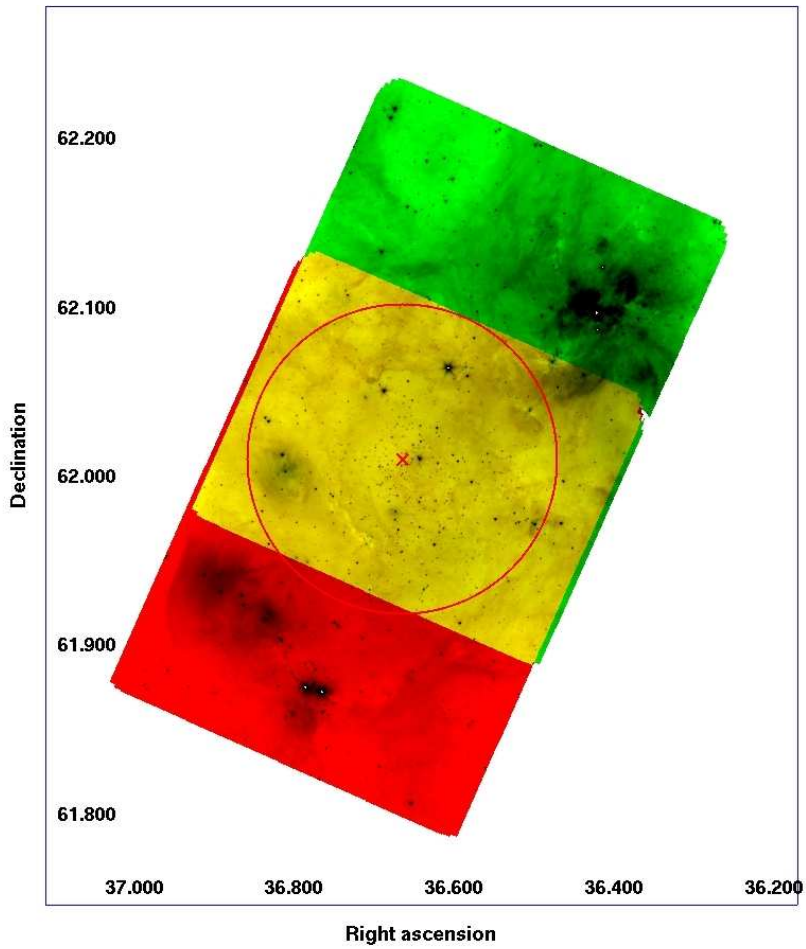

Figure 3.1 Combined image of the mosaics obtained with the long exposures of IRAC/ch1 and IRAC/ch2. The central part (*yellow*) is covered by both the channels. The *red* 'cross' and the circle represent the center and the edge of IC 1795, respectively. W3 Main is covered only by IRAC/ch2 (*red* part) and W3 OH only by IRAC/ch1 (*green* part).

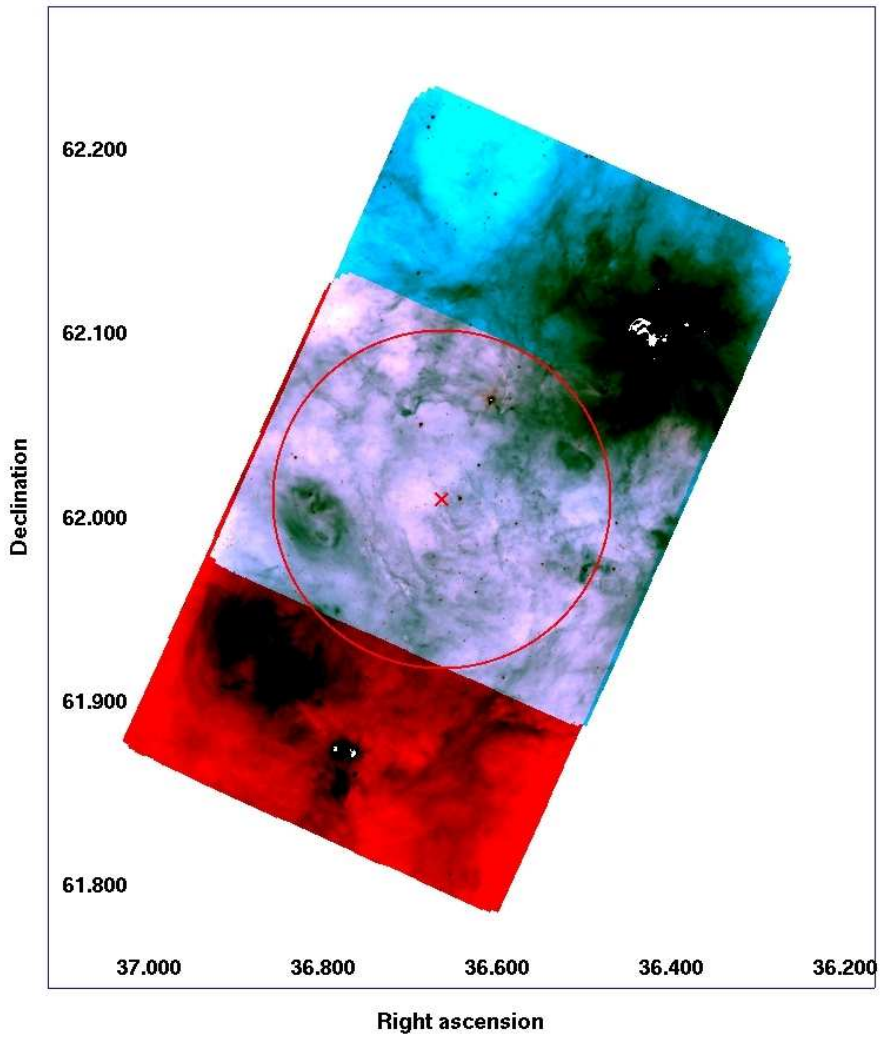

Figure 3.2 As Fig. 3.1, but for IRAC/ch3 and IRAC/ch4. The overlapping part of the 2 channels is shown in *violet*, while the *red*-one is covered only by IRAC/ch4 and the *cyan* only by IRAC/ch3.

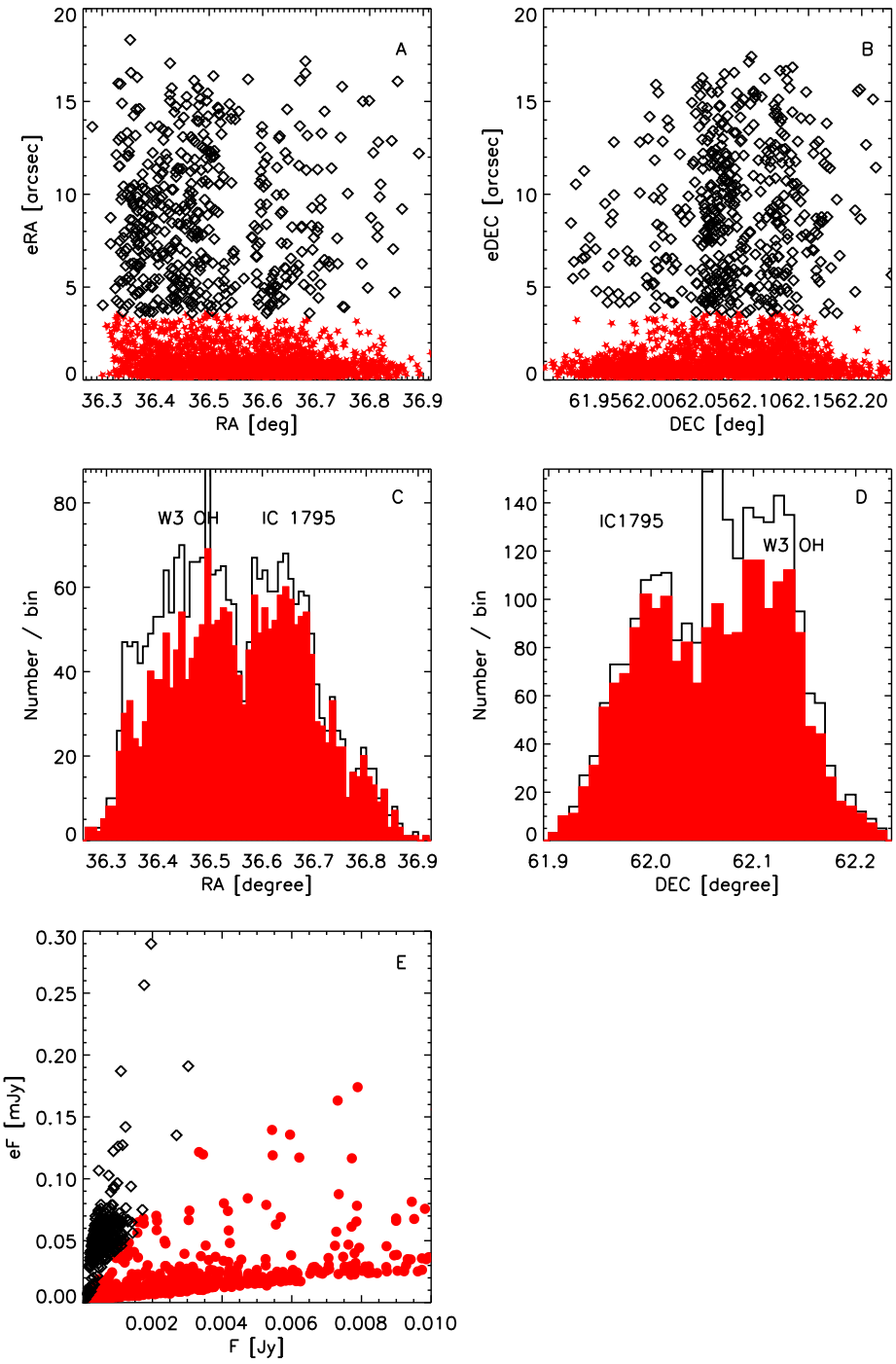

Figure 3.3 *A-B*: RA and DEC errors versus RA and DEC coordinates of all the sources detected in IRAC/ch1. The empty diamonds represent sources with coordinates errors larger than 3.6″. Sources with errors lower than 3.6″ are highlighted with filled red stars. *C-D*: Black empty histograms represent the RA and DEC coordinates of all sources shown in panels A-B with empty diamonds. The red filled histograms represent RA and DEC coordinates of sources of our final lists (filled red stars in panels A-B). *E*: Flux error versus the flux of the sources shown in the upper panels. The red filled stars represent the sources of our final lists selected with position errors in RA and DEC ≤3.6″. Positional errors >3.6″(black empty diamonds) correspond to the fainter sources with larger errors.

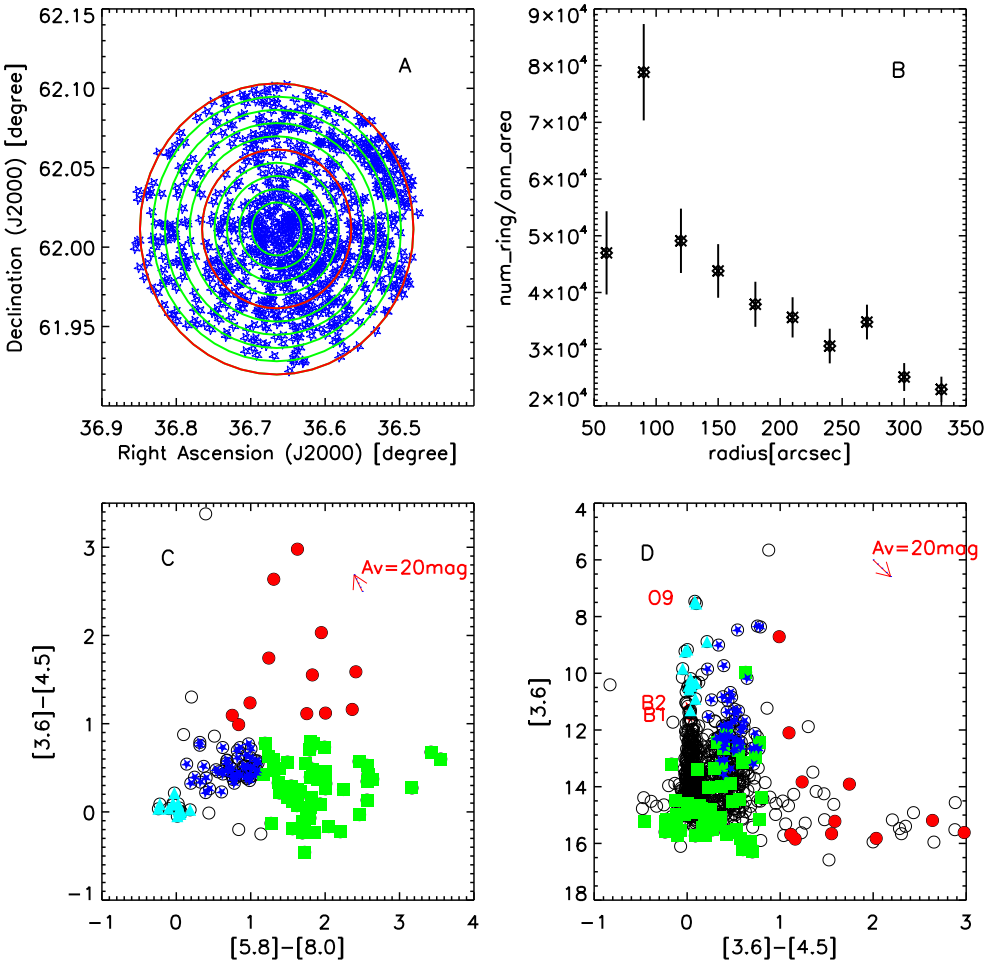

Figure 3.4 Spatial density distribution of all IR sources (*A*), and their spatial density distribution as a function of the distance from the center of the cluster (*B*). The green circles represent radii from 60″ from the center of the cluster to 330″ with 30″spacing. *C*: colour-colour Diagram (CCD) of the IRAC/*Spitzer* sources detected within 330″ from the center of the cluster. The different symbols and colours represent the disc classification from Megeath et al. (2005): *filled (cyan) triangles:* photosphere/Class III ; *filled (green) squares:* Class I/II; *filled (red) circles:* Class O/I; *D*: colour-Magnitude Diagram (CMD) of all the sources identified at 3.6μm and 4.5μm. The different symbols represent the sources detected in four IRAC channels classified in the CCD on the right. *Empty (black) circles:* sources with magnitudes that do not follow the previous classification. The arrows represent an extinction A_V= 20 mag.

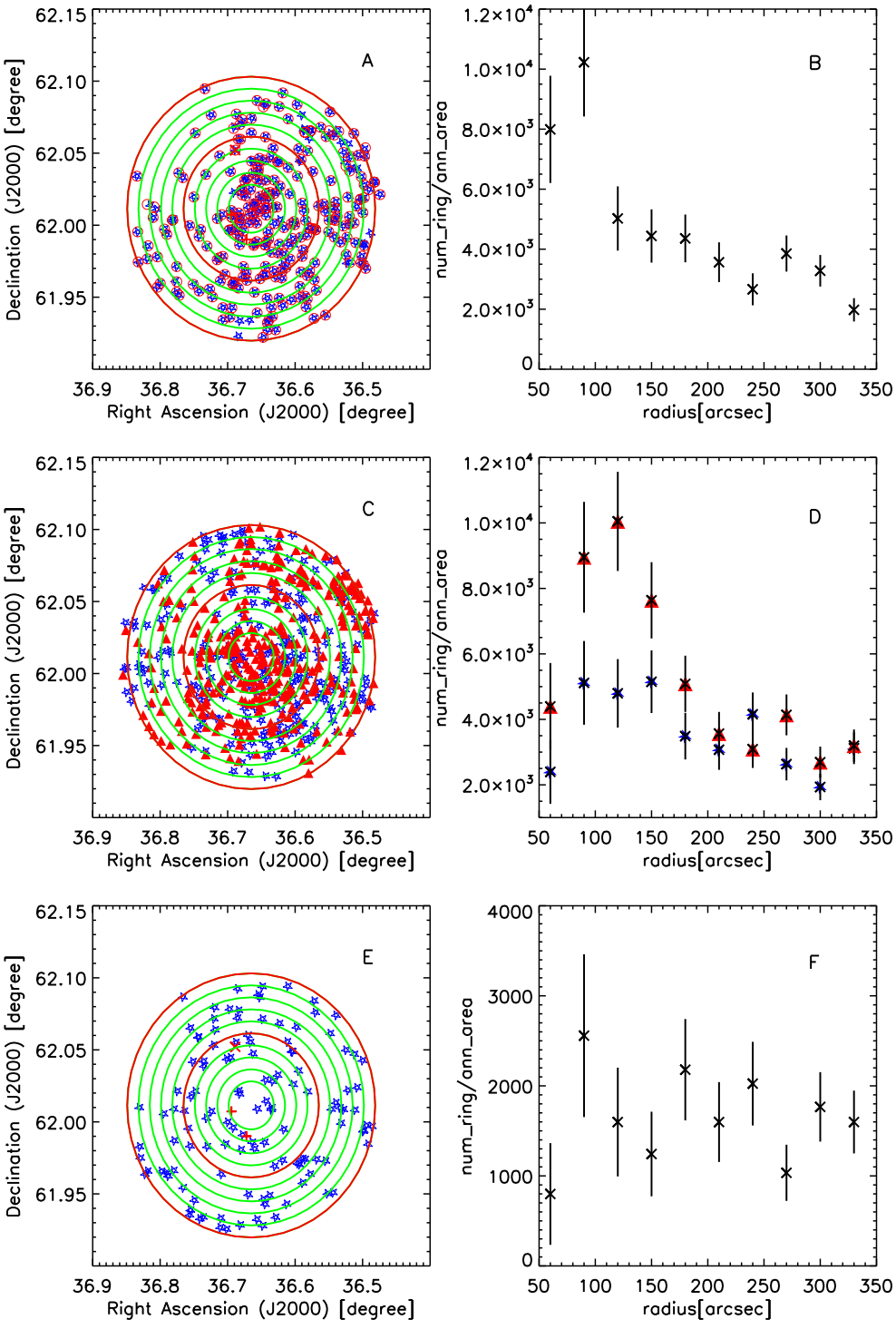

Figure 3.5 Spatial density distribution of all the IR sources (*left column - A, C, E*), and their spatial density distribution as a function of the distance from the center of the cluster (*right column - B, D, F*). The green circles represent annuli from 60″ from the center of the cluster to 330″ with a spacing of 30″. *A-B:* infrared sources with an X-ray counterpart. *C-D:* infrared sources without an X-ray counterpart: the triangles represent sources with excess and the stars sources without excess. *E-F:* X-ray sources without infrared counterpart.

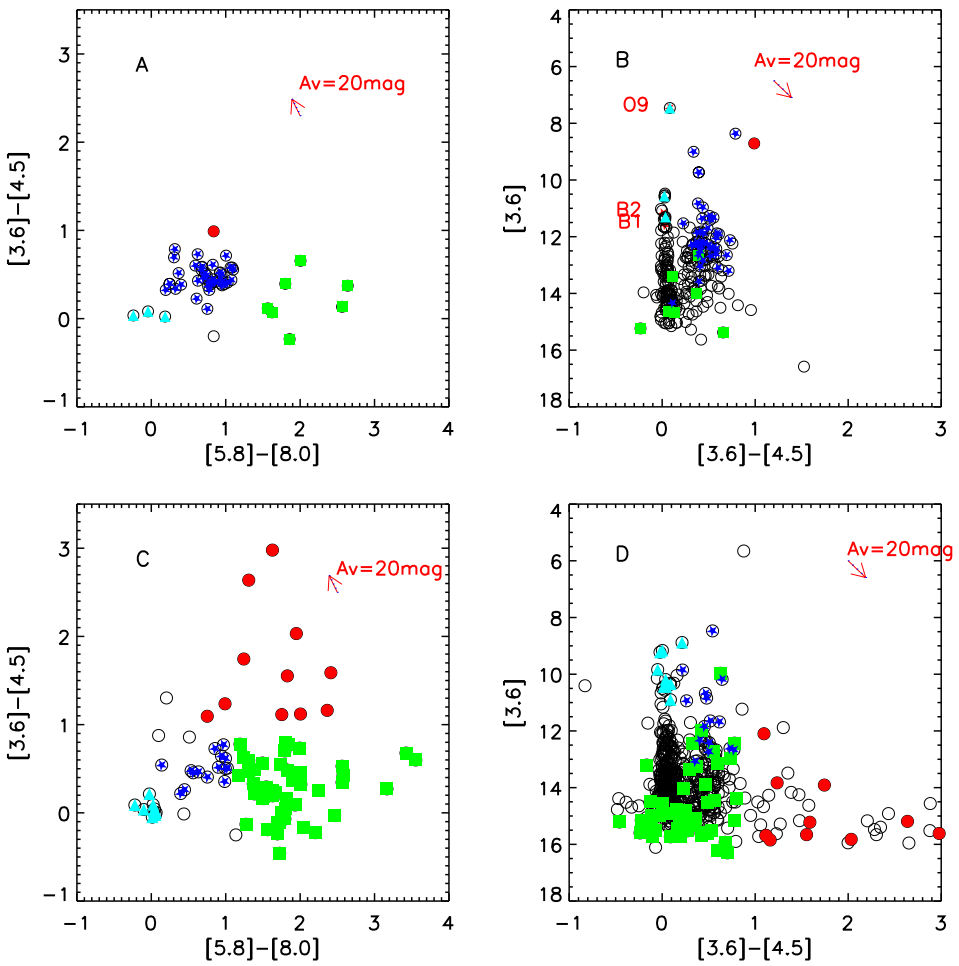

Figure 3.6 *Left*: CCD of the IRAC/Spitzer sources detected within 330″ from the center of the cluster (empty black circles). The different symbols and colours represent the disc classification from Megeath et al. (2005): *filled (cyan) triangles:* photosphere/Class III ; *filled (green) squares:* Class I/II; *filled (red) circles:* Class 0/I; *Right*: CMD of all sources identified in IRAC/ch1 and IRAC/ch2. The different symbols represent the sources detected in the 4 IRAC channels classified in the CCD on the right. The arrows represent an extinction $A_V = 20$ mag. *A-B:* infrared sources with an X-ray counterpart. *C-D:* infrared sources without an X-ray counterpart.

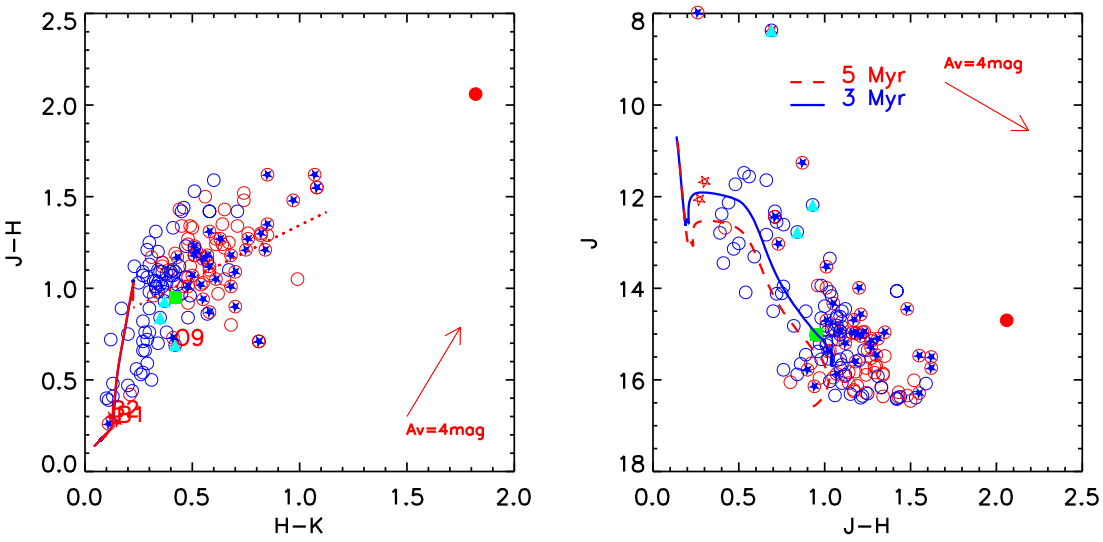

Figure 3.7 Near infrared CCD (*right panel*) and CMD (*left panel*) of the cluster member sources with a near-infrared 2MASS counterpart. The arrow represents an extinction A_V= 6 mag. The 5 Myr and (*dashed red line*) and the 3 Myr (*solid blue line*) are reddened using A_V = 2 mag. See panel A of Fig. 3.6 for the symbol key.

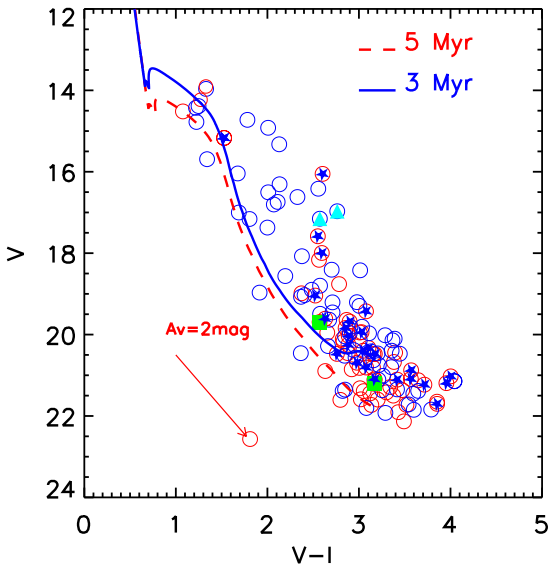

Figure 3.8 Optical CMD (optical catalog from Jose, Kim et al. in preparation) of the cluster members with an optical counterpart. The arrow represents an extinction $A_V = 6$ mag. See panel A of Fig. 3.6 for the symbol key.

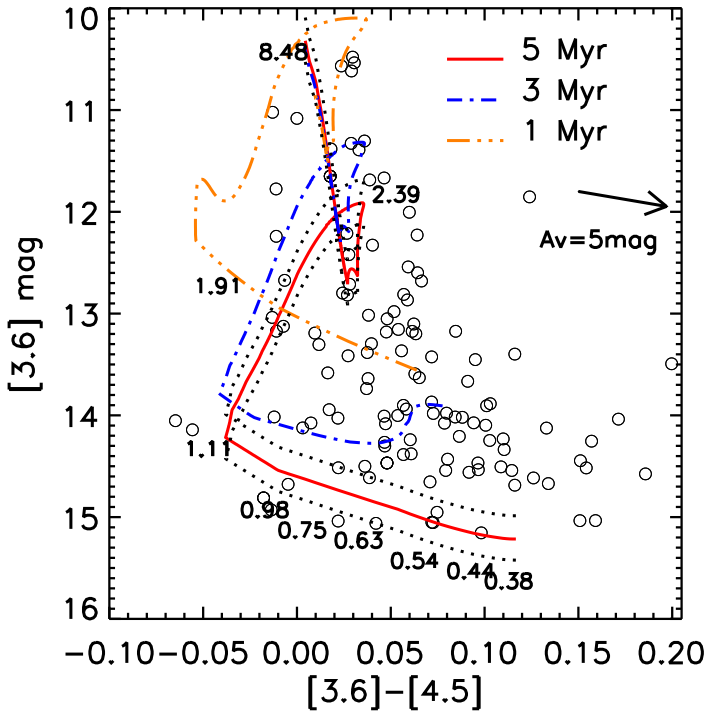

Figure 3.9 Close up of CMD in panel B in Fig. 3.6 around sources without infrared excess (empty circles) in the IRAC CMD (panel B in Fig. 3.6). Overlaid are the 1 Myr, 3 Myr and 5 Myr isochrones (shifted at a distance of the cluster of 2 kpc). The dotted lines represent the 5 Myr isochrones but shifted at a maximum and minimum distance of 2.2 and 1.8 kpc. The numbers along the 5 Myr isochrone represent the corresponding masses (in $M_{\odot}$).

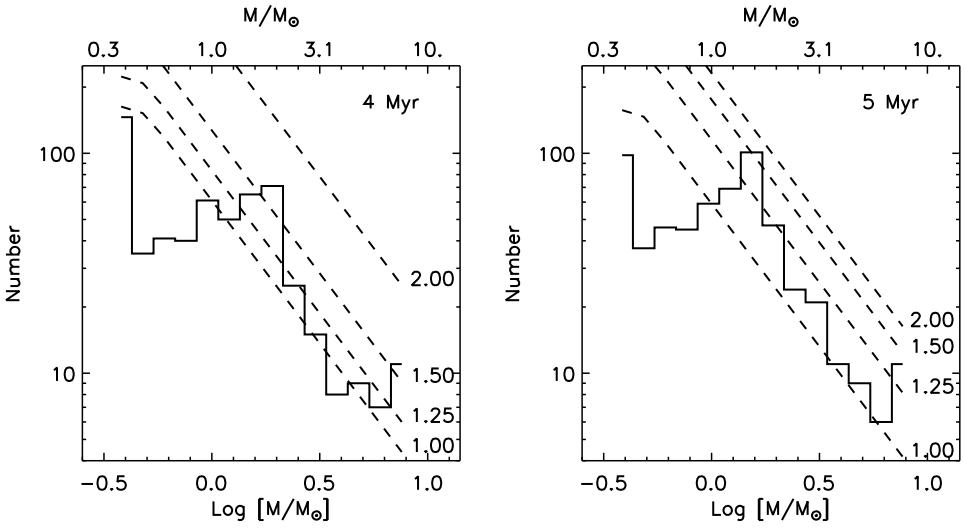

Figure 3.10 Mass function computed at [3.6] μm using isochrones at 4 and 5 Myr. Overplotted are the galactic IMFs (Kroupa, 2002) normalized at different completness masses: 1 $M_{\odot}$,1.25 $M_{\odot}$,1.5 $M_{\odot}$,2 $M_{\odot}$.

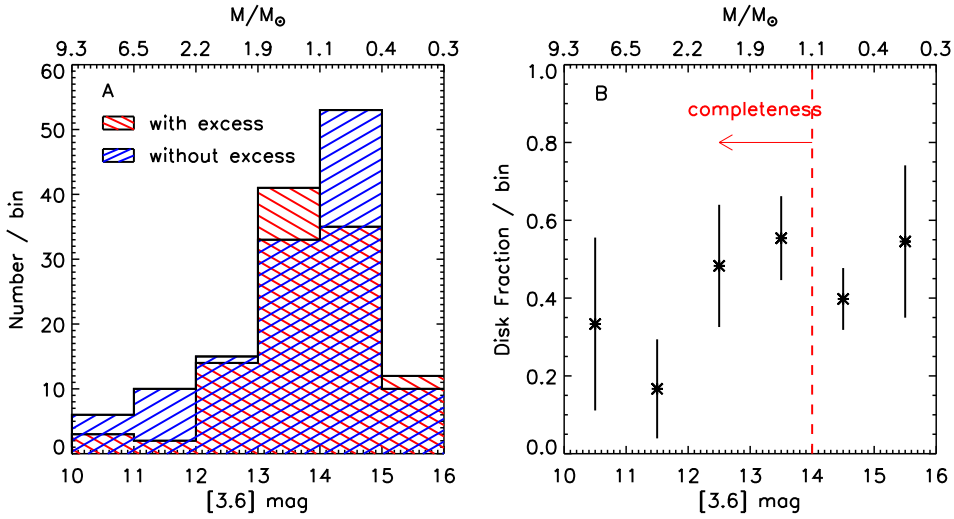

Figure 3.11 *Left column*: Histogram of cluster members (e.g. IRAC sources with an X ray counterpart) sources with excess (i.e. with [3.6]-[4.5]>0.2) with a bin of 1 magnitude. *Right column*: disc fraction computed as ratio of the sources with excess per [3.6] bin and the total number of sources per bin.

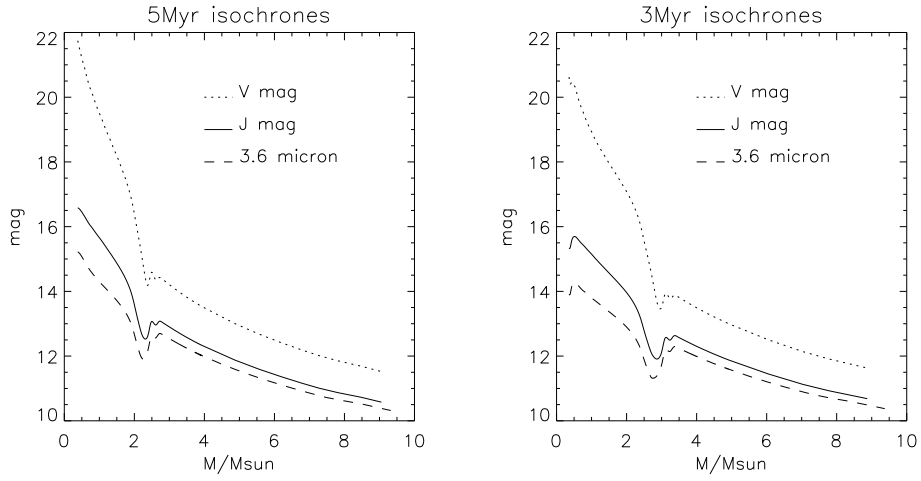

Figure 3.12 Relation between the V, J and 3.6μm magnitudes and the stellar masses computes by the 5 Myr (*left*) and 3 Myr (*right*) isochrones.

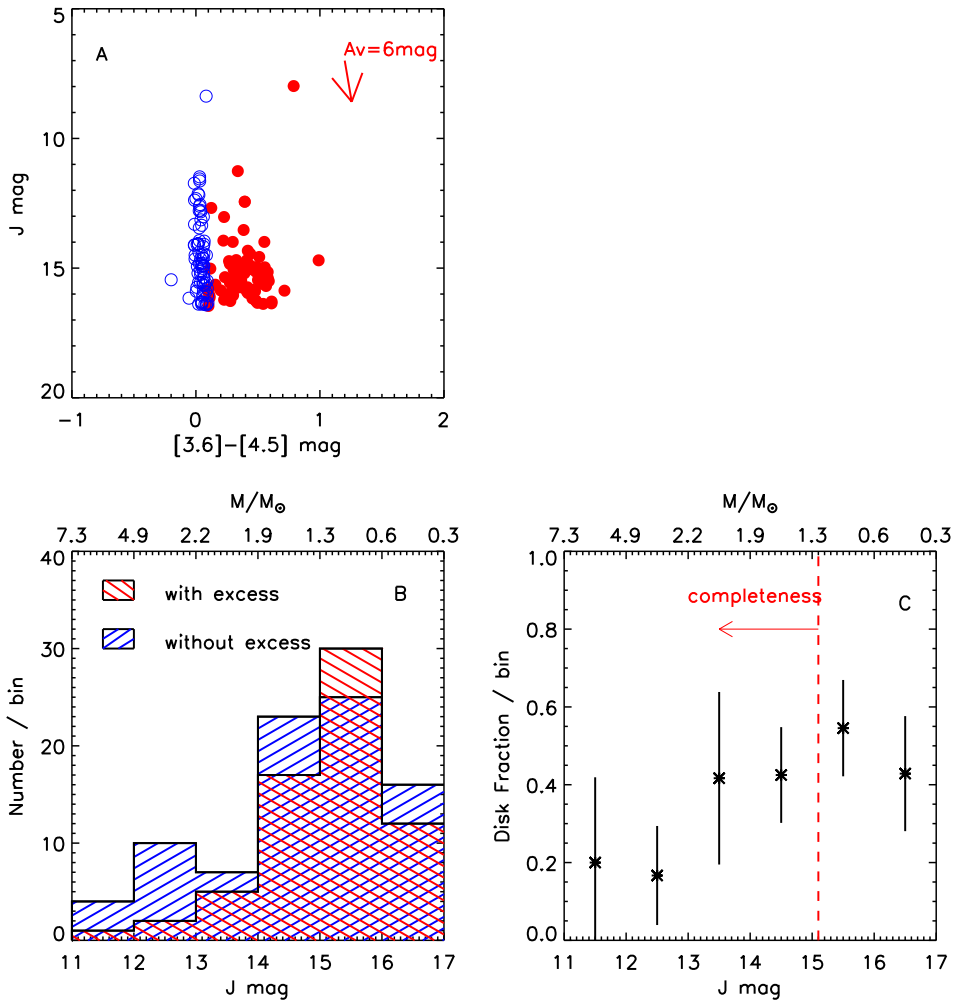

Figure 3.13 *A*: J – [3.6]-[4.5] CMD. The arrow represents an extinction $A_V = 6$ mag. Filled circles represent sources with excess (i.e. with [3.6]-[4.5]>0.2), and empty circles represent sources without excess. *B*: Number of sources with and without excess per bin of J=1 mag. *C*: Disk fraction computed as ratio of the sources with excess per Jmag bin and the total number of sources per bin.

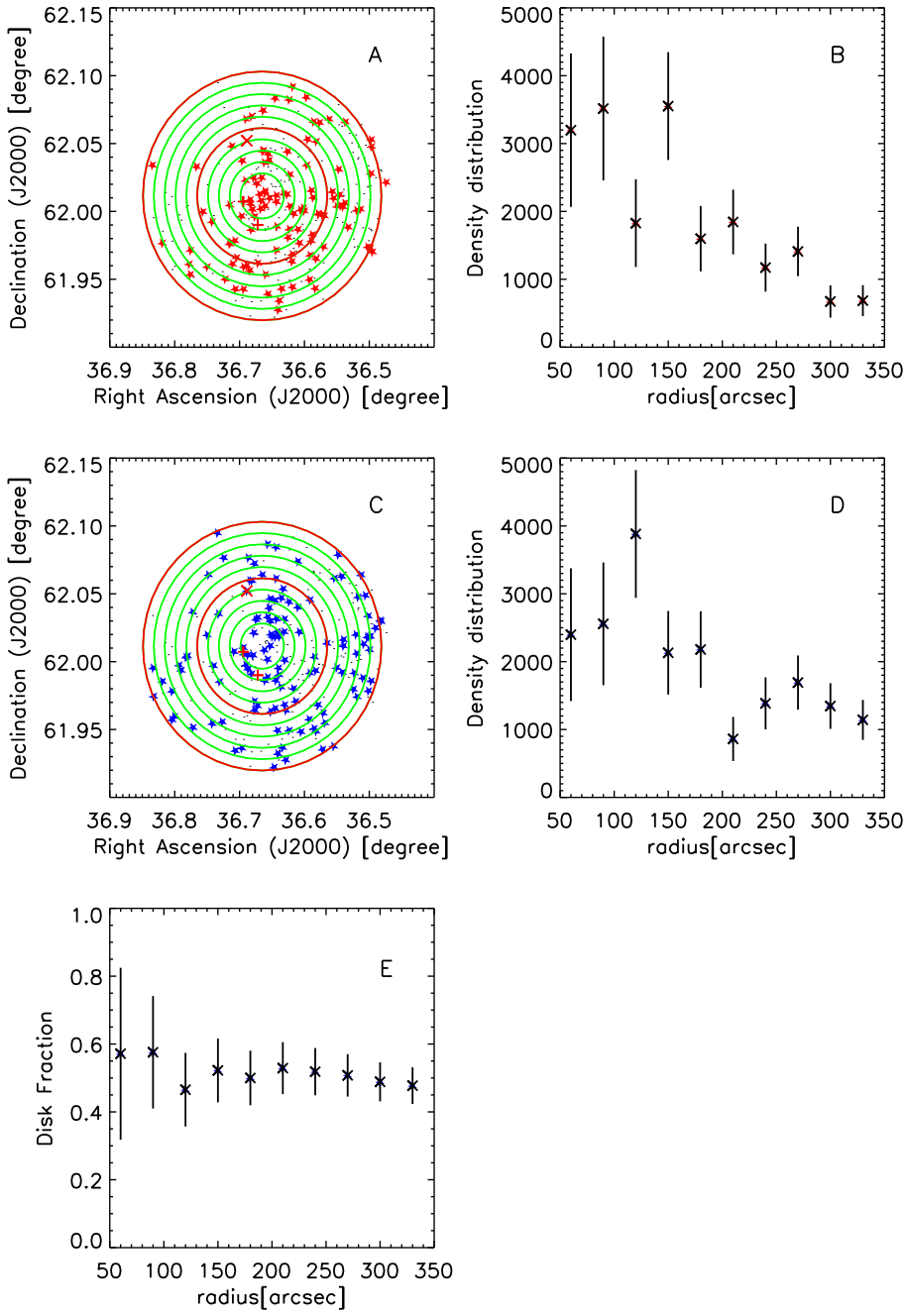

Figure 3.14 Spatial distribution (*A & C*) and spatial density distribution (*B & D*) of the sources with (*A & B*) and without (*B & C*) infrared excess. The excess has been selected with [3.6-4.5] > 0.2 from the panel B of Fig. 3.6. The circle are as in Fig. 3.5. In panel *E* the disc fraction is computed as a function of the distance from the centre of the cluster.

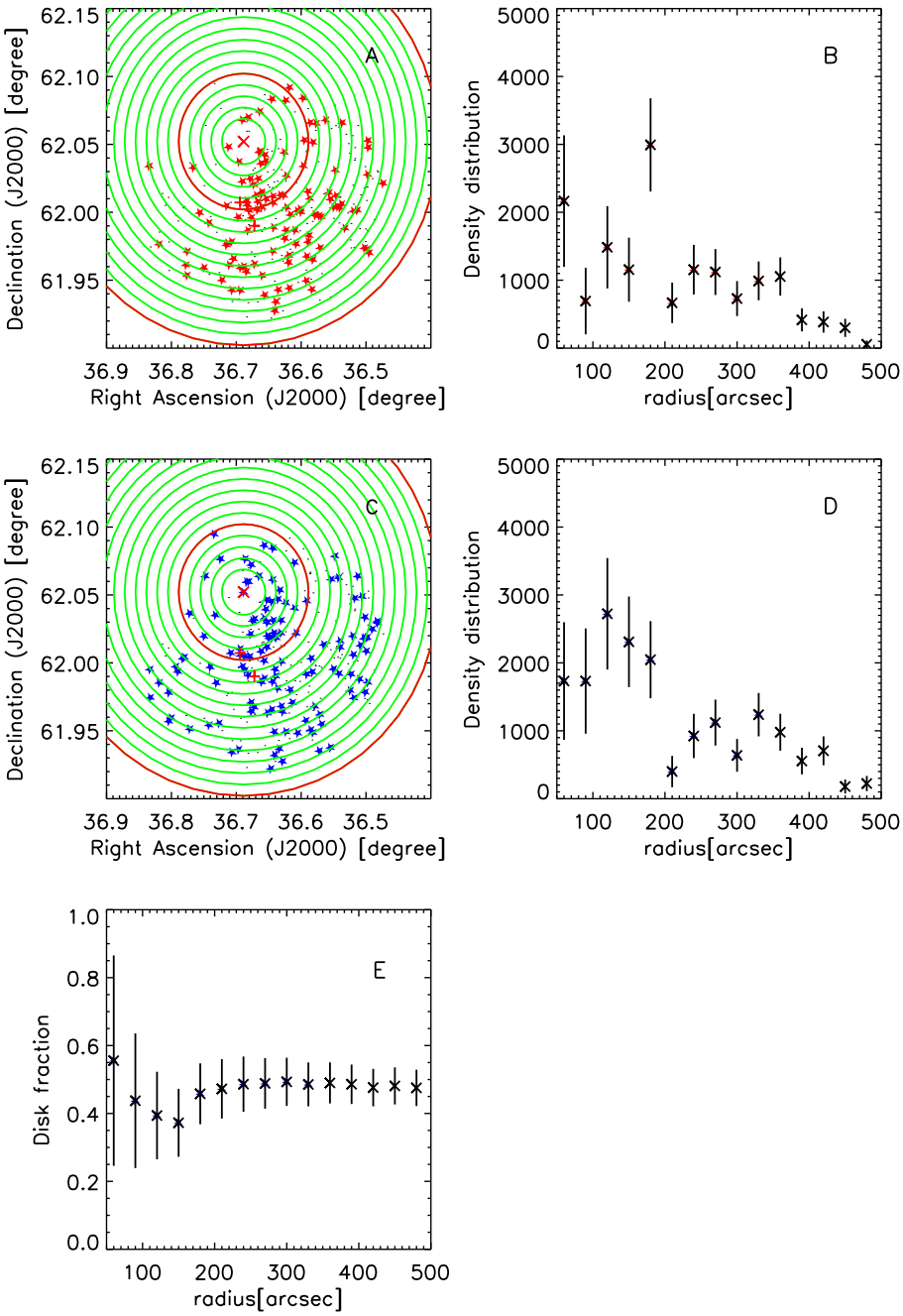

Figure 3.15 As Fig. 3.14 but using the O star as centre of the cluster.

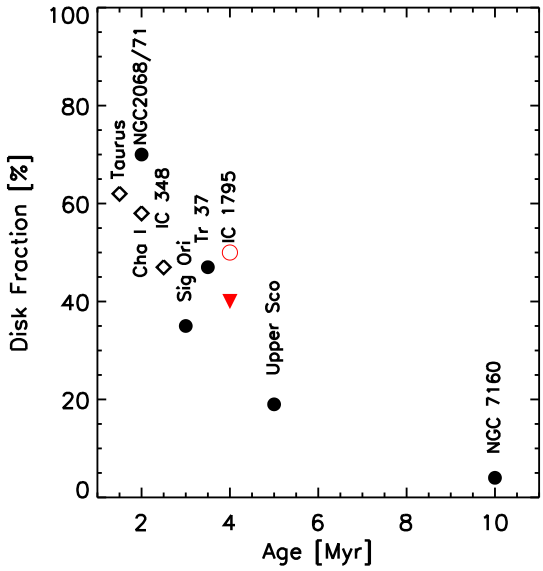

Figure 3.16 Disc fraction computed in the IRAC colours, as a function of the age of the cluster. The filled dots represent the OB associations, while the empty diamonds represent the low-mass star-forming regions. The disc fraction of solar type stars of IC 1795 is shown with an empty red circle, while the upper limit of the disc fraction down to 0.4 $M_{\odot}$ with a red down triangle.

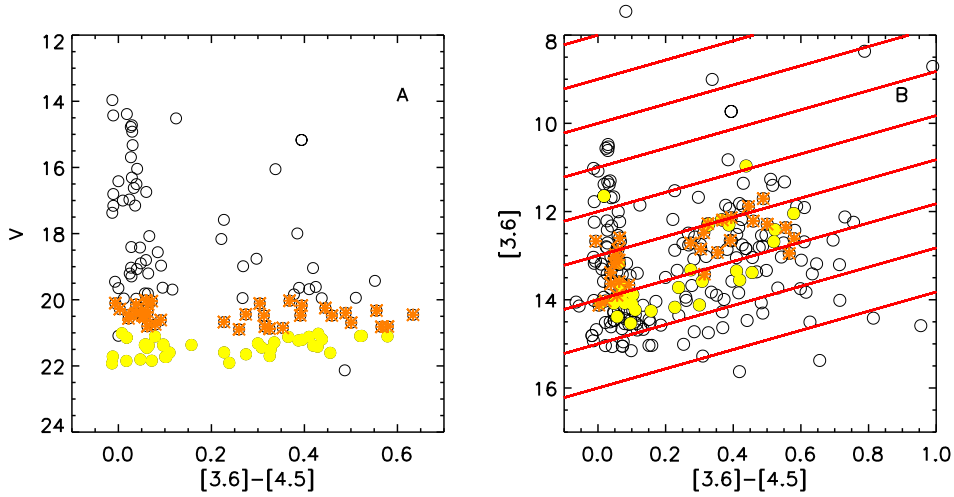

Figure 3.17 *A:* [[3.6]-[4.5], V] CMD and highlighted with different symbols are the stars in 2 consecutive horizontal slices with V between 20 and 21 and with V between 21 and 22. *B:* [[3.6]-[4.5],[3.6]] CMD with highlighted the same sources as in panel 1. The derived lines used to compute the disc fraction are overplotted.

Table 3.1. Total number of *Spitzer* and *Chandra* sources detected within 330″ from the centre of the cluster.

	Tot. number	
ch1	918	
ch2	841	
ch3	303	
ch4	243	
ch1+ch2+ch3+ch	143	
Class I		12
Class I/II		55
Class II		54
Class III/phot		13
not class.		9
X-ray	413	
X-ray + IR[a]	289	
X-ray + ch1+ch2+ch3+ch4	54	
Class I		1
Class I/II		6
Class II		41
Class III/phot		4
not class.		2
X-ray without IR	124	
IR without X-ray	636[b]	

[a]9 X-ray sources have multiple infrared counterparts and they were counted as a single source.

[b]340 sources (out of 636) show infrared excess.

Table 3.2. Identification, position and position errors of the IRAC/Spitzer sources with X-ray counterpart.

ID	ID 1	RA_{J2000} [deg]	RA error 10^{-4}[deg]	DEC_{J2000} [deg]	DEC error 10^{-4}[deg]	Notes
892	IRAC02255380+6201164	36.474186	1.13	62.021217	1.17	IR excess
919	IRAC02255585+6201477	36.482689	2.54	62.029911	2.38	no IR excess
922	IRAC02255585+6201477	36.482689	2.54	62.029911	2.38	no IR excess
936	IRAC02255717+6159399[a]	36.488209	4.14	61.994419	4.24	IR excess
944	IRAC02255780+6201287	36.490833	2.72	62.024651	2.44	IR excess
955	IRAC02255891+6158121	36.495461	0.48	61.970020	0.50	IR excess ; ClassII
960	IRAC02255931+6202527	36.497120	1.88	62.047962	1.84	IR excess
961	IRAC02255900+6203133	36.495831	4.03	62.053684	4.17	IR excess
962	IRAC02255940+6159089	36.497513	1.54	61.985809	1.62	no IR excess
966	IRAC02255945+6201413	36.497692	1.00	62.028152	1.03	IR excess
969	IRAC02255960+6159159[a]	36.498352	4.76	61.987751	4.92	IR excess
970	IRAC02255940+6201087	36.497509	0.88	62.019093	0.99	no IR excess
971	IRAC02255971+6158221	36.498806	0.27	61.972805	0.26	IR excess; Class I
977	IRAC02255988+6200312	36.499516	1.76	62.008663	1.96	IR excess
980	IRAC02255991+6159175[a]	36.499619	4.54	61.988201	4.93	IR excess
981	IRAC02260077+6201047	36.503204	3.00	62.017971	3.35	no IR excess
982	IRAC02260021+6158427	36.500893	3.94	61.978523	3.55	IR excess
985	IRAC02260047+6202012	36.501976	2.39	62.033657	2.45	no IR excess
986	IRAC02260057+6158256	36.502361	0.64	61.973778	0.63	IR excess
987	IRAC02260077+6201047	36.503204	3.00	62.017971	3.35	no IR excess
993	IRAC02260153+6202546	36.506386	0.49	62.048496	0.61	IR excess
999	IRAC02260186+6202185[a]	36.507736	2.46	62.038483	2.64	IR excess

Table 3.2 (continued)

ID	ID 1	RA_{J2000} [deg]	RA error 10^{-4}[deg]	DEC_{J2000} [deg]	DEC error 10^{-4}[deg]	Notes
1001	IRAC02260207+6200478	36.508621	2.13	62.013279	2.34	no IR excess
1008	IRAC02260242+6159163	36.510101	2.24	61.987873	2.22	no IR excess
1015	IRAC02260312+6203492	36.512981	2.74	62.063671	3.01	IR excess ; ClassI_II
1018	IRAC02260301+6200057	36.512524	1.84	62.001591	1.93	IR excess
1020	IRAC02260419+6202228[a]	36.517479	2.23	62.039669	2.53	IR excess
1021	IRAC02260415+6202510	36.517303	1.50	62.047504	1.55	no IR excess
1022	IRAC02260463+6202152	36.519287	3.30	62.037567	3.39	IR excess
1023	IRAC02260452+6158267	36.518814	0.36	61.974087	0.37	no IR excess; phot. or ClassIII
1025	IRAC02260466+6200027	36.519428	0.94	62.000759	0.99	IR excess
1028	IRAC02260469+6200216	36.519550	1.57	62.006008	1.55	IR excess
1030	IRAC02260527+6201098	36.521946	2.70	62.019398	2.79	IR excess
1034	IRAC02260410+6203266[a]	36.517082	6.88	62.057377	5.38	IR excess
1039	IRAC02260556+6159299	36.523186	1.15	61.991642	1.16	no IR excess
1040	IRAC02260544+6158244[b]	36.522663	0.96	61.973446	0.99	...
1041	IRAC02260587+6158465	36.524475	0.34	61.979580	0.34	no IR excess
1046	IRAC02260590+6202276	36.524574	7.70	62.040997	7.71	IR excess
1047	IRAC02260676+6203019	36.528187	9.55	62.050526	9.04	IR excess
1050	IRAC02260683+6159578	36.528469	1.37	61.999382	1.32	IR excess
1054	IRAC02260745+6203265[a]	36.531025	5.58	62.057350	5.60	IR excess
1058	IRAC02260787+6159179	36.532776	0.60	61.988308	0.60	IR excess ; ClassII

Table 3.2 (continued)

ID	ID 1	RA_{J2000} [deg]	RA error 10^{-4}[deg]	DEC_{J2000} [deg]	DEC error 10^{-4}[deg]	Notes
1069	IRAC02260849+6203544	36.535381	4.76	62.065098	4.93	IR excess; ClassI_II
1070	IRAC02260906+6200219	36.537758	1.69	62.006084	1.81	IR excess
1073	IRAC02260959+6200581	36.539974	0.51	62.016132	0.54	no IR excess
1074	IRAC02260960+6200414	36.540001	1.06	62.011494	1.02	no IR excess
1075	IRAC02260967+6200119	36.540306	0.80	62.003311	0.83	IR excess ; ClassII
1076	IRAC02261003+6159302	36.541798	2.66	61.991711	2.98	no IR excess
1077	IRAC02261007+6203454	36.541939	2.53	62.062611	2.63	no IR excess
1082	IRAC02261031+6200137	36.542953	8.10	62.003792	8.94	IR excess
1085	IRAC02261100+6200453	36.545849	1.34	62.012577	1.36	IR excess ; ClassII
1088	IRAC02261198+6203558	36.549911	8.38	62.065514	8.09	IR excess
1089	IRAC02261128+6201513	36.546993	1.49	62.030914	1.59	IR excess
1094	IRAC02261153+6204432	36.548027	2.31	62.078663	2.46	IR excess
1096	IRAC02261196+6200129	36.549847	0.58	62.003578	0.58	IR excess ; ClassII
1097	IRAC02261207+6159439	36.550289	1.29	61.995518	1.25	IR excess
1103	IRAC02261296+6203414	36.553982	1.82	62.061489	1.86	no IR excess
1105	IRAC02261320+6200346	36.554993	0.71	62.009617	0.73	IR excess
1107	IRAC02261320+6156152	36.554985	2.51	61.937565	2.64	no IR excess
1113	IRAC02261391+6200532	36.557976	0.45	62.014771	0.46	IR excess ; ClassII

Table 3.2 (continued)

ID	ID 1	RA_{J2000} [deg]	RA error 10^{-4}[deg]	DEC_{J2000} [deg]	DEC error 10^{-4}[deg]	Notes
1122	IRAC02261491+6204046	36.562115	1.08	62.067936	1.19	IR excess
1127	IRAC02261565+6200482	36.565212	1.39	62.013386	1.42	no IR excess
1133	IRAC02261645+6157174	36.568535	1.17	61.954838	1.18	no IR excess
1135	IRAC02261671+6159485[d]	36.569630	0.55	61.996803	0.56	IR excess ; ClassII
1139	IRAC02261699+6158262	36.570793	0.74	61.973946	0.73	IR excess
1142	IRAC02261717+6157438	36.571529	2.47	61.962166	2.88	no IR excess
1146	IRAC02261727+6156069	36.571945	0.68	61.935253	0.71	no IR excess
1147	IRAC02261739+6159512	36.572475	0.86	61.997562	0.88	IR excess
1154	IRAC02261769+6202141	36.573708	5.24	62.037254	5.40	IR excess
1162	IRAC02261849+6203556[d]	36.577049	0.76	62.065437	0.78	IR excess
1167	IRAC02261881+6159528	36.578392	0.20	61.998013	0.21	IR excess ; ClassII
1168	IRAC02261765+6203431[a]	36.573559	7.33	62.061977	7.98	IR excess
1170	IRAC02261881+6159528	36.578392	0.20	61.998013	0.21	IR excess ; ClassII
1171	IRAC02261888+6158048	36.578659	1.82	61.968006	2.03	no IR excess
1177	IRAC02261959+6203058	36.581619	0.58	62.051609	0.60	IR excess ; ClassII
1178	IRAC02261970+6156554	36.582077	1.78	61.948715	1.93	no IR excess
1180	IRAC02261967+6157541	36.581944	1.98	61.965038	1.79	IR excess
1181	IRAC02261990+6159357	36.582928	1.10	61.993240	1.14	IR excess
1182	IRAC02262010+6156358	36.583740	1.28	61.943279	1.35	IR excess

Table 3.2 (continued)

ID	ID 1	RA_{J2000} [deg]	RA error 10^{-4}[deg]	DEC_{J2000} [deg]	DEC error 10^{-4}[deg]	Notes
1185	IRAC02262029+6200119	36.584538	0.80	62.003304	0.83	no IR excess
1186	IRAC02262044+6157024	36.585178	0.91	61.950657	0.93	no IR excess
1191	IRAC02262048+6203521	36.585316	7.86	62.064484	8.74	IR excess
1194	IRAC02262048+6203521	36.585316	7.86	62.064484	8.74	IR excess
1195	IRAC02262082+6200365	36.586731	0.63	62.010132	0.63	IR excess ; ClassII
1197	IRAC02262048+6203521	36.585316	7.86	62.064484	8.74	IR excess
1199	IRAC02262112+6158582	36.587986	0.47	61.982826	0.47	IR excess; ClassII
1205	IRAC02262148+6158419	36.589508	0.45	61.978298	0.47	IR excess ; ClassII
1206	IRAC02262140+6200551	36.589153	2.18	62.015308	2.31	IR excess
1208	IRAC02262132+6204362[a]	36.588825	2.09	62.076733	2.08	IR excess
1213	IRAC02262191+6202438	36.591286	1.51	62.045509	1.58	no IR excess
1214	IRAC02262195+6158031	36.591454	0.68	61.967529	0.67	IR excess
1215	IRAC02262199+6159297	36.591637	1.87	61.991596	1.91	no IR excess
1217	IRAC02262219+6156592	36.592449	2.76	61.949768	2.36	IR excess
1219	IRAC02262231+6157267	36.592960	1.57	61.957405	1.62	no IR excess
1220	IRAC02262227+6202403[a]	36.592781	1.80	62.044525	1.68	IR excess
1225	IRAC02262273+6203109	36.594688	0.71	62.053017	0.77	IR excess ; ClassII
1227	IRAC02262318+6202023	36.596569	2.02	62.033985	1.99	IR excess
1228	IRAC02262328+6205020	36.597015	0.67	62.083889	0.71	IR excess

Table 3.2 (continued)

ID	ID 1	RA_{J2000} [deg]	RA error 10^{-4}[deg]	DEC_{J2000} [deg]	DEC error 10^{-4}[deg]	Notes
1238	IRAC02262411+6200012	36.600445	0.57	62.000320	0.57	IR excess ; ClassII
1239	IRAC02262440+6200090	36.601673	2.95	62.002487	2.92	IR excess
1242	IRAC02262447+6159106[a]	36.601963	1.76	61.986271	1.80	IR excess
1245	IRAC02262488+6159265	36.603672	1.14	61.990704	1.26	IR excess
1251	IRAC02262527+6156538	36.605293	2.31	61.948265	2.37	IR excess
1253	IRAC02262536+6200034	36.605682	0.49	62.000954	0.49	IR excess ; ClassII
1258	IRAC02262586+6201186	36.607735	3.72	62.021832	4.28	no IR excess
1259	IRAC02262587+6158354	36.607773	0.78	61.976490	0.76	IR excess
1262	IRAC02262637+6159124	36.609894	0.62	61.986782	0.79	IR excess
1264	IRAC02262646+6202241	36.610245	1.13	62.040028	1.19	no IR excess
1265	IRAC02262649+6204256	36.610363	2.30	62.073792	2.43	IR excess
1277	IRAC02262724+6158142	36.613483	0.42	61.970612	0.44	no IR excess; photosphere or ClassIII
1282	IRAC02262794+6159538	36.616409	0.70	61.998287	0.71	IR excess
1283	IRAC02262802+6158482	36.616756	1.46	61.980049	1.43	no IR excess
1286	IRAC02262817+6158218[a]	36.617367	1.06	61.972721	1.10	IR excess
1287	IRAC02262836+6205306	36.618172	1.13	62.091839	1.15	IR excess
1288	IRAC02262839+6156388	36.618271	1.17	61.944122	1.18	IR excess
1291	IRAC02262860+6158055	36.619156	0.45	61.968185	0.45	IR excess ; ClassII
1292	IRAC02262879+6157481	36.619976	1.00	61.963371	1.01	IR excess

Table 3.2 (continued)

ID	ID 1	RA_{J2000} [deg]	RA error 10^{-4}[deg]	DEC_{J2000} [deg]	DEC error 10^{-4}[deg]	Notes
1294	IRAC02262938+6200135[a]	36.622417	1.23	62.003757	1.26	IR excess
1295	IRAC02262940+6201375	36.622494	0.76	62.027077	0.79	IR excess
1298	IRAC02262962+6159126	36.623405	0.46	61.986824	0.47	IR excess ; ClassII
1300	IRAC02262966+6156575	36.623592	2.98	61.949306	3.08	no IR excess
1301	IRAC02262969+6202382	36.623714	2.30	62.043957	2.17	no IR excess
1302	IRAC02262966+6204566	36.623600	1.32	62.082382	1.40	IR excess
1303	IRAC02262989+6201223[a]	36.624561	3.42	62.022858	3.56	IR excess
1304	IRAC02263007+6158506	36.625282	0.77	61.980713	0.85	IR excess
1308	IRAC02263023+6202383	36.625965	2.52	62.043983	2.48	IR excess
1309	IRAC02263046+6200453	36.626926	0.80	62.012596	0.85	IR excess
1313	IRAC02263091+6157504	36.628803	1.56	61.963989	1.62	no IR excess
1315	IRAC02263094+6155383	36.628910	2.71	61.927319	2.85	no IR excess
1321	IRAC02263131+6200037	36.630466	0.74	62.001019	0.74	no IR excess
1324	IRAC02263135+6158054	36.630630	1.80	61.968163	1.85	no IR excess
1325	IRAC02263140+6201527	36.630852	1.87	62.031300	1.83	no IR excess
1327	IRAC02263150+6201191	36.631229	2.60	62.021965	2.67	no IR excess
1328	IRAC02263167+6200439	36.631962	2.00	62.012192	2.11	IR excess
1330	IRAC02263184+6203125	36.632648	2.62	62.053486	2.93	IR excess ; ClassI_II
1333	IRAC02263206+6156121	36.633568	0.64	61.936691	0.64	IR excess ; ClassII
1337	IRAC02263248+6156347	36.635338	0.56	61.942982	0.56	IR excess

Table 3.2 (continued)

ID	ID 1	RA_{J2000} [deg]	RA error 10^{-4}[deg]	DEC_{J2000} [deg]	DEC error 10^{-4}[deg]	Notes
1339	IRAC02263240+6202523	36.634998	2.21	62.047848	2.28	no IR excess
1342	IRAC02263230+6158525	36.634563	2.58	61.981243	2.35	IR excess ; ClassII
1344	IRAC02263287+6201220	36.636955	1.63	62.022789	1.65	IR excess
1349	IRAC02263323+6201062	36.638443	1.11	62.018394	1.17	no IR excess
1350	IRAC02263332+6156030	36.638844	0.49	61.934166	0.59	IR excess ; ClassII
1351	IRAC02263328+6156045[b]	36.638683	1.18	61.934570	1.30	....
1353	IRAC02263343+6159250	36.639301	1.48	61.990269	1.45	no IR excess
1355	IRAC02263362+6159431	36.640087	1.73	61.995312	1.73	no IR excess
1356	IRAC02263371+6155387	36.640465	0.91	61.927418	0.97	IR excess
1359	IRAC02263386+6155555	36.641064	0.87	61.932095	0.85	no IR excess
1360	IRAC02263394+6156573	36.641430	0.68	61.949242	0.66	no IR excess
1362	IRAC02263415+6201192[d]	36.642292	0.39	62.022011	0.42	no IR excess
1364	IRAC02263422+6159201	36.642582	0.58	61.988918	0.60	IR excess
1365	IRAC02263431+6200252	36.642952	1.05	62.006989	1.12	IR excess
1367	IRAC02263433+6201527	36.643028	0.57	62.031307	0.59	no IR excess
1370	IRAC02263443+6200419[e]	36.643478	0.40	62.011650	0.55	IR excess ; ClassII
1373	IRAC02263441+6205037	36.643356	2.74	62.084373	2.79	no IR excess
1374	IRAC02263455+6158169	36.643944	0.45	61.971359	0.45	IR excess ; ClassII
1375	IRAC02263455+6203404	36.643944	2.09	62.061234	2.01	IR excess

Table 3.2 (continued)

ID	ID 1	RA_{J2000} [deg]	RA error 10^{-4}[deg]	DEC_{J2000} [deg]	DEC error 10^{-4}[deg]	Notes
1377	IRAC02263463+6159107[d]	36.644291	0.46	61.986301	0.47	no IR excess
1384	IRAC02263480+6201053	36.645012	0.80	62.018150	0.85	no IR excess
1385	IRAC02263530+6204558	36.647102	7.39	62.082172	7.58	IR excess
1388	IRAC02263489+6157559[d]	36.645367	0.53	61.965519	0.54	no IR excess
1389	IRAC02263495+6202427	36.645634	1.59	62.045185	1.71	IR excess
1393	IRAC02263541+6155197	36.647522	2.93	61.922138	2.52	no IR excess
1404	IRAC02263585+6201062	36.649387	1.18	62.018379	1.22	no IR excess
1410	IRAC02263646+6201120	36.651913	0.39	62.020000	0.41	no IR excess
1411	IRAC02263648+6157462	36.651993	0.98	61.962841	1.00	no IR excess
1412	IRAC02263658+6201471	36.652416	1.34	62.029751	1.44	no IR excess
1415	IRAC02263667+6200416	36.652798	0.44	62.011562	0.45	no IR excess
1417	IRAC02263670+6202470	36.652905	0.47	62.046394	0.46	no IR excess
1421	IRAC02263693+6200345	36.653885	0.80	62.009590	0.83	IR excess
1424	IRAC02263709+6202222	36.654526	2.27	62.039505	2.30	no IR excess
1425	IRAC02263713+6202147	36.654709	1.14	62.037426	1.16	IR excess
1431	IRAC02263743+6202322	36.655949	0.84	62.042286	0.89	IR excess
1434	IRAC02263750+6156207	36.656258	0.76	61.939095	0.83	IR excess ; ClassII
1436	IRAC02263755+6201557	36.656471	1.53	62.032146	1.63	no IR excess
1438	IRAC02263768+6159187	36.656998	0.93	61.988541	0.91	no IR excess
1440	IRAC02263768+6200054	36.657005	0.83	62.001492	0.92	no IR excess
1441	IRAC02263755+6205115	36.656475	1.46	62.086525	1.55	IR excess
1446	IRAC02263928+6201034[b]	36.663658	9.63	62.017616	9.50	....

Table 3.2 (continued)

ID	ID 1	RA_{J2000} [deg]	RA error 10^{-4}[deg]	DEC_{J2000} [deg]	DEC error 10^{-4}[deg]	Notes
1454	IRAC02263847+6157126	36.660275	3.05	61.953499	2.79	IR excess
1455	IRAC02263851+6200490	36.660465	0.53	62.013611	0.54	IR excess
1456	IRAC02263862+6200142	36.660904	0.83	62.003944	0.88	IR excess
1457	IRAC02263865+6200533	36.661022	0.48	62.014793	0.52	IR excess ; ClassII
1458	IRAC02263865+6159135	36.661049	2.37	61.987080	2.61	IR excess
1459	IRAC02263868+6159094	36.661156	1.06	61.985931	1.10	no IR excess
1464	IRAC02263885+6200303	36.661873	0.52	62.008419	0.50	no IR excess
1465	IRAC02263882+6202112	36.661732	0.84	62.036434	0.86	IR excess
1473[c]	IRAC02263954+6202400[b]	36.664753	3.18	62.044449	3.40	IR excess ; ClassII
1477	IRAC02263958+6204263	36.664906	4.40	62.073975	4.71	IR excess
1478	IRAC02263953+6202401	36.664722	0.80	62.044468	0.81	IR excess
1481	IRAC02263962+6203506	36.665073	0.90	62.064049	0.97	IR excess ; ClassI_II
1483	IRAC02263987+6201292	36.666126	1.22	62.024773	1.25	IR excess
1486	IRAC02263999+6200279	36.666618	0.52	62.007748	0.51	IR excess ; ClassII
1488	IRAC02264011+6200068	36.667145	0.72	62.001896	0.70	IR excess ; ClassI_II
1489	IRAC02263983+6156038[a]	36.665943	6.51	61.934395	6.27	IR excess
1495	IRAC02264061+6200448	36.669224	1.25	62.012436	1.27	IR excess
1502	IRAC02264113+6157424	36.671383	0.94	61.961773	0.93	IR excess

Table 3.2 (continued)

ID	ID 1	RA_{J2000} [deg]	RA error 10^{-4}[deg]	DEC_{J2000} [deg]	DEC error 10^{-4}[deg]	Notes
1504	IRAC02264126+6201566[d]	36.671932	0.63	62.032402	0.66	no IR excess
1506	IRAC02264140+6158026	36.672482	1.08	61.967381	1.04	no IR excess
1508	IRAC02264157+6201129	36.673222	0.61	62.020248	0.64	IR excess
1510	IRAC02264193+6201516	36.674725	0.90	62.031013	0.96	no IR excess
1513	IRAC02264238+6159456	36.676575	1.14	61.995995	1.29	IR excess
1514	IRAC02264247+6157511	36.676975	2.19	61.964203	2.19	no IR excess
1515	IRAC02264279+6204237	36.678291	3.30	62.073254	3.36	IR excess
1516	IRAC02264240+6158162	36.676651	2.14	61.971180	1.95	no IR excess
1519	IRAC02264279+6201156	36.678280	2.13	62.020992	2.17	no IR excess
1520	IRAC02264290+6201282[d]	36.678761	0.43	62.024494	0.46	IR excess ; ClassII
1524	IRAC02264297+6200166	36.679024	0.94	62.004616	1.00	no IR excess
1529	IRAC02264334+6200044	36.680576	0.64	62.001228	0.59	IR excess
1533	IRAC02264342+6203347	36.680908	0.99	62.059635	0.98	no IR excess
1534	IRAC02264353+6159270	36.681362	1.05	61.990829	1.20	no IR excess
1537	IRAC02264359+6204115	36.681625	0.79	62.069874	0.83	IR excess ; ClassII
1540	IRAC02264438+6155548[a]	36.684906	8.17	61.931881	8.42	IR excess
1541	IRAC02264376+6159113	36.682331	0.67	61.986485	0.75	IR excess
1544	IRAC02264391+6200191	36.682941	1.05	62.005299	1.05	IR excess
1546	IRAC02264413+6200305	36.683865	0.50	62.008461	0.49	IR excess ; ClassII
1550	IRAC02264423+6203348	36.684284	0.95	62.059669	1.00	no IR excess

Table 3.2 (continued)

ID	ID 1	RA_{J2000} [deg]	RA error 10^{-4}[deg]	DEC_{J2000} [deg]	DEC error 10^{-4}[deg]	Notes
1551	IRAC02264425+6155223[a]	36.684391	2.92	61.922852	2.83	IR excess
1552	IRAC02264421+6157229	36.684216	0.89	61.956352	0.91	IR excess ; ClassII
1558	IRAC02264480+6159395	36.686676	1.69	61.994293	1.95	no IR excess
1559	IRAC02264490+6204378	36.687080	3.92	62.077160	3.64	IR excess ; ClassI_II
1560	IRAC02264497+6200170	36.687363	0.79	62.004730	0.81	no IR excess
1567	IRAC02264527+6203075	36.688641	0.69	62.052090	0.60	no IR excess; photosphere or ClassIII
1568	IRAC02264562+6157382	36.690098	2.44	61.960613	2.76	IR excess
1571	IRAC02264571+6159505	36.690472	0.55	61.997360	0.60	no IR excess
1572	IRAC02264592+6204019	36.691319	1.95	62.067184	1.97	IR excess ; ClassI_II
1573[c]	IRAC02264606+6201220[b]	36.691906	2.27	62.022778	2.40	IR excess ; ClassII
1585	IRAC02264607+6157332	36.691956	1.99	61.959213	2.01	IR excess
1587	IRAC02264649+6200196[d]	36.693714	0.97	62.005455	1.00	no IR excess
1588	IRAC02264651+6156331	36.693771	1.27	61.942516	1.36	IR excess
1591	IRAC02264674+6200367	36.694752	0.89	62.010181	0.96	no IR excess
1596	IRAC02264702+6202144	36.695930	0.79	62.037327	0.83	IR excess ; ClassII
1599	IRAC02264720+6156102	36.696674	2.43	61.936153	2.61	IR excess
1600	IRAC02264736+6159478[d]	36.697319	0.81	61.996601	0.91	IR excess

Table 3.2 (continued)

ID	ID 1	RA_{J2000} [deg]	RA error 10^{-4}[deg]	DEC_{J2000} [deg]	DEC error 10^{-4}[deg]	Notes
1622	IRAC02264898+6157567	36.704075	1.01	61.965763	1.03	IR excess ; ClassII
1627	IRAC02264970+6156338	36.707085	1.15	61.942734	1.29	IR excess
1628	IRAC02264963+6156035	36.706783	1.06	61.934315	1.07	no IR excess
1632	IRAC02264974+6158419	36.707260	1.42	61.978306	1.43	IR excess
1634	IRAC02265007+6200263	36.708637	0.71	62.007298	0.74	no IR excess
1642	IRAC02265061+6157404	36.710880	0.71	61.961216	0.77	IR excess ; ClassII
1645	IRAC02265084+6202534	36.711823	0.57	62.048153	0.59	IR excess ; ClassII
1649	IRAC02265100+6158384	36.712509	0.70	61.977337	0.72	IR excess ; ClassII
1652	IRAC02265167+6200166	36.715282	1.68	62.004604	1.62	IR excess
1653	IRAC02265171+6158335	36.715439	0.74	61.975979	0.78	IR excess ; ClassII
1672	IRAC02265339+6157007	36.722443	0.58	61.950188	0.58	IR excess ; ClassII
1679	IRAC02265387+6204355	36.724449	0.90	62.076534	0.91	no IR excess
1684	IRAC02265444+6157204	36.726822	1.16	61.955658	1.18	no IR excess
1695	IRAC02265534+6159075	36.730579	0.53	61.985413	0.56	no IR excess
1699	IRAC02265574+6202069	36.732258	1.31	62.035236	1.38	no IR excess
1702	IRAC02265607+6205409	36.733643	0.85	62.094688	0.86	no IR excess
1718	IRAC02265761+6159490	36.740036	1.99	61.996937	2.08	IR excess

Table 3.2 (continued)

ID	ID 1	RA_{J2000} [deg]	RA error 10^{-4}[deg]	DEC_{J2000} [deg]	DEC error 10^{-4}[deg]	Notes
1721	IRAC02265809+6157155	36.742058	3.01	61.954308	2.72	IR excess
1722	IRAC02265816+6159319	36.742332	0.59	61.992203	0.61	IR excess
1736	IRAC02265948+6203506	36.747852	1.78	62.064056	1.81	no IR excess
1742	IRAC02270002+6201106	36.750099	1.63	62.019604	1.83	no IR excess
1743	IRAC02270024+6157320	36.751011	2.75	61.958893	2.40	IR excess
1767	IRAC02270155+6159589	36.756439	0.81	61.999706	0.85	IR excess
1801	IRAC02270392+6201588	36.766327	0.68	62.032990	0.69	IR excess
1815	IRAC02270523+6157048	36.771774	1.19	61.951324	1.22	no IR excess
1817	IRAC02270536+6202109	36.772339	2.41	62.036358	2.47	no IR excess
1831	IRAC02270613+6158166	36.775528	0.62	61.971279	0.62	IR excess ; ClassII
1835	IRAC02270616+6157127	36.775681	2.07	61.953529	2.00	IR excess
1842	IRAC02270608+6157387	36.775322	3.38	61.960743	3.22	IR excess
1857	IRAC02270756+6200131	36.781513	0.74	62.003643	0.73	no IR excess
1867	IRAC02270756+6200131	36.781513	0.74	62.003643	0.73	no IR excess
1887	IRAC02270964+6159369	36.790161	3.11	61.993595	2.95	no IR excess
1891	IRAC02271047+6159501	36.793606	1.77	61.997246	1.83	no IR excess
1915	IRAC02271197+6157347	36.799881	3.91	61.959637	3.72	no IR excess
1921	IRAC02271295+6157250	36.803951	2.89	61.956944	2.67	no IR excess
1924	IRAC02271296+6158407	36.803982	2.08	61.977985	1.97	no IR excess
1926	IRAC02271410+6200456	36.808746	6.27	62.012680	6.23	IR excess
1935	IRAC02271452+6200193	36.810486	8.57	62.005371	9.03	IR excess
1940	IRAC02271660+6200520	36.819168	9.19	62.014439	9.46	IR excess

Table 3.2 (continued)

ID	ID 1	RA_{J2000} [deg]	RA error 10^{-4}[deg]	DEC_{J2000} [deg]	DEC error 10^{-4}[deg]	Notes
1950	IRAC02271627+6159086	36.817772	2.68	61.985733	2.82	IR excess
1951	IRAC02271656+6158358	36.818981	1.67	61.976612	1.73	IR excess
1984	IRAC02271981+6158281	36.832546	1.74	61.974464	1.75	no IR excess
1985	IRAC02271999+6159435	36.833271	1.75	61.995407	1.65	no IR excess
1990	IRAC02272024+6202025	36.834324	0.26	62.034016	0.28	IR excess ; ClassII

Note. —

[a]Source position in IRAC/channel 2.

[b]Source position in IRAC/channel 3.

[c]The counterparts at different wavelengths were found using a different matching procedure.

[d]IRAC source with 2 X-ray counterparts ('X binary').

[e]IRAC source with 3 X-ray counterparts.

Table 3.3. Optical, near-infrared and IRAC/Spitzer fluxes of the IRAC/Spitzer sources with X-ray counterpart.

ID	F_V [Jy]	F_I [Jy]	F_J [Jy]	F_H [Jy]	F_K [Jy]	$F_{3.6\mu m}$ [Jy]	$F_{4.5\mu m}$ [Jy]	$F_{5.8\mu m}$ [Jy]	$F_{8.0\mu m}$ [Jy]
IRAC02255380+6201164	....	....	....	....	....	1.3026± 0.0073	1.3182± 0.0088	....	....
IRAC02255585+6201477	....	....	....	....	....	0.4586± 0.0048	0.3066± 0.0055	....	....
IRAC02255585+6201477	....	....	....	....	....	0.4586± 0.0048	0.3066± 0.0055	....	....
IRAC02255717+6159399	0.0073	0.0707	....	....	....	....	0.1901± 0.0033	....	....
IRAC02255780+6201287	....	....	....	....	....	0.4427± 0.0048	0.3130± 0.0054	....	....
IRAC02255891+6158121	0.0616	0.7341	4.0410	7.8397	8.2401	8.2684± 0.0247	8.7915± 0.0271	9.0294± 0.2101	9.3836± 0.0890
IRAC02255931+6202527	....	....	....	....	....	0.7768± 0.0065	0.6863± 0.0088	2.1174± 0.0455	....
IRAC02255900+6203133	....	....	....	....	....	0.4109± 0.0073	0.6331± 0.0088	....	....
IRAC02255940+6159089	0.0582	0.4375	1.0532	1.5357	1.1693	0.7298± 0.0054	0.3884± 0.0039	1.7319± 0.0251	2.0907± 0.0523
IRAC02255945+6201413	....	....	....	....	....	2.3144± 0.0117	2.4546± 0.0133	2.5519± 0.0399	....
IRAC02255960+6159159	....	....	....	....	....	....	0.1395± 0.0030	1.7319± 0.0251	2.0907± 0.0523
IRAC02255940+6201087	0.2143	1.3407	4.1542	5.3740	4.5283	2.3800± 0.0116	1.6186± 0.0094	....	....
IRAC02255971+6158221	....	....	2.1013	9.0012	31.3278	92.1254± 0.2143	146.6403± 0.3530	239.5303± 0.5788	289.0532± 0.8720
IRAC02255988+6200312	0.0074	0.1328	0.6831	1.2311	1.1167	0.6453± 0.0055	0.4529± 0.0049	....	....
IRAC02255991+6159175	....	....	....	....	....	....	0.1447± 0.0028	....	2.0907± 0.0523
IRAC02260077+6201047	....	....	....	....	....	0.3343± 0.0049	0.2104± 0.0046	....	....
IRAC02260021+6158427	....	....	....	....	....	0.2721± 0.0039	0.2000± 0.0039	....	....
IRAC02260047+6202012	0.0131	0.1769	0.9430	1.8294	1.6290	0.6576± 0.0071	0.4523± 0.0074	....	....
IRAC02260057+6158256	0.0099	0.1442	....	....	....	5.0000± 0.0175	4.7460± 0.0179	....	13.1657± 0.1163
IRAC02260077+6201047	....	....	....	....	....	0.3343± 0.0049	0.2104± 0.0046	....	....
IRAC02260153+6202546	5.6794	10.7285	13.5048	12.7732	10.0909	5.0970± 0.0159	3.6551± 0.0160	2.3376± 0.0394	....
IRAC02260186+6202185	....	....	....	....	....	....	0.8064± 0.0091	2.3934± 0.0281	4.7682± 0.1050
IRAC02260207+6200478	0.0102	0.0959	....	....	....	0.4585± 0.0047	0.3205± 0.0045	....	....
IRAC02260242+6159163	0.0183	0.2481	....	....	....	0.4286± 0.0041	0.2950± 0.0034	....	....
IRAC02260312+6203492	....	....	....	....	....	0.3805± 0.0046	0.2754± 0.0060	1.2573± 0.0352	7.4349± 0.1988
IRAC02260301+6200057	....	....	....	....	....	0.5342± 0.0047	0.5353± 0.0044	....	....
IRAC02260419+6202228	....	....	....	....	....	....	0.6206± 0.0065	....	4.7682± 0.1050
IRAC02260415+6202510	....	....	0.5476	1.1976	1.1374	0.6190± 0.0045	0.3762± 0.0057	....	....
IRAC02260463+6202152	....	....	....	....	....	0.2958± 0.0043	....	....	4.7682± 0.1050
IRAC02260452+6158267	0.5931	5.2935	21.4037	32.3817	29.6436	16.6699± 0.0443	10.8992± 0.0316	8.1086± 0.0425	5.3639± 0.0766
IRAC02260466+6200027	....	....	0.4472	1.0723	1.2704	1.7228± 0.0082	1.8162± 0.0077	....	....
IRAC02260469+6200216	....	....	0.4154	1.0624	1.1586	0.7696± 0.0059	0.5404± 0.0046	....	....
IRAC02260527+6201098	....	....	....	....	....	0.4385± 0.0050	0.3233± 0.0054	....	....
IRAC02260410+6203266	....	....	....	....	....	....	0.3165± 0.0089	1.1409± 0.0308	4.6667± 0.1059
IRAC02260556+6159299	0.0889	0.5714	1.8814	2.5722	2.1475	1.2096± 0.0066	0.7935± 0.0047	....	....
IRAC02260544+6158244	0.0503	0.7207	....	....	....	....	....	14.1683± 0.0583	14.1716± 0.0996
IRAC02260587+6158465	3.9219	17.4639	40.7838	42.6874	35.3127	18.0509± 0.0457	11.8676± 0.0324	7.7691± 0.0390	....
IRAC02260590+6202276	....	....	....	....	....	0.1318± 0.0041	....	1.6879± 0.0364	11.4398± 0.1975
IRAC02260676+6203019	....	....	....	....	....	0.0844± 0.0031	....	1.3532± 0.0290	....
IRAC02260683+6159578	....	....	1.1028	1.8806	1.6902	1.0098± 0.0062	....	....	....
IRAC02260745+6203265	....	....	....	....	....	....	0.1902± 0.0043	1.5196± 0.0297	....
IRAC02260787+6159179	0.0521	0.4117	1.6691	2.9262	3.6302	3.7698± 0.0126	3.5652± 0.0121	3.4941± 0.0298	4.7396± 0.0584
IRAC02260849+6203544	....	....	....	....	....	0.1986± 0.0039	0.2324± 0.0052	1.0900± 0.0332	3.8531± 0.0957

Table 3.3 (continued)

ID	F_V [Jy]	F_I [Jy]	F_J [Jy]	F_H [Jy]	F_K [Jy]	$F_{3.6\mu m}$ [Jy]	$F_{4.5\mu m}$ [Jy]	$F_{5.8\mu m}$ [Jy]	$F_{8.0\mu m}$ [Jy]
IRAC02260906+6200219	0.0159	0.1262	....	....	....	0.7450± 0.0060	0.6052± 0.0049	....	3.2949± 0.0710
IRAC02260959+6200581	6.1645	13.2843	17.8028	16.5310	11.8013	5.4760± 0.0174	3.4674± 0.0126	....	....
IRAC02260960+6200414	0.1369	0.7240	2.5263	3.0924	2.7538	1.5103± 0.0078	1.0445± 0.0060	....	....
IRAC02260967+6200119	0.0173	0.2061	1.1233	1.8463	1.9766	2.5289± 0.0107	2.7589± 0.0101	3.2730± 0.0316	4.9645± 0.0618
IRAC02261003+6159302	....	....	....	....	....	0.2655± 0.0034	0.1766± 0.0032	....	1.8659± 0.0490
IRAC02261007+6203454	....	....	....	....	....	0.4013± 0.0045	0.2660± 0.0048	1.0900± 0.0332	....
IRAC02261031+6200137	....	....	....	....	....	1.2635± 0.0452	1.2451± 0.0064	....	....
IRAC02261100+6200453	....	....	....	....	....	1.0392± 0.0064	0.9574± 0.0058	1.9951± 0.0271	2.6391± 0.0587
IRAC02261198+6203558	....	....	....	....	....	0.1196± 0.0041	....	1.0900± 0.0332	....
IRAC02261128+6201513	0.0108	0.1213	0.6060	0.8134	0.9907	0.6335± 0.0046	0.5342± 0.0046	1.0832± 0.0226	....
IRAC02261153+6204432	....	....	....	....	....	0.6820± 0.0074	0.5109± 0.0093	1.5851± 0.0414	....
IRAC02261196+6200129	0.0354	0.3546	1.6387	3.1210	3.2503	3.7277± 0.0126	3.3468± 0.0110	3.4648± 0.0308	3.9014± 0.0568
IRAC02261207+6159439	0.0074	0.0931	0.7490	1.4266	1.4857	0.7841± 0.0045	0.5516± 0.0039	....	1.8659± 0.0490
IRAC02261296+6203414	0.0281	0.2283	0.7022	1.2656	1.0184	0.6300± 0.0053	0.4041± 0.0053	0.9759± 0.0306	....
IRAC02261320+6200346	....	....	1.4012	2.3458	2.2281	2.7003± 0.0103	2.6966± 0.0093	3.0861± 0.0303	....
IRAC02261320+6156152	0.0103	0.1450	0.6173	1.0240	0.8393	0.4949± 0.0055	0.3336± 0.0037	....	....
IRAC02261391+6200532	....	....	1.0339	2.7688	4.8745	7.6964± 0.0224	7.9229± 0.0214	6.9452± 0.0384	5.4349± 0.0609
IRAC02261491+6204046	....	....	....	....	....	1.4946± 0.0083	1.7342± 0.0095	2.0313± 0.0378	....
IRAC02261565+6200482	0.0105	0.1716	0.8760	1.2425	1.3675	0.7470± 0.0049	0.5042± 0.0038	....	....
IRAC02261645+6157174	0.0174	0.2678	1.7002	2.9806	2.7035	1.6131± 0.0089	1.0929± 0.0072	....	....
IRAC02261671+6159485	0.0133	0.1724	0.9172	1.7470	2.1278	2.3732± 0.0076	2.4506± 0.0079	2.5969± 0.0201	3.3826± 0.0975
IRAC02261699+6158262	0.0926	0.5767	....	....	....	2.2164± 0.0087	1.8152± 0.0091	....	....
IRAC02261717+6157438	....	....	....	....	....	0.3781± 0.0046	0.2408± 0.0047	....	....
IRAC02261727+6156069	0.0758	0.8244	3.7195	6.1702	5.4945	3.6082± 0.0144	2.4486± 0.0086	....	....
IRAC02261739+6159512	0.0096	0.1196	0.7421	1.3624	1.2358	1.0372± 0.0045	0.8811± 0.0043	....	3.3826± 0.0975
IRAC02261769+6202141	....	....	....	....	....	0.2175± 0.0047	....	0.9204± 0.0310	....
IRAC02261849+6203556	....	....	....	....	....	2.6170± 0.0107	2.1788± 0.0120	1.7622± 0.0323	....
IRAC02261881+6159528	3.1124	8.8990	16.8457	20.8113	28.5713	35.9941± 0.0794	33.0929± 0.0736	28.1996± 0.0736	19.7041± 0.0763
IRAC02261765+6203431	....	....	....	....	....	....	0.1631± 0.0054	1.4315± 0.0338	....
IRAC02261881+6159528	3.1124	8.8990	16.8457	20.8113	28.5713	35.9941± 0.0794	33.0929± 0.0736	28.1996± 0.0736	19.7041± 0.0763
IRAC02261888+6158048	....	....	0.4770	0.8837	0.9726	0.5528± 0.0050	0.3692± 0.0048	....	....
IRAC02261959+6203058	....	....	1.0058	2.8728	5.0111	4.9716± 0.0172	5.4634± 0.0197	5.5616± 0.0405	5.8156± 0.0979
IRAC02261970+6156554	0.0069	0.0827	0.4597	0.9085	0.9461	0.6540± 0.0058	0.4370± 0.0043	....	....
IRAC02261967+6157541	0.0084	0.0952	0.5182	0.9779	0.8471	0.6031± 0.0049	0.4757± 0.0051	....	....
IRAC02261990+6159357	0.0084	0.1122	0.5950	1.0922	0.9907	0.5702± 0.0030	0.4037± 0.0032	....	....
IRAC02262010+6156358	0.0083	0.0765	0.5426	1.1866	1.2244	1.2468± 0.0077	1.2134± 0.0061	....	....
IRAC02262029+6200119	0.0433	0.4411	1.7478	2.9262	2.5818	1.4760± 0.0061	1.0010± 0.0041	....	....
IRAC02262044+6157024	0.0434	0.4977	2.2829	3.9292	3.7319	2.1077± 0.0100	1.4210± 0.0074	....	....
IRAC02262048+6203521	....	....	....	....	....	0.1110± 0.0039	10.5435± 0.0341	11.1644± 0.0564	7.5089± 0.1310
IRAC02262048+6203521	....	....	....	....	....	0.1110± 0.0039	....	....	7.5089± 0.1310
IRAC02262082+6200365	0.0489	0.4940	2.1013	3.4222	3.4668	2.7640± 0.0097	2.5800± 0.0079	2.8239± 0.0225	3.3343± 0.0365
IRAC02262048+6203521	....	....	....	....	....	0.1110± 0.0039	....	1.7701± 0.0287	7.5089± 0.1310
IRAC02262112+6158582	0.0162	0.3043	2.1207	4.0022	3.8720	3.4545± 0.0101	2.9812± 0.0105	2.7241± 0.0194	1.8166± 0.0446

Table 3.3 (continued)

ID	F_V [Jy]	F_I [Jy]	F_J [Jy]	F_H [Jy]	F_K [Jy]	$F_{3.6\mu m}$ [Jy]	$F_{4.5\mu m}$ [Jy]	$F_{5.8\mu m}$ [Jy]	$F_{8.0\mu m}$ [Jy]
IRAC02262148+6158419	0.0131	0.2141	1.3883	2.8728	3.7664	4.2733± 0.0126	4.6581± 0.0149	5.9031± 0.0271	8.7761± 0.0600
IRAC02262140+6200551	....	....	....	....	....	0.3941± 0.0038	0.3541± 0.0033	....	....
IRAC02262132+6204362	....	....	....	....	....	....	0.6992± 0.0064	0.9339± 0.0282	3.5138± 0.0972
IRAC02262191+6202438	0.0203	0.2609	....	....	....	1.0970± 0.0077	0.2386± 0.0051	....	....
IRAC02262195+6158031	0.0234	0.3010	1.4537	3.0082	3.4350	2.8531± 0.0106	2.4348± 0.0102	2.6262± 0.0251	....
IRAC02262199+6159297	0.0062	0.0896	....	....	....	0.2997± 0.0025	0.1893± 0.0026	....	....
IRAC02262219+6156592	....	....	....	....	....	0.4430± 0.0045	0.5047± 0.0042	....	....
IRAC02262231+6157267	....	....	0.6831	1.4666	1.2940	0.7198± 0.0055	0.4955± 0.0047	....	....
IRAC02262227+6202403	....	....	0.9005	1.5216	1.7058	....	1.0089± 0.0079	....	....
IRAC02262273+6203109	0.0269	0.3288	1.6387	3.0641	3.3108	3.1841± 0.0128	3.3963± 0.0151	4.2446± 0.0380	6.5168± 0.1083
IRAC02262318+6202023	....	....	....	....	....	0.9024± 0.0081	0.9420± 0.0075	....	....
IRAC02262328+6205020	0.0034	0.0127	....	....	....	3.5602± 0.0137	4.5682± 0.0220	5.8689± 0.0456	....
IRAC02262411+6200012	0.0235	0.2092	1.3258	2.3895	2.6542	2.4358± 0.0080	2.2342± 0.0073	2.3161± 0.0171	3.1943± 0.0930
IRAC02262440+6200090	....	....	....	....	....	0.2177± 0.0028	0.1853± 0.0026	....	3.1943± 0.0930
IRAC02262447+6159106	....	....	....	....	....	....	0.5632± 0.0045	....	7.5838± 0.1242
IRAC02262488+6159265	0.0100	0.1270	0.6060	0.9339	1.0963	0.7803± 0.0044	....	1.0460± 0.0182	2.4428± 0.0506
IRAC02262527+6156538	....	....	....	....	....	0.3750± 0.0040	0.2670± 0.0030	....	....
IRAC02262536+6200034	0.0117	0.2515	1.6691	3.3289	3.4668	3.3614± 0.0103	3.0712± 0.0094	2.7515± 0.0178	3.1943± 0.0930
IRAC02262586+6201186	0.0239	0.1478	....	....	....	0.2711± 0.0046	0.1770± 0.0037	....	....
IRAC02262587+6158354	0.0051	0.0892	0.4903	0.9870	1.1586	2.1528± 0.0089	2.1561± 0.0082	2.1409± 0.0224	....
IRAC02262637+6159124	0.0242	0.3870	1.8471	3.2681	3.0474	2.3066± 0.0085	1.8992± 0.0078	2.0538± 0.0193	....
IRAC02262646+6202241	0.1003	0.6927	2.5263	3.6838	3.1618	1.6905± 0.0099	1.1304± 0.0080	....	....
IRAC02262649+6204256	....	....	....	....	....	0.4154± 0.0043	0.3153± 0.0055	....	....
IRAC02262724+6158142	0.5011	3.7544	12.4305	17.3101	15.5572	8.4515± 0.0238	5.5889± 0.0164	3.9824± 0.0282	1.7791± 0.0511
IRAC02262794+6159538	....	....	0.7353	1.5499	2.1475	1.7052± 0.0065	1.6611± 0.0067	1.4931± 0.0172	....
IRAC02262802+6158482	0.0067	0.1532	0.8600	1.5216	1.3550	0.7961± 0.0056	0.5441± 0.0042	....	....
IRAC02262817+6158218	0.0060	0.0824	....	....	....	....	1.0039± 0.0053	....	....
IRAC02262836+6205306	0.0172	0.2201	1.1442	1.8980	2.0508	1.2018± 0.0064	1.0277± 0.0090	....	....
IRAC02262839+6156388	....	....	1.1547	2.3458	2.8309	1.3046± 0.0072	1.0356± 0.0046	....	....
IRAC02262860+6158055	0.0385	0.4387	2.3686	4.6377	6.5453	8.7307± 0.0252	8.9387± 0.0243	9.0890± 0.0430	9.8422± 0.0711
IRAC02262879+6157481	0.0130	0.1685	0.7022	1.4135	1.4320	1.2889± 0.0064	1.2026± 0.0056	....	....
IRAC02262938+6200135	....	....	....	....	....	0.6970± 0.0409	0.8615± 0.0049	....	....
IRAC02262940+6201375	0.0310	0.2944	1.6538	3.2681	3.8720	3.9207± 0.0166	3.6057± 0.0137	3.0411± 0.0357	....
IRAC02262962+6159126	0.0252	0.2928	1.6538	3.6838	5.2472	5.8257± 0.0177	5.8458± 0.0181	5.8718± 0.0330	6.5099± 0.0639
IRAC02262966+6156575	....	....	....	....	....	0.2673± 0.0035	0.1828± 0.0024	....	....
IRAC02262969+6202382	....	....	....	....	....	0.6724± 0.0066	0.4052± 0.0059	....	....
IRAC02262966+6204566	....	....	....	....	....	0.6962± 0.0045	0.5665± 0.0048	....	....
IRAC02262989+6201223	0.0108	0.0886	....	....	....	....	0.2633± 0.0040	....	....
IRAC02263007+6158506	0.0381	0.4271	2.0440	3.6166	4.0173	2.8374± 0.0120	2.3211± 0.0096	1.7916± 0.0268	....
IRAC02263023+6202383	....	....	....	....	....	0.5083± 0.0058	0.4052± 0.0059	....	....
IRAC02263046+6200453	....	....	1.7159	2.9262	2.9644	2.2390± 0.0098	1.8933± 0.0078	....	....
IRAC02263091+6157504	0.0075	0.1373	....	....	....	0.6954± 0.0051	0.4399± 0.0037	....	....
IRAC02263094+6155383	....	....	....	....	....	0.4451± 0.0057	0.2944± 0.0038	....	....

Table 3.3 (continued)

ID	F_V [Jy]	F_I [Jy]	F_J [Jy]	F_H [Jy]	F_K [Jy]	$F_{3.6\mu m}$ [Jy]	$F_{4.5\mu m}$ [Jy]	$F_{5.8\mu m}$ [Jy]	$F_{8.0\mu m}$ [Jy]
IRAC02263131+6200037	0.0359	0.5182	2.2620	3.9655	3.7319	2.0059± 0.0081	1.3547± 0.0069	....	....
IRAC02263135+6158054	....	....	....	....	....	0.5834± 0.0049	0.4041± 0.0039	....	....
IRAC02263140+6201527	0.0226	0.2168	0.9694	1.5933	1.5415	0.7723± 0.0064	0.5206± 0.0053	....	....
IRAC02263150+6201191	....	....	0.4431	0.8676	0.7378	0.4391± 0.0052	0.2867± 0.0040	....	....
IRAC02263167+6200439	....	....	....	....	....	0.5492± 0.0051	0.4928± 0.0043	....	....
IRAC02263184+6203125	....	....	....	....	....	0.3865± 0.0044	0.2639± 0.0051	1.8542± 0.0286	4.6085± 0.0894
IRAC02263206+6156121	0.6910	3.2579	7.5594	8.3618	7.1110	3.5671± 0.0128	2.2589± 0.0077	....	....
IRAC02263248+6156347	....	....	0.4858	1.3011	2.2905	4.8413± 0.0163	5.4338± 0.0141	5.5039± 0.0331	6.5651± 0.0469
IRAC02263240+6202523	....	....	....	....	....	0.4981± 0.0051	0.3371± 0.0051	....	....
IRAC02263230+6158525	....	....	0.5578	0.8517	0.9203	0.5176± 0.0054	0.3666± 0.0044	3.2701± 0.0381	3.6499± 0.0749
IRAC02263287+6201220	....	....	0.9874	1.6379	1.4994	0.8331± 0.0064	....	....	....
IRAC02263323+6201062	0.0249	0.3114	1.4272	2.4791	2.2905	1.2458± 0.0071	0.8250± 0.0050	....	....
IRAC02263332+6156030	0.0141	0.3950	....	....	....	8.0323± 0.0257	7.6334± 0.0199	6.6761± 0.0338	6.6351± 0.0487
IRAC02263328+6156045	0.0133	0.3720	....	....	....	....	....	6.6761± 0.0338	6.6351± 0.0487
IRAC02263343+6159250	0.0319	0.3575	1.2779	2.0811	1.8877	0.9843± 0.0067	0.6521± 0.0056	....	....
IRAC02263362+6159431	0.0143	0.2025	0.8063	1.4135	1.1801	0.6586± 0.0052	0.4242± 0.0054	1.1292± 0.0233	....
IRAC02263371+6155387	....	....	0.7022	1.5499	1.9406	2.1068± 0.0102	2.0909± 0.0084	....	....
IRAC02263386+6155555	0.0320	0.4972	2.6454	4.7676	4.6551	2.5651± 0.0114	1.7411± 0.0068	....	....
IRAC02263394+6156573	4.4741	9.6859	12.2036	11.2279	8.0897	3.6641± 0.0133	2.4022± 0.0072	1.8014± 0.0239	....
IRAC02263415+6201192	4.6936	16.9723	37.8868	40.7662	33.1078	15.9256± 0.0438	10.4644± 0.0278	6.9814± 0.0413	....
IRAC02263422+6159201	0.1141	1.0369	4.0410	6.5811	6.5453	5.9951± 0.0207	5.0415± 0.0182	4.1879± 0.0331	....
IRAC02263431+6200252	0.0239	0.2375	....	....	....	1.2116± 0.0067	1.3893± 0.0527	....	....
IRAC02263433+6201527	6.4077	14.1690	22.4124	21.5924	17.2159	7.8609± 0.0268	5.1136± 0.0170	3.4814± 0.0342	....
IRAC02263443+6200419	....	....	1024.4441	836.1803	602.4631	126.5426± 0.4112	167.2925± 0.3872	130.3327± 0.3150	97.2387± 0.2737
IRAC02263441+6205037	....	....	....	....	....	0.2437± 0.0030	0.1707± 0.0032	....	....
IRAC02263455+6158169	0.2307	1.7625	6.1729	10.0531	12.2442	13.1244± 0.0384	11.9664± 0.0328	10.4599± 0.0510	8.4359± 0.0703
IRAC02263455+6203404	....	....	....	....	....	0.4005± 0.0037	0.2878± 0.0048	....	....
IRAC02263463+6159107	2.6984	13.4320	35.1956	41.5241	34.6681	17.1499± 0.0517	11.2846± 0.0340	8.1037± 0.0462	....
IRAC02263480+6201053	0.0755	0.6423	2.7957	4.5113	3.9804	2.1342± 0.0094	1.3963± 0.0066	....	....
IRAC02263530+6204558	....	....	....	....	....	0.0655± 0.0021	0.1707± 0.0032	....	2.2613± 0.0534
IRAC02263489+6157559	0.1558	1.7512	7.2860	12.0865	11.1668	6.0500± 0.0193	4.0395± 0.0124	....	....
IRAC02263495+6202427	....	....	....	....	....	0.6289± 0.0049	0.4547± 0.0049	....	....
IRAC02263541+6155197	....	....	....	....	....	0.7046± 0.0085	0.4736± 0.0040	....	....
IRAC02263585+6201062	0.0350	0.3377	....	....	....	1.1978± 0.0069	0.8187± 0.0050	....	....
IRAC02263646+6201120	9.4515	22.5393	32.3958	32.3817	23.7646	10.9598± 0.0306	6.9279± 0.0192	4.8630± 0.0318	....
IRAC02263648+6157462	0.0375	0.4602	2.2003	3.7870	3.1618	1.7463± 0.0085	1.1571± 0.0054	....	....
IRAC02263658+6201471	....	....	0.9605	1.6838	1.5133	0.8986± 0.0058	0.5949± 0.0046	....	....
IRAC02263667+6200416	0.8187	4.8949	15.2226	18.9802	16.1410	7.8002± 0.0227	5.1443± 0.0164	3.3170± 0.0270	....
IRAC02263670+6202470	1.0922	5.4568	14.4042	18.6337	15.9930	8.2723± 0.0242	5.4348± 0.0177	3.8660± 0.0289	....
IRAC02263693+6200345	0.0328	0.3097	1.5083	2.7183	2.7793	2.0323± 0.0087	1.7204± 0.0082	....	....
IRAC02263709+6202222	0.0105	0.1011	0.4640	0.7912	0.7942	0.4315± 0.0043	0.3018± 0.0042	....	....
IRAC02263713+6202147	0.0101	0.1180	0.6584	1.0335	1.1911	1.0637± 0.0062	1.0010± 0.0060	....	....
IRAC02263743+6202322	0.0171	0.1913	0.8443	1.7960	2.3547	1.8570± 0.0081	2.0000± 0.0089	2.3571± 0.0259	....

Table 3.3 (continued)

ID	F_V [Jy]	F_I [Jy]	F_J [Jy]	F_H [Jy]	F_K [Jy]	$F_{3.6\mu m}$ [Jy]	$F_{4.5\mu m}$ [Jy]	$F_{5.8\mu m}$ [Jy]	$F_{8.0\mu m}$ [Jy]
IRAC02263750+6156207	....	....	....	....	....	3.0078± 0.0123	3.2885± 0.0103	3.3875± 0.0300	3.5306± 0.0466
IRAC02263755+6201557	....	....	0.5950	1.0527	1.2704	0.6596± 0.0050	0.4602± 0.0044	....	....
IRAC02263768+6159187	0.1580	1.3333	4.2314	6.7035	5.7535	3.0206± 0.0137	1.9822± 0.0101	....	....
IRAC02263768+6200054	0.0236	0.3953	1.8988	3.2681	3.0756	1.8041± 0.0079	1.2105± 0.0070	....	....
IRAC02263755+6205115	....	....	....	....	....	0.5622± 0.0040	0.3954± 0.0039	....	....
IRAC02263928+6201034	....	....	....	....	....	....	....	0.5198± 0.0171	5.0335± 0.0596
IRAC02263847+6157126	....	....	....	....	....	0.3548± 0.0047	0.3065± 0.0030	....	....
IRAC02263851+6200490	0.0508	0.4977	....	....	....	4.7355± 0.0153	4.3330± 0.0142	....	5.0335± 0.0596
IRAC02263862+6200142	....	....	0.6645	1.1228	1.8194	1.6513± 0.0074	1.3715± 0.0071	....	....
IRAC02263865+6200533	0.0423	0.4102	....	....	....	5.0764± 0.0157	4.5978± 0.0146	3.7603± 0.0292	5.0335± 0.0596
IRAC02263865+6159135	0.0132	0.1858	0.7286	1.2891	1.0091	0.5273± 0.0060	....	....	....
IRAC02263868+6159094	0.0697	0.7772	....	....	....	2.3105± 0.0121	1.5168± 0.0091	....	....
IRAC02263885+6200303	0.9110	4.0601	11.7622	13.8771	11.6931	5.9422± 0.0180	3.9397± 0.0136	2.7006± 0.0254	....
IRAC02263882+6202112	0.0196	0.3091	....	....	....	1.9824± 0.0086	1.5632± 0.0070	....	....
IRAC02263954+6202400	....	....	....	....	....	2.0549± 0.0086	1.9664± 0.0086	2.0519± 0.0251	2.6854± 0.1303
IRAC02263958+6204263	....	....	....	....	....	0.1574± 0.0028	0.1480± 0.0037	1.1800± 0.0200	....
IRAC02263953+6202401	0.0380	0.3069	1.7478	2.9532	3.4989	2.0549± 0.0086	1.9664± 0.0086	2.0519± 0.0251	....
IRAC02263962+6203506	0.0483	0.3612	1.5649	2.4116	2.3117	1.2282± 0.0059	0.8744± 0.0059	1.2867± 0.0172	3.0335± 0.0497
IRAC02263987+6201292	0.0111	0.1689	....	....	....	0.8273± 0.0048	0.7207± 0.0042	....	....
IRAC02263999+6200279	0.0289	0.2890	1.5363	3.0082	3.9078	4.9402± 0.0152	4.7619± 0.0158	5.6742± 0.0297	6.8067± 0.0623
IRAC02264011+6200068	0.0119	0.1549	....	....	....	2.4182± 0.0097	2.2253± 0.0098	1.6389± 0.0237	4.7998± 0.0644
IRAC02263983+6156038	....	....	....	....	....	....	0.1332± 0.0034	....	2.4231± 0.0595
IRAC02264061+6200448	....	....	0.5041	0.9513	1.0374	0.6620± 0.0040	0.6607± 0.0047	....	....
IRAC02264113+6157424	....	....	0.4555	1.0053	1.0278	2.3653± 0.0115	2.6532± 0.0098	2.6752± 0.0349	....
IRAC02264126+6201566	0.1100	0.8259	3.4236	5.7319	5.0111	2.7042± 0.0096	1.8271± 0.0075	....	....
IRAC02264140+6158026	0.0332	0.5274	2.5263	4.4699	4.2455	2.3947± 0.0123	1.5227± 0.0076	....	....
IRAC02264157+6201129	0.0166	0.1713	0.8063	1.6229	1.8532	1.8903± 0.0067	1.6749± 0.0063	....	....
IRAC02264193+6201516	0.0856	0.5303	1.8814	3.0641	2.7035	1.3497± 0.0062	0.8956± 0.0048	....	....
IRAC02264238+6159456	0.0080	0.1942	0.9430	1.6229	1.8027	1.3173± 0.0074	1.0850± 0.0071	....	....
IRAC02264247+6157511	....	....	0.4431	1.1649	1.2132	0.7006± 0.0068	0.4678± 0.0043	....	2.1519± 0.0602
IRAC02264279+6204237	....	....	....	....	....	0.2723± 0.0037	0.2017± 0.0042	1.0773± 0.0221	....
IRAC02264240+6158162	0.0066	0.1279	....	....	....	0.7427± 0.0066	0.4827± 0.0047	....	....
IRAC02264279+6201156	....	....	....	....	....	0.2682± 0.0026	0.1833± 0.0025	....	....
IRAC02264290+6201282	0.0880	0.6300	2.9545	4.9923	5.7007	5.2625± 0.0151	4.9496± 0.0137	5.0147± 0.0266	5.7396± 0.0426
IRAC02264297+6200166	0.0509	0.4193	....	....	....	1.1685± 0.0056	0.8159± 0.0056	....	....
IRAC02264334+6200044	0.0130	0.2612	1.0244	2.2819	2.6787	3.7483± 0.0129	3.3567± 0.0138	2.9462± 0.0260	....
IRAC02264342+6203347	0.0095	0.1832	1.1547	2.3030	2.3117	1.5093± 0.0074	1.0217± 0.0054	....	....
IRAC02264353+6159270	0.0253	0.3899	1.7318	2.9532	2.5115	1.5005± 0.0083	1.0030± 0.0068	....	....
IRAC02264359+6204115	....	....	0.7771	1.1437	1.4188	1.6983± 0.0072	1.5840± 0.0080	2.0186± 0.0227	2.8955± 0.0738
IRAC02264438+6155548	....	....	....	....	....	....	0.1055± 0.0037	....	5.1055± 0.0934
IRAC02264376+6159113	0.1977	1.4687	4.2314	6.5811	5.7535	3.7767± 0.0154	2.9625± 0.0131	2.5607± 0.0311	....
IRAC02264391+6200191	....	....	....	....	....	0.8262± 0.0044	0.9313± 0.0060	....	....
IRAC02264413+6200305	0.0192	0.2094	1.0435	2.2197	3.0756	3.4172± 0.0106	3.4664± 0.0116	3.5274± 0.0198	4.6913± 0.0445

Table 3.3 (continued)

ID	F_V [Jy]	F_I [Jy]	F_J [Jy]	F_H [Jy]	F_K [Jy]	$F_{3.6\mu m}$ [Jy]	$F_{4.5\mu m}$ [Jy]	$F_{5.8\mu m}$ [Jy]	$F_{8.0\mu m}$ [Jy]
IRAC02264423+6203348	0.0377	0.3814	1.7002	2.7945	2.5115	1.3389± 0.0067	0.8658± 0.0051	....	....
IRAC02264425+6155223	0.0316	0.2861	0.8063	1.1023	0.9907	....	0.3237± 0.0039	....	....
IRAC02264421+6157229	0.0076	0.1851	1.2204	2.5252	2.9372	3.3369± 0.0151	2.8804± 0.0100	2.8063± 0.0384	3.2091± 0.0582
IRAC02264480+6159395	....	....	0.7087	0.9870	0.9998	0.5660± 0.0047	0.3828± 0.0047	....	....
IRAC02264490+6204378	....	....	....	....	....	0.2263± 0.0035	0.1168± 0.0040	1.5293± 0.0238	4.7258± 0.0768
IRAC02264497+6200170	0.0601	0.5116	2.2003	3.4858	3.1041	1.5798± 0.0065	1.0039± 0.0063	....	....
IRAC02264527+6203075	....	....	715.3001	867.5608	831.6306	291.0872± 0.8387	200.8893± 0.6110	215.4599± 0.4909	115.3846± 0.3012
IRAC02264562+6157382	....	....	....	....	....	0.4807± 0.0058	0.6510± 0.0044	....	....
IRAC02264571+6159505	0.7323	3.5887	9.8739	10.0531	8.7082	4.4349± 0.0150	2.9980± 0.0121	1.9941± 0.0210	....
IRAC02264592+6204019	....	....	....	....	....	0.7097± 0.0059	0.6400± 0.0053	1.5656± 0.0322	9.9310± 0.1698
IRAC02264606+6201220	....	....	....	....	....	1.6131± 0.0055	1.7954± 0.0062	1.8337± 0.0159	1.7643± 0.0806
IRAC02264607+6157332	....	....	....	....	....	0.8157± 0.0070	0.7654± 0.0048	....	2.7209± 0.0606
IRAC02264649+6200196	....	....	1.3258	2.0811	2.0508	1.0362± 0.0050	0.6730± 0.0051	....	....
IRAC02264651+6156331	....	....	....	....	....	2.0206± 0.0131	1.8370± 0.0092	....	3.0858± 0.0813
IRAC02264674+6200367	0.0207	0.2435	1.0150	1.8463	1.5846	0.9603± 0.0044	0.6681± 0.0045	....	....
IRAC02264702+6202144	....	....	0.7153	1.2311	1.2704	1.4691± 0.0062	1.8142± 0.0066	2.1438± 0.0225	3.0148± 0.0929
IRAC02264720+6156102	....	....	0.7219	1.5933	1.5701	1.1254± 0.0122	0.8653± 0.0068	....	....
IRAC02264736+6159478	....	....	0.9783	2.0244	2.0508	1.7424± 0.0079	1.4961± 0.0074	....	....
IRAC02264898+6157567	....	....	....	....	....	2.4535± 0.0122	2.9773± 0.0103	4.7730± 0.0452	3.5246± 0.0613
IRAC02264970+6156338	....	....	0.4640	1.1649	1.4994	2.7228± 0.0169	2.7520± 0.0125	2.5411± 0.0469	....
IRAC02264963+6156035	0.9870	7.2801	18.8143	23.2434	19.4058	10.3722± 0.0570	6.6354± 0.0226	4.7926± 0.0663	....
IRAC02264974+6158419	....	....	0.4949	1.1866	1.1586	0.9502± 0.0063	0.7849± 0.0052	....	....
IRAC02265007+6200263	0.0238	0.3184	1.5794	2.7688	2.6542	1.5358± 0.0059	1.0326± 0.0055	....	....
IRAC02265061+6157404	....	....	....	....	....	3.9765± 0.0163	4.9832± 0.0150	4.7593± 0.0448	4.7120± 0.0588
IRAC02265084+6202534	0.3369	2.4737	9.7834	12.3112	11.6931	6.8825± 0.0234	5.4259± 0.0179	3.9990± 0.0367	3.9063± 0.0633
IRAC02265100+6158384	....	....	0.8063	2.3030	3.2804	3.1959± 0.0125	2.9990± 0.0107	3.1546± 0.0315	3.8797± 0.0575
IRAC02265167+6200166	....	....	....	....	....	0.4579± 0.0033	0.4397± 0.0039	....	....
IRAC02265171+6158335	0.0133	0.2497	1.4537	3.1210	3.4668	3.0470± 0.0121	3.1561± 0.0104	2.9677± 0.0309	3.8797± 0.0575
IRAC02265339+6157007	0.0121	0.3246	2.6454	6.6420	10.5665	11.5377± 0.0406	11.0474± 0.0308	11.0176± 0.0650	16.5582± 0.1019
IRAC02265387+6204355	1.9262	4.6402	6.6449	6.2273	4.5701	2.0960± 0.0094	1.3745± 0.0082	....	....
IRAC02265444+6157204	....	....	0.5895	1.6379	1.8532	1.2654± 0.0074	0.8522± 0.0050	....	....
IRAC02265534+6159075	1.3941	4.5724	8.8407	8.7559	6.8538	3.2938± 0.0109	2.1868± 0.0078	....	....
IRAC02265574+6202069	....	....	0.4513	1.0922	1.0862	0.6931± 0.0043	0.4809± 0.0032	....	....
IRAC02265607+6205409	0.5764	1.9113	3.6854	3.8931	3.2503	1.4858± 0.0066	0.9589± 0.0070	....	....
IRAC02265761+6159490	....	....	....	....	....	0.4680± 0.0043	0.3441± 0.0034	....	....
IRAC02265809+6157155	....	....	....	....	....	0.4284± 0.0048	0.3045± 0.0032	....	....
IRAC02265816+6159319	0.0091	0.1435	0.8289	1.7470	2.4885	3.4329± 0.0120	2.9694± 0.0098	....	....
IRAC02265948+6203506	....	....	0.4390	1.0430	1.3060	0.7178± 0.0061	0.4910± 0.0050	....	....
IRAC02270002+6201106	....	....	0.4814	0.9779	0.8393	0.5347± 0.0042	0.3571± 0.0039	....	....
IRAC02270024+6157320	....	....	....	....	....	0.3620± 0.0039	0.3010± 0.0030	....	....
IRAC02270155+6159589	....	....	....	....	....	2.2194± 0.0095	2.1028± 0.0086	....	....
IRAC02270392+6201588	....	....	0.6288	1.6379	2.1083	2.2821± 0.0085	1.8399± 0.0078	....	....
IRAC02270523+6157048	0.4099	1.8119	3.6182	4.6377	3.6302	1.7121± 0.0101	1.0820± 0.0052	....	....

Table 3.3 (continued)

ID	F_V [Jy]	F_I [Jy]	F_J [Jy]	F_H [Jy]	F_K [Jy]	$F_{3.6\mu m}$ [Jy]	$F_{4.5\mu m}$ [Jy]	$F_{5.8\mu m}$ [Jy]	$F_{8.0\mu m}$ [Jy]
IRAC02270536+6202109	....	....	....	....	....	0.2934± 0.0033	0.2011± 0.0031	....	....
IRAC02270613+6158166	0.0235	0.3054	1.6087	3.0641	3.3723	3.6474± 0.0126	3.5613± 0.0101	3.4481± 0.0291	3.6647± 0.0452
IRAC02270616+6157127	....	....	....	....	....	0.8901± 0.0078	0.9881± 0.0050	....	....
IRAC02270608+6157387	....	....	....	....	....	0.2784± 0.0039	0.2249± 0.0025	....	....
IRAC02270756+6200131	0.0127	0.3679	3.7887	9.0012	9.9984	6.1469± 0.0243	3.9970± 0.0171	2.4041± 0.0473	....
IRAC02270756+6200131	0.0127	0.3679	3.7887	9.0012	9.9984	6.1469± 0.0243	3.9970± 0.0171	2.4041± 0.0473	....
IRAC02270964+6159369	....	....	....	....	....	0.4745± 0.0061	0.3269± 0.0046	....	....
IRAC02271047+6159501	0.0102	0.2050	1.1233	1.7470	1.7862	0.9922± 0.0082	0.6740± 0.0060	....	....
IRAC02271197+6157347	0.0942	0.3849	0.7771	1.0053	0.9288	0.4215± 0.0064	0.2934± 0.0036	....	....
IRAC02271295+6157250	....	....	0.4310	1.0240	1.0091	0.6950± 0.0089	0.4805± 0.0045	....	....
IRAC02271296+6158407	0.0216	0.2321	0.9605	1.5216	1.3929	0.6880± 0.0065	0.4491± 0.0040	....	....
IRAC02271410+6200456	....	....	....	....	....	0.2598± 0.0069	....	2.0117± 0.0485	5.1065± 0.1374
IRAC02271452+6200193	0.1127	0.8491	2.7195	3.8575	3.5639	1.7522± 0.0639	....	....	....
IRAC02271660+6200520	....	....	....	....	....	1.5926± 0.0649	....	1.7456± 0.0482	....
IRAC02271627+6159086	0.0104	0.1777	0.8841	1.3253	1.3426	0.5586± 0.0070	0.4129± 0.0042	....	....
IRAC02271656+6158358	0.0063	0.1038	0.5630	1.0822	1.0374	0.9119± 0.0071	0.7267± 0.0049	....	....
IRAC02271981+6158281	0.0256	0.2700	1.3630	2.2197	1.9585	1.0274± 0.0082	0.6964± 0.0049	....	....
IRAC02271999+6159435	0.4979	1.8388	3.5850	4.4699	3.2503	1.5113± 0.0114	0.9571± 0.0068	....	4.6479± 0.0940
IRAC02272024+6202025	1.3813	10.6400	49.9446	71.4990	79.4201	70.2547± 0.1635	61.3439± 0.1532	53.6399± 0.1421	40.4043± 0.1594

Note. — The near-infrared fluxes are from the 2MASS catalog Skrutskie et al. (2006), selecting only sources flagged 'AAA'. The optical fluxes are from José et al. in preparation.

Table 3.4. Cluster member candidates: designation and positions of IRAC sources with excess without X-ray counterpart.

ID	RA_{J2000} [deg]	RA error 10^{-4}[deg]	DEC_{J2000} [deg]	DEC error 10^{-4}[deg]
IRAC022724.18+620148.4	36.850746	1.04	62.030109	1.05
IRAC022712.69+620345.3	36.802887	2.60	62.062580	2.52
IRAC022710.52+620418.5	36.793823	2.17	62.071796	2.28
IRAC022725.20+615956.8	36.854996	1.56	61.999111	1.47
IRAC022719.95+620118.7	36.833122	2.15	62.021870	2.23
IRAC022710.80+620300.6	36.795010	2.85	62.050163	2.81
IRAC022700.33+620529.1	36.751377	1.09	62.091415	1.12
IRAC022716.05+620050.6	36.816875	0.43	62.014042	0.44
IRAC022708.82+620303.8	36.786747	1.79	62.051060	1.94
IRAC022711.47+620157.8	36.797775	0.57	62.032722	0.60
IRAC022659.77+620454.2	36.749031	1.83	62.081726	1.85
IRAC022715.12+620015.2	36.813011	0.45	62.004215	0.46
IRAC022700.50+620420.0	36.752094	1.30	62.072227	1.18
IRAC022704.83+620257.5	36.770123	1.96	62.049297	2.03
IRAC022709.85+620127.5	36.791046	2.24	62.024292	2.32
IRAC022706.08+620220.2	36.775326	0.83	62.038940	0.81
IRAC022700.94+620333.5	36.753929	1.72	62.059319	1.74
IRAC022714.14+615923.6	36.808918	1.52	61.989902	1.67
IRAC022700.06+620301.2	36.750267	1.36	62.050343	1.36
IRAC022718.02+615816.0	36.825100	2.23	61.971123	2.56
IRAC022715.04+615848.2	36.812668	2.01	61.980068	2.20
IRAC022704.24+620102.0	36.767677	1.94	62.017212	2.06
IRAC022715.98+615748.3	36.816570	2.64	61.963428	2.93
IRAC022656.14+620244.1	36.733910	0.75	62.045570	0.76
IRAC022658.71+620200.8	36.744625	0.68	62.033562	0.70
IRAC022659.94+620142.2	36.749737	0.98	62.028393	1.04
IRAC022711.75+615826.5	36.798965	0.65	61.974022	0.67
IRAC022709.91+615852.1	36.791275	1.63	61.981152	1.73
IRAC022643.97+620524.7	36.683205	1.40	62.090183	1.45
IRAC022714.20+615727.8	36.809181	3.21	61.957718	3.25
IRAC022643.51+620530.2	36.681278	3.98	62.091713	3.92
IRAC022645.66+620446.9	36.690266	0.60	62.079685	0.60
IRAC022700.58+620056.7	36.752430	1.13	62.015759	1.13
IRAC022640.42+620603.8	36.668407	0.82	62.101067	0.81
IRAC022647.31+620416.2	36.697117	5.87	62.071171	6.49
IRAC022702.43+620009.2	36.760136	1.02	62.002544	1.05
IRAC022639.85+620535.6	36.666031	5.19	62.093216	5.15
IRAC022647.12+620351.1	36.696339	1.60	62.064194	1.58

Table 3.4 (continued)

ID	RA_{J2000} [deg]	RA error 10^{-4}[deg]	DEC_{J2000} [deg]	DEC error 10^{-4}[deg]
IRAC022649.26+620313.1	36.705231	1.63	62.053650	1.71
IRAC022641.13+620508.4	36.671391	4.04	62.085659	4.17
IRAC022652.58+620217.9	36.719074	2.50	62.038315	2.40
IRAC022654.87+620141.3	36.728638	1.50	62.028137	1.53
IRAC022711.66+615711.9	36.798573	1.27	61.953308	1.74
IRAC022654.91+620130.7	36.728779	1.39	62.025185	1.42
IRAC022657.04+620058.7	36.737675	2.37	62.016312	2.66
IRAC022657.70+620043.0	36.740398	0.95	62.011936	0.92
IRAC022639.60+620524.1	36.665001	1.04	62.090019	1.09
IRAC022642.30+620441.2	36.676254	2.29	62.078098	2.46
IRAC022636.48+620606.9	36.652004	1.45	62.101921	1.60
IRAC022657.87+620028.3	36.741112	1.13	62.007870	1.08
IRAC022643.96+620405.4	36.683167	5.15	62.068153	5.35
IRAC022701.90+615913.1	36.757904	7.53	61.986961	8.26
IRAC022642.99+620410.0	36.679127	4.42	62.069454	4.61
IRAC022700.71+615922.6	36.752964	0.38	61.989597	0.40
IRAC022641.01+620436.4	36.670876	2.35	62.076767	2.41
IRAC022702.17+615858.3	36.759029	2.45	61.982857	2.49
IRAC022654.33+620058.4	36.726395	1.50	62.016228	1.58
IRAC022658.24+615956.6	36.742676	2.14	61.999046	2.32
IRAC022705.36+615800.2	36.772343	2.05	61.966709	2.23
IRAC022708.38+615702.4	36.784935	1.46	61.950680	1.32
IRAC022654.30+620044.8	36.726261	2.01	62.012451	2.27
IRAC022653.98+620039.6	36.724911	0.50	62.010986	0.50
IRAC022700.91+615847.8	36.753777	0.83	61.979946	0.87
IRAC022650.46+620132.4	36.710236	1.51	62.025658	1.60
IRAC022637.97+620437.8	36.658195	6.49	62.077168	6.77
IRAC022704.33+615736.3	36.768024	1.67	61.960075	1.73
IRAC022651.49+620058.7	36.714550	1.60	62.016319	1.71
IRAC022644.23+620246.4	36.684288	0.89	62.046223	0.88
IRAC022700.54+615824.6	36.752254	0.72	61.973495	0.68
IRAC022647.98+620137.2	36.699936	1.56	62.027012	1.52
IRAC022656.82+615914.2	36.736732	2.36	61.987274	2.36
IRAC022641.80+620303.3	36.674149	0.94	62.050911	0.96
IRAC022649.70+620058.8	36.707077	0.91	62.016335	0.95
IRAC022654.84+615937.9	36.728500	2.78	61.993855	2.78
IRAC022655.60+615914.3	36.731674	2.75	61.987297	2.70
IRAC022635.42+620430.6	36.647594	1.71	62.075161	1.79

Table 3.4 (continued)

ID	RA_{J2000} [deg]	RA error 10^{-4}[deg]	DEC_{J2000} [deg]	DEC error 10^{-4}[deg]
IRAC022657.82+615837.7	36.740898	2.64	61.977142	2.76
IRAC022641.97+620242.8	36.674873	1.04	62.045235	1.09
IRAC022647.81+620112.3	36.699203	0.92	62.020096	1.02
IRAC022629.52+620551.8	36.623009	0.86	62.097713	0.87
IRAC022634.65+620431.3	36.644382	0.53	62.075348	0.52
IRAC022646.05+620122.1	36.691887	0.59	62.022797	0.62
IRAC022648.00+620057.6	36.700001	1.96	62.016006	1.93
IRAC022702.53+615704.6	36.760521	1.12	61.951283	1.02
IRAC022647.66+620059.2	36.698593	1.67	62.016449	1.71
IRAC022655.60+615851.7	36.731667	1.41	61.981014	1.38
IRAC022644.41+620148.0	36.685043	1.40	62.030003	1.47
IRAC022648.08+620049.0	36.700348	1.44	62.013607	1.56
IRAC022641.94+620223.7	36.674759	3.04	62.039909	3.22
IRAC022655.75+615842.9	36.732285	2.67	61.978573	2.71
IRAC022645.15+620132.0	36.688110	2.02	62.025558	2.04
IRAC022657.11+615819.0	36.737968	1.28	61.971947	1.27
IRAC022646.75+620102.6	36.694805	1.56	62.017384	1.57
IRAC022629.86+620520.1	36.624416	2.08	62.088928	2.11
IRAC022653.24+615912.4	36.721840	1.76	61.986790	1.65
IRAC022656.57+615816.7	36.735699	1.53	61.971313	1.58
IRAC022643.34+620143.2	36.680584	1.64	62.028675	1.65
IRAC022645.54+620108.8	36.689766	2.00	62.019104	1.98
IRAC022659.22+615728.9	36.746742	2.32	61.958027	2.60
IRAC022632.51+620425.4	36.635445	2.75	62.073727	2.89
IRAC022630.45+620455.2	36.626877	1.53	62.081989	1.57
IRAC022651.39+615925.2	36.714127	1.92	61.990337	2.05
IRAC022644.72+620103.9	36.686325	1.61	62.017742	1.60
IRAC022645.31+620054.4	36.688805	1.36	62.015099	1.42
IRAC022649.94+615942.3	36.708065	0.64	61.995083	0.70
IRAC022630.66+620441.1	36.627762	6.30	62.078075	6.63
IRAC022648.56+615957.6	36.702320	2.02	61.999344	2.03
IRAC022650.62+615914.4	36.710911	2.52	61.987347	2.56
IRAC022645.73+620025.1	36.690525	0.75	62.006966	0.73
IRAC022629.62+620441.4	36.623398	1.58	62.078167	1.63
IRAC022647.71+615955.0	36.698799	2.01	61.998615	2.02
IRAC022655.63+615746.6	36.731796	1.52	61.962933	1.53
IRAC022632.41+620351.8	36.635040	3.08	62.064396	3.05
IRAC022653.43+615818.8	36.722610	2.31	61.971893	2.33

Table 3.4 (continued)

ID	RA_{J2000} [deg]	RA error 10^{-4}[deg]	DEC_{J2000} [deg]	DEC error 10^{-4}[deg]
IRAC022629.93+620427.9	36.624710	2.20	62.074406	2.33
IRAC022639.51+620152.0	36.664631	0.99	62.031105	1.07
IRAC022645.72+620013.1	36.690487	1.06	62.003635	1.12
IRAC022628.83+620436.5	36.620129	0.95	62.076797	1.02
IRAC022641.07+620121.1	36.671124	1.73	62.022541	1.85
IRAC022643.79+620038.9	36.682449	1.87	62.010811	1.92
IRAC022630.81+620350.2	36.628380	1.64	62.063934	1.68
IRAC022631.52+620333.1	36.631325	1.96	62.059208	2.16
IRAC022638.39+620145.9	36.659939	0.76	62.029404	0.83
IRAC022640.99+620107.6	36.670776	2.30	62.018787	2.38
IRAC022644.33+620002.7	36.684719	0.83	62.000736	0.86
IRAC022647.10+615923.8	36.696262	0.96	61.989952	0.99
IRAC022639.03+620129.8	36.662609	1.50	62.024940	1.65
IRAC022640.00+620054.5	36.666649	0.65	62.015137	0.66
IRAC022631.31+620307.5	36.630451	3.48	62.052086	3.44
IRAC022623.64+620508.2	36.598507	1.34	62.085621	1.41
IRAC022626.25+620357.9	36.609371	0.65	62.066078	0.59
IRAC022625.16+620355.5	36.604820	0.74	62.065430	0.73
IRAC022651.24+615751.3	36.713505	1.87	61.964245	1.86
IRAC022655.82+615637.9	36.732563	1.11	61.943851	1.12
IRAC022641.45+620024.5	36.672718	1.16	62.006809	1.17
IRAC022652.10+615736.2	36.717083	1.41	61.960068	1.39
IRAC022630.59+620315.2	36.627441	3.69	62.054234	3.90
IRAC022650.19+615757.7	36.709145	1.87	61.966015	1.77
IRAC022643.40+615938.2	36.680817	0.73	61.993931	0.83
IRAC022637.00+620112.9	36.654163	6.04	62.020256	5.51
IRAC022640.67+620014.7	36.669445	1.40	62.004074	1.53
IRAC022647.55+615819.2	36.698109	0.95	61.972008	0.96
IRAC022639.74+620010.9	36.665581	0.72	62.003033	0.70
IRAC022634.47+620134.2	36.643616	0.79	62.026169	0.78
IRAC022636.26+620055.9	36.651093	1.18	62.015522	1.16
IRAC022641.77+615940.2	36.674049	1.28	61.994495	1.31
IRAC022637.98+620036.4	36.658241	1.41	62.010124	1.49
IRAC022629.84+620244.1	36.624340	1.77	62.045589	1.52
IRAC022620.16+620510.6	36.583988	2.51	62.086273	2.33
IRAC022642.07+615924.3	36.675278	2.06	61.990089	1.85
IRAC022627.54+620310.8	36.614742	3.30	62.053005	3.17
IRAC022620.15+620510.6	36.583969	2.90	62.086277	2.88

Table 3.4 (continued)

ID	RA_{J2000} [deg]	RA error 10^{-4}[deg]	DEC_{J2000} [deg]	DEC error 10^{-4}[deg]
IRAC022634.87+620110.7	36.645279	1.39	62.019642	1.43
IRAC022632.43+620148.0	36.635120	2.30	62.029995	2.24
IRAC022639.11+620000.6	36.662975	1.08	62.000172	1.08
IRAC022636.13+620046.8	36.650528	1.92	62.013004	1.94
IRAC022640.07+615945.3	36.666950	1.66	61.995907	1.69
IRAC022622.84+620413.0	36.595158	2.46	62.070282	2.57
IRAC022642.98+615853.5	36.679089	1.58	61.981522	1.65
IRAC022621.98+620421.9	36.591591	1.54	62.072754	1.65
IRAC022638.26+615958.7	36.659424	1.31	61.999649	1.42
IRAC022631.20+620147.1	36.630016	1.63	62.029747	1.58
IRAC022635.46+620037.8	36.647755	1.99	62.010502	2.06
IRAC022641.76+615850.3	36.674004	0.62	61.980648	0.59
IRAC022622.08+620408.2	36.592018	4.33	62.068935	4.68
IRAC022636.29+620022.8	36.651199	3.34	62.006340	3.27
IRAC022617.95+620459.5	36.574806	0.43	62.083206	0.42
IRAC022632.38+620114.4	36.634914	2.44	62.020657	2.31
IRAC022638.67+615940.6	36.661110	1.95	61.994610	2.00
IRAC022644.79+615756.3	36.686630	2.25	61.965633	2.08
IRAC022637.49+615953.8	36.656216	1.90	61.998287	1.91
IRAC022648.92+615654.1	36.703846	1.88	61.948353	2.01
IRAC022635.09+620028.6	36.646210	1.78	62.007942	1.76
IRAC022620.53+620357.3	36.585541	0.56	62.065926	0.59
IRAC022622.21+620348.1	36.592525	1.07	62.063354	1.09
IRAC022629.07+620200.0	36.621117	1.88	62.033325	1.78
IRAC022620.64+620406.8	36.585991	0.75	62.068542	0.78
IRAC022621.56+620352.2	36.589840	0.92	62.064491	0.94
IRAC022629.23+620148.1	36.621777	0.40	62.030014	0.40
IRAC022638.87+615921.2	36.661957	1.25	61.989231	1.24
IRAC022620.02+620338.8	36.583420	0.27	62.060768	0.28
IRAC022643.67+615756.7	36.681976	1.02	61.965744	1.02
IRAC022640.23+615844.6	36.667641	2.92	61.979065	2.83
IRAC022644.51+615736.7	36.685448	2.66	61.960186	2.33
IRAC022642.88+615756.8	36.678658	1.90	61.965778	1.90
IRAC022630.81+620102.5	36.628357	1.92	62.017365	1.84
IRAC022636.48+615932.4	36.652008	2.23	61.992340	2.44
IRAC022639.25+615847.6	36.663555	3.04	61.979877	3.08
IRAC022631.11+620055.3	36.629620	1.99	62.015350	2.09
IRAC022627.79+620139.5	36.615810	1.60	62.027645	1.79

Table 3.4 (continued)

ID	RA_{J2000} [deg]	RA error 10^{-4}[deg]	DEC_{J2000} [deg]	DEC error 10^{-4}[deg]
IRAC022635.82+615931.8	36.649265	1.23	61.992157	1.29
IRAC022637.93+615859.9	36.658058	2.93	61.983311	2.76
IRAC022632.07+620029.5	36.633617	1.61	62.008198	1.65
IRAC022633.51+620006.1	36.639633	1.80	62.001694	1.89
IRAC022647.16+615628.1	36.696507	2.23	61.941135	2.16
IRAC022624.60+620220.6	36.602512	1.52	62.039051	1.74
IRAC022640.94+615755.7	36.670597	1.35	61.965462	1.50
IRAC022643.27+615718.0	36.680298	1.04	61.955002	1.05
IRAC022641.86+615737.4	36.674408	2.20	61.960377	2.26
IRAC022630.40+620033.8	36.626671	1.52	62.009396	1.62
IRAC022635.32+615916.2	36.647175	1.53	61.987839	1.60
IRAC022636.34+615900.2	36.651421	3.04	61.983398	2.88
IRAC022617.68+620353.3	36.573673	3.44	62.064819	3.63
IRAC022643.74+615702.0	36.682247	1.75	61.950546	1.98
IRAC022613.12+620454.8	36.554668	3.02	62.081898	2.91
IRAC022630.89+620012.3	36.628719	2.08	62.003429	2.06
IRAC022632.65+615939.0	36.636040	4.43	61.994171	3.12
IRAC022636.45+615842.2	36.651855	2.04	61.978397	2.27
IRAC022628.24+620046.1	36.617680	1.31	62.012794	1.33
IRAC022632.65+615939.0	36.636051	2.22	61.994171	2.41
IRAC022636.95+615825.3	36.653969	0.89	61.973694	0.99
IRAC022625.84+620114.1	36.607647	1.97	62.020576	1.97
IRAC022634.77+615852.2	36.644855	1.29	61.981155	1.31
IRAC022635.97+615834.9	36.649887	2.12	61.976360	2.20
IRAC022640.17+615723.3	36.667385	0.66	61.956478	0.68
IRAC022639.77+615724.9	36.665695	0.66	61.956909	0.67
IRAC022629.06+620016.2	36.621078	1.39	62.004505	1.41
IRAC022644.17+615621.4	36.684036	2.38	61.939289	2.03
IRAC022629.62+620006.7	36.623421	1.56	62.001865	1.59
IRAC022632.04+615930.4	36.633484	2.83	61.991768	3.03
IRAC022632.64+615920.3	36.635986	2.35	61.988976	2.30
IRAC022615.82+620342.3	36.565907	7.35	62.061756	7.45
IRAC022633.13+615855.6	36.638035	0.72	61.982124	0.78
IRAC022624.53+620115.0	36.602200	1.52	62.020844	1.58
IRAC022630.72+615936.1	36.628014	1.18	61.993362	1.27
IRAC022638.28+615737.6	36.659508	1.02	61.960442	1.04
IRAC022629.92+615941.7	36.624687	5.48	61.994930	5.11
IRAC022623.39+620115.9	36.597473	6.28	62.021088	7.05

Table 3.4 (continued)

ID	RA_{J2000} [deg]	RA error 10^{-4}[deg]	DEC_{J2000} [deg]	DEC error 10^{-4}[deg]
IRAC022630.99+615916.2	36.629112	3.54	61.987827	3.28
IRAC022626.59+620012.6	36.610809	1.13	62.003498	1.18
IRAC022626.79+620008.7	36.611645	1.28	62.002426	1.33
IRAC022609.09+620445.1	36.537888	6.82	62.079201	6.46
IRAC022626.91+620003.6	36.612110	1.90	62.001007	1.94
IRAC022631.54+615850.8	36.631401	2.36	61.980770	2.51
IRAC022615.86+620237.9	36.566078	6.78	62.043861	7.65
IRAC022624.35+620029.8	36.601448	2.38	62.008282	2.30
IRAC022610.08+620353.9	36.542019	5.68	62.064960	5.79
IRAC022611.13+620331.9	36.546360	3.74	62.058861	3.73
IRAC022637.68+615639.2	36.657013	1.31	61.944225	1.32
IRAC022610.08+620350.2	36.542004	6.24	62.063934	6.58
IRAC022626.65+615932.3	36.611061	2.42	61.992313	2.47
IRAC022632.69+615757.0	36.636223	1.69	61.965843	1.87
IRAC022612.02+620316.1	36.550064	1.05	62.054482	1.06
IRAC022628.38+615902.5	36.618248	3.24	61.984032	3.05
IRAC022617.34+620138.5	36.572254	6.22	62.027363	6.84
IRAC022620.06+620105.7	36.583599	1.33	62.018246	1.38
IRAC022627.52+615909.7	36.614651	3.06	61.986019	3.06
IRAC022608.61+620403.3	36.535892	3.52	62.067593	3.62
IRAC022610.13+620336.6	36.542225	1.40	62.060158	1.39
IRAC022610.52+620330.3	36.543831	0.94	62.058414	0.96
IRAC022632.36+615745.8	36.634819	2.66	61.962730	2.49
IRAC022626.96+615907.9	36.612316	0.95	61.985519	0.96
IRAC022632.51+615737.6	36.635452	2.94	61.960445	2.77
IRAC022622.34+620013.7	36.593098	0.97	62.003815	1.05
IRAC022625.62+615920.8	36.606750	2.21	61.989124	2.41
IRAC022631.30+615747.8	36.630428	3.25	61.963284	3.16
IRAC022626.69+615855.4	36.611221	1.87	61.982067	2.02
IRAC022628.53+615818.7	36.618858	0.90	61.971859	0.89
IRAC022606.43+620407.8	36.526806	4.97	62.068821	4.84
IRAC022607.32+620343.3	36.530510	2.05	62.062019	2.11
IRAC022631.75+615730.6	36.632278	2.73	61.958488	2.91
IRAC022624.78+615914.1	36.603256	0.66	61.987259	0.68
IRAC022616.26+620128.4	36.567768	4.48	62.024544	4.87
IRAC022608.36+620324.5	36.534851	0.50	62.056801	0.51
IRAC022620.07+620017.7	36.583611	2.46	62.004925	2.40
IRAC022605.36+620405.2	36.522316	0.76	62.068115	0.78

Table 3.4 (continued)

ID	RA_{J2000} [deg]	RA error 10^{-4}[deg]	DEC_{J2000} [deg]	DEC error 10^{-4}[deg]
IRAC022606.71+620325.9	36.527969	3.31	62.057201	3.42
IRAC022621.66+615932.3	36.590260	1.66	61.992294	1.79
IRAC022625.00+615834.9	36.604187	0.79	61.976368	0.78
IRAC022607.28+620314.3	36.530346	5.05	62.053967	4.99
IRAC022607.83+620300.9	36.532642	0.61	62.050243	0.62
IRAC022613.14+620139.0	36.554729	4.11	62.027500	4.35
IRAC022620.34+615945.0	36.584766	1.00	61.995838	1.02
IRAC022626.24+615810.9	36.609352	1.26	61.969707	1.35
IRAC022605.16+620328.7	36.521511	3.63	62.057972	3.74
IRAC022627.96+615732.2	36.616486	1.15	61.958935	1.18
IRAC022617.92+620006.7	36.574650	2.00	62.001865	2.13
IRAC022603.64+620342.8	36.515186	6.42	62.061882	6.07
IRAC022620.88+615906.8	36.586994	2.30	61.985210	2.31
IRAC022616.14+620014.9	36.567265	1.59	62.004143	1.52
IRAC022614.10+620043.9	36.558743	2.35	62.012188	2.34
IRAC022602.73+620338.3	36.511391	5.38	62.060650	5.29
IRAC022607.20+620226.6	36.529999	7.25	62.040718	7.14
IRAC022615.44+620021.1	36.564346	1.99	62.005852	2.00
IRAC022603.32+620328.9	36.513847	4.63	62.058022	4.66
IRAC022605.00+620251.1	36.520821	0.50	62.047527	0.51
IRAC022601.58+620346.0	36.506577	1.89	62.062775	1.89
IRAC022627.60+615656.0	36.615009	2.26	61.948883	2.41
IRAC022606.88+620218.6	36.528656	5.35	62.038502	5.21
IRAC022619.71+615856.1	36.582123	1.08	61.982254	1.10
IRAC022624.46+615742.7	36.601933	1.70	61.961861	1.74
IRAC022607.20+620211.0	36.530014	5.89	62.036377	6.23
IRAC022602.22+620328.3	36.509258	7.22	62.057858	7.61
IRAC022602.51+620317.1	36.510445	1.62	62.054737	1.75
IRAC022617.02+615931.0	36.570900	2.28	61.991932	2.49
IRAC022617.17+615923.7	36.571560	0.84	61.989914	0.81
IRAC022617.71+615915.5	36.573807	0.67	61.987633	0.69
IRAC022622.46+615754.7	36.593582	1.46	61.965191	1.35
IRAC022601.75+620320.1	36.507286	3.63	62.055592	3.82
IRAC022604.24+620237.7	36.517670	5.61	62.043819	5.81
IRAC022606.72+620159.2	36.528019	3.75	62.033119	3.85
IRAC022600.51+620319.1	36.502117	9.31	62.055294	9.85
IRAC022600.99+620308.3	36.504139	1.70	62.052303	1.80
IRAC022601.21+620224.3	36.505024	0.41	62.040092	0.43

Table 3.4 (continued)

ID	RA_{J2000} [deg]	RA error 10^{-4}[deg]	DEC_{J2000} [deg]	DEC error 10^{-4}[deg]
IRAC022611.61+615955.1	36.548382	0.98	61.998638	1.00
IRAC022608.36+620043.4	36.534821	1.54	62.012062	1.61
IRAC022621.95+615706.8	36.591454	2.66	61.951885	2.60
IRAC022602.40+620159.6	36.510014	5.35	62.033211	6.10
IRAC022558.14+620302.5	36.492268	6.66	62.050694	6.61
IRAC022601.96+620204.0	36.508171	3.50	62.034431	3.84
IRAC022612.51+615918.7	36.552143	2.83	61.988541	2.72
IRAC022611.09+615938.2	36.546188	2.54	61.993958	2.45
IRAC022559.01+620159.9	36.495857	3.49	62.033318	3.51
IRAC022559.13+620236.6	36.496380	2.55	62.043491	2.55
IRAC022601.37+620202.3	36.505718	3.18	62.033978	2.88
IRAC022621.05+615624.3	36.587715	1.42	61.940090	1.63
IRAC022608.92+615932.2	36.537155	1.05	61.992275	1.17
IRAC022616.24+615735.3	36.567684	2.58	61.959797	2.57
IRAC022556.96+620237.0	36.487343	7.45	62.043606	8.23
IRAC022602.51+620103.5	36.510460	1.70	62.017639	1.66
IRAC022556.26+620218.7	36.484402	4.02	62.038525	4.37
IRAC022619.01+615625.0	36.579205	2.06	61.940285	1.95
IRAC022558.28+620143.6	36.492817	4.57	62.028790	4.61
IRAC022558.12+620138.0	36.492149	7.19	62.027218	7.72
IRAC022603.32+620013.1	36.513851	1.17	62.003643	1.24
IRAC022606.97+615912.2	36.529022	2.11	61.986710	2.31
IRAC022619.24+615551.2	36.580158	1.03	61.930901	0.97
IRAC022604.08+615939.9	36.517010	0.80	61.994427	0.87
IRAC022612.76+615709.6	36.553162	1.82	61.952656	1.73
IRAC022603.05+615912.0	36.512718	2.94	61.986671	3.02
IRAC022605.44+615824.6	36.522675	0.35	61.973492	0.41
IRAC022608.68+615737.9	36.536163	1.61	61.960537	1.55
IRAC022602.92+615856.5	36.512161	0.60	61.982368	0.60
IRAC022602.37+615830.8	36.509884	0.49	61.975220	0.52
IRAC022601.87+615834.8	36.507786	0.64	61.976341	0.65
IRAC022607.60+615649.1	36.531658	1.15	61.946983	1.16
IRAC022604.45+615734.8	36.518532	4.54	61.959667	5.16
IRAC022556.11+615935.9	36.483784	1.22	61.993294	1.17
IRAC022557.60+615852.8	36.490013	4.85	61.981339	5.00
IRAC022625.73+620355.8	36.607193	0.31	62.065487	0.32

Table 3.5. Cluster member candidates: IRAC sources with excess without X-ray counterpart.

ID	F_V [Jy]	F_I [Jy]	F_J [Jy]	F_H [Jy]	F_K [Jy]	$F_{3.6\mu m}$ [Jy]	$F_{4.5\mu m}$ [Jy]	$F_{5.8\mu m}$ [Jy]	$F_{8.0\mu m}$ [Jy]
IRAC022724.18+620148.4	....	....	0.000952	0.002873	0.003664	0.002667±0.000014	0.001876±0.000009	....	....
IRAC022712.69+620345.3	0.000012	0.000058	....	....	....	0.000420±0.000005	0.000308±0.000004	....	....
IRAC022710.52+620418.5	....	....	....	....	....	0.000529±0.000005	0.000373±0.000005	....	....
IRAC022725.20+615956.8	0.000019	0.000243	0.001350	0.001933	0.001888	0.001174±0.000008	0.000828±0.000005	....	....
IRAC022719.95+620118.7	....	....	....	....	....	0.000599±0.000006	0.000432±0.000005	....	....
IRAC022710.80+620300.6	....	....	....	....	....	0.000310±0.000004	0.000230±0.000003	....	....
IRAC022700.33+620529.1	....	....	....	....	....	0.001132±0.000006	0.002515±0.000012	0.003250±0.000028	....
IRAC022716.05+620050.6	0.001078	0.014579	0.208204	0.371792	0.619342	0.114789±0.000333	0.120949±0.000327	0.115460±0.000337	0.073205±0.000305
IRAC022708.82+620303.8	....	....	....	....	....	0.000608±0.000005	0.000430±0.000004	....	....
IRAC022711.47+620157.8	0.000014	0.000183	0.000909	0.001668	0.002249	0.003111±0.000011	0.003049±0.000011	0.002947±0.000023	....
IRAC022659.77+620454.2	....	....	....	....	....	0.000716±0.000006	0.000504±0.000006	....	0.002824±0.000084
IRAC022715.12+620015.2	0.004724	0.024085	0.065840	0.068913	0.060246	0.032174±0.000098	0.025178±0.000072	0.017016±0.000094	0.013649±0.000128
IRAC022700.50+620420.0	....	....	....	....	....	0.001856±0.000010	0.001419±0.000008	....	....
IRAC022704.83+620257.5	....	....	....	....	....	0.000471±0.000004	0.000351±0.000003	....	....
IRAC022709.85+620127.5	....	....	....	....	....	0.000377±0.000004	0.000265±0.000004	....	....
IRAC022706.08+620220.2	0.000008	0.000157	0.001255	0.002572	0.003019	0.001707±0.000007	0.001243±0.000006	....	....
IRAC022700.94+620333.5	....	....	....	....	....	0.000896±0.000007	0.000632±0.000005	....	....
IRAC022714.14+615923.6	....	....	0.001034	0.001881	0.002167	0.001302±0.000010	0.000918±0.000006	0.001541±0.000042	....
IRAC022700.06+620301.2	0.000008	0.000140	0.001165	0.001668	0.001977	0.001057±0.000007	0.000763±0.000005	....	....
IRAC022718.02+615816.0	....	....	....	....	....	0.000572±0.000006	0.000419±0.000004	....	....
IRAC022715.04+615848.2	....	....	....	....	....	0.000639±0.000007	0.000463±0.000004	....	....
IRAC022704.24+620102.0	....	....	....	....	....	0.000481±0.000004	0.000347±0.000004	....	....
IRAC022715.98+615748.3	....	....	....	....	....	0.000600±0.000008	0.000427±0.000005	....	....
IRAC022656.14+620244.1	....	....	0.001053	0.003150	0.004285	0.002955±0.000012	0.002084±0.000008	....	....
IRAC022658.71+620200.8	0.000073	0.000555	0.002719	0.003718	0.003404	0.001922±0.000007	0.001353±0.000006	....	....
IRAC022659.94+620142.2	0.000025	0.000231	0.001388	0.001969	0.001995	0.001046±0.000005	0.000762±0.000005	....	....
IRAC022711.75+615826.5	....	....	....	....	....	0.005841±0.000021	0.004946±0.000015	0.003618±0.000039	....
IRAC022709.91+615852.1	....	....	....	....	....	0.000923±0.000007	0.000753±0.000004	....	....
IRAC022643.97+620524.7	....	....	0.000563	0.001144	0.001406	0.000819±0.000005	0.000603±0.000005	....	....
IRAC022714.20+615727.8	0.000010	0.000068	....	....	....	0.000624±0.000009	0.000475±0.000005	....	....
IRAC022643.51+620530.2	....	....	....	....	....	0.000242±0.000004	0.000603±0.000005	....	....
IRAC022645.66+620446.9	....	....	....	....	....	0.002997±0.000010	0.003927±0.000014	0.005782±0.000031	0.009668±0.000082
IRAC022700.58+620056.7	....	....	0.000806	0.001747	0.001923	0.001179±0.000006	0.000869±0.000008	....	....
IRAC022640.42+620603.8	....	....	0.001522	0.004429	0.005495	0.003306±0.000015	0.002462±0.000015	....	....
IRAC022647.31+620416.2	....	....	....	....	....	0.000145±0.000004	0.000111±0.000004	0.001088±0.000025	0.002729±0.000071
IRAC022702.43+620009.2	....	....	....	....	....	0.001494±0.000008	0.001667±0.000008	....	....
IRAC022639.85+620535.6	....	....	....	....	....	0.000206±0.000004	0.000177±0.000004	0.001178±0.000032	0.004181±0.000090
IRAC022647.12+620351.1	....	....	0.000664	0.001427	0.001786	0.001072±0.000008	0.000790±0.000006	....	....
IRAC022649.26+620313.1	....	....	....	....	....	0.000734±0.000006	0.000721±0.000005	....	....
IRAC022641.13+620508.4	....	....	....	....	....	0.000188±0.000003	0.000139±0.000004	0.001285±0.000022	0.002855±0.000063
IRAC022652.58+620217.9	....	....	....	....	....	0.000326±0.000003	0.000268±0.000003	....	....
IRAC022654.87+620141.3	....	....	....	....	....	0.000521±0.000004	0.000385±0.000003	....	....
IRAC022711.66+615711.9	....	....	0.000722	0.002479	0.004168	0.004456±0.000030	0.004214±0.000014	0.004719±0.000063	0.007746±0.000092

Table 3.5 (continued)

ID	F_V [Jy]	F_I [Jy]	F_J [Jy]	F_H [Jy]	F_K [Jy]	$F_{3.6\mu m}$ [Jy]	$F_{4.5\mu m}$ [Jy]	$F_{5.8\mu m}$ [Jy]	$F_{8.0\mu m}$ [Jy]
IRAC022654.91+620130.7	....	....	....	....	....	0.000535±0.000003	0.000381±0.000003	....	....
IRAC022657.04+620058.7	0.000064	0.000660	....	....	....	0.000304±0.000003	0.001828±0.000008	....	....
IRAC022657.70+620043.0	....	....	0.000518	0.000987	0.001445	0.001345±0.000006	0.001357±0.000007	....	....
IRAC022639.60+620524.1	....	....	0.000969	0.001846	0.002108	0.001184±0.000006	0.000891±0.000006	....	....
IRAC022642.30+620441.2	0.000152	0.000583	0.001103	0.001133	0.001086	0.000357±0.000004	0.000287±0.000004	....	....
IRAC022636.48+620606.9	....	....	0.000412	0.001092	0.001368	0.000918±0.000006	0.000726±0.000010	....	....
IRAC022657.87+620028.3	....	....	....	....	....	0.001090±0.000006	0.001019±0.000006	....	....
IRAC022643.96+620405.4	....	....	0.000777	0.001144	0.001419	0.000159±0.000004	0.001584±0.000008	0.002019±0.000023	0.005041±0.000146
IRAC022701.90+615913.1	0.000007	0.000056	0.001494	0.004388	0.007046	0.000091±0.000003	0.000101±0.000002	0.000704±0.000021	0.010365±0.000067
IRAC022642.99+620410.0	....	....	0.000777	0.001144	0.001419	0.000175±0.000003	0.001584±0.000008	0.002019±0.000023	....
IRAC022700.71+615922.6	0.000006	0.000147	0.001494	0.004388	0.007046	0.012948±0.000036	0.012866±0.000032	0.011360±0.000052	0.010365±0.000067
IRAC022641.01+620436.4	....	....	....	....	....	0.000375±0.000004	0.000299±0.000005	....	....
IRAC022702.17+615858.3	....	....	....	....	....	0.000363±0.000004	0.000352±0.000003	....	....
IRAC022654.33+620058.4	....	....	....	....	....	0.000444±0.000003	0.000571±0.000004	....	....
IRAC022658.24+615956.6	....	....	....	....	....	0.000418±0.000004	0.000388±0.000004	....	....
IRAC022705.36+615800.2	....	....	....	....	....	0.000381±0.000004	0.000272±0.000002	....	....
IRAC022708.38+615702.4	....	....	0.001083	0.002324	0.003435	0.002966±0.000020	0.002569±0.000010	0.005485±0.000074	0.010799±0.000114
IRAC022654.30+620044.8	....	....	....	....	....	0.000290±0.000003	0.000259±0.000003	....	....
IRAC022653.98+620039.6	0.000007	0.000122	0.001053	0.002199	0.002754	0.002992±0.000009	0.002825±0.000010	0.002669±0.000019	....
IRAC022700.91+615847.8	....	....	....	....	....	0.001661±0.000007	0.001474±0.000005	0.001818±0.000026	0.002514±0.000043
IRAC022650.46+620132.4	....	....	....	....	....	0.000361±0.000003	0.000320±0.000003	....	....
IRAC022637.97+620437.8	....	....	....	....	....	0.000085±0.000002	0.000104±0.000003	0.001115±0.000017	0.003250±0.000056
IRAC022704.33+615736.3	....	....	....	....	....	0.000668±0.000005	0.000530±0.000003	....	....
IRAC022651.49+620058.7	....	....	....	....	....	0.000352±0.000003	0.000265±0.000003	....	....
IRAC022644.23+620246.4	0.000008	0.000096	0.000568	0.001043	0.001445	0.001528±0.000007	0.001505±0.000007	....	....
IRAC022700.54+615824.6	....	....	....	....	....	0.002559±0.000010	0.001920±0.000006	....	....
IRAC022647.98+620137.2	....	....	....	....	....	0.000417±0.000003	0.000306±0.000002	....	....
IRAC022656.82+615914.2	....	....	....	....	....	0.000315±0.000003	0.000339±0.000003	....	....
IRAC022641.80+620303.3	....	....	0.000606	0.001550	0.001722	0.001216±0.000006	0.000881±0.000005	....	....
IRAC022649.70+620058.8	....	....	....	....	....	0.000775±0.000004	0.000767±0.000004	....	....
IRAC022654.84+615937.9	....	....	....	....	....	0.000277±0.000003	0.000204±0.000003	....	....
IRAC022655.60+615914.3	....	....	....	....	....	0.000272±0.000003	0.000208±0.000003	....	....
IRAC022635.42+620430.6	0.000027	0.000289	0.000735	0.001015	0.000929	0.000399±0.000003	0.000298±0.000004	....	....
IRAC022657.82+615837.7	....	....	....	....	....	0.000260±0.000003	0.000204±0.000002	....	....
IRAC022641.97+620242.8	0.000033	0.000244	0.000960	0.001440	0.001355	0.000978±0.000005	0.000795±0.000005	....	....
IRAC022647.81+620112.3	0.000043	0.000242	0.000829	0.001388	0.001159	0.000661±0.000003	0.000569±0.000003	....	....
IRAC022629.52+620551.8	....	....	....	....	....	0.001554±0.000007	0.001222±0.000011	....	....
IRAC022634.65+620431.3	....	....	0.000892	0.002743	0.003435	0.002462±0.000008	0.001742±0.000008	0.001231±0.000017	....
IRAC022646.05+620122.1	....	....	0.000528	0.000900	0.001247	0.001613±0.000005	0.001795±0.000006	0.001834±0.000016	....
IRAC022648.00+620057.6	....	....	....	....	....	0.000255±0.000002	0.000281±0.000003	....	....
IRAC022702.53+615704.6	....	....	....	....	....	0.002400±0.000013	0.002621±0.000009	0.002985±0.000033	....
IRAC022647.66+620059.2	....	....	....	....	....	0.000299±0.000002	0.000281±0.000003	....	....
IRAC022655.60+615851.7	....	....	....	....	....	0.000713±0.000005	0.000765±0.000004	....	....

Table 3.5 (continued)

ID	F_V [Jy]	F_I [Jy]	F_J [Jy]	F_H [Jy]	F_K [Jy]	$F_{3.6\mu m}$ [Jy]	$F_{4.5\mu m}$ [Jy]	$F_{5.8\mu m}$ [Jy]	$F_{8.0\mu m}$ [Jy]
IRAC022644.41+620148.0	....	....	....	....	....	0.000539±0.000003	0.000513±0.000003	....	....
IRAC022648.08+620049.0	....	....	....	....	....	0.000385±0.000003	0.000387±0.000003	....	....
IRAC022641.94+620223.7	....	....	....	....	....	0.000251±0.000003	0.000180±0.000003	....	....
IRAC022655.75+615842.9	....	....	....	....	....	0.000277±0.000003	0.000211±0.000002	0.001618±0.000023	0.003614±0.000046
IRAC022645.15+620132.0	....	....	....	....	....	0.000295±0.000003	0.000300±0.000003	....	....
IRAC022657.11+615819.0	....	....	....	....	....	0.000827±0.000005	0.000629±0.000003	....	....
IRAC022646.75+620102.6	....	....	....	....	....	0.000321±0.000002	0.000297±0.000003	....	....
IRAC022629.86+620520.1	....	....	....	....	....	0.000435±0.000004	0.000335±0.000005	....	....
IRAC022653.24+615912.4	....	....	....	....	....	0.000559±0.000004	0.000571±0.000004	....	....
IRAC022656.57+615816.7	....	....	....	....	....	0.000626±0.000005	0.000730±0.000004	....	....
IRAC022643.34+620143.2	....	....	....	....	....	0.000458±0.000003	0.000479±0.000003	....	....
IRAC022645.54+620108.8	....	....	....	....	....	0.000246±0.000002	0.000177±0.000002	....	....
IRAC022659.22+615728.9	....	....	....	....	....	0.000382±0.000004	0.000377±0.000003	....	....
IRAC022632.51+620425.4	....	....	....	....	....	0.000226±0.000003	0.000159±0.000004	....	....
IRAC022630.45+620455.2	....	....	....	....	....	0.000583±0.000004	0.000650±0.000005	....	....
IRAC022651.39+615925.2	....	....	....	....	....	0.000416±0.000004	0.000369±0.000004	....	....
IRAC022644.72+620103.9	0.000008	0.000089	0.000770	0.001401	0.001432	0.000381±0.000003	0.000665±0.000004	....	....
IRAC022645.31+620054.4	....	....	....	....	....	0.000449±0.000003	0.000388±0.000003	....	....
IRAC022649.94+615942.3	0.000019	0.000185	0.000952	0.001715	0.002535	0.002645±0.000010	0.002673±0.000010	0.002589±0.000024	....
IRAC022630.66+620441.1	....	....	....	....	....	0.000132±0.000004	0.000548±0.000005	0.000878±0.000024	0.002949±0.000074
IRAC022648.56+615957.6	....	....	....	....	....	0.000419±0.000004	0.000448±0.000004	....	....
IRAC022650.62+615914.4	....	....	....	....	....	0.000373±0.000004	0.000447±0.000005	....	....
IRAC022645.73+620025.1	....	....	....	....	....	0.001667±0.000007	0.001759±0.000008	....	....
IRAC022629.62+620441.4	....	....	....	....	....	0.000695±0.000005	0.000548±0.000005	0.001006±0.000023	0.002612±0.000074
IRAC022647.71+615955.0	....	....	....	....	....	0.000429±0.000004	0.000424±0.000004	....	....
IRAC022655.63+615746.6	....	....	....	....	....	0.000689±0.000005	0.000507±0.000003	....	....
IRAC022632.41+620351.8	....	....	....	....	....	0.000282±0.000004	0.000228±0.000005	....	....
IRAC022653.43+615818.8	....	....	....	....	....	0.000435±0.000004	0.000434±0.000003	0.001563±0.000029	0.004729±0.000108
IRAC022629.93+620427.9	....	....	....	....	....	0.000343±0.000003	0.000254±0.000004	0.000884±0.000024	0.002612±0.000074
IRAC022639.51+620152.0	0.000114	0.000563	0.001988	0.002199	0.002167	0.001117±0.000006	0.000800±0.000005	....	....
IRAC022645.72+620013.1	....	....	0.000460	0.000951	0.001127	0.000910±0.000005	0.000832±0.000006	....	....
IRAC022628.83+620436.5	....	....	....	....	....	0.001388±0.000007	0.001249±0.000008	0.000884±0.000024	0.002835±0.000078
IRAC022641.07+620121.1	....	....	0.000419	0.000777	0.000832	0.000400±0.000003	0.000352±0.000003	....	....
IRAC022643.79+620038.9	....	....	....	....	....	0.000299±0.000003	0.000213±0.000003	....	....
IRAC022630.81+620350.2	....	....	....	....	....	0.000550±0.000004	0.000524±0.000006	....	....
IRAC022631.52+620333.1	....	....	....	....	....	0.000489±0.000004	0.000651±0.000007	0.001156±0.000023	0.003390±0.000075
IRAC022638.39+620145.9	0.000011	0.000096	0.000860	0.001579	0.001754	0.001940±0.000008	0.002008±0.000008	0.002184±0.000024	....
IRAC022640.99+620107.6	....	....	....	....	....	0.000269±0.000003	0.000231±0.000003	0.000520±0.000017	....
IRAC022644.33+620002.7	0.000005	0.000087	....	....	....	0.001749±0.000008	0.001763±0.000009	0.001858±0.000022	....
IRAC022647.10+615923.8	....	....	0.000490	0.000934	0.001057	0.001520±0.000007	0.001395±0.000008	....	....
IRAC022639.03+620129.8	....	....	....	....	....	0.000591±0.000004	0.000568±0.000004	....	....
IRAC022640.00+620054.5	0.000047	0.000399	0.001565	0.002693	0.002805	0.002090±0.000007	0.001664±0.000007	0.001441±0.000018	....
IRAC022631.31+620307.5	....	....	....	....	....	0.000338±0.000005	0.000273±0.000005	0.001854±0.000029	0.004608±0.000089

Table 3.5 (continued)

ID	F_V [Jy]	F_I [Jy]	F_J [Jy]	F_H [Jy]	F_K [Jy]	$F_{3.6\mu m}$ [Jy]	$F_{4.5\mu m}$ [Jy]	$F_{5.8\mu m}$ [Jy]	$F_{8.0\mu m}$ [Jy]
IRAC022623.64+620508.2	....	....	....	....	....	0.000913±0.000006	0.000682±0.000008	....	....
IRAC022626.25+620357.9	....	....	....	....	....	0.026954±0.000091	0.019980±0.000064	....	0.004061±0.000091
IRAC022625.16+620355.5	....	....	....	....	....	0.020979±0.000077	0.015059±0.000061	....	0.004061±0.000091
IRAC022651.24+615751.3	....	....	....	....	....	0.000551±0.000005	0.001013±0.000005	0.002206±0.000030	....
IRAC022655.82+615637.9	....	....	0.000987	0.002794	0.004017	0.003836±0.000022	0.003623±0.000015	0.003482±0.000046	....
IRAC022641.45+620024.5	0.000009	0.000136	0.000926	0.001325	0.001355	0.000813±0.000005	0.000580±0.000005	....	....
IRAC022652.10+615736.2	....	....	....	....	....	0.001068±0.000007	0.001195±0.000006	....	....
IRAC022630.59+620315.2	....	....	....	....	....	0.000246±0.000004	0.000273±0.000005	....	0.004608±0.000089
IRAC022650.19+615757.7	....	....	....	....	....	0.000767±0.000006	0.002447±0.000009	0.003625±0.000040	0.006352±0.000132
IRAC022643.40+615938.2	0.000010	0.000196	0.001123	0.002434	0.003280	0.002985±0.000013	0.002621±0.000012	0.002412±0.000027	....
IRAC022637.00+620112.9	0.009452	0.022539	0.032396	0.032382	0.023765	0.000190±0.000004	0.006928±0.000019	0.004863±0.000032	....
IRAC022640.67+620014.7	....	....	0.000523	0.000852	0.001137	0.000705±0.000005	0.000532±0.000005	....	....
IRAC022647.55+615819.2	....	....	....	....	....	0.002571±0.000012	0.002632±0.000010	0.002528±0.000035	....
IRAC022639.74+620010.9	....	....	....	....	....	0.002531±0.000010	0.003169±0.000012	0.003915±0.000029	0.004800±0.000064
IRAC022634.47+620134.2	0.000028	0.000195	0.000884	0.002006	0.002754	0.003161±0.000013	0.003140±0.000011	0.002524±0.000030	....
IRAC022636.26+620055.9	....	....	0.000917	0.001564	0.001541	0.001184±0.000007	0.001292±0.000006	0.001740±0.000025	....
IRAC022641.77+615940.2	....	....	....	....	....	0.001145±0.000007	0.001187±0.000008	....	....
IRAC022637.98+620036.4	....	....	....	....	....	0.000808±0.000005	0.000597±0.000005	....	....
IRAC022629.84+620244.1	....	....	....	....	....	0.001163±0.000008	0.001086±0.000008	....	....
IRAC022620.16+620510.6	....	....	....	....	....	0.000503±0.000005	0.000731±0.000010	....	....
IRAC022642.07+615924.3	....	....	....	....	....	0.000687±0.000006	0.000658±0.000006	....	....
IRAC022627.54+620310.8	....	....	....	....	....	0.000313±0.000004	0.000334±0.000005	....	....
IRAC022620.15+620510.6	....	....	....	....	....	0.000443±0.000005	0.000731±0.000010	....	....
IRAC022634.87+620110.7	....	....	....	....	....	0.000933±0.000006	0.001161±0.000006	....	....
IRAC022632.43+620148.0	....	....	0.000543	0.001033	0.000839	0.000480±0.000005	0.000345±0.000004	....	....
IRAC022639.11+620000.6	....	....	0.000715	0.001638	0.001853	0.001346±0.000007	0.001075±0.000007	....	....
IRAC022636.13+620046.8	....	....	....	....	....	0.000558±0.000005	0.000577±0.000005	....	....
IRAC022640.07+615945.3	....	....	....	....	....	0.000705±0.000006	0.000642±0.000006	....	....
IRAC022622.84+620413.0	....	....	....	....	....	0.000397±0.000004	0.001086±0.000008	0.000934±0.000028	....
IRAC022642.98+615853.5	....	....	....	....	....	0.001244±0.000009	0.000973±0.000009	....	....
IRAC022621.98+620421.9	....	....	....	....	....	0.000825±0.000006	0.001647±0.000010	0.003119±0.000035	0.004331±0.000089
IRAC022638.26+615958.7	....	....	....	....	....	0.000856±0.000006	0.000883±0.000007	....	....
IRAC022631.20+620147.1	0.000027	0.000211	0.001187	0.001813	0.001888	0.000899±0.000007	0.000631±0.000005	....	....
IRAC022635.46+620037.8	....	....	....	....	....	0.000560±0.000005	0.001389±0.000053	....	....
IRAC022641.76+615850.3	0.000325	0.003234	0.014945	0.020059	0.020320	0.011841±0.000041	0.009644±0.000033	0.006174±0.000053	0.005192±0.000095
IRAC022622.08+620408.2	....	....	....	....	....	0.000195±0.000004	0.001086±0.000008	0.001328±0.000027	....
IRAC022636.29+620022.8	....	....	....	....	....	0.000266±0.000004	0.000213±0.000004	....	....
IRAC022617.95+620459.5	....	....	0.000468	0.002769	0.009035	0.023810±0.000069	0.027579±0.000098	0.030078±0.000118	0.039970±0.000274
IRAC022632.38+620114.4	....	....	....	....	....	0.000442±0.000005	0.000584±0.000004	....	....
IRAC022638.67+615940.6	....	....	....	....	....	0.000589±0.000005	0.000525±0.000005	....	....
IRAC022644.79+615756.3	....	....	....	....	....	0.000706±0.000006	0.000589±0.000005	....	....
IRAC022637.49+615953.8	....	....	0.000523	0.000943	0.000964	0.000536±0.000005	0.000384±0.000005	....	....
IRAC022648.92+615654.1	....	....	....	....	....	0.000818±0.000007	0.000824±0.000006	....	....

Table 3.5 (continued)

ID	F_V [Jy]	F_I [Jy]	F_J [Jy]	F_H [Jy]	F_K [Jy]	$F_{3.6\mu m}$ [Jy]	$F_{4.5\mu m}$ [Jy]	$F_{5.8\mu m}$ [Jy]	$F_{8.0\mu m}$ [Jy]
IRAC022635.09+620028.6	....	....	....	....	....	0.000605±0.000005	0.001389±0.000053	....	....
IRAC022620.53+620357.3	....	....	....	....	....	0.004967±0.000017	0.010543±0.000034	0.011164±0.000056	0.007509±0.000131
IRAC022622.21+620348.1	....	....	....	....	....	0.001298±0.000007	0.001678±0.000010	0.001920±0.000031	....
IRAC022629.07+620200.0	0.000010	0.000122	0.000860	0.001301	0.001419	0.000797±0.000007	0.000568±0.000006	....	....
IRAC022620.64+620406.8	....	....	....	....	....	0.002262±0.000009	0.002298±0.000012	0.003817±0.000034	0.005321±0.000086
IRAC022621.56+620352.2	....	....	....	....	....	0.001821±0.000009	0.002290±0.000013	0.001770±0.000029	0.006187±0.000095
IRAC022629.23+620148.1	0.002286	0.007240	0.014272	0.015933	0.018362	0.028972±0.000081	0.033073±0.000085	0.040205±0.000131	0.070256±0.000231
IRAC022638.87+615921.2	0.000008	0.000192	0.000868	0.001325	0.001202	0.001500±0.000009	0.001185±0.000008	....	....
IRAC022620.02+620338.8	....	....	0.002390	0.027689	0.072432	0.078688±0.000184	0.061294±0.000158	0.056389±0.000158	0.030710±0.000190
IRAC022643.67+615756.7	....	....	....	....	....	0.002585±0.000013	0.002699±0.000010	....	....
IRAC022640.23+615844.6	....	....	0.000490	0.000892	0.000895	0.000508±0.000006	0.000379±0.000006	....	....
IRAC022644.51+615736.7	....	....	....	....	....	0.000583±0.000006	0.000594±0.000004	....	0.002152±0.000060
IRAC022642.88+615756.8	....	....	....	....	....	0.000896±0.000008	0.000965±0.000006	....	....
IRAC022630.81+620102.5	....	....	....	....	....	0.000662±0.000006	0.000629±0.000005	....	....
IRAC022636.48+615932.4	....	....	....	....	....	0.000431±0.000004	0.000395±0.000005	....	....
IRAC022639.25+615847.6	....	....	....	....	....	0.000419±0.000005	0.000297±0.000005	....	....
IRAC022631.11+620055.3	....	....	....	....	....	0.000516±0.000005	0.000430±0.000004	....	....
IRAC022627.79+620139.5	0.000008	0.000078	0.000523	0.000852	0.000982	0.000945±0.000007	0.001041±0.000007	....	....
IRAC022635.82+615931.8	....	....	0.001144	0.002199	0.002208	0.001088±0.000007	0.000804±0.000006	....	....
IRAC022637.93+615859.9	....	....	0.000460	0.000749	0.000752	0.000436±0.000005	0.000313±0.000005	....	....
IRAC022632.07+620029.5	....	....	....	....	....	0.000596±0.000004	0.000440±0.000004	....	....
IRAC022633.51+620006.1	....	....	....	....	....	0.000527±0.000004	0.000447±0.000005	....	....
IRAC022647.16+615628.1	....	....	....	....	....	0.001091±0.000011	0.000947±0.000007	....	....
IRAC022624.60+620220.6	....	....	0.000460	0.000892	0.000929	0.001158±0.000009	0.001294±0.000009	....	....
IRAC022640.94+615755.7	0.000006	0.000081	0.000579	0.001123	0.001355	0.001235±0.000008	0.001303±0.000007	....	....
IRAC022643.27+615718.0	....	....	0.000495	0.001231	0.002208	0.002479±0.000012	0.002431±0.000009	....	0.003209±0.000058
IRAC022641.86+615737.4	....	....	....	....	....	0.000714±0.000007	0.000887±0.000005	0.001054±0.000033	....
IRAC022630.40+620033.8	....	....	0.000595	0.001015	0.001180	0.000654±0.000005	0.000472±0.000004	....	....
IRAC022635.32+615916.2	0.000010	0.000127	0.000518	0.000960	0.000982	0.000957±0.000007	0.000859±0.000007	....	....
IRAC022636.34+615900.2	....	....	....	....	....	0.000400±0.000005	0.000393±0.000005	....	....
IRAC022617.68+620353.3	....	....	....	....	....	0.000281±0.000004	0.000241±0.000005	0.001762±0.000032	....
IRAC022643.74+615702.0	....	....	....	....	....	0.000758±0.000006	0.000818±0.000005	....	....
IRAC022613.12+620454.8	....	....	....	....	....	0.000571±0.000007	0.000469±0.000013	....	....
IRAC022630.89+620012.3	....	....	....	....	....	0.000431±0.000004	0.000439±0.000004	....	....
IRAC022632.65+615939.0	....	....	....	....	....	0.000369±0.000007	0.000393±0.000005	0.001129±0.000023	....
IRAC022636.45+615842.2	....	....	....	....	....	0.000614±0.000006	0.000552±0.000006	....	....
IRAC022628.24+620046.1	....	....	0.000909	0.001401	0.001472	0.001033±0.000007	0.000870±0.000005	....	....
IRAC022632.65+615939.0	....	....	....	....	....	0.000379±0.000004	0.000393±0.000005	0.001129±0.000023	....
IRAC022636.95+615825.3	0.000024	0.000262	0.000821	0.001550	0.001690	0.002410±0.000012	0.003138±0.000012	0.004261±0.000040	0.005804±0.000069
IRAC022625.84+620114.1	0.000049	0.000112	....	....	....	0.000672±0.000006	0.000628±0.000005	....	....
IRAC022634.77+615852.2	0.000032	0.000295	0.001006	0.001731	0.001803	0.001415±0.000009	0.001227±0.000007	....	....
IRAC022635.97+615834.9	....	....	....	....	....	0.000606±0.000006	0.000508±0.000005	....	....
IRAC022640.17+615723.3	0.000009	0.000246	....	....	....	0.005970±0.000023	0.006735±0.000019	0.006176±0.000050	0.008625±0.000067

Table 3.5 (continued)

ID	F_V [Jy]	F_I [Jy]	F_J [Jy]	F_H [Jy]	F_K [Jy]	$F_{3.6\mu m}$ [Jy]	$F_{4.5\mu m}$ [Jy]	$F_{5.8\mu m}$ [Jy]	$F_{8.0\mu m}$ [Jy]
IRAC022639.77+615724.9	....	....	....	....	....	0.006163±0.000023	0.006350±0.000018	0.006176±0.000050	0.007904±0.000124
IRAC022629.06+620016.2	....	....	....	....	....	0.000821±0.000005	0.000913±0.000005	....	....
IRAC022644.17+615621.4	....	....	....	....	....	0.001037±0.000010	0.000740±0.000005	....	....
IRAC022629.62+620006.7	....	....	....	....	....	0.000560±0.000004	0.000480±0.000004	....	....
IRAC022632.04+615930.4	....	....	....	....	....	0.000316±0.000004	0.000268±0.000004	....	....
IRAC022632.64+615920.3	....	....	....	....	....	0.000401±0.000004	0.000288±0.000004	....	....
IRAC022615.82+620342.3	....	....	....	....	....	0.000123±0.000004	0.000163±0.000005	0.001169±0.000032	....
IRAC022633.13+615855.6	....	....	0.000784	0.001699	0.002376	0.003290±0.000014	0.003058±0.000012	0.003270±0.000038	0.003650±0.000075
IRAC022624.53+620115.0	....	....	....	....	....	0.000842±0.000006	0.000818±0.000005	....	0.002256±0.000058
IRAC022630.72+615936.1	....	....	....	....	....	0.000859±0.000005	0.000860±0.000006	....	....
IRAC022638.28+615737.6	....	....	....	....	....	0.001798±0.000009	0.001954±0.000007	....	....
IRAC022629.92+615941.7	....	....	....	....	....	0.000117±0.000003	0.000860±0.000006	....	....
IRAC022623.39+620115.9	....	....	....	....	....	0.000153±0.000004	0.000818±0.000005	....	0.002256±0.000058
IRAC022630.99+615916.2	....	....	....	....	....	0.000283±0.000004	0.000291±0.000004	....	....
IRAC022626.59+620012.6	....	....	0.000447	0.000821	0.000973	0.000727±0.000004	0.000679±0.000004	....	0.003194±0.000093
IRAC022626.79+620008.7	....	....	....	....	....	0.000658±0.000004	0.000676±0.000004	....	0.003194±0.000093
IRAC022609.09+620445.1	0.006250	0.012863	0.016846	0.015076	0.011064	0.000195±0.000005	0.000197±0.000008	0.001324±0.000040	....
IRAC022626.91+620003.6	....	....	....	....	....	0.000368±0.000003	0.000288±0.000003	....	0.003194±0.000093
IRAC022631.54+615850.8	....	....	....	....	....	0.000447±0.000005	0.000391±0.000004	....	....
IRAC022615.86+620237.9	0.000288	0.000881	0.001669	0.001684	0.001294	0.000153±0.000005	0.000410±0.000005	0.001517±0.000033	0.004556±0.000102
IRAC022624.35+620029.8	....	....	....	....	....	0.000372±0.000004	0.000332±0.000003	0.000637±0.000019	....
IRAC022610.08+620353.9	....	....	....	....	....	0.000166±0.000004	0.000162±0.000005	0.001090±0.000033	0.003853±0.000096
IRAC022611.13+620331.9	....	....	....	....	....	0.000236±0.000004	0.001713±0.000009	0.002375±0.000041	0.004423±0.000101
IRAC022637.68+615639.2	....	....	....	....	....	0.000985±0.000006	0.001166±0.000005	....	....
IRAC022610.08+620350.2	....	....	....	....	....	0.000148±0.000004	0.000266±0.000005	0.001090±0.000033	0.003853±0.000096
IRAC022626.65+615932.3	....	....	....	....	....	0.000250±0.000003	0.000185±0.000003	....	....
IRAC022632.69+615757.0	....	....	....	....	....	0.000546±0.000004	0.000578±0.000004	....	....
IRAC022612.02+620316.1	0.000006	0.000098	0.000579	0.001350	0.001318	0.001277±0.000006	0.001070±0.000007	0.001698±0.000030	0.003929±0.000106
IRAC022628.38+615902.5	....	....	....	....	....	0.000254±0.000004	0.000243±0.000004	....	....
IRAC022617.34+620138.5	....	....	....	....	....	0.000160±0.000004	0.000161±0.000004	0.001391±0.000033	0.002783±0.000080
IRAC022620.06+620105.7	0.000030	0.000273	0.001278	0.001731	0.001722	0.000953±0.000006	0.000690±0.000004	....	....
IRAC022627.52+615909.7	....	....	....	....	....	0.000240±0.000003	0.001173±0.000006	....	....
IRAC022608.61+620403.3	....	....	....	....	....	0.000262±0.000004	0.000232±0.000005	0.001090±0.000033	0.003853±0.000096
IRAC022610.13+620336.6	....	....	....	....	....	0.000780±0.000005	0.000766±0.000006	0.002375±0.000041	0.004423±0.000101
IRAC022610.52+620330.3	....	....	....	....	....	0.001552±0.000007	0.001713±0.000009	0.002375±0.000041	0.004423±0.000101
IRAC022632.36+615745.8	....	....	....	....	....	0.000349±0.000004	0.000295±0.000003	....	....
IRAC022626.96+615907.9	....	....	....	....	....	0.001215±0.000006	0.001173±0.000006	....	....
IRAC022632.51+615737.6	....	....	....	....	....	0.000324±0.000004	0.000239±0.000003	....	....
IRAC022622.34+620013.7	0.000014	0.000193	0.000934	0.001623	0.001629	0.001040±0.000005	0.000889±0.000004	....	....
IRAC022625.62+615920.8	....	....	....	....	....	0.000290±0.000003	0.000217±0.000003	....	0.002443±0.000051
IRAC022631.30+615747.8	0.000007	0.000137	....	....	....	0.000286±0.000004	0.000440±0.000004	....	....
IRAC022626.69+615855.4	....	....	....	....	....	0.000412±0.000004	0.000292±0.000003	....	....
IRAC022628.53+615818.7	....	....	0.000742	0.001401	0.001722	0.001688±0.000008	0.001527±0.000007	....	0.001779±0.000051

Table 3.5 (continued)

ID	F_V [Jy]	F_I [Jy]	F_J [Jy]	F_H [Jy]	F_K [Jy]	$F_{3.6\mu m}$ [Jy]	$F_{4.5\mu m}$ [Jy]	$F_{5.8\mu m}$ [Jy]	$F_{8.0\mu m}$ [Jy]
IRAC022606.43+620407.8	0.000029	0.000187	....	....	....	0.000190±0.000004	0.000232±0.000005	0.001041±0.000035	....
IRAC022607.32+620343.3	....	....	....	....	....	0.000469±0.000004	0.000505±0.000005	0.001375±0.000032	0.003037±0.000088
IRAC022631.75+615730.6	....	....	....	....	....	0.000289±0.000004	0.000244±0.000003	....	....
IRAC022624.78+615914.1	0.000013	0.000212	0.000934	0.001898	0.002128	0.002306±0.000008	0.002446±0.000009	0.002733±0.000023	0.007584±0.000124
IRAC022616.26+620128.4	....	....	....	....	....	0.000227±0.000004	0.000177±0.000004	0.001391±0.000033	0.002783±0.000080
IRAC022608.36+620324.5	....	....	....	....	....	0.004063±0.000012	0.007125±0.000022	0.010245±0.000049	0.011420±0.000110
IRAC022620.07+620017.7	0.000007	0.000054	....	....	....	0.000303±0.000003	0.000224±0.000002	....	....
IRAC022605.36+620405.2	....	....	....	....	....	0.002114±0.000009	0.002298±0.000012	0.002920±0.000038	....
IRAC022606.71+620325.9	....	....	....	....	....	0.000235±0.000003	0.000190±0.000004	0.001520±0.000030	0.006707±0.000169
IRAC022621.66+615932.3	0.000006	0.000090	....	....	....	0.000341±0.000003	0.000344±0.000003	....	....
IRAC022625.00+615834.9	....	....	0.001669	0.002981	0.003467	0.002260±0.000009	0.001638±0.000007	....	....
IRAC022607.28+620314.3	....	....	....	....	....	0.000160±0.000003	0.000151±0.000004	0.001353±0.000029	....
IRAC022607.83+620300.9	....	....	....	....	....	0.002255±0.000008	0.001754±0.000009	0.001482±0.000025	....
IRAC022613.14+620139.0	0.000008	0.000039	....	....	....	0.000191±0.000003	0.000182±0.000004	0.001083±0.000023	....
IRAC022620.34+615945.0	....	....	0.000447	0.000868	0.001057	0.000760±0.000004	0.000701±0.000004	0.000991±0.000014	....
IRAC022626.24+615810.9	....	....	0.000573	0.001043	0.001236	0.000738±0.000005	0.000519±0.000004	....	0.001779±0.000051
IRAC022605.16+620328.7	....	....	....	....	....	0.000242±0.000004	0.000316±0.000009	0.001526±0.000033	0.004667±0.000106
IRAC022627.96+615732.2	....	....	....	....	....	0.000977±0.000005	0.000976±0.000005	....	....
IRAC022617.92+620006.7	....	....	....	....	....	0.000346±0.000003	0.000351±0.000003	....	0.001623±0.000039
IRAC022603.64+620342.8	....	....	....	....	....	0.000176±0.000004	0.000183±0.000005	0.001257±0.000035	0.007435±0.000199
IRAC022620.88+615906.8	....	....	....	....	....	0.000269±0.000003	0.000239±0.000003	....	0.001817±0.000045
IRAC022616.14+620014.9	....	....	0.000419	0.000884	0.000773	0.000564±0.000004	0.000408±0.000003	....	0.001623±0.000039
IRAC022614.10+620043.9	....	....	....	....	....	0.000425±0.000004	0.000460±0.000004	....	0.004328±0.000126
IRAC022602.73+620338.3	0.000005	0.000034	....	....	....	0.000208±0.000005	0.000183±0.000005	0.001257±0.000035	0.007435±0.000199
IRAC022607.20+620226.6	....	....	....	....	....	0.000120±0.000003	0.000143±0.000005	0.000877±0.000030	0.011440±0.000198
IRAC022615.44+620021.1	....	....	....	....	....	0.000378±0.000003	0.000421±0.000003	....	....
IRAC022603.32+620328.9	0.000005	0.000034	0.002480	0.002596	0.002070	0.000216±0.000004	0.000445±0.000006	0.001141±0.000031	....
IRAC022605.00+620251.1	....	....	0.000431	0.001813	0.003564	0.003330±0.000010	0.002800±0.000012	0.002040±0.000029	....
IRAC022601.58+620346.0	....	....	....	....	....	0.000764±0.000006	0.000627±0.000008	0.001204±0.000040	....
IRAC022627.60+615656.0	....	....	....	....	....	0.000375±0.000004	0.000271±0.000003	....	....
IRAC022606.88+620218.6	....	....	....	....	....	0.000174±0.000004	0.000143±0.000005	0.000877±0.000030	0.009040±0.000209
IRAC022619.71+615856.1	....	....	....	....	....	0.000759±0.000004	0.000815±0.000005	....	0.001817±0.000045
IRAC022624.46+615742.7	....	....	0.000464	0.000844	0.000847	0.000539±0.000004	0.000380±0.000004	....	....
IRAC022607.20+620211.0	....	....	....	....	....	0.000151±0.000004	0.000143±0.000005	0.001511±0.000029	0.009040±0.000209
IRAC022602.22+620328.3	0.000005	0.000034	....	....	....	0.000144±0.000004	0.000240±0.000006	....	0.007435±0.000199
IRAC022602.51+620317.1	....	....	....	....	....	0.000807±0.000006	0.001117±0.000008	....	....
IRAC022617.02+615931.0	....	....	....	....	....	0.000249±0.000003	0.000183±0.000003	....	....
IRAC022617.17+615923.7	....	....	....	....	....	0.001096±0.000005	0.001280±0.000006	0.001324±0.000016	....
IRAC022617.71+615915.5	0.000014	0.000172	0.000860	0.001508	0.001585	0.001551±0.000006	0.001480±0.000006	0.001726±0.000016	....
IRAC022622.46+615754.7	....	....	....	....	....	0.000865±0.000006	0.000780±0.000006	....	....
IRAC022601.75+620320.1	....	....	....	....	....	0.000328±0.000005	0.000240±0.000006	....	....
IRAC022604.24+620237.7	0.000602	0.001625	0.002550	0.002693	0.002013	0.000118±0.000003	0.000474±0.000005	....	....
IRAC022606.72+620159.2	0.000005	0.000020	....	....	....	0.000248±0.000004	0.000214±0.000005	....	....

Table 3.5 (continued)

ID	F_V [Jy]	F_I [Jy]	F_J [Jy]	F_H [Jy]	F_K [Jy]	$F_{3.6\mu m}$ [Jy]	$F_{4.5\mu m}$ [Jy]	$F_{5.8\mu m}$ [Jy]	$F_{8.0\mu m}$ [Jy]
IRAC022600.51+620319.1	....	....	....	....	....	0.000129±0.000005	0.000240±0.000006	0.001558±0.000045	0.007666±0.000174
IRAC022600.99+620308.3	....	....	....	....	....	0.000850±0.000006	0.000899±0.000008	0.001558±0.000045	....
IRAC022601.21+620224.3	....	....	....	....	....	0.009033±0.000026	0.012747±0.000041	0.010656±0.000049	0.009523±0.000103
IRAC022611.61+615955.1	....	....	....	....	....	0.001203±0.000006	0.001277±0.000006	0.001192±0.000023	....
IRAC022608.36+620043.4	0.000012	0.000139	0.000844	0.001198	0.001282	0.000802±0.000006	0.000566±0.000005	....	....
IRAC022621.95+615706.8	....	....	....	....	....	0.000374±0.000004	0.000326±0.000004	....	....
IRAC022602.40+620159.6	....	....	....	....	....	0.000211±0.000005	0.000357±0.000007	0.001295±0.000041	....
IRAC022558.14+620302.5	....	....	....	....	....	0.000229±0.000007	0.000633±0.000009	0.002117±0.000045	0.010897±0.000305
IRAC022601.96+620204.0	....	....	....	....	....	0.000314±0.000005	0.000357±0.000007	0.001295±0.000041	....
IRAC022612.51+615918.7	....	....	....	....	....	0.000238±0.000003	0.000244±0.000004	....	....
IRAC022611.09+615938.2	....	....	....	....	....	0.000302±0.000003	0.000244±0.000003	....	0.001866±0.000049
IRAC022559.01+620159.9	....	....	....	....	....	0.000494±0.000007	0.000388±0.000008	....	0.011371±0.000275
IRAC022559.13+620236.6	....	....	....	....	....	0.000421±0.000005	0.003831±0.000019	....	....
IRAC022601.37+620202.3	....	....	....	....	....	0.000467±0.000006	0.000357±0.000007	0.001295±0.000041	....
IRAC022621.05+615624.3	0.000007	0.000121	....	....	....	0.000910±0.000007	0.000639±0.000004	....	....
IRAC022608.92+615932.2	....	....	....	....	....	0.001035±0.000006	0.000905±0.000005	....	0.001964±0.000053
IRAC022616.24+615735.3	....	....	....	....	....	0.000400±0.000005	0.000292±0.000005	....	....
IRAC022556.96+620237.0	0.000016	0.000088	....	....	....	0.000149±0.000005	0.000267±0.000007	0.001927±0.000050	0.005401±0.000162
IRAC022602.51+620103.5	0.000059	0.000357	0.001388	0.001653	0.001527	0.000921±0.000007	0.000652±0.000006	....	....
IRAC022556.26+620218.7	....	....	....	....	....	0.000282±0.000005	0.000209±0.000006	....	....
IRAC022619.01+615625.0	....	....	....	....	....	0.000568±0.000005	0.000586±0.000004	....	....
IRAC022558.28+620143.6	....	....	....	....	....	0.000286±0.000005	0.000267±0.000006	....	....
IRAC022558.12+620138.0	....	....	....	....	....	0.000158±0.000005	0.000313±0.000005	0.002552±0.000040	....
IRAC022603.32+620013.1	....	....	0.000623	0.001508	0.001472	0.001229±0.000007	0.001050±0.000006	....	....
IRAC022606.97+615912.2	....	....	....	....	....	0.000368±0.000004	0.000321±0.000004	....	....
IRAC022619.24+615551.2	0.000011	0.000159	0.000876	0.001715	0.002089	0.002035±0.000010	0.001824±0.000008	....	....
IRAC022604.08+615939.9	....	....	0.001609	0.002899	0.003133	0.002217±0.000010	0.001587±0.000007	....	....
IRAC022612.76+615709.6	0.000006	0.000095	0.000664	0.000996	0.000982	0.000723±0.000006	0.000509±0.000005	....	....
IRAC022603.05+615912.0	....	....	....	....	....	0.000277±0.000004	0.000203±0.000003	....	....
IRAC022605.44+615824.6	0.000050	0.000721	0.004770	0.010527	0.013929	0.015054±0.000040	0.014773±0.000041	0.014168±0.000058	0.014172±0.000100
IRAC022608.68+615737.9	0.000014	0.000140	0.000901	0.001266	0.001419	0.000880±0.000007	0.000619±0.000006	....	....
IRAC022602.92+615856.5	0.000018	0.000258	0.001579	0.003179	0.003944	0.003765±0.000013	0.003644±0.000013	0.002798±0.000028	....
IRAC022602.37+615830.8	0.000016	0.000180	0.001103	0.002926	0.003872	0.005139±0.000016	0.004995±0.000017	0.004921±0.000034	0.004606±0.000068
IRAC022601.87+615834.8	0.000016	0.000205	0.001220	0.002820	0.003162	0.003049±0.000011	0.003109±0.000012	0.003222±0.000028	0.004606±0.000068
IRAC022607.60+615649.1	....	....	0.000435	0.000756	0.001037	0.001488±0.000008	0.001477±0.000008	....	....
IRAC022604.45+615734.8	0.000018	0.000148	0.000777	0.000908	0.000904	0.000256±0.000005	0.000229±0.000004	....	....
IRAC022556.11+615935.9	0.000008	0.000169	0.001113	0.001780	0.001959	0.001166±0.000007	0.000858±0.000005	....	....
IRAC022557.60+615852.8	0.000402	0.001738	0.003652	0.003857	0.003019	0.000181±0.000004	0.000947±0.000006	....	....
IRAC022625.73+620355.8	....	....	0.056818	0.485624	1.354972	1.536729±0.003608	2.204545±0.005332	2.234834±0.005060	1.363905±0.003450

Table 3.6. Disc fraction of solar type stars.

Cluster	disc fraction	Age [Myr]	Reference
NGC 2362	19%±5%	5±1	Dahm & Hillenbrand (2007)
Tr 37	47%±1%	4±1	Sicilia-Aguilar et al. (2006)
σ Ori	35%±1%[a]	3±1	Hernández et al. (2007)
Upper Sco	19%±5%	5±0.5	Carpenter et al. (2006)
NGC 2068/71	70.%±1%	2±0.5	Flaherty & Muzerolle (2008)
Taurus	62%±5%	1.5±0.5	Hartmann et al. (2005)
Cha I	58%±5%	2±0.5	Luhman et al. (2008)

4

Long-wavelength observations of debris discs around sun-like stars

Based on the paper: 'Long-wavelength observations of debris discs around sun-like stars' - Roccatagliata, V., Henning Th., Wolf S., Rodman J., Corder S., Carpenter J. M., Meyer M. R. & Dowell D. 2009 , A&A 497, 409

4.1 Introduction

The late stages of a disc, the so called "debris disc phase", is characterised by a remnant of material after the dispersion of gas and dust in the disc. Different studies have been carried out so far to understand the dissipation mechanism in debris discs using the decrease of the disc flux as a function of time.
Spangler et al. (2001) measured the fractional luminosity ($L_{\rm IR}/L_{\rm star}$) of pre- and main sequence stars with ISO. They found that the fractional luminosity, which is proportional to the dust present in the disc, decreases with time as $t^{-1.76}$. While the analysis of Spangler et al. (2001) included

also pre-main sequence stars, Habing et al. (2001) analysed the ISO and IRAS data of nearby main-sequence stars alone: they concluded that most of the stars reach the main-sequence surrounded by a disc which decays in about 400 Myr. Decin et al. (2003) reviewed the different studies on the time dependency of Vega-like systems done with ISO/IRAS. They concluded that the observations only indicated a large spread in fractional luminosity for stars at most ages, that the maximum excess was independent of time and that the debris disc phenomenon was more common in younger stars. An analysis of the near to far infrared excess, carried out with Spitzer, led to the finding of a general decrease of the fractional luminosity with time as t^{-1}, starting later at longer wavelengths (Su et al., 2006). This suggested a disc clearing more efficiently in the inner parts (Su et al., 2006). Deviations from these trends have been associated with a recent or still ongoing collisional cascade that produces a small dust grain population which is rapidly removed by radiation pressure or by the action of the Poynting-Robertson drag (Song et al., 2005; Wyatt et al., 2007b).
A complementary picture of the evolution of the outer part of the debris discs is provided by (sub)millimetre observations. These show a decline in the dust mass as a function of age and significant evolution of the circumstellar dust mass within the first 10 Myr and between 10 Myr and a few Gyr (e.g. Liu et al., 2004; Carpenter et al., 2005, hereafter C05).
In this chapter I present the results of two deep sub-millimetre and millimetre surveys of circumstellar discs around solar-type stars with ages between 3 Myr and 3 Gyr. The characteristics of our sample are presented in section 4.3.1. The observations carried out at 350 μm and at 1.2 mm are reported in section 4.2 The discussion of the dust disc mass evolution as a function of the age of the systems, compared with the history of our solar system, is presented in section 4.3. A detailed analysis of the debris disc properties by modelling their spectral energy distribution (SED) is provided in section 4.4 and finally the summary is presented in section 4.5.

4.2 Observations

4.2.1 Sample

Nearby sources (d<150 pc) were selected from *The Formation and Evolution of Planetary Systems (FEPS) Spitzer* Legacy Program (Meyer et al., 2006). The FEPS sample contains 314 stars with stellar masses between $\sim$0.5 and 2 $M_{\odot}$, ages spanning the range from 3 Myr to 3 Gyr and spectral types between K7 and F5. In addition, 14 objects were initially included in the FEPS sample because of an infrared excess previously detected with IRAS/ISO. Since these sources can introduce a bias in the FEPS sample with respect to the presence of a disc, they are not taken into account in any statistical analysis in this paper.
The characteristics of the entire star sample have been extensively analysed by the FEPS team (e.g. Meyer et al., 2006; Mamajek & Hillenbrand, 2008). The stellar ages are based on pre-main sequence tracks for stars younger than 10 Myr, X-ray activity and the strength of the CaII H and K emission for nearby solar-type stars ($\leq$50 pc), and the association of stars with clusters or star-forming regions of known age. A new calibration presented in Mamajek & Hillenbrand (2008) has been applied. Final ages will be presented by Hillenbrand et al. (2009), (see also Mamajek & Hillenbrand, 2008). The distances of the sources were determined by the FEPS team on the basis of Hipparcos parallaxes for nearby stars and kinematic distances for stars associated with young moving groups and associations.
Our total sample contains 141 sources of which:
- 16 targets were observed at 350 μm with the CSO (*Caltech Submillimetre Observatory*) 10-m telescope (see col. 6 Table 4.1)
- 40 targets were observed at 1.2 mm with the IRAM (*Institut de Radioastronomie Millimétrique*) 30-m telescope (see col. 7 Table 4.1)
- 121 targets are taken from the SEST (*Swedish-ESO Submillimetre Telescope*) and OVRO (*Owens Valley Radio Observatory*) surveys performed by Carpenter et al. (2005), of which 17 have been re-observed during our surveys.
The sample includes 15 sources younger than 10 Myr, 16 intermediate-age systems (10-20 Myr) and 110 evolved systems (> 20 Myr). In section 4.3 we only consider the evolved systems in order to search for a correlation between the mass of the debris disc and the age of the system. In particular, 104 out of the 110 evolved systems are analysed excluding the

sources not compatible with the FEPS sample selection (see above). The 104 sources analysed here include 45% of the FEPS sample older than 20 Myr and in particular: 35% of the systems with no infrared excess (until 70 μm) and 89% with excess.

4.2.2 CSO observations at 350 μm

Observations of the sources listed in Table 4.1 were carried out at the CSO between 17 and 21 April 2005, using the Submillimetre High Angular Resolution Camera II (SHARC-II) with the 350 μm filter. The full width at half maximum (FWHM) for the 10.4 m telescope beam profile is 8.5″ at this wavelength. The median zenith opacity at 225 GHz was 0.04. The typical on-source integration times varied from 40 minutes to 2 hours depending on source elevation and zenith opacity, although a deeper 3.5 hour integration was obtained for HD 107146 Corder et al. (2009). Pointing and instrumental flux calibrators were selected from the CSO SHARC-II list of calibrators. Data imaging and reduction were carried out using the Comprehensive Reduction Utility for SHARC-II. The errors associated with each detection are the quadratic sum of the instrumental error (between 5.3 and 45 mJy) and the calibration errors (between 12% and 22% of the flux). Instrumental errors are computed based on the rms computed in a sky annulus, and propagated over the photometric aperture. Calibration errors were determined based on repeatability of the flux calibrators over the entire observing run.

4.2.3 IRAM observations at 1.2 mm

Millimetre continuum observations of 40 sources at 1.2 mm were carried out between May and December 2005 (*Projects num. 013-05, 141-05*) and between January and April 2008 (*Project num. 185-07*) at the IRAM 30-m telescope at Pico Veleta with MAMBO2, the 117 channel IRAM bolometer. The FWHM of the 30-m telescope beam is 11″ at 1.2 mm. The median zenith opacity at 230 GHz was 0.5 during the first run between May and November 2005, and 0.3 during the second run carried out in December 2005 and during the last run in 2008. Pointing and calibrator sources were selected from a standard list provided by IRAM. The observations were carried out in *on-off integration mode* using a standard calibration. An rms of 0.7 mJy was obtained in one hour (blocks of three times 20 minutes) of on-off integration. The weather conditions were sta-

ble during most of the nights and the calibrators were observed within a few hours from the science targets. The data were reduced with the data reduction package MOPSIC (R. Zylka 2006).
Observations of the same target at different dates were coadded to increase the signal to noise. The uncertainties associated with each flux are the quadratic sum of the statistical error and the calibration error. The statistical error is the rms of the flux over the entire telescope field of view, while the calibrator error is based on the agreement between the predicted calibrator fluxes and those measured over 48 hours before and after the observations. I obtained statistical errors between 0.8 and 2.8 mJy and calibration errors between 11% and 16% in flux. The final uncertainties are dominated by the statistical error in the IRAM observations.

4.2.4 Detections and upper limits

The fluxes (in the case of detections) and the 3σ upper limits (in the case of non-detections) measured at 350 μm and 1.2 mm are listed in Table 4.1. The detection errors and the upper limits include only the statistical error. The calibration uncertainty is reported in the note to Table 4.1. The 3σ upper limits were computed as 3 times the statistical error described above. 31 sources have been observed with IRAM, 7 sources only with CSO and 9 sources with both telescopes. We detected 11 sources in total: 5 sources with IRAM, 8 with the CSO. Two of the sources were detected with both IRAM and CSO. Five of them are primordial discs younger than 10 Myr, and six are debris discs. All sources were unresolved with the exception of HD 107146 which had a deconvolved size at 350 μm of $8\farcs9 \times 8\farcs2$ with an uncertainty of about $0\farcs6$ per axis (Corder et al., 2009).

4.3 Disc dust mass

The main goal of this project is to analyse the temporal evolution of circumstellar debris discs and the mechanism of their dissipation around solar-type stars.
The dust mass in debris discs is expected to decrease with time. Depending on which process (collisions or Poynting-Robertson drag) is the main driver of dust removal, I expect a different power-law dependence of

the dust mass as a function of the age of the system (Dominik & Decin, 2003).
In this analysis I include the dust masses computed from the *millimetre* observations of nearby solar-type stars obtained with IRAM presented here and with SEST and OVRO (from C05).
The disc is assumed to be isothermal and optically thin ($\tau << 1$) at millimetre wavelengths. The dust disc mass can then be derived from the millimetre flux, using the following equation:

$$M_{\rm dust} = \frac{S_\nu D^2}{k_\nu B_\nu(T_{\rm dust})} \tag{4.1}$$

where $k_\nu = k_0(\nu/\nu_0)^\beta$ is the mass absorption coefficient, β parametrises the frequency dependence of k_ν and S_ν is the observed flux. D is the distance to the source, $T_{\rm dust}$ is the dust temperature and $B_\nu(T_{\rm dust})$ is the Planck function. In order to be consistent with C05, I compute the dust masses assuming β=1, k_0=2cm^2g^{-1} at 1.3 mm (Beckwith et al., 1990) and $T_{\rm dust}$=40 K. The uncertainty in the dust mass is computed using error propagation. In the following, I discuss the principal systematic errors which are present in the final dust mass uncertainty.

The mass absorption coefficient is poorly constrained. I consider as limit the commonly used value for debris discs of k_0=1.7cm^2g^{-1} at 800 μm adopted by Zuckerman & Becklin (1993), which corresponds to k_0=1.0cm^2g^{-1} at 1.3 mm. The mass absorption coefficient alone introduces at least a factor 2 in the final uncertainty associated to the mass. In order to be consistent with the previous analysis of C05, we adopted a temperature of 40 K. This represents a compromise between the temperature associated with cold dust in protoplanetary discs ($T\sim$20-30 K, e.g. Beckwith et al., 1990) and warm dust in debris discs ($T\sim$40-100 K Zuckerman & Song, 2004).
Since the mass is proportional to $T_{\rm dust}^{-1}$, the temperature alone introduces a factor of 2 in the uncertainty of the masses.
Another source of uncertainty in the final mass error is introduced by the source's distance. Nevertheless, the parallax of most of the sources older than 20 Myr (which will be in the following analysed), has been measured by *Hipparcos*, and the distance uncertainty is directly computed from the parallax uncertainty. This contributes an uncertainty of at least $\sim$10% of the dust masses.

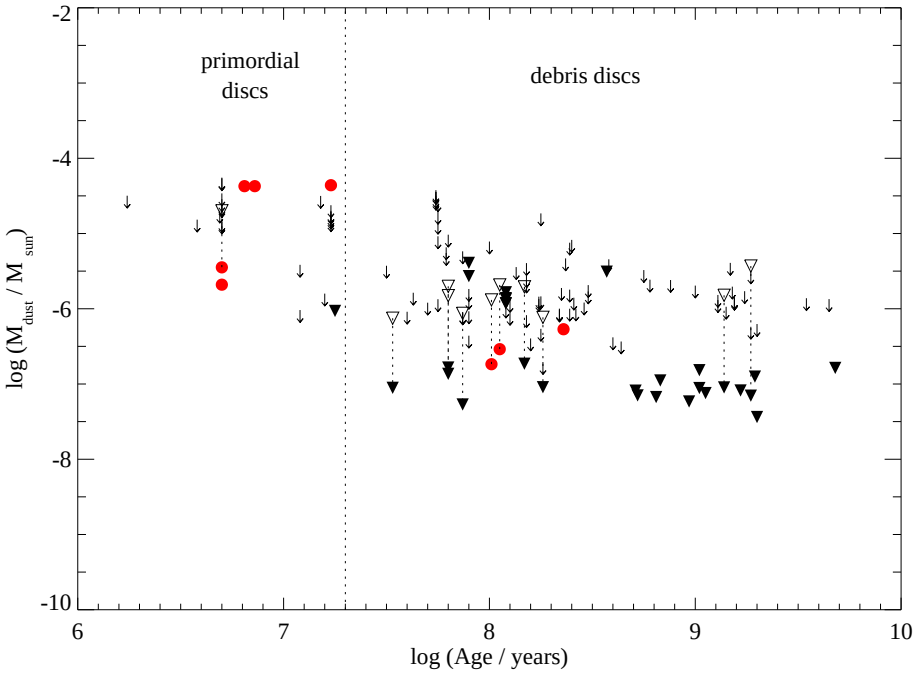

Figure 4.1 Disc mass versus age of the system. Filled circles are the masses determined from the IRAM detections (this work) and from the detections presented by C05. Upper limits are shown as filled triangles (new IRAM observations), empty and filled triangles (objects measured by C05 and re-observed here with higher sensitivity) and down arrows (from C05). The sources observed in both studies are connected by dashed lines. The vertical line separates the sources younger than 20 Myr and evolved systems older than 20 Myr.

The 3σ upper limits to the dust mass have been computed when the sources were not detected with a signal to noise ratio of at least three. The mass of the newly observed sources younger than 20 Myr is also plotted as reference [1]. Taking into account the uncertainty on distance, temperature, measured flux and mass absorption coefficient, the final uncertainty is $\sim$55% of the dust mass.

[1]Note however, that the assumption of optically thin emission at millimetre wavelength cannot be generalised to all primordial discs

4.3.1 Evolution of the dust mass

Mass detections and upper limits are presented in Fig. 4.1 as a function of age. In total, I plotted 132 upper limits and 9 detections computed from the millimetre measurements. 17 sources have been observed in both surveys, C05 and with IRAM (connected by a dotted line in Fig. 4.1). Due to the higher sensitivity of the IRAM bolometer compared to SEST and OVRO, I detected 4 discs with dust masses down to $5 \times 10^{-7} M_{\odot}$, about one order of magnitude smaller than those in C05.
Primordial discs are shown in Fig 4.1 only as comparison with systems older than 20 Myr but they are not taken into account in any statistical analysis in this paper.
The other variable which can strongly affect our analysis is the age determination of the discs older than 20 Myr. Their ages derived using different techniques are summarised in Table 4.2. The final ages are computed as the average and the standard deviation is adopted as uncertainty (Table 4.2). A more detailed discussion of the ages of the whole FEPS sample will be presented by Hillenbrand et al. (2009), see also Mamajek & Hillenbrand (2008).
In the following subsection I present the statistical analysis aimed at constraining the physical characteristics of the dust in circumstellar discs at ages older than 20 Myr, in order to understand the timescale and the dissipation mechanism in debris discs.
Method: statistical analysis
A quantitative analysis of the dust mass-age relation was performed for systems older than ∼20 Myr. I carried out a *survival analysis* (Feigelson & Nelson, 1985) in order to include the information contained in the dust mass upper limits derived from the millimetre non-detections. I use the program ASURV Rev. 1.2 (Lavalley et al., 1992), which implements the survival analysis methods presented in Feigelson & Nelson (1985) and Isobe et al. (1986).
The *generalised Kendall's tau correlation* (Brown et al., 1974) was used to measure the degree of correlation between age and disc mass among debris discs. Such a method includes the analysis of both detections and upper limits. The probability that the disc mass is correlated with the age is 76%.
To determine whether there is a different dust mass distribution in debris disc systems older than 20 Myr, I used *two-sample tests*. I applied three different tests: the Gehan, logrank, and Peto-Prentice tests (e.g.

Feigelson & Nelson, 1985). In order to investigate the evolution of the debris dust I divided the sample of objects older than 20 Myr in two sub-samples with almost the same number of objects: the first with ages between 20 and ∼180 Myr, and the second sub-sample with ages between ∼180 Myr and 5 Gyr.
The three *two-sample tests* give a probability between 70 and 83% that younger and older debris systems belong to different parent populations in terms of dust mass. The relatively low significance of our results comes from the low number of detected sources, compared to the upper limits, and the narrow range in age of the detected debris discs. This leads to a high probability to assign a detected disc to a different sub-sample in age. I could not perform any conclusive linear regression to the data points since the detected objects span a very narrow range in age and masses, and in general there are too many upper limits compared to detections.

4.3.2 Discussion

The detection limit of our survey does not allow us to draw any firm conclusion about the evolution of the debris dust around solar-like stars as a function of age. Even more sensitive millimetre observations are needed to find statistically reliable trends. Our sample is biased toward sources with infrared excess. However, with the current sensitivity limit, additional observations of sources without infrared excess, which have a lower probability to be detected in the millimetre, would only increase the number of upper limits. This would not change the result of our statistical analysis.
I recall that all the mass derivations are valid only if the mass absorption coefficient k, which is inversely proportional to the mass of the dust in the disc, remains constant with time.
While in the protoplanetary disc phase I would expect a strong change of the mass absorption coefficient with time, in the debris disc phase we expect an equilibrium phase which is characterised by an almost constant second generation of dust. The assumption of a roughly time-independent dust opacity seems to be reasonable as long as I consider discs in the debris phase.

4.4 SED analysis of debris discs detected at 350 μm and/or 1.2 mm

The debris discs detected by our surveys offer the opportunity to characterise and compare the disc properties around solar type stars. This is the case for the following objects: HD 104860, HD 8907, HD 377, HD 107146, HD 61005 and HD 191089.
I compiled the spectral energy distributions from the infrared data available in the literature and our new detections at sub-millimetre and/or millimetre wavelengths. Synthetic photometric points at 13 and 33 μm, derived from the IRS spectrum (Hillenbrand et al., 2008), were also included in the SEDs. These data points allow us to distinguish the infrared excess of the debris disc from the stellar photosphere, determined by a Kurucz model. The IRS spectrum is overplotted in Figures 4.2-4.7, but was not considered during the SED modelling.
To further characterise the debris discs detected during our survey, we compute:
- the β index from their SED to derive the dust grain size present in the disc,
- the collisional and Poynting-Robertson drag timescales
- the blowout grain size ($a_{\rm blow}$)
- best fit model parameters by modelling the SED.

β Index - In the millimetre wavelength range, where $h\nu/KT << 1$, the Planck function can be approximated with the Rayleigh-Jeans relation ($B_\nu \sim 2k\nu^2Tc^{-2}$). The disc is assumed to be optically thin with the optical depth $\tau_\nu(r) = k_\nu \sum(r) < 1$. Under these conditions $F_\nu \sim k_\nu \nu^2 \frac{4\pi k}{D^2} \int_{R_{\rm in}}^{R_{\rm out}} \Sigma(r)T(r)rdr$. At wavelengths $\lambda > 0.1mm$ the mass absorption coefficient k_ν is $k_\nu \propto \nu^\beta$, where β is the dust opacity index. Since the slope of the SED in the millimetre wavelength range is proportional to ν^α, the measure of the spectral index α enables us to directly constrain the β index via the relation $\beta = \alpha - 2$ and to derive the index β. The index β is 2 for interstellar medium grain sizes, between 0 and 2 for pebbles of the order of $1mm$ in size, and 0 for even larger grains (e.g. Beckwith et al., 2000). The slope α of the SED in the sub-millimetre/millimetre wavelength range is derived, using a linear regression that gives the errors in slope of the best-fit. The values for the β index of the power law of the dust absorption coefficient are always < 1 (see Table 4.3), which suggests the presence of dust with at least mil-

limetre size particles (e.g. Henning & Stognienko, 1996; Rodmann et al., 2006).

Blowout grain size - Small grains are affected by the interaction with the stellar radiation field. This causes a force acting on the particles which is parametrised by the ratio of the radiation force to the stellar gravity. I compute the blowout grain size ($a_{\rm blow}$) in the debris disc systems using the equations presented in Hillenbrand et al. (2008), based on Burns et al. (1979) and Backman & Paresce (1993):

$$a_{\rm blow} = 0.52\mu m \frac{2.7 g/cm^3}{\rho} \frac{1+p}{1.1} \frac{L_\star/L_\odot}{(M_\star/M_\odot)(T_\star/5780)} \tag{4.2}$$

where, ρ is the grain density, p the grain albedo (0.1 for silicate grains) and a the grain radius. Sub-micron sized particles are therefore blown out from the disc near a Sun-like star.

Poynting-Robertson and collisional timescales Defining $\eta_0 = t_{\rm PR}/t_{\rm coll}$ (Wyatt et al., 1999; Wyatt, 2005), where $t_{\rm PR}$ and $t_{\rm coll}$ are the Poynting-Robertson drag ($t_{\rm PR}$) and collisional timescales respectively, it is possible to distinguish between discs in collisionale regime ($\eta_0 \gg 1$) and Poynting-Robertson drag regime ($\eta_0 \ll 1$). When $\eta_0 \gg 1$ the disc is dense and the collisions occur faster than the P-R drag: the dynamically bound dust remains at the same radial location as the planetesimals, while unbound grains are blown out and their surface density distribution falls off as r^{-1} (where r is the distance from the star).
The Poynting-Robertson drag ($t_{\rm PR}$) and collisional timescales ($t_{\rm coll}$) of the debris discs are computed, using the equations presented in Hillenbrand et al. (2008), based on Burns et al. (1979) and Backman & Paresce (1993):

$$t_{\rm PR} = 720 yr \frac{(\rho/g/cm^3)(a/\mu m)(r/AU)^2}{(L_\star/L_\odot)(1+p)} \tag{4.3}$$

where, ρ is the grain density, p the grain albedo (again 0.1 for silicate grains) and a the grain radius. I assume silicate grains of 10 μm in size and a grain density of 2.7 g/cm^3 at the inner radius of the disc (computed by our model, see Table 4.4).
Under the assumption of circular orbits and completely destructive collisions between grains of the same size, the collisional timescale is computed using the equation:

$$t_{\rm coll} = \Big(\frac{r}{AU}\Big)^{1.5} \frac{1}{9\sigma(r)\sqrt{M_\star/M_\odot}} yr \tag{4.4}$$

where $\sigma(r)$ is the face-on fractional surface density: for a constant surface density, $\sigma(r) = 2f/ln(R_{\rm OUT}/R_{\rm in})$, with $R_{\rm in}$ the inner disc boundary, $R_{\rm OUT}$ the outer disc radius and $f = L_{dust}/L_\odot$ (e.g. Backman, 2004).
The collisional timescale has been computed for grains of 10 μm in size at the inner radius of the disc (computed by our model, see Table 4.4). According to Wyatt (2005), the ratio $t_{\rm coll}/t_{\rm PR}$ is proportional to $1/\sqrt{a}$, where a is the grain size. These values are summarised in Table 4.3.
SED modelling - The SEDs were modelled using the radiative transfer model of Wolf & Hillenbrand (2003).
The model assumes that the dust grains are compact spherical particles heated only by the direct stellar radiation. The interaction between stellar radiation and dust particles can be described by the following radiative processes: scattering (neglecting multiple scattering), absorption and re-emission of stellar radiation by dust grains. The disc is then checked to be optically thin to the stellar radiation and to the dust re-emission at all wavelengths. The contribution to the SED from a single dust grain results from the integration of the scattering and re-emission processes over all wavelengths. Finally the emergent spectrum is the sum of all the dust grain contributions.
The model parameters are the radiation emitted by the central star, the total disc mass, the disc size, the radial density distribution, the minimum and maximum grain size in the disc, the grain size distribution, and the chemical composition of the grains. The radial density distribution is described by a power-law, $n(r) \propto r^{-q}$ where $q = 1$ corresponds to a disc with a constant surface density $\Sigma(r) \propto r^0$.

The grain size distribution is also described by a power-law $n(a) \propto a^{-p}$ where the canonical value $p = 3.5$ characterises a size distribution initially produced by a collisional cascade. I always use this grain size distribution in our models. For each grain size a temperature distribution over the disc size is computed.
The model parameter space has been extensively analysed by Wolf & Hillenbrand (2003). They found that the increase of the inner radius $R_{\rm in}$ causes a loss of the warm dust that is mainly responsible for the near-infrared (NIR)/ mid-infrared (MIR) shape of the SED; the excess emission over the stellar photosphere starts at longer wavelengths. This

is more pronounced when the minimum grain size a_{min} increases, because the main contribution to the NIR/MIR spectrum at high temperatures comes from small grains. The presence of an inner gap causes the loss of warm dust which is mainly responsible for the NIR/MIR shape of the SED. Increasing the size of the gap, the MIR flux decreases and the excess is shifted to longer wavelengths. Keeping the disc mass constant, the flux in the millimetre region increases slightly, but the net flux is smaller compared to a disc without an inner gap. This is because the fraction of the stellar flux absorbed by a single dust grain decreases with increasing radial distance from the star.

I assumed *astronomical silicate* grains (optical data from Draine & Lee, 1984; Weingartner & Draine, 2001)) since they are expected to be the main component of the dust in protoplanetary discs (Pollack et al., 1994). Since the outer radius cannot be constrained from the SED alone, it was assumed to be 150 AU, consistent with the location of the most distant object of the Kuiper belt in our Solar System (e.g. Gladman et al., 2002). The choice of such a value is supported by a recent resolved millimetre map of one of the debris discs analysed (Corder et al., 2009), where the millimetre emission is extended up to 150 AU from the central star. The maximum grains size is assumed to be 3 mm, since the β index measurements suggested the presence of at least millimetre-sized particles in the discs; this is the grain size which strongly contributes to the millimetre emission that I detect. The Levenberg-Marquardt method was applied to find the best-fit parameters of the model leaving the *inner radius (R_{in}), minimum grain size (a_{min}) and dust mass (M_{dust})* as free parameters.

The reduced χ^2, associated with each best-fit model, was computed for each fit normalising the standard statistic χ^2 to the number of free parameters of the fit (Bevington, 1969). These parameter uncertainties are estimated from the covariance matrix (inverse of the χ^2 curvature function) by the Levenberg-Marquardt algorithm. The modelling results are listed in Table 4.4.

The degeneracy of the SED models was checked using the σ-confidence regions delineated by lines of constant $\Delta\chi^2$. The model parameter space (R_{in}xM_{dust}xa_{min}) was explored around the best fit values. The 2-dimensional confidence regions in Figs. 4.2-4.7 are the projections of the 3-dimensional isosurfaces defined by fixed $\Delta\chi^2$ (Press et al., 1992). The shape of the confidence regions confirm an intrinsic degeneracy of our model probably between inner radius, minimum grain size and dust mass.

4.4.1 HD 104860

HD 104860 is an F8 star at a distance of 47 pc from the Sun. It was classified as a γ Doradus variable candidate by Handler (1999). Wichmann et al. (2003) identified the object as a young zero age main sequence star using LiI in absorption (Wichmann et al., 2003). In Table 4.2 I summarise the ages derived from different methods (L. Hillenbrand, private communication). The average age is ∼140 Myr, the value that we adopted in our analysis.

The SED of HD 104860 is presented in Fig. 4.2. It includes the Spitzer/IRAC and Spitzer/MIPS photometry from 3.6 to 160 μm, synthetic photometry at 13 and 33 μm obtained from the IRS low resolution spectrum (Hillenbrand et al., 2008), our CSO and IRAM detections at 350 μm and 1.2 mm, SCUBA detections at 450 and 850 μm (Najita & Williams, 2005), and an OVRO 3.1 mm upper limit (Carpenter et al., 2005). The infrared-excess emission detected by Spitzer suggests the presence of debris material around this main sequence star (Carpenter et al., 2009).

Early modelling of the spectral energy distribution of HD 104860 was presented by (Najita & Williams, 2005). Treating dust grains as simple blackbody radiators, their sub-millimetre observations at 450 and 850 μm indicate a dust temperature of $T_{\rm dust}$=33 K and a mass of the disc of 0.16 $M_\oplus$. Our new detection allows us to sample the SED at longer wavelengths and hence constrain the slope of the far-infrared to millimetre excess. The best-fit model parameters are reported in Table 4.4 and the computed best-fit model is plotted in Fig. 4.2. The confidence regions of the fit (see lower plots in Fig. 4.2) show some degree of degeneracy of the model. The dust mass is constrained between 0.07 $M_\oplus$ and 0.15 $M_\oplus$, while the inner radius is located between 10 and 50 AU and the minimum grain size is between 5 and 15 μm. The dust mass computed by the model (see Table 4.4) is of the same order of magnitude as the masses computed using a simple black-body model (Najita & Williams, 2005) and Eq. 4.1. The minimum grain size obtained is one order of magnitude higher than the blowout grain size of the system. The confidence regions delineated by constant $\Delta\chi^2$ contours suggest that a minimum grain size of the same order of magnitude of the blowout size is a poor fit to the data.

4.4.2 HD 8907

HD 8907 is a F8 star, located at 34 pc from the Sun, which has already reached the main sequence. In our analysis I adopt an age of the system of 680 Myr, which is the average of the ages derived from different methods (Table 4.2, L. Hillenbrand, private communication).
The SED of HD 8907 is presented in Fig. 4.3. The ISO photometry at 60 and 90 μm are from Silverstone (2000), the SCUBA detections at 450 and 850 μm from Najita & Williams (2005), IRAM detection at 1.2 mm from this work and the OVRO 2.6 and 3.1 mm upper limits from C05. The IRAS detections (Helou & Walker, 1988); empty squares in Fig. 4.3), are systematically larger than the Spitzer photometry, due to the bigger beam and they were not taken into account during the model fitting. The infrared excess detected by ISO (Zuckerman & Song, 2004) suggested the presence of debris dust. Under the assumption that the dust particles radiate as a black body, a temperature of $\sim$ 60 K was inferred for particles orbiting at $\sim$30 AU from the central star (Zuckerman & Song, 2004). The SED infrared excess has also been detected by Spitzer between 3.6 and 70 μm by Kim et al. (2005), and they found an inner radius of $\sim$48 AU with a temperature of $\sim$ 48 K.
Our new detection allows us to sample the SED at longer wavelengths and hence constrain the slope of the far-infrared to millimetre excess. The best-fit model parameters are reported in Table 4.4 and the computed best-fit model is plotted in Fig. 4.3. The confidence regions of the fit which show some degree of degeneracy of the model (see lower plots in Fig. 4.3): the dust mass is constrained between 0.03 $M_\oplus$ and 0.1 $M_\oplus$, while the inner radius is located between 15 and 30 AU and the minimum grain size is between 5 and 10 μm.
As in the case of HD 104860, the dust mass computed by the model of HD 8907 (see Table 4.4) is comparable to the value computed using Eq. 4.1. The minimum grain size is between 4 and 8 μm. This is one order of magnitude higher than the blowout grain size of the system and is consistent with previous modelling (Kim et al., 2005). The inner radius computed by our model is poorly constrained since it has an uncertainty of 50%.

4.4.3 HD 377

HD 377 is a G2V star at a distance of 40 pc which has already reached the main sequence. It is surrounded by a debris disc with a high fractional luminosity ($L_{\rm IR}/L_{\rm star}$), 4.0×10^{-4} (Moór et al., 2006). The ages of HD 377 derived from different methods (L. Hillenbrand, private communication) are summarised in Table 4.2. The average age is ∼110 Myr, the value that we adopted in our analysis.
Pascucci et al. (2006) investigated the presence of gas in the disc of HD 377, but they did not detect any gas emission lines in the infrared nor in the millimetre wavelength range.
The SED was compiled from the literature including our new detection at 1.2 mm (Fig. 4.4). The OVRO 2.6 and 3.1 mm upper limits are from C05. The best-fit model parameters are reported in Table 4.4 and the computed best-fit model is plotted in Fig. 4.4. The confidence regions of the fit (see lower plots in Fig. 4.4) show a high degree of degeneracy of the model compared to the other debris discs modelled. This results from the poor constraints on the SED in the sub-millimetre region.
As for HD 104860 and HD 8907, the dust mass computed by the model (see Table 4.4) is comparable to the value computed using Eq. 4.1. The inner radius is the smallest in our sample, but the disc seems to lack small dust grains with sizes up to 14 μm. The minimum grain size obtained is one order of magnitude higher than the blowout grain size of the system.

4.4.4 HD 107146

HD 107146 is a G2 V star located 28.5 pc from the Sun. The star is a candidate periodic V-band photometric variable (Koen & Eyer, 2002). From the average between the ages derived with different methods (Table 4.2), I obtain an age of ∼230 Myr. HD 107146 is also the first debris disc around a solar-type star resolved in scattered light by the Hubble Space Telescope (Ardila et al., 2004). They resolved a ring-like disc with most of the material concentrated between 86 and 130 AU, using a coronograph of 1.8″in radius. The disc was also marginally resolved at 450 and 850 μm and the observations suggested the presence of an inner hole with a radius larger than 31 AU (Williams et al., 2004). Such an inner hole would also explain the lack of an IRAS 25 μm excess and a far-infrared excess at 60 and 100 μm (Silverstone, 2000). C05 presented OVRO 3 mm images of this source. HD 107146 has also been resolved

during our survey at 350 μm with CSO and at 1.3 mm with CARMA (Corder et al., 2009). The millimetre image shows a clumpy disc extended between ∼60 AU and ∼150 AU with a symmetric peak of the emission at ∼97 AU from the central star.
The SED was compiled from the literature, including our new detection at 350 μm (Fig. 4.5) and the CARMA detection at 1.3 mm Corder et al. (2009). HD 107146 is the only disc detected at 3.1 mm. The IRAS detections (Helou & Walker, 1988, empty squares in Fig. 4.5);, are systematically higher than the Spitzer photometry, due to the bigger beam and they were not taken into account during the model fitting. The best-fit model parameters are reported in Table 4.4 and the computed best-fit model is plotted in Fig. 4.5. The degree of degeneracy of the model is shown in the confidence regions of the fit (see lower plots in Fig. 4.5). The dust mass is constrained between 0.08 $M_\oplus$ and 0.15 $M_\oplus$, while the inner radius is located between 7 and 15 AU and the minimum grain size is between 8 and 15 μm. It is interesting to notice that the inner radius computed by our model, is more than 7 times smaller than the inner radius of the ring-like disc in the HST images. This is because different grain populations are traced by our model and the HST image: while the HST traces only the distribution of the sub-micron size population (below $a_{\rm blow}$), our model includes the re-emission from grains from micron to millimetre in size. This explanation is also supported by the resolved images in the sub-millimetre wavelength range of HD 107146 which suggest the presence of grains at radii smaller compared to the ring-like structure seen in the HST image.

4.4.5 HD 61005

HD 61005 is a G3/G5V star with a Hipparcos distance of 35±1 pc, located in the local bubble, a region that is thought to be almost completely free of diffuse dust clouds (Franco et al., 1990). From an average of the chromospheric activity available from the literature, and a new calibration of the chromospheric activity-age relation (FEPS, private communication), I adopt an age of 135 Myr. The SED was previously modelled by Hines et al. (2007): under the assumption that dust particles of ∼10 μm radiate as a black body with a temperature of ∼50-70 K, they obtained a minimum distance for the circumstellar material of ∼7 AU. This star was also monitored during a radial velocity survey looking for planets around active stars, but no planets were detected

(Setiawan et al., 2008). HST/NICMOS observations (Hines et al., 2007) reveal dust-scattered starlight extending to distances of ∼240 AU from the occulted star. The structure is strongly asymmetric about its major axis, but is mirror-symmetric about its minor axis; morphologically, the object resembles a wing-spread moth with the star as the head.
HST scattered light images reveal a swept shape of the disc with an inner radius ≤10 AU and an outer radius up to 240 AU (Hines et al., 2007). Such emission is thought to be associated to the local interstellar medium that scatters the stellar light, so that the movement of HD 61005 through the medium causes the swept shape of the disc (Hines et al., 2007). These observations give a complementary picture of the circumstellar material present in the disc since different grain populations are traced in our model and in the scattered light images.
The SED was compiled from the literature including our new detection at 350 μm (Fig. 4.6) and the SEST upper limit at 1.2 mm from C05. The best-fit model parameters are reported in Table 4.4 and the computed best-fit model is plotted in Fig. 4.6. The confidence regions of the fit (see lower plots in Fig. 4.6) show that the best fit parameters represent only a local minimum of the model parameters space. This is probably due to the fact that the model assumptions are not valid in this case. As suggested from the HST images, the object seems to be located in the local interstellar medium material, which probably introduces an additional small grain population which contributes to the scattered light in the SED. Our model assumes that all the detected flux is stellar light scattered and/or absorbed and re-emitted only by the dust particles in the disc.

4.4.6 HD 191089

HD 191089 is an F5V star with a Hipparcos distance of 54±3 pc from the Sun. This star was selected for the FEPS programme because it was known to have a debris disc based on ISO and IRAS measurements and it was not considered in our statistical analysis presented in section 4.3. An upper limit of the age (∼3 Gyr) for the system was presented by Nordström et al. (2004), using main-sequence isochrones. I adopt an age of ∼300 Myr (Hillenbrand et al., 2008).
The SED was compiled from the literature (Fig. 4.7) including the Spitzer spectro-photometry (Carpenter et al., 2009), CSO detection at 350 μm and IRAM upper limit at 1.2 mm from this work and OVRO 3.1 mm up-

per limit from C05. The IRAS detections (Helou & Walker, 1988, empty squares in Fig.4.7), are systematically higher than the Spitzer photometry, due to the bigger beam and they were not taken into account during the model fitting. Since there is no IRS spectrum of the source constraining the beginning of the infrared excess close to the stellar photosphere, the IRAS detection at 12 μm was taken into account during the SED fitting. The best-fit model parameters are reported in Table 4.4 and the computed best-fit model is plotted in Fig. 4.7. The confidence regions of the fit show some degree of degeneracy of the model (see lower plots in Fig. 4.7). I note that the model result is not significant at all. This is due to the few data points which constrain the SED.

4.4.7 Modelling discussion

Comparing the collisional timescale to the Poynting-Robertson timescale, we conclude that all the detected debris disc are systems in the collision dominated regime.
The SED of the debris discs has been modelled leaving 3 parameters simultaneously free: inner radius, dust mass and minimum grain size.
I notice that the slope of the SEDs seems to change from the sub-millimetre to the millimetre wavelength range, but is well reproduced by our models within the errors. Including grains larger than 3 mm in the model would decrease the steepness of the slope in the sub-millimetre, but would not reproduce at the same time the sub-millimetre and millimetre fluxes.
A degeneracy between the inner radius and minimum grain size can still exist: in this case the σ-contours plots would represent only a local minimum in the parameter space, instead of the absolute solution. Only a resolved image of the entire grain population which delineates the inner radius of the disc will allow us to break the degeneracy between smallest grain size present in the disc and inner radius.
I now discuss how well constrained the fixed model parameters are (i.e. $R_{\rm OUT}$, $a_{\rm max}$, dust composition and size distribution) and in particular if and how they can alter our conclusions about $M_{\rm dust}$, $R_{\rm in}$ and $a_{\rm min}$. I am not going to further discuss the cases of HD 61005 and HD 191089 because our modelling was not significant at all, nor the case of HD 107146 because the assumption on the outer radius is supported by millimetre resolved images (Corder et al., 2009).
- The *outer radius* was assumed to be 150 AU. While in the case of

HD107146 such an assumption is supported by resolved millimetre images, in the other cases, I need to investigate the robustness of our model results. While the most distant objects of the Kuiper belt have been observed up to 150 AU from the Sun (Gladman et al., 2002), the edge of the Kuiper belt is commonly considered close to the 2:1 resonance with Neptune at about 50 AU from the Sun (e.g. Trujillo & Brown, 2001). There is also no reason why all discs would be expected to have the same outer edge. For these reasons I use five different outer radii (1000, 500, 300, 100 and 50 AU, or 60 AU when the fitting routine was not able to find any reasonable inner radius smaller than 50 AU), leaving free the dust mass ($M_{\rm dust}$), the inner radius ($R_{\rm in}$) and the minimum grain size $a_{\rm min}$. The results are summarised in Table 4.5.
I notice that, in the case of HD104860 and HD 8907, changing the outer radius from 500 to 50 AU affects only the dust mass. In the case of HD 377 fixing the outer radius to 100 and 50 AU the model fitting is no longer satisfactory, while I find a better result increasing the outer radius up to 500 AU (see different $\chi^2_{\rm red.}$ in Table 4.5). The minimum grain size remains at least one order of magnitude bigger than the blowout size, despite the case of an outer radius of 1000 AU where it becomes of the same order of magnitude or smaller than the blowout size.
- The *maximum grain size* has been fixed to 3 mm; despite the fact that a collisional cascade generates a distribution of grain size which does not stop at the millimetre size, I include in our model the maximum particle size which contributes significantly to the emission which I detect during our observations. I remind the reader that the mass derived by our model represents the mass of the grains smaller than 3 mm present in the disc and that increasing the maximum grain size would increase the disc mass.
- The dust has been assumed to be made up of *astronomical silicate*; this is expected to be the main component in protoplanetary discs (Pollack et al., 1994). Although a different composition of the dust can be present in the disc, Spitzer infrared spectroscopic observations do not allow us to constrain the material properties due to the lack of diagnostic features, caused by large grain sizes (see the IRS spectra overplotted in the SEDs, Fig.4.2-4.7). A different dust composition would change the blow-out size as well as the minimum grain size present in the disk computed by our model. A detailed investigation of different dust compositions is beyond the goal of this paper.
- I finally recall that a more realistic *grain size distribution* can also affect

our modelling results. Departures from the canonical size distribution we assumed, have been highlighted by collisional evolution studies of spatially resolved debris disks (e.g. Thébault & Augereau, 2007).
Despite previously discussed degeneracies, the objects HD 104860, HD 8907 and HD 107146 show the inner part of their discs cleared from small micron-sized dust grains because of the lack of near/mid-infrared emission (Wolf & Hillenbrand, 2003). These inner holes can be maintained by the presence of a planet-sized body (e.g. Roques et al., 2004), which avoids the filling of the central cavity by Poynting-Robertson drag.

4.5 Summary and conclusions

I have carried out two deep surveys at 350 μm and 1.2 mm of circumstellar discs around solar-type stars at ages between 3 Myr and 3 Gyr. These new observations are an order of magnitude more sensitive to dust emission than previous observations of C05. The dust disc masses have been computed from the millimetre emission, where the discs are assumed to be optically thin. A survival analysis of the dust disc masses as a function of time has been carried out of systems older than 20 Myr, including the dust mass upper limits. The spectral energy distributions of the debris discs detected by our sub-millimetre and millimetre surveys have been modelled. I draw the following main conclusions from our work:

1. The *Kendall's tau correlation* yields a probability of 76% that the mass of debris discs and their age are correlated. Similarly, the three different *two-sample tests* gives a probability between 70 and 83% that younger and older debris systems belong to different parent populations in terms of dust mass. Our result on the relation between dust mass and age is limited by the sensitivity of our millimetre survey. Deeper millimetre observations are needed to confirm the evolution of debris material around solar-like stars.

2. The spectral energy distributions of the debris discs detected at 350 μm and/or 1.2 mm were modelled. I found a degeneracy in the best fit parameters which will only be broken with high-resolution images which resolve the entire disc. Nevertheless, this approach allows us to identify debris discs with an inner region that has been evacuated from small micron-sized dust grains.

3. In the case of the detected debris discs, the comparison between collision and Poynting-Robertson timescales suggests that the debris discs are collision dominated.

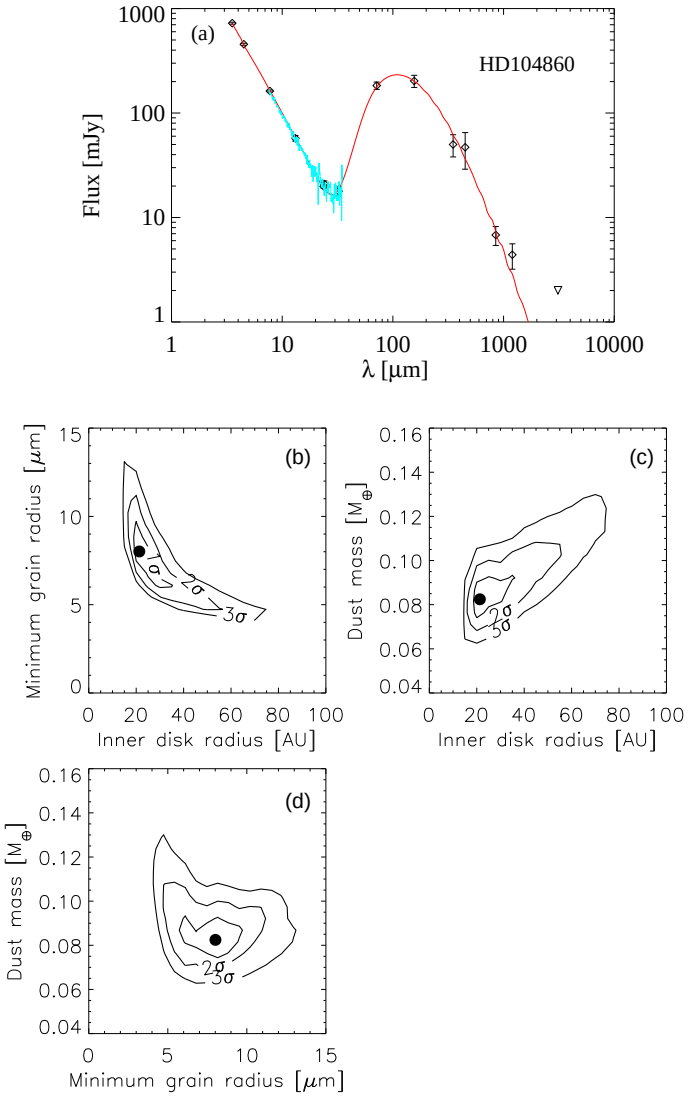

Figure 4.2 SED of HD 104860 (upper plot (a)): Detections are shown as empty diamonds while 3σ upper limits are shown with empty triangles. The solid line shows the best fit model (see details in section 4.4). The lower plots (b, c, d) represent the 2D projections of the 3D surfaces of constant $\Delta\chi^2$ obtained varying at the same time the dust mass, minimum grain size and inner disc radius.

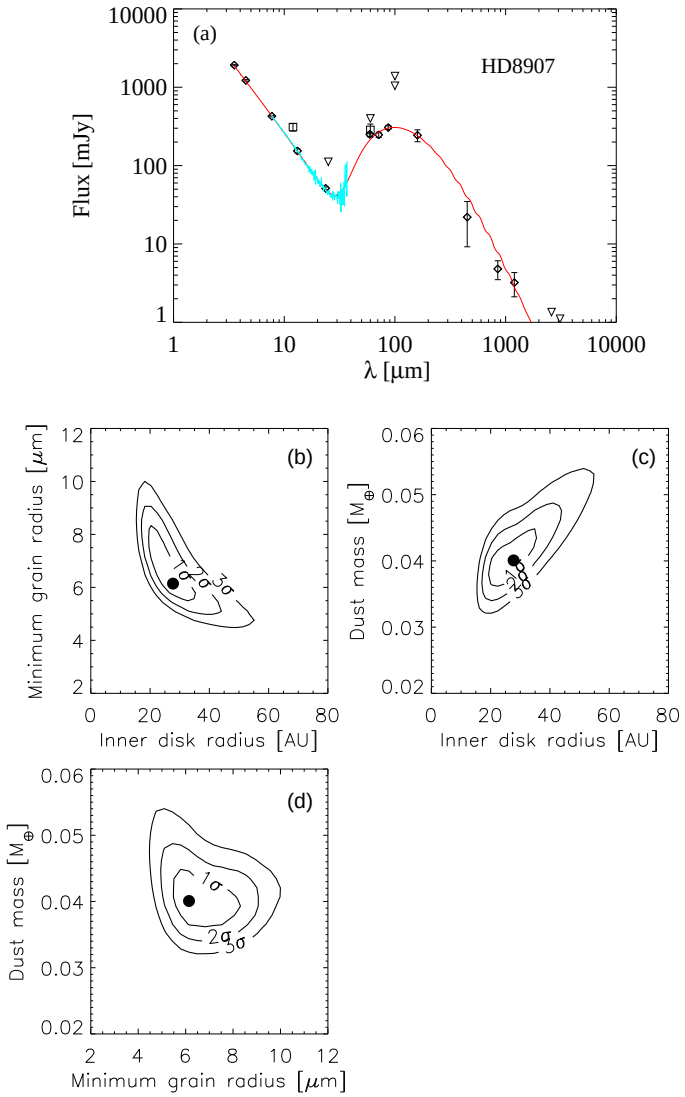

Figure 4.3 As Fig. 4.2 but for HD 8907.

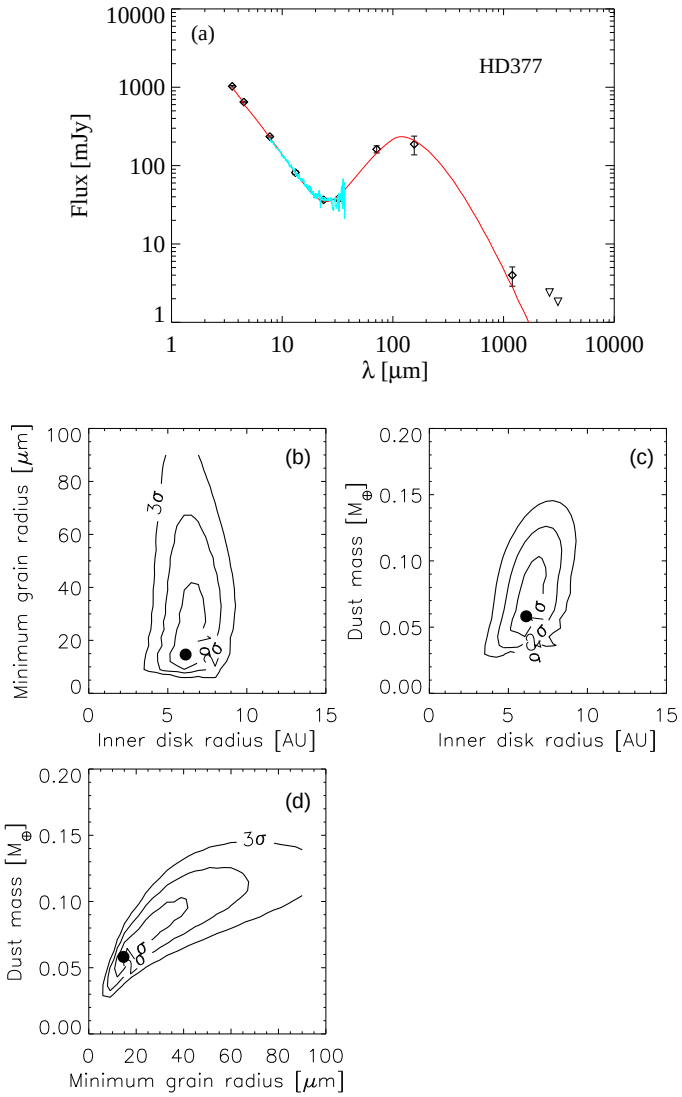

Figure 4.4 As Fig. 4.2 but for HD 377.

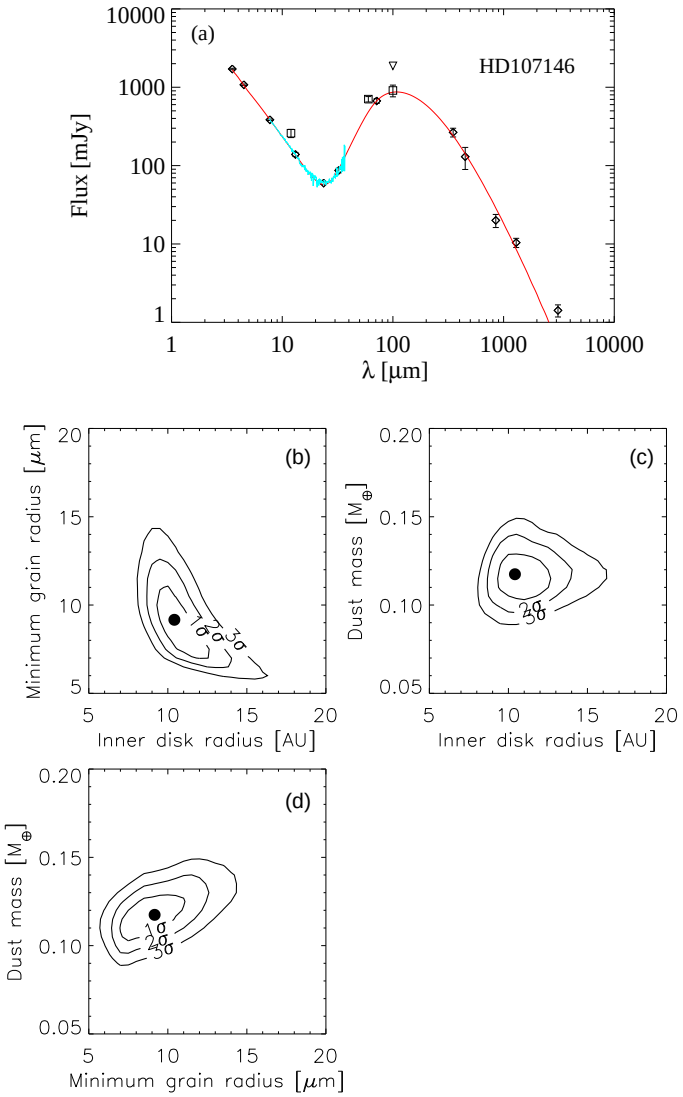

Figure 4.5 As Fig. 4.2 but for HD 107146.

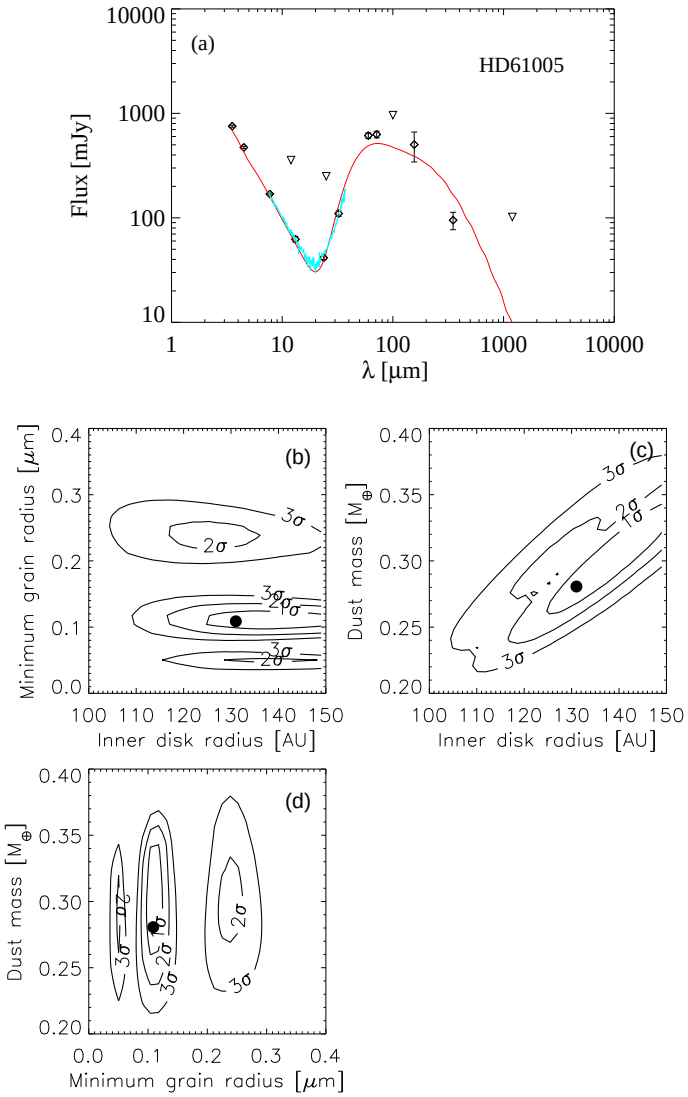

Figure 4.6 As Fig. 4.2 but for HD 61005.

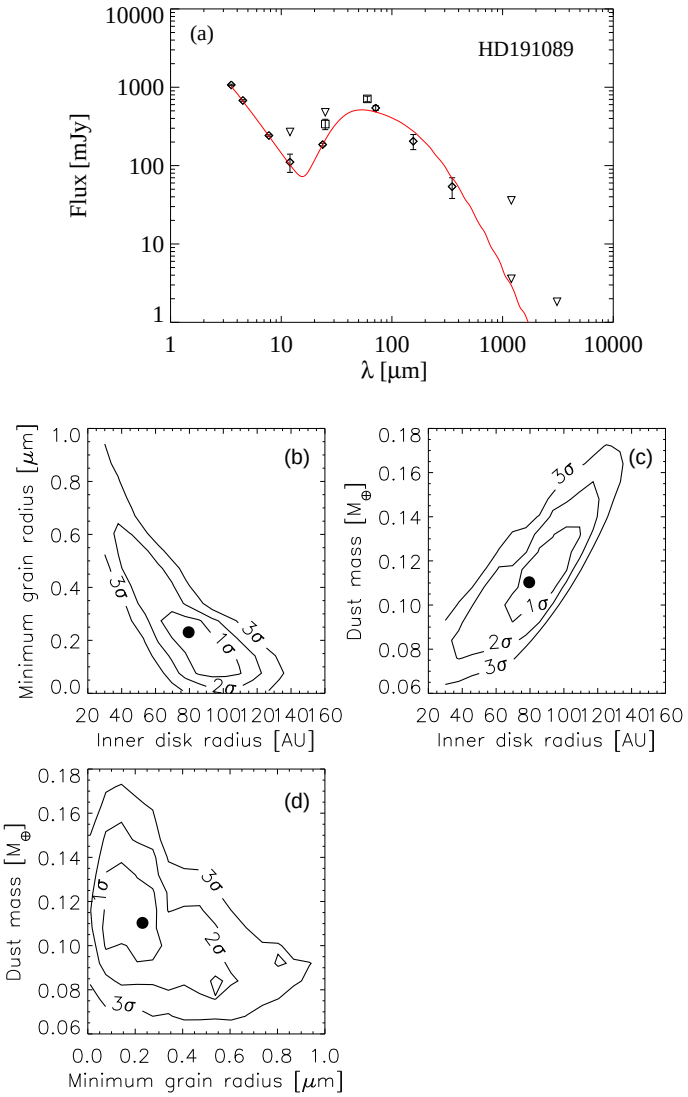

Figure 4.7 As Fig. 4.2 but for HD191089.

Table 4.1: The stellar properties, e.g. spectral type, temperature, luminosity and age range are reported in the first columns (from Meyer et al., 2006, 2008; Hillenbrand et al., 2008). CSO 350 μm and IRAM 1.2 mm measured fluxes and upper limits are reported in the sixth and seventh column. The detected sources are highlighted in bold. In the ninth column are the references to the stellar distances (listed in the eighth column). *: The errors and the upper limits refer to the statistical errors (flux rms) and do not include the calibration uncertainty (between 12 and 22% of the flux). **: The errors and the upper limits refer to the statistical errors (flux rms) and do not include the calibration uncertainty (between 11 and 16% of the flux). Distance references: [1] de Zeeuw et al. (1999); [2] Perryman et al. (1997); [3] Hillenbrand et al. (2008); [4] Pinsonneault et al. (1998); [5] based on recent Pleiades distances: de Zeeuw et al. (1999), Zwahlen et al. (2004), Soderblom et al. (2004) and Pan et al. (2004).

Source	Spectral Type	T_{eff} [^{o}K]	$log(L_{\star}/L_{\odot})$	$log(Age)$	$S^{\star}_{350\mu m}$ [mJy]	$S^{\star\star}_{1.2\ mm}$ [mJy]	Distance [pc]	Ref.
FEPS sources older than 10 Myr								
HD 60737	G0	5895	0.01	8.0 - 8.5		<4.5	38±2	(2)
HII1101	G0V	5988	0.08	8.0 - 8.5		<2.3	133±4	(5)
HII152	G5V	5823	−0.10	8.0 - 8.5		<2.7	133±4	(5)
HII1200	F6V	6217	0.35	8.0 - 8.5		<2.3	133±4	(5)
HD 90905	G1V	6028	0.16	8.0 - 8.5		<3	32±1	(2)
HII514	—	5727	0.11	8.0 - 8.5		<2.6	133±4	(5)
HD 104860	F8	5950	0.12	8.0 - 8.5	50.1±9.3	4.4 ±1.1	48±2	(2)
HD 377	G2V	5852	0.09	8.0 - 8.5		4.0 ±1.0	40±2	(2)
HD 61005	G8V	5456	−0.25	8.0 - 8.5	95±12		35±1	(2)
HD 107146	G2V	5859	0.04	8.0 - 8.5	319±6		29±1	(2)
HD 72687	G5V	5738	−0.05	8.0 - 8.5	<54		46±2	(2)
HII250	—	5767	−0.04	8.0 - 8.5		<3.28	133±4	(5)

Table 4.1: continued.

Source	Spectral Type	T_{eff} [°K]	$log(L_\star/L_\odot)$	$log(Age)$	$S^{\star}_{350\mu m}$ [mJy]	$S^{\star\star}_{1.2\ mm}$ [mJy]	Distance [pc]	Ref.
HD 219498	G5	5671	0.69	8.5 - 9.0		<4.8	150±13	(3)
HD 61994	G6V	5538	0.01	8.5 - 9.0		<2.6	28±2	(2)
HD 145229	G0	5893	−0.02	8.5 - 9.0	<22.5	<2.8	33±1	(2)
HD 150706	G3(V)	5883	−0.02	8.5 - 9.0		<3.2	27±1	(2)
HD 204277	F8V	6190	0.29	8.5 - 9.0		<2.1	34±1	(2)
HD 85301	G5	5605	−0.15	8.5 - 9.0	<17.4	<2.7	32±1	(2)
HD 69076	K0V	5405	−0.28	9.0 - 9.7	<42	<2.1	34±1	(2)
HD 205905	G2V	5925	0.04	9.0 - 9.7		< 4.6	26±1	(2)
HD 201219	G5	5604	−0.16	9.0 - 9.7		<4.1	36±2	(2)
HD 206374	G6.5V	5580	−0.17	9.0 - 9.7		<3.9	27±1	(2)
HD 38529	G8III/IV	5361	0.82	9.0 - 9.7		<3.2	42±2	(2)
HD 136923	G9V	5343	−0.29	9.0 - 9.7		<3.2	20±1	(2)
HD 6963	G7V	5517	−0.26	9.0 - 9.7		<4.2	27±1	(2)
HD 122652	F8	6157	0.18	9.0 - 9.7	<19.5	3.2	37±1	(2)
HD 187897	G5	5875	0.12	9.0 - 9.7		<2.4	33±1	(2)
FEPS sources older than 10 Myr not included in the statistical analysis								
HD 134319	G5(V)	5660	−0.14	7.5 - 8.0	<25.2	<8.5	44±1	(2)
HD 191089	F5V	6441	0.50	8.0 - 8.5	54±15	<3.6	54±3	(2)
HD 25457	F7V	6172	0.32	8.0 - 8.5		<2.2	19±1	(2)
HD 8907	F8	6250	0.32	8.5 - 9.0		3.2±0.9	34±1	(2)
FEPS sources younger than 10 Myr								
[PZ99] J161411.0-230536	K0	4963	0.50	6.5 - 7.0	<21.9	3.5±1.1	145±2	(1)
RXJ1612.6-1859a	K0IV	5372	0.38	6.5 - 7.0	43±8.7	5.9 ±1.4	145±2	(1)

Table 4.1: continued.

Source	Spectral Type	T_{eff} [°K]	$log(L_\star/L_\odot)$	$log(Age)$	$S^{\star}_{350\mu m}$ [mJy]	$S^{\star\star}_{1.2\ mm}$ [mJy]	Distance [pc]	Ref.
HD 143006	G6/8	5884	0.39	6.5 - 7.0	1400 ±39		145±2	(1)
SCOPMS214	K0IV	5318	0.26	6.5 - 7.0	<72		145±2	(1)
RX J1842.9-3532	K0IV	4995	−0.01	6.5 - 7.0	650±29		130±10	(3)
RX J1852.3-3700	K3	4759	−0.23	6.5 - 7.0	1200 ±45		130±10	(3)
HD 35850	F7/8V	6047	0.25	7.0 - 7.5		<3.7	27±1	(2)
HE848	F9V	6309	0.47	7.5 - 8.0		<3.1	176±5	(4)
HD 77407	G0(V)	5986	0.08	7.5 - 8.0		<3.45	30±1	(2)
HD 22179	G0	5986	0.36	7.5 - 8.0		<3.3	100±20	(3)
HD 12039	G3/5V	5688	−0.05	7.5 - 8.0		<2.7	42±2	(2)
HD 70573	G1/2V	5896	0.14	7.5 - 8.0		<2.73	46±15	(3)
HE750	F5	6421	0.28	7.5 - 8.0		<4.60	176±5	(4)
HD 135363	G5(V)	4728	−0.48	7.5 - 8.0		<2.22	29±1	(2)
Not in the FEPS list								
HD 82943						<27.9		
HD 38207	F2V	6769	0.72	8.0 - 8.5		<0.33	127±25	(3)
HD 117176						<14.1		
HD 218738					<21.9	<3.3		

Table 4.2 Ages (in logarithmic scale) of the debris discs detected at the millimetre wavelength, with IRAM (this work), SEST and OVRO (from C05). They have been derived using different techniques: the strength of the CaII H and K (R'_{HK}) and Lithium (Li) emission, X-ray activity ($X\text{-}ray$), and the rotational period-age ($p_{\rm rot}$) relation (L.Hillenbrand, private communication). The ages are averaged and the standard deviation is adopted as error.

Method	HD 377	HD 8907	HD 104860	HD 107146
R'_{HK}	8.34	8.78	8.44	8.09
$v\ sini$	7.99	8.1	-	8.89
$p_{\rm rot}$	–	-	7.62	-
$X\text{-}ray$	7.9	7.88	8.06	-
Li	7.8	9.28	8.08	8.1
average	8.01	8.51	8.05	8.36
stdev	0.23	0.64	0.34	0.46

Table 4.3 Blowout grain size, P-R drag timescales of the debris discs detected in the CSO and/or IRAM surveys. The β-index discs only for the stars with the SED sampled in the submillimetre/millimetre range (details in section 4.4) is reported

	HD 104860	HD 8907	HD 377	HD 107146	HD 61005	HD 191089
$a_{\rm blow,Si}[\mu m]$	0.64	0.81	0.54	0.49	0.34	1.14
$t_{\rm P-R,Si}[Myr]$	0.39	0.5	0.03	0.08	9.85	1.86
$t_{\rm coll}$ [Myr]	0.007	0.007	0.003	0.002	0.009	0.005
β	0.5±0.7	-0.1±1.3	–	0.4±0.2	–	–

Table 4.4 Model results, reduced χ^2 ($\chi^2_{\rm red.}$) assuming a fixed outer radius ($R_{\rm OUT}$) of 150 AU and a maximum grain size ($a_{\rm max}$) of 3 mm.

	HD 104860	HD 8907	HD 377	HD 107146	HD 61005	HD 191089
$M_{\rm dust}/{\rm M}_\oplus$	0.082±0.007	0.040±0.005	0.058±0.013	0.110±0.008	0.261±0.023	0.110±0.037
$R_{\rm in}$ [AU]	21±5	27.8±13.9	6.1±0.8	10.2±0.8	95.6±23	79±98
$a_{\rm min}$ [μm]	8±2	6±2	14±5	8.6±1.2	0.4±0.3	0.23±0.78
$\chi^2_{\rm red.}$	2.6	4.3	5.0	4.5	16.3	8.7

Table 4.5 Model results leaving as free parameters using $M_{\rm dust}/{\rm M}_{\oplus}$, $R_{\rm in}$ and $a_{\rm min}$ for 6 different outer radii: 1000, 500, 300, 150, 100 and 50 AU.

HD 104860						
$R_{\rm OUT}$	1000 AU	500 AU	300 AU	150 AU	100 AU	50 AU
$M_{\rm dust}/{\rm M}_{\oplus}$	5.843±0.652	2.930±0.245	1.774 0.133	0.082±0.007	0.053±0.005	0.039±0.004
$R_{\rm in}$ [AU]	185± 23	20.3±7.8	20±7	21±5	22±2	30±3
$a_{\rm min}$ [μm]	0.07±0.03	4.5±0.9	6±2	8±5	11±2	21±4
$\chi^2_{\rm red.}$	6.1	7.0	4.1	2.6	2.7	3.0
HD 8907						
$R_{\rm OUT}$	1000 AU	500 AU	300 AU	150 AU	100 AU	60 AU
$M_{\rm dust}/{\rm M}_{\oplus}$	3.097±184	1.614±0.099	0.931±0.050	0.040±0.005	0.024±0.002	0.017±0.003
$R_{\rm in}$ [AU]	89±14	29±14	19.4±5.4	27±17	27±7	41±15
$a_{\rm min}$ [μm]	0.5±0.08	3.1±0.8	5.6±1.1	6±2	8±2	7.7±2.6
$\chi^2_{\rm red.}$	22.8	17.8	9.2	4.3	3.6	3.5
HD 377						
$R_{\rm OUT}$	1000 AU	500 AU	300 AU	150 AU	100 AU	60 AU
$M_{\rm dust}/{\rm M}_{\oplus}$	3.655±0.507	2.649±0.322	1.339 ±0.367	0.058±0.013	0.034±0.006	0.039±0.012
$R_{\rm in}$ [AU]	70±12	4.6±1.1	4.6±0.65	6.1±0.8	38±8	51±8
$a_{\rm min}$ [μm]	0.02±0.001	6.5±1.5	9.1±3.5	14±5	14±4	38±20
$\chi^2_{\rm red.}$	8.6	7.7	4.6	5.0	395.	395.

5

Conclusions and Future Work

In this chapter I will briefly summarise the major results of my PhD research project. I will also address the future work on the field discussed here with respect to the new astronomical instrumentation.

Chapter 2 presents a multi-wavelength study of the young binary system Haro 6-10. The analysis of the optical and infrared data suggests the presence of a common dusty envelope which surrounds both stellar components of Haro 6-10. Such an envelope has a dust composition similar to the interstellar medium and is likely to be a remnant of the molecular cloud from which the binary formed. Moreover, each component of the system is surrounded by its own protoplanetary disc. The analysis of the mid-infrared spectro-interferometric data allows to determine the relative inclination of the two discs. Interestingly the discs are found to be highly misaligned: the disc around the northern component of Haro 6-10 is almost edge-on while the one around the southern component is seen an almost face-on. This finding triggers an interesting discussion about the formation of this binary star: fragmentation of the molecular cloud versus gravitational capture. For the specific case of Haro 6-10, the most likely scenario seems to be the fragmentation of the cloud. A statistical significant sample is necessary to draw firm conclusions on the frequency of these systems and hence to understand how binary stars forms.

The multi-wavelengths approach results to be very efficient in determining the properties of young binary systems and greatly improves our comprehension of the binary formation process. This field will highly benefit from the higher angular resolution of next generation infrared and millimetre interferometry. In particular, the second generation VLTI mid-infrared interferometer, (*MATISSE; Lopez et al., 2009)*, is a promising tool of investigation given its imaging capability. The angular resolution of MATISSE (Fig. 5.1) and the imaging mode will allow to create interferometric maps of the small spatial scale of circumstellar and circumbinary discs. With regards to the study of binary systems where one of the components is an infrared companion, as the case of Haro 6-10, the resolved images in the mid-infrared (where the flux ratio between primary and companion is favourable) will allow e.g. to address the nature of the infrared companion as well as to understand where the enhanced extinction of the latter comes from. MATISSE will be able to construct maps with a resolution of 7 milliarcsec (mas) to 20 mas in the L- and N-band respectively[1]. This corresponds to a scale of 1 - 3 astronomical units at a distance of 150 parsec (distance of the Taurus star forming region). In the statistical studies of binary systems such an enhanced resolution will allow also to detect binaries at distance never covered in young systems so far.

Chapter 3 reports on a deep Spitzer/IRAC (3 - 8 μm) survey of the OB association IC 1795. Using pre-main sequence isochrones, computed for the first time in the Spitzer/IRAC colours, the age of the cluster is found to be in the range of 3 - 5 Myr. The disc fraction in IC 1795 does depend on the stellar mass: high mass stars (>2 $M_{\odot}$) have a lower disc fraction compared to low mass objects (2-0.8 $M_{\odot}$). This implies that the discs around massive stars dissipate faster. The average disc fraction in IC 1795 is 50%±10%. This result is in agreement with the general trend identified by the disc evolution studies in low-mass environment. This suggests that the presence of the O star in IC 1795 does not influence the disc evolution.

The combination of X-ray and infrared surveys together with optical spectroscopy and deep near-infrared observations will complete the study of the disc evolution in OB associations: The optical spectroscopy will

[1]for a 100 meter baseline

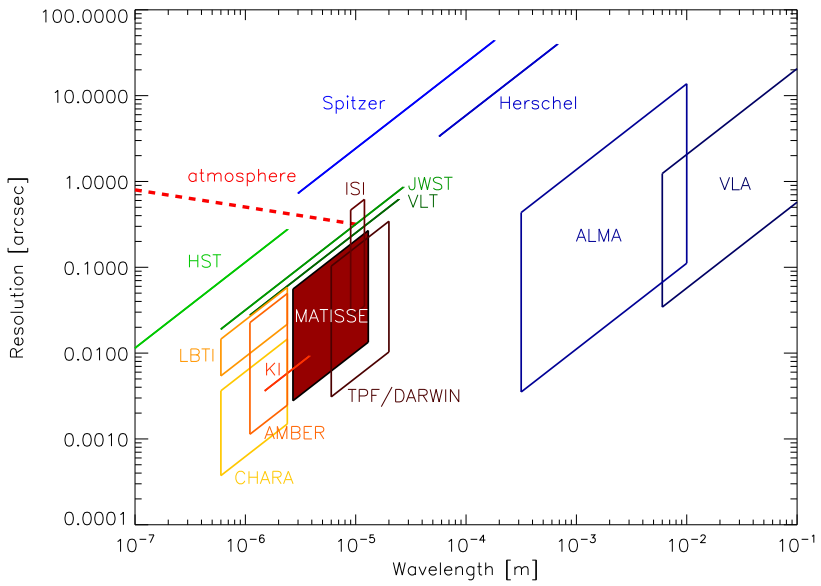

Figure 5.1 Comparison of the performances of the new instrumentations compared to the current resolutions available at different wavelengths (Wolf et al., 2007).

allow to confirm the membership using the age indicators (e.g. H_α, Li) and to compute the optical extinction towards each source. With this information I will use the near-infrared de-reddened photometry to fit the PMS isochrones. In these regards our group already obtained telescope time to carry out a deep near-infrared photometric survey and a multi-object optical spectroscopy of the members of IC 1795. A similar study will be done on two younger OB associations, the 1-2 Myr old Pismis 24, and the 2-3 Myr old NGC2244.

Chapter 4 presents the results of a survey in the millimetre wavelengths of discs around solar-type stars older than 30 Myr during the "debris" phase. The statistical analysis of the dust disc masses as a function of time of systems older than 20 Myr shows a probability of 76% that the mass of debris discs and their age are correlated and a probability between 70 and 83% that younger and older debris systems belong to different parent populations in terms of dust mass. This may suggest an evolution of the debris dust mass in systems older than 30 Myr. The modelling of the spectral energy distributions of the debris discs

detected by the sub-millimetre and millimetre surveys reveals that debris discs have inner regions evacuated from small micron-sized dust grains. The comparison between collision and Poynting-Robertson timescales suggests that the debris discs are collision dominated.

In this study of the late stages of discs dissipation future work can be done at shorter wavelengths where the disc is still optically thin but the flux is expected to be higher. The fundamental improvement that will help to finally constrain the dissipation mechanism of the dust in debris discs comes from the detection of the flux from most of the sources at different ages. In this regards the *Herschel Space Telescope*[2] will provide unprecedented high sensitivity observations of debris discs in the solar neighbourhoods. As an example the *DUNES (DUst around NEarby Stars, PI: C. Eiroa)* Key Program is aimed at finding and characterising faint extra-solar analogues to the Edgeworth-Kuiper Belt in an unbiased, statistical sample of nearby FGK main-sequence stars, spanning a broad range of stellar ages from 0.1 to 10 Gyr.
A step forward to resolve the cold millimetre emission of debris discs will be possible with *ALMA*[3]. The combination of its high sensitivity and resolution in the millimetre wavelength range will allow to spatially resolve the discs and analyse the dust grain size as a function of disc radius.

[2]http://sci.esa.int/science-e/www/area/index.cfm?fareaid=16
[3]http://www.eso.org/sci/facilities/alma/

Acknowledgment

I want to thank all the people who have helped me, through the years, to reach this goal!
First of all I wish to thank Thomas Henning: in addition to his fundamental scientific advises, he gave me the possibility and the support to carry on my thesis while having two kids.
Thanks go also to Sebastian Wolf, for his help and guidance from Kiel.
I acknowledge the enthusiasm and pragmatism of Jeroen Bouwman during the last year of my thesis.
Thanks go to my friends and colleagues Aurora Sicilia-Aguilar, Arian Bik and Anna Pasquali, for their suggestions, discussions and for reading so many times my manuscripts. I acknowledge the collaboration, the discussions and help of Thorsten Ratzka.
I acknowledge the friendship of the italian and spanish community at MPIA: Fulvio, Andrea, Stefano, Anna G. and Anna P., Aday, Alejo, Aurora, Victoria, José, Javier.
Special thanks are for the Borelli's family, Victoria, José and Camila for their deep friendship, and to my nextdoor neighbour and colleague Micaela Stumpf for helping me and my family so many times.
Thanks go to Victoria for reading my thesis.
I warmly thank a great person, Francesco Rizzoli, who is "responsible" for my passion for astronomy.
I wish to thank also my two Angels, **Giovanni and Elena***, who have been making wonderful these years.*
My last and warmest thanks are for **Davide** *for his love.*

Bibliography

Alexander, R. D., Begelman, M. C., & Armitage, P. J. 2007, ApJ, 654, 907

Alibert, Y., Mordasini, C., Benz, W., & Winisdoerffer, C. 2005, A&A, 434, 343

Andrews, S. M., & Williams, J. P. 2008, Ap&SS, 313, 119

Anglada, G., Villuendas, E., Estalella, R., Beltrán, M. T., Rodríguez, L. F., Torrelles, J. M., & Curiel, S. 1998, AJ, 116, 2953

Ardila, D. R., et al. 2004, ApJL, 617, L147

Asplund, M., Grevesse, N., & Sauval, A. J. 2005, in ASP Conf. Ser. 336: Cosmic Abundances as Records of Stellar Evolution and Nucleosynthesis, ed. T. G. Barnes, III & F. N. Bash, 25

Backman, D. 2004, in Astronomical Society of the Pacific Conference Series, Vol. 324, Debris Disks and the Formation of Planets, ed. L. Caroff, L. J. Moon, D. Backman, & E. Praton, 9–+

Backman, D. E., & Paresce, F. 1993, in Protostars and Planets III, ed. E. H. Levy & J. I. Lunine, 1253–1304

Balog, Z., Muzerolle, J., Rieke, G. H., Su, K. Y. L., Young, E. T., & Megeath, S. T. 2007, ApJ, 660, 1532

Bate, M. R., & Bonnell, I. A. 1997, MNRAS, 285, 33

Bate, M. R., Bonnell, I. A., Clarke, C. J., Lubow, S. H., Ogilvie, G. I., Pringle, J. E., & Tout, C. A. 2000, MNRAS, 317, 773

Beckwith, S. V. W., Henning, T., & Nakagawa, Y. 2000, Protostars and Planets IV, 533

Beckwith, S. V. W., Sargent, A. I., Chini, R. S., & Guesten, R. 1990, AJ, 99, 924

Bevington, P. R. 1969, Data reduction and error analysis for the physical sciences, ed. Bevington, P. R.

Binney, J., & Tremaine, S. 1987, Galactic dynamics, ed. S. Binney, J. & Tremaine

Boffin, H. M. J., Watkins, S. J., Bhattal, A. S., Francis, N., & Whitworth, A. P. 1998, MNRAS, 300, 1189

Bonatto, C., Santos, Jr., J. F. C., & Bica, E. 2006, A&A, 445, 567

Bonnell, I. A., & Davies, M. B. 1998, MNRAS, 295, 691

Boss, A. P. 1997, Science, 276, 1836

Bouwman, J., Lawson, W. A., Dominik, C., Feigelson, E. D., Henning, T., Tielens, A. G. G. M., & Waters, L. B. F. M. 2006, ApJL, 653, L57

Bouwman, J., Meeus, G., de Koter, A., Hony, S., Dominik, C., & Waters, L. B. F. M. 2001, A&A, 375, 950

Brott, I., & Hauschildt, P. H. 2005, in ESA Special Publication, Vol. 576, The Three-Dimensional Universe with Gaia, ed. C. Turon, K. S. O'Flaherty, & M. A. C. Perryman, 565

Brown, B. W. M., Hollander, M., & Korwar, R. M. 1974, Reliability and Biometry, ed. F. Proschan & R. J. Serfling (Philadelphia: SIAM), 327

Burns, J. A., Lamy, P. L., & Soter, S. 1979, Icarus, 40, 1

Carpenter, J. M., Mamajek, E. E., Hillenbrand, L. A., & Meyer, M. R. 2006, ApJL, 651, L49

Carpenter, J. M., Wolf, S., Schreyer, K., Launhardt, R., & Henning, T. 2005, AJ, 129, 1049

Carpenter, J. M., et al. 2009, ApJS, 181, 197

Castelli, F., & Kurucz, R. L. 2003, in IAU Symposium, Vol. 210, Modelling of Stellar Atmospheres, ed. N. Piskunov, W. W. Weiss, & D. F. Gray, 20

Chandler, C. J., Barsony, M., & Moore, T. J. T. 1998, MNRAS, 299, 789

Chieffi, A., & Straniero, O. 1989, ApJS, 71, 47

Clarke, C. J., Gendrin, A., & Sotomayor, M. 2001, MNRAS, 328, 485

Clarke, C. J., & Pringle, J. E. 1991a, MNRAS, 249, 584

—. 1991b, MNRAS, 249, 588

Cohen, M., Walker, R. G., Carter, B., Hammersley, P., Kidger, M., & Noguchi, K. 1999, AJ, 117, 1864

Corder, S., et al. 2009, ApJL, 690, L65

Dahm, S. E., & Hillenbrand, L. A. 2007, AJ, 133, 2072

Davis, C. J., Eisloeffel, J., Ray, T. P., & Jenness, T. 1997, A&A, 324, 1013

Davis, C. J., Mundt, R., & Eisloeffel, J. 1994, ApJL, 437, L55

de Zeeuw, P. T., Hoogerwerf, R., de Bruijne, J. H. J., Brown, A. G. A., & Blaauw, A. 1999, AJ, 117, 354

Decin, G., Dominik, C., Waters, L. B. F. M., & Waelkens, C. 2003, ApJ, 598, 636

Degl'Innocenti, S., Prada Moroni, P. G., Marconi, M., & Ruoppo, A. 2008, Ap&SS, 316, 25

Dent, W. R. F., Matthews, H. E., & Ward-Thompson, D. 1998, MNRAS, 301, 1049

Dominik, C., & Decin, G. 2003, ApJ, 598, 626

Doppmann, G. W., Najita, J. R., & Carr, J. S. 2008, ApJ, 685, 298

Draine, B. T., & Lee, H. M. 1984, ApJ, 285, 89

Duchêne, G., Bontemps, S., Bouvier, J., André, P., Djupvik, A. A., & Ghez, A. M. 2007, A&A, 476, 229

Dullemond, C. P., Hollenbach, D., Kamp, I., & D'Alessio, P. 2007, in Protostars and Planets V, ed. B. Reipurth, D. Jewitt, and K. Keil (University of Arizona Press, Tucson), 555–572

Eislöffel, J., Smith, M. D., Davis, C. J., & Ray, T. P. 1996, AJ, 112, 2086

Evans, N. J., et al. 2009, ApJS, 181, 321

Fazio, G. G., et al. 2004, ApJS, 154, 10

Fedele, D., van den Ancker, M. E., Henning, T., Jayawardhana, R., & Oliveira, J. M. 2010, A&A, in press

Fedele, D., et al. 2008, A&A, 491, 809

Feigelson, E., Townsley, L., Güdel, M., & Stassun, K. 2007, in Protostars and Planets V, ed. B. Reipurth, D. Jewitt, & K. Keil, 313–328

Feigelson, E. D., Martin, A. L., McNeill, C. J., Broos, P. S., & Garmire, G. P. 2009, AJ, 138, 227

Feigelson, E. D., & Nelson, P. I. 1985, ApJ, 293, 192

Feigelson, E. D., & Townsley, L. K. 2008, ApJ, 673, 354

Ferguson, J. W., Alexander, D. R., Allard, F., Barman, T., Bodnarik, J. G., Hauschildt, P. H., Heffner-Wong, A., & Tamanai, A. 2005, ApJ, 623, 585

Flaherty, K. M., & Muzerolle, J. 2008, AJ, 135, 966

Franco, J., Tenorio-Tagle, G., & Bodenheimer, P. 1990, ApJ, 349, 126

Furlan, E., et al. 2008, ApJS, 176, 184

Getman, K. V., Feigelson, E. D., Luhman, K. L., Sicilia-Aguilar, A., Wang, J., & Garmire, G. P. 2009, ApJ, 699, 1454

Getman, K. V., Feigelson, E. D., Townsley, L., Broos, P., Garmire, G., & Tsujimoto, M. 2006, ApJS, 163, 306

Gibb, E. L., Van Brunt, K. A., Brittain, S. D., & Rettig, T. W. 2007, ApJ, 660, 1572

Gladman, B., Holman, M., Grav, T., Kavelaars, J., Nicholson, P., Aksnes, K., & Petit, J. 2002, Icarus, 157, 269

Gorti, U., & Hollenbach, D. 2009, ApJ, 690, 1539

Habing, H. J., et al. 2001, A&A, 365, 545

Hachisuka, K., et al. 2006, ApJ, 645, 337

Haisch, Jr., K. E., Lada, E. A., & Lada, C. J. 2001, ApJL, 553, L153

Handler, G. 1999, MNRAS, 309, L19

Hanner, M. S., Brooke, T. Y., & Tokunaga, A. T. 1998, ApJ, 502, 871

Hartmann, L. 1998, Accretion Processes in Star Formation, ed. Hartmann, L.

Hartmann, L., Megeath, S. T., Allen, L., Luhman, K., Calvet, N., D'Alessio, P., Franco-Hernandez, R., & Fazio, G. 2005, ApJ, 629, 881

Hatchell, J., Fuller, G. A., Richer, J. S., Harries, T. J., & Ladd, E. F. 2007, A&A, 468, 1009

Heller, C. H. 1993, ApJ, 408, 337

—. 1995, ApJ, 455, 252

Helou, G., & Walker, D. W., eds. 1988, Infrared astronomical satellite (IRAS) catalogs and atlases. Volume 7: The small scale structure catalog, Vol. 7

Henning, T., & Stognienko, R. 1996, A&A, 311, 291

Hernández, J., et al. 2007, ApJ, 662, 1067

Hillenbrand, L., Mamajek, E., Stauffer, J., Soderblom, D., Carpenter, J., & Meyer, M. 2009, in American Institute of Physics Conference Series, Vol. 1094, American Institute of Physics Conference Series, ed. E. Stempels, 800–803

Hillenbrand, L. A. 1997, AJ, 113, 1733

Hillenbrand, L. A., Strom, S. E., Calvet, N., Merrill, K. M., Gatley, I., Makidon, R. B., Meyer, M. R., & Skrutskie, M. F. 1998, AJ, 116, 1816

Hillenbrand, L. A., et al. 2008, ApJ, 677, 630

Hines, D. C., et al. 2007, ApJL, 671, L165

Hogerheijde, M. R., van Dishoeck, E. F., Blake, G. A., & van Langevelde, H. J. 1997, ApJ, 489, 293

Holtzman, J. A., Burrows, C. J., Casertano, S., Hester, J. J., Trauger, J. T., Watson, A. M., & Worthey, G. 1995, PASP, 107, 1065

Ida, S., & Lin, D. N. C. 2004, ApJ, 616, 567

Iglesias, C. A., & Rogers, F. J. 1996, ApJ, 464, 943

Isobe, T., Feigelson, E. D., & Nelson, P. I. 1986, ApJ, 306, 490

Jaffe, W., et al. 2004, Nature, 429, 47

Jeffries, R. D. 2007, MNRAS, 376, 1109

Jensen, E. L. N., Mathieu, R. D., Donar, A. X., & Dullighan, A. 2004, ApJ, 600, 789

Johnstone, D., Hollenbach, D., & Bally, J. 1998, ApJ, 499, 758

Kemper, F., Vriend, W. J., & Tielens, A. G. G. M. 2004, ApJ, 609, 826

Kenyon, S. J., & Bromley, B. C. 2004, AJ, 127, 513

Kim, J. S., et al. 2005, ApJ, 632, 659

Koen, C., & Eyer, L. 2002, VizieR Online Data Catalog, 733, 10045

Koresko, C. D. 1998, ApJL, 507, L145

Koresko, C. D., Blake, G. A., Brown, M. E., Sargent, A. I., & Koerner, D. W. 1999, ApJL, 525, L49

Kroupa, P. 2002, Science, 295, 82

Lada, C. J. 1987, in IAU Symposium, Vol. 115, Star Forming Regions, ed. M. Peimbert & J. Jugaku, 1–17

Lada, C. J., et al. 2006, AJ, 131, 1574

Lavalley, M., Isobe, T., & Feigelson, E. 1992, in Astronomical Society of the Pacific Conference Series, Vol. 25, Astronomical Data Analysis Software and Systems I, ed. D. M. Worrall, C. Biemesderfer, & J. Barnes, 245–+

Leinert, C., Beck, T. L., Ligori, S., Simon, M., Woitas, J., & Howell, R. R. 2001, A&A, 369, 215

Leinert, C., & Haas, M. 1989, ApJL, 342, L39

Leinert, C., Zinnecker, H., Weitzel, N., Christou, J., Ridgway, S. T., Jameson, R., Haas, M., & Lenzen, R. 1993, A&A, 278, 129

Liu, M. C., Matthews, B. C., Williams, J. P., & Kalas, P. G. 2004, ApJ, 608, 526

Löhne, T., Krivov, A. V., & Rodmann, J. 2008, ApJ, 673, 1123

Lopez, B., et al. 2009, in Science with the VLT in the ELT Era, ed. A. Moorwood, 353–+

Luhman, K. L., et al. 2008, ApJ, 675, 1375

Mamajek, E. E., & Hillenbrand, L. A. 2008, ApJ, 687, 1264

Mathieu, R. D., Ghez, A. M., Jensen, E. L. N., & Simon, M. 2000, in Protostars and Planets IV, ed. Mannings, V., Boss, A.P., Russell, S. S. (Tucson: University of Arizona Press), 703–+

Mathis, J. S. 1998, ApJ, 497, 824

Megeath, S. T., Hartmann, L., Luhman, K. L., & Fazio, G. G. 2005, ApJL, 634, L113

Menard, F., Monin, J., Angelucci, F., & Rouan, D. 1993, ApJL, 414, L117

Mercer, E. P., Miller, J. M., Calvet, N., Hartmann, L., Hernandez, J., Sicilia-Aguilar, A., & Gutermuth, R. 2009, AJ, 138, 7

Meyer, M. R., Backman, D. E., Weinberger, A. J., & Wyatt, M. C. 2007, Protostars and Planets V, 573

Meyer, M. R., et al. 2006, PASP, 118, 1690

—. 2008, ApJL, 673, L181

Moeckel, N., & Bally, J. 2006, ApJ, 653, 437

—. 2007a, ApJL, 661, L183

—. 2007b, ApJ, 656, 275

Momose, M., Ohashi, N., Kawabe, R., Hayashi, M., & Nakano, T. 1996, ApJ, 470, 1001

Monin, J., Menard, F., & Duchene, G. 1998, A&A, 339, 113

Monin, J., Ménard, F., & Peretto, N. 2006, A&A, 446, 201

Moór, A., Ábrahám, P., Derekas, A., Kiss, C., Kiss, L. L., Apai, D., Grady, C., & Henning, T. 2006, ApJ, 644, 525

Najita, J., & Williams, J. P. 2005, ApJ, 635, 625

Nordström, B., et al. 2004, A&A, 418, 989

O'dell, C. R., & Wong, K. 1996, AJ, 111, 846

Oey, M. S., Watson, A. M., Kern, K., & Walth, G. L. 2005, AJ, 129, 393

Oliveira, J. M., Jeffries, R. D., van Loon, J. T., & Rushton, M. T. 2006, MNRAS, 369, 272

Padgett, D. L., Brandner, W., Stapelfeldt, K. R., Strom, S. E., Terebey, S., & Koerner, D. 1999, AJ, 117, 1490

Pan, X., Shao, M., & Kulkarni, S. R. 2004, Nature, 427, 326

Pascucci, I., et al. 2006, ApJ, 651, 1177

Perryman, M. A. C., et al. 1997, A&A, 323, L49

Pinsonneault, M. H., Stauffer, J., Soderblom, D. R., King, J. R., & Hanson, R. B. 1998, ApJ, 504, 170

Pollack, J. B., Hollenbach, D., Beckwith, S., Simonelli, D. P., Roush, T., & Fong, W. 1994, ApJ, 421, 615

Pollack, J. B., Hubickyj, O., Bodenheimer, P., Lissauer, J. J., Podolak, M., & Greenzweig, Y. 1996, Icarus, 124, 62

Press, W. H., Teukolsky, S. A., Vetterling, W. T., & Flannery, B. P. 1992, Numerical recipes in C. The art of scientific computing, ed. Press, W. H., Teukolsky, S. A., Vetterling, W. T., & Flannery, B. P.

Pringle, J. E. 1989, MNRAS, 239, 361

Przygodda, F. 2004, PhD thesis, University of Heidelberg

Quanz, S. P., Apai, D., & Henning, T. 2007, ApJ, 656, 287

Quanz, S. P., Henning, T., Bouwman, J., Ratzka, T., & Leinert, C. 2006, ApJ, 648, 472

Ratzka, T., et al. 2009, A&A, 502, 623

Reach, W. T., et al. 2005, PASP, 117, 978

Reipurth, B., Rodríguez, L. F., Anglada, G., & Bally, J. 2004, AJ, 127, 1736

Rodmann, J., Henning, T., Chandler, C. J., Mundy, L. G., & Wilner, D. J. 2006, A&A, 446, 211

Rogers, F. J., Swenson, F. J., & Iglesias, C. A. 1996, ApJ, 456, 902

Roques, F., et al. 2004, in Bulletin of the American Astronomical Society, Vol. 36, Bulletin of the American Astronomical Society, 1069–+

Ruch, G. T., Jones, T. J., Woodward, C. E., Polomski, E. F., Gehrz, R. D., & Megeath, S. T. 2007, ApJ, 654, 338

Sauter, J., et al. 2009, A&A, 505, 1167

Schegerer, A., Wolf, S., Voshchinnikov, N. V., Przygodda, F., & Kessler-Silacci, J. E. 2006, A&A, 456, 535

Schegerer, A. A., Wolf, S., Hummel, C. A., Quanz, S. P., & Richichi, A. 2009, A&A, 502, 367

Schegerer, A. A., Wolf, S., Ratzka, T., & Leinert, C. 2008, A&A, 478, 779

Setiawan, J., et al. 2008, in Precision Spectroscopy in Astrophysics, ed. N. C. Santos, L. Pasquini, A. C. M. Correia, & M. Romaniello , 201–204

Sicilia-Aguilar, A., Henning, T., & Hartmann, L. 2010, ApJ, in press

Sicilia-Aguilar, A., Henning, T., Juhász, A., Bouwman, J., Garmire, G., & Garmire, A. 2008, ApJ, 687, 1145

Sicilia-Aguilar, A., et al. 2006, ApJ, 638, 897

—. 2009, ApJ, 701, 1188

Silverstone, M. D. 2000, PhD thesis, UNIVERSITY OF CALIFORNIA, LOS ANGELES

Skrutskie, M. F., et al. 2006, AJ, 131, 1163

Soderblom, D. R., et al. 2004, in Bulletin of the American Astronomical Society, Vol. 36, Bulletin of the American Astronomical Society, 735–+

Song, I., Zuckerman, B., Weinberger, A. J., & Becklin, E. E. 2005, Nature, 436, 363

Spangler, C., Sargent, A. I., Silverstone, M. D., Becklin, E. E., & Zuckerman, B. 2001, ApJ, 555, 932

Stapelfeldt, K. R., Krist, J. E., Menard, F., Bouvier, J., Padgett, D. L., & Burrows, C. J. 1998a, ApJL, 502, L65+

Stapelfeldt, K. R., et al. 1998b, ApJ, 508, 736

Stelzer, B., & Scholz, A. 2009, A&A, 507, 227

Su, K. Y. L., et al. 2006, ApJ, 653, 675

Telleschi, A., Güdel, M., Briggs, K. R., Audard, M., & Palla, F. 2007, A&A, 468, 425

Thébault, P., & Augereau, J. 2007, A&A, 472, 169

Trujillo, C. A., & Brown, M. E. 2001, ApJL, 554, L95

van Dokkum, P. G. 2001, PASP, 113, 1420

Wang, J., Feigelson, E. D., Townsley, L. K., Román-Zúñiga, C. G., Lada, E., & Garmire, G. 2009, ApJ, 696, 47

Wang, J., Townsley, L. K., Feigelson, E. D., Broos, P. S., Getman, K. V., Román-Zúñiga, C. G., & Lada, E. 2008, ApJ, 675, 464

Weingartner, J. C., & Draine, B. T. 2001, ApJ, 548, 296

Weisskopf, M. C., Brinkman, B., Canizares, C., Garmire, G., Murray, S., & Van Speybroeck, L. P. 2002, PASP, 114, 1

Werner, M. W., et al. 2004, ApJS, 154, 1

Wichmann, R., Schmitt, J. H. M. M., & Hubrig, S. 2003, A&A, 399, 983

Williams, G. G., Olszewski, E., Lesser, M. P., & Burge, J. H. 2004, in Society of Photo-Optical Instrumentation Engineers (SPIE) Conference Series, Vol. 5492, Society of Photo-Optical Instrumentation Engineers (SPIE) Conference Series, ed. A. F. M. Moorwood & M. Iye, 787–798

Winston, E., et al. 2007, ApJ, 669, 493

Wolf, S., & Hillenbrand, L. A. 2003, ApJ, 596, 603

Wolf, S., Padgett, D. L., & Stapelfeldt, K. R. 2003, ApJ, 588, 373

Wolf, S., Schegerer, A., Beuther, H., Padgett, D. L., & Stapelfeldt, K. R. 2008, ApJL, 674, L101

Wolf, S., Stecklum, B., & Henning, T. 2001, in IAU Symposium, Vol. 200, The Formation of Binary Stars, ed. H. Zinnecker & R. Mathieu, 295–+

Wolf, S., et al. 2007, Very Large Telescope MATISSE Science Cases, Tech. Rep. VLT-TRE-MAT-15860-4325 2007, MATISSE consortium

Wyatt, M. C. 2005, A&A, 433, 1007

Wyatt, M. C., Dermott, S. F., Telesco, C. M., Fisher, R. S., Grogan, K., Holmes, E. K., & Piña, R. K. 1999, ApJ, 527, 918

Wyatt, M. C., Smith, R., Greaves, J. S., Beichman, C. A., Bryden, G., & Lisse, C. M. 2007a, ApJ, 658, 569

Wyatt, M. C., Smith, R., Su, K. Y. L., Rieke, G. H., Greaves, J. S., Beichman, C. A., & Bryden, G. 2007b, ApJ, 663, 365

Xu, Y., Reid, M. J., Zheng, X. W., & Menten, K. M. 2006, Science, 311, 54

Zuckerman, B., & Becklin, E. E. 1993, ApJ, 414, 793

Zuckerman, B., & Song, I. 2004, ApJ, 603, 738

Zwahlen, N., North, P., Debernardi, Y., Eyer, L., Galland, F., Groenewegen, M. A. T., & Hummel, C. A. 2004, A&A, 425, L45